Simon Nils Grossjohann

Static and Dynamic Properties of low dimensional Quantum Spin Systems

Cuvillier Verlag Göttingen
Internationaler wissenschaftlicher Fachverlag

Static and Dynamic Properties of low dimensional Quantum Spin Systems

DISSERTATION

zur Erlangung des Grades

Doktor der Naturwissenschaften (Dr.rer.nat.)

der Fakultät für Elektrotechnik, Informationstechnik, Physik
der Technischen Universität Carolo-Wilhelmina zu Braunschweig

vorgelegt von Simon Nils Grossjohann aus Salzgitter

am July 25, 2010

1. Referent: Prof. Dr. W. Brenig
2. Referentin: Prof. Dr. G. Zwicknagl

Bibliografische Information der Deutschen Nationalbibliothek
Die Deutsche Nationalbibliothek verzeichnet diese Publikation in der Deutschen Nationalbibliografie detaillierte bibliografische Daten sind im Internet über http://dnd.d-nb.de abrufbar.
1. Aufl. - Göttingen: Cuvillier, 2010
Zugl.: (TU) Braunschweig, Univ., Diss., 2010

978-3-86955-419-8

Nonnenstieg 8, 37075 Göttingen
Telefon: 0551-54724-0
Telefax: 0551-54724-21
www.cuvillier.de

1. Auflage, 2010
Gedruckt auf säurefreiem Papier

978-3-86955-419-8

Vorveröffentlichungen der Dissertation

1. N. Fukushima, A. Honecker, S. Wessel, S. Grossjohann, and W. Brenig, *Specific Heat and Magnetic Susceptibility of Ferromagnetic Mixed-Spin Chain Systems*, Physica B **359-361**, 1409 (2005).

2. C. Mennerich, H.-H. Klauss, M. Broekelmann, F. J. Litterst, C. Golze, R. Klingeler, V. Kataev, B. Büchner, S.-N. Grossjohann, W. Brenig, M. Goiran, H. Rakoto, J.-M. Broto, O. Kataeva, and D. J. Price, *Antiferromagnetic dimers of Ni(II) in the S=1 spin ladder* $Na_2Ni_2(C_2O_4)_3(H_2O)_2$, Phys. Rev. B **73**, 174415 (2006).

3. S. Grossjohann and W. Brenig, *Spin-Dynamics of the antiferromagnetic S=1/2-Chain at finite magnetic Fields and intermediate Temperatures*, Phys. Rev. B **79**, 094409 (2009).

4. H. Kühne, H.-H. Klauss, S. Grossjohann, W. Brenig, F. J. Litterst, A. P. Reyes, P. L. Kuhns, M. M. Turnbull and C. P. Landee, *Quantum critical dynamics of a S=1/2 antiferromagnetic Heisenberg chain studied by* ^{13}C*-NMR spectroscopy*, Phys. Rev. B **80**, 045110 (2009).

5. H. Kühne, M. Günther, S. Grossjohann, W. Brenig, F. J. Litterst, A. P. Reyes, P. L. Kuhns, M. M. Turnbull, C. P. Landee, and H.-H. Klauss, *Low frequency spin dynamics in the quantum magnet copper pyrazine dinitrate*, Physica B **247**, 671 (2010), Front Cover.

6. S. Grossjohann and W. Brenig, *Hydrodynamic limit for the spin dynamics of the Heisenberg chain from quantum Monte Carlo calculations*, Phys. Rev. B **81**, 012404 (2010).

Tagungsbeiträge

1. S. Grossjohann, A. Honecker and W. Brenig, *Interchain Coupling in Mixed-Spin Quantum-Ferrimagnets*, Poster, DPG Frühjahrstagung Berlin, 04.03-09.03.2005

2. C. Mennerich, C. Golze, V. Kataev, A. Alfonsov, R. Klingeler, B. Büchner, D.J. Price, M. Goiran, H. Rakoto, J.-M. Broto, O. Kataeva, M. Broekelmann, S. Grossjohann, W. Brenig, and H.-H. Klauss, *High Field Magnetization and ESR on a $S = 1$ Spin Ladder*, Poster, DPG Frühjahrstagung Dresden, 27.03.-31.03.2006

3. H.-H. Klauss, F. Gouider, F.J. Litterst, S. Grossjohann, A. Honecker, W. Brenig, and D.J. Price, *Mössbauer Study of the Fe(II) S=2 Spin Chain System $K_2Fe(C_2O_4)_2$*, Poster, DPG Frühjahrstagung Dresden, 27.03.-31.03.2006

4. S. Grossjohann and W. Brenig, *Thermodynamics of intermediate-spin Heisenberg-chains*, Poster, DPG Frühjahrstagung Dresden, 27.03.-31.03.2006

5. S. Grossjohann and W. Brenig, *Dynamics of the spin-1/2 Heisenberg chain in magnetic fields*, Poster, Korrelationstage Dresden, 26.02.-02.03.2007

6. H. Kühne, J. Litterst, H.-H. Klauss, S. Grossjohann, W. Brenig, A.P. Reyes, P.L. Kuhns, C.P. Landee, M. M. Turnbull, H.-J. Grafe, J. Haase, and B. Büchner, *Quantum Critical Spin Dynamics of a Cu(II) S=1/2 antiferromagnetic Heisenberg chain studied by ^{13}C-NMR spectroscopy*, Poster, DPG Frühjahrstagung Regensburg, 26.03.-30.03.2007

7. S. Grossjohann, W. Brenig, H. Kühne and H.-H. Klauss, *High-Field NMR Relaxation Rates in Spin-1/2 Heisenberg-Chains*, Poster, DPG Frühjahrstagung Regensburg, 26.03.-30.03.2007

8. H. Kühne, H.-H. Klauss, J. Litterst, S. Grossjohann, W. Brenig, A.P. Reyes, P.L. Kuhns, C.P. Landee, M. M. Turnbull, H.-J. Grafe, J. Haase, and B. Büchner, and J. Haase, *Quantum Critical Spin Dynamics of a Cu(II) S=1/2 antiferromagnetic Heisenberg chain studied by ^{13}C-NMR spectroscopy*, Talk, DPG Frühjahrstagung Berlin, 25.02.-29.02.2008

9. S. Grossjohann, W. Brenig, H. Kühne and H.-H. Klauss, *Quantum Critical Dynamics of the S=1/2 AFM Heisenberg Chain in Finite Magnetic Fields: a QMC Study*, Talk, DPG Frühjahrstagung Berlin, 25.02.-29.02.2008

10. M. Günther, H. Kühne, H.-H. Klauss, M. Falkner, J. Litterst, S. Grossjohann, W. Brenig, A.P. Reyes, P.L. Kuhns, C.P. Landee, and M.M. Turnbull, *Low frequency spin dynamics in the S=1/2 Heisenberg chain compound* $Cu(C_4H_4N_2)(NO_3)_2$ *(CuPzN) measured by* ^{13}C *and* ^{14}N*-NMR spectroscopy*, Poster, DPG Frühjahrstagung Dresden, 22.03.-27.03.2009

11. S. Grossjohann and W. Brenig, *Spin-Dynamics of the antiferromagnetic S=1/2-Chain at finite magnetic Fields and intermediate Temperatures*, Poster, DPG Frühjahrstagung Dresden, 22.03.-27.03.2009

12. B. Willenberg, S. Grossjohann, and W. Brenig, *Magnetic impurities in two-dimensional spin-1/2 antiferromagnets*, Poster, DPG Frühjahrstagung Dresden, 22.03.-27.03.2009.

Contents

1 Introduction **11**

2 Methods **19**

2.1 Basic working principle of (Quantum) Monte Carlo 21

2.2 Stochastic Series Expansion: general framework 22

2.3 Updates 25

2.3.1 Diagonal update 25

2.3.2 Loop update 29

2.3.3 Directed loop and generalization to spin S 30

2.4 Observables 34

2.4.1 Static quantities 34

2.4.2 Dynamic quantities 37

2.4.3 Errors 44

2.5 Maximum Entropy 46

2.5.1 The continuation problem 46

2.5.2 Singular value decomposition 49

2.5.3 Regularization – the Maximum Entropy formalism 51

2.5.4 Meshkov-Algorithm 58

2.5.5 Bryan-Algorithm 61

2.5.6 Conclusion 63

3 Static properties of low dimensional quantum magnets **65**

3.1 Spin S chains – searching the classical limit . . . 67
3.1.1 Magnetic susceptibilities . . . 68
3.1.2 Padé-fits . . . 70
3.1.3 Conclusion . . . 73
3.2 Spin S=1 ladder system . . . 74
3.2.1 Magnetic susceptibility . . . 75
3.2.2 High-field magnetization . . . 79
3.2.3 Conclusion . . . 83
3.3 Spin S grid systems . . . 84
3.3.1 The effect of center-spin coupling . . . 84
3.3.2 The effect of single-ion anisotropy . . . 87
3.3.3 Comparison to experimental data . . . 92
3.3.4 Conclusion . . . 94

4 Dynamic properties of 1D quantum magnets 95
4.1 Dynamic structure factors of the spin 1/2 Heisenberg chain . . . 99
4.1.1 Longitudinal dynamic structure factor $S^{zz}(q,\omega)$ . . . 99
4.1.2 Transverse dynamic structure factor $S^{xx}(q,\omega)$ . . . 106
4.1.3 T_1-relaxation rate of the spin 1/2 Heisenberg chain . . . 110
4.1.4 Sum rules . . . 116
4.1.5 Conclusion . . . 118
4.2 Dynamic structure factors of the Haldane chain . . . 119
4.2.1 Temperature dependence of the transverse DSF . . . 119
4.2.2 Temperature dependence of the gap $\Delta(T)$ . . . 121
4.2.3 Low-q behavior . . . 122
4.2.4 Field dependence of the transverse DSF . . . 124
4.2.5 NMR rates . . . 128
4.2.6 Sum rules . . . 131
4.2.7 Conclusion . . . 132

4.3 Hydrodynamic limit for the spin dynamics of the Heisenberg chain 134

5 Conclusion **143**

Bibliography **149**

The very last lines ... **163**

Chapter 1

Introduction

Most of the properties of simple metals can be accounted for by models where the conduction electrons are described by effectively free fermions, i.e. are described by a kinetic energy, an effective mass, and Pauli's principle. In some systems however, the Coulomb repulsion between electrons and the effects of exchange-correlations cannot be ignored. Once the interaction energy between electrons becomes comparable to their kinetic energy, the notion of *strongly correlated electron systems* (see [1] for an overview) has been established. Such systems exhibit a diversity of exotic and interesting properties, e.g. high-temperature superconductivity [2], heavy fermion behavior [3], and quantum magnetism [4].
Among the simplest models to describe itinerant electrons with strong correlations mediated via Coulomb repulsion is the Hubbard model

$$H = -t \sum_{\langle i,j\rangle,\sigma} \left(c^{\dagger}_{i,\sigma} c_{j,\sigma} + h.c. \right) + U \sum_{i} n_{i\uparrow} n_{i\downarrow}. \tag{1.1}$$

This Hamiltonian describes a hopping of electrons from one lattice site to another through creation $c^{\dagger}_{i,\sigma}$ and annihilation operators $c_{j,\sigma}$ with an additional Coulomb repulsion U between two electrons on the same site. At half filling and in the strong coupling limit $U >> t$, the Hubbard model can be reduced to the Heisenberg model

$$H = J \sum_{\langle i,j\rangle} \left[\Delta S^z_i S^z_j + \frac{1}{2} \left(S^+_i S^-_j + S^-_i S^+_j \right) \right] + g\mu_B B \sum_i S^z_i + D \sum_i (S^z_i)^2 \tag{1.2}$$

with $J = t^2/U$. While the kinetic and potential energies in real space are not of similar magnitude in the Heisenberg limit, this phenomenon still pertains to the spin space. In fact the exchange energy $\frac{J}{2} \left(S^+_i S^-_j + S^-_i S^+_j \right)$ is of identical magnitude as the Ising energy $J\Delta S^z_i S^z_j$ for the isotropic point $\Delta = 1$. These play a role similar to that of the

kinetic and potential energy, which becomes particularly evident in one dimension by a mapping to spinless fermions via the Jordan Wigner transformation $S_j^- = e^{-i\phi_j} a_j$, $S_j^+ = e^{i\phi_j} a_j^\dagger$, $S_j^z = a_j^\dagger a_j - \frac{1}{2} = n_j - \frac{1}{2}$. The phase $\phi_j = \pi \sum_{q=1}^{j-1} n_j$ counts the number of spinless fermions left of lattice site j to fulfill fermion commutation relations [5].

$$H = J \sum_{\langle i,j \rangle} \left[\Delta \left(n_i - \frac{1}{2} \right) \left(n_j - \frac{1}{2} \right) + \left(a_i^\dagger a_j + h.c. \right) \right] + g\mu_B B \sum_i \left(n_i - \frac{1}{2} \right) \quad (1.3)$$

In this picture, the coupling anisotropy Δ sets the ratio of kinetic to potential energy similar to the ratio U/t, and the the application of a magnetic field (Zeeman term) translates into the notion of a chemical potential, regulating the filling of the conduction band. Furthermore, the single-ion anisotropy D was introduced in eqn. (1.2) as a relevant model parameter for this thesis, owing to orbital quenching and spin-orbit coupling for spin $S \geq 1$ materials.

Despite its simplicity, the Heisenberg Hamiltonian is still a challenging subject for theory. Up to present times only static properties of the spin S=1/2 chain have been given exactly by Bethe in 1931 [6, 7] while it still proves to be challenging to calculate matrix elements of dynamic correlation functions for this particular system. Next to the well established Bethe ansatz [6] and field theoretical approaches (e.g. bosonization, conformal field theory, non-linear σ-model ([8–12]), *numerical* methods such as exact diagonalization (ED), lanczos diagonalization ([13, 14]), density matrix renormalization group (DMRG, [15] and ref. therein) and quantum Monte Carlo (QMC, [16] and ref. therein) play a key role in evaluating static and dynamic properties of quantum spin models.

The physics of the Heisenberg model, its critical behavior, and its ground state phases are influenced by the interplay of intrinsic properties, such as dimensionality, spin magnitude (i.e. quantum fluctuations), or magnetic frustration, and by extrinsic influences, such as magneto-elastic coupling or disorder. In particular the interplay of quantum fluctuations and reduced dimensions leads to many unusual effects. Focusing on one dimension, the absence of long range order has been established by Bethe's exact solution of the eigenvalue problem [6] for the spin S=1/2 chain. Field theoretical methods resulted in a critical exponent $\eta = 1$ of the algebraically decaying spin-spin correlation function $\langle S_i S_j \rangle \propto (-1)^{|i-j|} (\log |i-j|)^{1/2} / |i-j|^\eta$ (extensive review see [17]) and its low-energy properties are well described by those of a Luttinger liquid (LL) [9, 18], i.e. a description of bosonic collective excitations (spinons) with only two defining parameters: the spinon velocity v of the linear dispersion and the renormalized Luttinger parameter K which establishes interactions and governs the

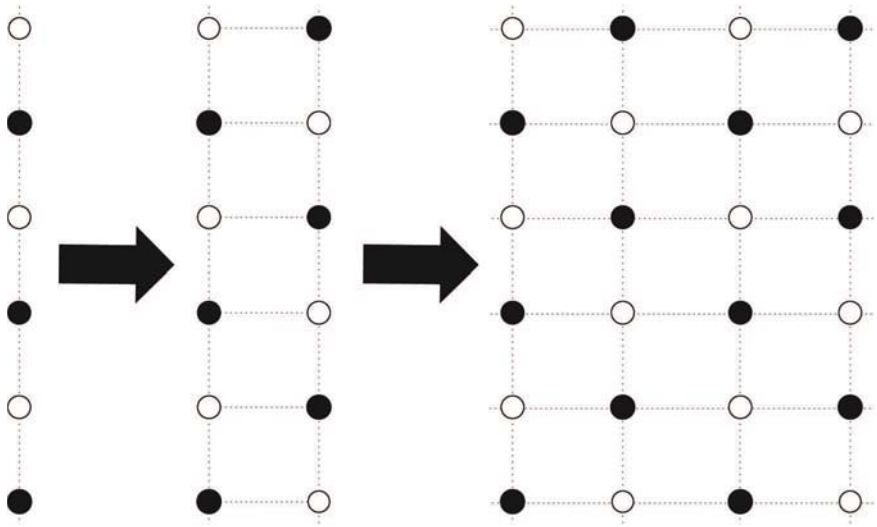

Figure 1.1: Illustration of the transition from a spin chain over a two-leg spin ladder to a two-dimensional plane. Empty, respectively closed circles stand for spins pointing up/down.

power-law decay of most correlation functions. With static properties well understood [7], dynamic and spin transport properties are however *still* subjects of discussions.

After establishing quantum criticality for the spin-1/2 chain, it came as a surprise when Haldane, employing the non-linear O(3) σ-model (NLσM) in a semi-classical large-spin approximation, suggested that only the half-integer spin chains are critical whereas all integer spin-chains have an energy gap Δ in the excitation spectrum [19]. As consequence, all thermodynamic properties activate exponentially and the spin-spin correlation function decays as $\langle S_i S_j \rangle \propto e^{-|i-j|/\xi}$ with a finite correlation length $\xi \propto 1/\Delta$[1].

The existence of a finite correlation length in the integer spin chains categorizes them as spin liquids, i.e. spin systems with no long range order and only short-range correlations. Another class of spin liquids relevant for my thesis is found in form of spin ladders [23], i.e. by increasing the dimensionality through linking chains into a two-dimensional alignment (see Fig. 1.1 for illustration). Such ladder systems alternate between spin liquid behaviour for even and critical behavior for odd number

[1] Note, that the ground state of the spin S=1 chain was found to have a hidden topological *string*-order [20–22].

of legs. A particularly interesting aspect of spin liquids in dimensions $d \geq 2$ is their field driven quantum phase transition into an ordered phase by condensing of the lowest magnon excitations (Bose-Einstein condensate). In the vicinity of the critical eld B_c, a universal scaling of the critical temperature T_c as function of magnetic field strength was predicted $T_c \propto (B - B_c)^\alpha$ with $\alpha = 3/2$ [24]. For $d = 1$, a breaking of the continuous XY-symmetry is permitted by Mermin-Wagner's theorem, therefore a critical temperature does not exist. However, in an already magnetized state there remains no conceptual difference in the low energy properties between spin ladders, integer and half-integer spin chains [25, 26]. Interestingly, this crossover into a Luttinger liquid is driven by *increasing* the magnetic field. For the spin S=1/2 chain it is observed upon *decreasing* the magnetic field through its critical value.

In my thesis, the main points of interest are (i) numerical methods and (ii) static and dynamic properties of spin systems in reduced dimensionality and in the vicinity of quantum critical points. The thesis is structured threefold. In the first part, the employed QMC method will be introduced. In a small introduction of the most common numerical methods, I will motivate our choice as QMC proves to be a very powerful and flexible tool, tailored for evaluation of large systems in any dimension down to essentially zero temperature. Its adjacent discussion features a small introduction to quantum Monte Carlo and systematically explains its implementation for the particular case of the stochastic series expansion (SSE). The latter provides a detailed discussion about measuring longitudinal and transverse imaginary time observables which, to the best of my knowledge, is still insufficiently documented in literature. As a consequence of results in imaginary time, two common analytic continuation algorithms will be introduced in section 2.5. Such continuations from imaginary to real axis are required to perform comparisons with experiments such as inelastic neutron scattering (INS) or nuclear magnetic resonance (NMR). After the methodical aspect of this thesis, results will be presented in chapter 3 and 4. While the first part of my results (chapter 3) features exclusively static quantities of low-dimensional spin systems, the second part (chapter 4) focuses on dynamic properties of the spin S=1/2 and S=1 chain with a short introduction to spin transport of the spin S=1/2 system.

In further detail, chapter 3 is divided threefold: the first section 3.1 deals with thermodynamic properties of quantum spin S chains with $S \in \{1/2, 1, 3/2, 2, 5/2\}$. By means of the static susceptibility we contrast the quantum spin model with a classical $S \to \infty$ limit by Fisher [27]. After a finite size analysis for all spin magnitudes in a temperature range $0.01 \leq T/J \leq 100$, we find that even for the largest evaluated spin S=5/2 there are considerable differences in terms of the maximum position and the

low temperature behavior compared to the $S \to \infty$ limit. Additionally, Padé-fits are given for the whole evaluated temperature region to allow for an analytical access to our numerical data. We evaluate our fit quality through a comparison to high-accuracy Bethe-ansatz data in the case of spin S=1/2 and suggest improvements of commonly used fit formulas available in literature for all evaluated spin magnitudes.

In section 3.2, we analyze thermodynamic properties of a spin S=1 two-leg ladder as function of rung/leg coupling and single-ion anisotropy. Such a ladder system is unique in many regards: first of all we know that even-leg spin S=1/2 ladders show spin liquid behavior and naturally we expect the same for a spin S=1 ladder system. In the coupling limits of zero inter-chain and zero intra-chain coupling, we find two uncoupled Haldane chains, respectively uncoupled dimers – both systems which display a strong spin gap. In the region of intermediate coupling however, Todo *et al.* showed a weakening of the gap by nearly two orders of magnitude. At this point we utilize QMC in the thermodynamic limit to show that for intermediate coupling ratios and an additional small easy-plane anisotropy, the system seems to become *gapless*. This results in finite susceptibilities even at lowest elevated temperatures $T/J = 0.001$ and the low-temperature magnetization profile loses the typical step-structure of a spin ladder. Additionally we compare our results to susceptibility and magnetization measurements of Mennerich *et al.* [28] on a Ni(II) based spin S=1 ladder material in order to elaborate on its coupling constants. Ultimately, all comparisons point at weakly coupled dimers for this system with a small easy-plane anisotropy – too small to lift the gap.

In the last section of chapter 3, we study an essentially zero-dimensional [3 × 3]-grid system with large spin S=5/2, motivated by susceptibility and magnetization measurements on a molecular magnet based on Mn(II) ions [29]. Such molecular magnet with such a large effective magnetic moment may have many technically interesting applications, such as e.g. storage device for conventional bits due to the large relaxation time of the magnetization (one month at 2K) or as basis for quantum computing if the tunnel barrier of the Néel vector is not too large. Interestingly, the system exceeds the computational limits of exact diagonalization despite its small size, which means exact theoretical results are largely absent. Among the observables we compute are susceptibility, magnetization and (staggered) static structure factor as function of temperature, center spin coupling, magnetic field and single-ion anisotropy. As far as the temperature and center-spin coupling variation is concerned, we find very low impact on the form of the susceptibility. High- as well as low temperatures show solely Curie behavior with very marginal variation in an intermediate temperature region $1 \leq T/J \leq 10$. Upon variation of the single- ion anisotropy however, strong

effects occur. For a small easy-plane anisotropy, the system aligns immediately in-plane, leading to an Ising-like total spin S=1/2 with clear fingerprints in the magnetization steps and (staggered) structure factor. Likewise we find an immediate aligning along the z-axis with the application of a small easy-axis anisotropy, leading to a total spin S=5/2 with clear indications given in the magnetization profile and (staggered) structure factor. Finally, with an extensive parameter study, we provide a very accurate description for the whole available temperature region $1K \leq T \leq 300$K to the experimental susceptibility of the Mn-[3×3] grid and our magnetization profile qualitatively reflects magneto-torque measurements performed by O. Waldmann [30].

Chapter 4 is also divided threefold. In section 4.1 we study dynamic properties of the Heisenberg spin S=1/2 chain as function of temperature and magnetic field – a parameter-combination where theoretical results are lacking. Among our observables are longitudinal as well as the transverse structure factor for the Luttinger liquid regime $0 \leq B < B_c$ up to fields beyond the saturation field. We detail the field and temperature dependence of the incommensurate fermi vectors and clarify finite temperature q-dependence of the system at full polarization by a two-magnon excitation model. Additionally we analyze the $1/T_1$-relaxation rate and successfully compare it to experiments by H. Kühne *et al.* [31]. Their experiments and our numerical results strongly reflect the condensation of magnons upon *decreasing* the field through the saturation field B_c in a diverging relaxation rate for $T \to 0$. Interestingly, the maximum of the $1/T_1$-relaxation rate at finite temperatures is found *below* the critical field for both, theory and experiment.
The same critical behavior of a level-crossing magnon dispersion has mostly been looked at upon *increasing* the magnetic field for gapped systems such as Haldane chain or spin ladder materials. With that in mind, we look at the dynamics of the Haldane system as function of temperature and magnetic field in section 4.2, which, in the case of $B = 0$, is fundamentally different from the dynamics of the spin S=1/2 chain. The Haldane dynamics are dominated by a sharp, gapped magnon dispersion while the spin S=1/2 system is known to consist of spinons spanning an energy continuum. However, upon increasing the field for the Haldane system, the spin gap closes and the system can be described by a Luttinger liquid again, resembling the dynamic properties of the spin S=1/2 system discussed earlier. In that regard, we look at the evolution of the transverse dynamic structure factor as function of field and temperature and discuss it for the gapped $0 \leq B \leq B_{c_1}$ and the LL regime $B_{c_1} \leq B \leq B_{c_2}$. Furthermore we extract the relaxation rate and show its exponential increase by populating the gap through heating, respectively upon approaching the first critical field at a fixed finite temperature. Both, section 4.1 as well as 4.2, close with a discussion of sum rules as a consistency check for our analytic continuations from the imaginary to the real axis.

This leads to section 4.3 (as follow-up to dynamic properties of the spins S=1/2 Heisenberg chain), dealing with transport properties of the isotropic spin S=1/2 Heisenberg chain, which has been under intense scrutiny since one decade without coherent results for the nature of the transport at the SU(2) symmetric point, e.g. ballistic or diffusive. Unfortunately our analytical continuations with the commonly assumed error of 10-20% are not sufficiently accurate to enter this discussion with reasonable arguments on the real axis. Very recently however, spin diffusion has been conjectured to governs the low-frequency spectrum of the regular conductivity which provides for an approximate expression of the Fourier transform of the retarded spin susceptibility [32]. This expression can be transformed to imaginary time, where our QMC results are *only* subject to statistical errors. With considerable numerical effort we show that our data is supporting a diffusive channel for the XXZ-model, which opens up the intriguing possibility of a finite temperature dynamical spin conductivity of the Heisenberg model which comprises both, a finite Drude weight and a regular part with a large mean free path at low temperatures.

Chapter 2

Methods

The wide field of correlated electrons supported the development of numerous numerical and analytical methods in order to deal with static and dynamic quantities of the here considered Heisenberg Hamiltonian (eqn. (1.2)). On the one hand there are analytical methods (often combined with numerical evaluation) such as the Bethe-Ansatz (BA, mapping to fermion systems, [6, 33, 34]), quantum field theoretical approaches (bosonization [8–10], non-linear σ-model (NLSM) [11, 12, 19]) and perturbational approaches such as high order series expansions [35–37]. On the other hand there are numerical approaches with the most prominent methods being exact (ED) and Lanczos diagonalization [13, 14], density matrix renormalization group (DMRG, [15] and ref. therein) and finally Quantum Monte Carlo (QMC, [16] and ref. therein). In order to get a small overview let me introduce the most dominant methods up to date briefly.

Bethe-Ansatz: Bethe-Ansatz was introduced in 1931 [6] and provided the first exact eigenvalues and eigenstates to the spin 1/2 Heisenberg chain. It is based on a mapping of the spin operators to spinless fermions which is very well described in a tutorial work for the ferromagnetic [33], antiferromagnetic [34] and the two-spinon dynamics of the antiferromagnetic S=1/2 Heisenberg chain [38]. The method is doubtless the best choice in the limited framework of spin S=1/2 and one dimension. However it still proves to be challenging to calculate matrix elements of spectral functions and only *very* recently, higher spinon contributions to the dynamic structure factor have been evaluated.

Conclusion: *First choice method for static properties of spin S=1/2 Heisenberg chains, dynamic properties nevertheless challenging.*

ED & Lanczos: Exact diagonalization is based on setting up the whole Hamilton-operator in a chosen basis and find its eigenvalues and eigenstates by diagonalization. This technique has the advantage of being applicable to all models and topologies at all temperatures with the downside of suffering from finite size effects due to memory limitations of the exponentially growing matrix dimensions with system size. To get an idea about the computational limits: without abusing symmetries a spin S=1/2 chain with 24 spins has a matrix dimension of 2^{24} which leads to storage requirements of 10^{15} Byte or roughly 1000TByte. A Lanzcos diagonalization can handle bigger systems on cost of the full spectrum – in contrast to ED only the lowest eigenvalues are extracted by an iterative procedure which accumulates rounding errors, resulting eventually in a loss of orthogonality of the eigenstates.

Conclusion: *Excellent all-around method without any model and observable limitations, only drawback set through excessive memory consumption due to exponentially increasing Hilbert space (ED), respectively numerical rounding errors (Lanzcos).*

DMRG: While ED works on the full Hilbert space and is thus limited to small systems, DMRG methods are based on an efficient truncation of the density matrix. This is achieved by an iterative increasing of the system size with adjacent reduction of the density matrix to its most significant (instead of the lowest-lying!) eigenstates. This way the system is approaching the thermodynamic limit with high numerical accuracy and an efficient control on memory consumption. For an extensive review see [15] and references therein. Currently this method is among the best methods to study one dimensional problems at finite and zero temperatures. It has also been applied to real time dynamics very recently [39–41] but numerical results also show the major drawback of this method: for longer timescales as well as for higher dimensions the needed spectral dimensions in order to achieve the desired numerical accuracy is exponentially growing, which currently limits the method to one dimension and short time scales.

Conclusion: *Currently the strongest method for 1D systems without model limitations. System dynamics are only accessible for small time scales.*

QMC: QMC methods are based on efficient sampling of the Hilbert space by intelligent picking of configurations with high thermodynamic weight and will be explained in depth in the next chapter (for an extensive overview see [16]). Advanced methods such as the stochastic series expansion (SSE) [42] achieve linear scaling in system size and

inverse temperature which allows impressive numerical simulations such as one million spins S=1/2 on a Heisenberg square lattice [43]. The strengths of performing well at the thermodynamic limit for any spin magnitude and any finite temperatures with exact treatment of the Hamiltonian makes the QMC one of the best choices method for comparisons with experiments, only hindered by the so called *sign problem*. The sign problem is an issues that affects the method generally when frustration comes into play, which in return limits the applicability of the method to bipartite lattices, respectively non-frustrating coupling topologies (even though there exist workarounds for the sign problem in some special cases [44, 45]). In addition to the sign-problem, dynamic correlations can only be measured in imaginary time, which leads to challenging analytic continuations to the real axis in oder to compare with experimental observables such as the inelastic neutron scattering or T_1-relaxation rates.

Conclusion: *Very flexible method in one and higher dimensions, favorable for direct comparisons with experiments since thermodynamic limit and impurity concentrations of any kind are relatively simple to reach/implement. Frustration hardly accessible due to sign problem, dynamic observables require analytic continuation.*

It is apparent that all introduced methods share a common denominator while each of them also comes with their very own limitations. In this thesis we went for an implementation of a QMC algorithm for its broad field of possible applications, its independency of spin magnitude, dimension or system size at all temperatures and magnetic fields. This broadness of applications will become most obvious in chapter 3 and it led to numerous cooperations with experiments over the course of this thesis.

2.1 Basic working principle of (Quantum) Monte Carlo

The basic idea behind (Quantum) Monte Carlo is based on the thermodynamic expectation value of an observable A as a sum over all configurations c of the Hilbert space

$$\langle A \rangle = \sum_c A_c e^{-\beta E_c} / Z$$

with the partition function

$$Z = \sum_c e^{-\beta E_c}$$

and $\beta = 1/k_B T$ as inverse temperature. A few things are hindering the simple evaluation of the sum. First of all the Eigenvalues $E_c|\psi_c\rangle = H|\psi_c\rangle$ are unknown in a quantum

problem and if they were known there would have been no problem left to evaluate. The second drawback is the evaluation of the sum itself, which is exponentially growing with system size. For a better understanding consider the example of an Ising spin system with N spins: each spin can either be pointing up or down which relates to an exponentially growing configurational space of 2^N. To overcome this scaling issue, the Metropolis-algorithm [46] offers an efficient sampling of the most important configurations of the Hilbert space by means of a Markov-chain process with transition probabilities between two configurations c_i and c_j given by

$$P_{c_i \to c_j} = \frac{W_{c_j}}{W_{c_i}} = e^{-\beta(E_{c_j} - E_{c_i})}. \tag{2.1}$$

Here $W_{c_i} = e^{-\beta E_{c_i}}/Z$ is the thermodynamic weight of a configuration. Note how ergodicity

$$\forall c_i, c_j \quad \exists n \quad : \quad P^n_{c_i \to c_j} \neq 0 \tag{2.2}$$

and detailed balance

$$P_{c_i \to c_j} W_{c_i} = P_{c_j \to c_i} W_{c_j} \tag{2.3}$$

is fulfilled per construction of the transition probabilities. Thanks to the canceling out of the partition function in eqn. (2.1) one can apply this scheme directly to any classical problem, measure observables in any update step and finally average over all measurements, which ultimately yields

$$\langle A \rangle \approx \bar{A} = \frac{1}{M} \sum_{n=1}^{M} A_n. \tag{2.4}$$

For quantum problems, one more hurdle has to be overcome, namely the eigenvalues E_{c_i} in order to calculate transition probabilities. To deal with this final problem is what distinguishes different QMC methods – the general idea is a mapping of the N-dimensional quantum problem to an (N+1)-dimensional problem where only local matrix elements have to be calculated in order to create new configurations. Leaving the path of generality, i want to introduce one example of a state of the art QMC method, the so called Stochastic Series Expansion (SSE). Its implementation was already part of my diploma thesis and throughout the course of my thesis it has been extended and speed-up considerably.

2.2 Stochastic Series Expansion: general framework

The general idea behind the SSE is a series expansion of the partition function Z in β which goes back to D. C. Handscomb [47] whose algorithm built the basis for further

development by A. Sandvik in collaboration with O. F. Syljuåsen and J. Kurkijärvi in the early 90s [42, 48–51]. Sampling in such a representation is carried out on summands of the expansion, i.e. expectation values of operator products with variable length. To set up the cornerstone for sampling we introduce a local presentation by rewriting the Hamiltonian (1.2) into N_b bond-operators

$$H = -J \sum_{b=1}^{N_b} H_b \tag{2.5}$$

and splitting the bond-operators further into a diagonal and an off-diagonal part

$$H_b = H_{1,b} + H_{2,b} \tag{2.6}$$

where

$$H_{1,b} = C - \Delta S^z_{i(b)} S^z_{j(b)} + h_b \left(S^z_{i(b)} + S^z_{j(b)} \right) \tag{2.7}$$

$$H_{2,b} = \frac{1}{2} \left(S^+_{i(b)} S^-_{j(b)} + S^-_{i(b)} S^+_{j(b)} \right). \tag{2.8}$$

For bipartite lattices, the number of bonds is determined by the number of sites N, the dimension d and the boundary conditions. For periodic boundary conditions in a non-diluted d-dimensional system N_b reads $N_b = Nd$. Care has to be taken of the magnetic field h_b, which is to be seen as a fractional contribution per neighbor and therefore is a number that changes on dimensionality and dilution. To pick an example, we find $h_b = g\mu_B B/2$ for an undiluted chain. Note that we left out the single-ion anisotropy D from eqn. (1.2) for convenience – D gives a diagonal contribution and has to be treated exactly as the Zeeman term. The constant C in (2.7) is chosen in a way that all matrix elements are positive, ensuring non-negative Metropolis weights during the sampling procedure. For now its value does not play any important role – details regarding its choice will be discussed in Section 2.3.

With the localization of the Heisenberg-Hamiltonian in mind, we now expand the partition function Z

$$Z = Tr(e^{-\beta H}) = Tr \left(\sum_{n=0}^{\infty} \frac{(-\beta)^n}{n!} H^n \right) = \sum_{\alpha} \sum_{n=0}^{\infty} \frac{(-\beta)^n}{n!} \langle \alpha | H^n | \alpha \rangle \tag{2.9}$$

where the trace is carried out as a sum over basis states $|\alpha\rangle = |S^z_1, S^z_2, \ldots, S^z_N\rangle$ in a chosen eigenbasis (here S^z). A more elegant way to rewrite the series expansion follows from introducing the so called operator string $S_n = [a_1, b_1], [a_2, b_2], \ldots, [a_n, b_n]$ with $a_i \in \{1, 2\}$ and $b_i \in \{1, 2, \ldots, N_b\}$

$$\sum_{n=0}^{\infty} \sum_{b=1}^{N_b} (H_{1,b} - H_{2,b})^n \Longrightarrow \sum_{S_n} \prod_{i=1}^{n} H_{a_i, b_i} \tag{2.10}$$

which takes care of all possible operator products of length n in the expansion. With this change, (2.9) reads

$$Z = \sum_{\alpha} \sum_{n=0}^{\infty} \sum_{S_n} \frac{(-\beta)^n}{n!} \langle \alpha | \prod_{i=1}^{n} H_{a_i,b_i} | \alpha \rangle. \tag{2.11}$$

An algorithmic simplification follows from changing the sum over n and product $1 \ldots n$ into a fixed length representation of length $M = M(\beta)$[1], where we use $M - n$ $\mathbb{1}$-operators to fill up the operator string. In other words, S_n is extended by a new a_i ($\Rightarrow a_i \in \{0, 1, 2\}$) which enables all possible orders in the fixed string representation up to a maximum order M. Taking the $\binom{M}{n}$ possibilities of distributing $M - n$ $\mathbb{1}$-operators into account, we end up with

$$Z = \sum_{\alpha} \sum_{S_M} \frac{(-1)^n \beta^n (M-n)!}{M!} \langle \alpha | \prod_{i=1}^{M} H_{a_i,b_i} | \alpha \rangle \tag{2.12}$$

for the expansion of the partition function. One main weakness of the method stems from the sign $(-1)^n$ of the operator strings with various order. On a bipartite lattices and nearest neighbor coupling this sign will automatically vanish since initial state $|\alpha(0)\rangle$ and final state $|\alpha(M)\rangle = \prod_{i=1}^{M} H_{a_i,b_i} |\alpha(0)\rangle$ need to be equal to contribute which is ensured by a pairwise occurrence of off-diagonal operators. On frustrated lattices however (for example triangular geometries, frustrated next-nearest neighbor couplings on bipartite lattices, also fermion systems), an uneven number of off-diagonal operators is possible and the algorithm develops the so called *sign problem*. The sign itself is not problematic since observables can be sampled along with the sign – the problem is rather the statistics of the sign at low temperatures which makes frustrated systems in general hardly accessible for QMC methods. There exist workarounds for specific problems ([44, 45, 52]), but since the sign problem plays no role in this thesis it will not be discussed in more detail here.

To summarize what has been done: the partition function has been expanded in a series with a Hamiltonian which was split into local diagonal and off-diagonal bond-operators. The expansion was cut off at large enough $M(\beta)$ in a fixed length representation where low orders $n < M$ are achieved by filling in $M - n$ $\mathbb{1}$-operators into the system. Demands on a sampling procedure are changes of

- the number of non-unit operators in the system
- the number of diagonal versus off-diagonal operators

[1] Section 2.3 will explain, why a finite cutoff does *not* introduce systematic errors to the algorithm.

- the state of spins when there is no operator acting on a lattice site

while being *ergodic* (2.2) and preserving *detailed balance* (2.3). The algorithmic details of the update-procedure will be discussed in the next section 2.3.

2.3 Updates

In this section it will be discussed, how new operator strings S_M are created, or in other words, how updates of the kind $[a_i, b_i] \leftrightarrow [a_i', b_i']$ are performed under the constraint of preserving *detailed balance* and *ergodicity*. While an algorithm is certainly ergodic by using Metropolis transition weights, there is still a problem of rapidly growing autocorrelation times near a system's critical points. This is probably best portrayed on the two-dimensional classical Ising-system near its critical temperature $T/J = 2.269$, displayed in Fig. 2.1: at high temperatures local updates still provide efficient sampling of the configuration space. At temperatures at or below the critical temperature (here $T/J = 1$), clusters form and extremely long autocorrelation times prevent any meaningful output. By flipping whole clusters of equally aligned spins instead of energetically expensive local changes, Swendsen-Wang and Wolff cluster algorithms have provided major improvements in update-efficiency near this critical point.

Similar cluster updates exist for QMC methods such as the SSE or algorithms in continuous time (for an extensive overview, see [16]). In the case of the SSE, the update is splitted into two different updates. Firstly the so called *diagonal* update, which performs *local* changes of the expansion order $n \rightarrow n \pm 1$ by replacing unit-operators with diagonal operators and vice versa $[0, b_i] \leftrightarrow [1, b_i]$. Secondly the so called *loop* update which performs changes of the kind $[1, b_i] \leftrightarrow [2, b_i]$ in a cluster type of upgrade.

In the following subsections, the update procedures will be discussed in depth, including corresponding Metropolis weights, generalizations to spin-S models, and an efficiency tuning of the *loop update*, known as *directed loop*.

2.3.1 Diagonal update

In this section the working principle of the *diagonal update* will be explained. The update, as the name suggests, acts solely on diagonal operators and samples the

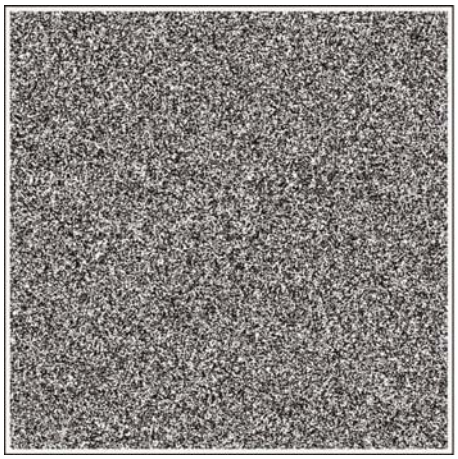
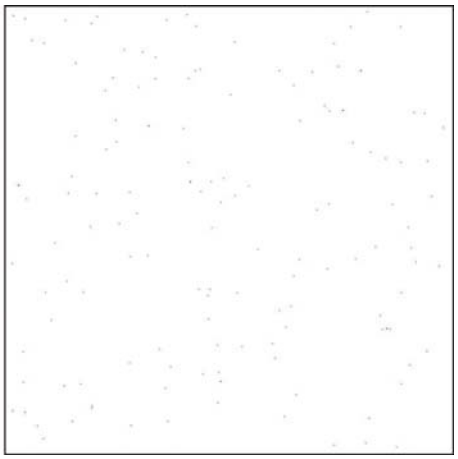

Figure 2.1: Left: Ferromagnetic *ISING* spin system with 640x640 spins (white dot=↑, black dot=↓) at $T/J = 5$. Local updates are able to create new configurations efficiently. Right: Below the critical temperature (here $T/J = 1$), clusters form (large white region). Local updates are not able to create new configurations efficiently since the energy cost to flip a local spin against its neighbors is too high – the system starts to freeze in one orientation and autocorrelation times diverge.

operator string *length n* by performing *local* changes of the kind $[0, b_i] \leftrightarrow [1, b_i]$ at every position of the operator string. For the following, a typical graphical representation is helpful to understand the basic algorithm (see Fig. 2.2). Shown is an expanded 5-site spin S=1/2 chain up to maximum order of $n = 6$ with one diagonal H_{1,b_0}, two off-diagonal H_{2,b_2} and the rest of the expansion filled up with $\mathbb{1}$-operators. We therefore look at the summand $\langle\alpha|H_{2,b_2}H_{1,b_0}H_{2,b_2}|\alpha\rangle$ – one among many contributions to eqn. (2.12).

Following the Metropolis updating scheme (2.1), the probability to accept a change leading from a configuration c_i to a new configuration c_j is given by

$$P_{c_{i\to j}} = \min\left(1, \frac{W_j}{W_i}\right) \tag{2.13}$$

with

$$W_i = \frac{1}{Z}\frac{\beta^n (M-n)!}{M!}\langle\alpha|\prod_{i=1}^{M} H_{a_i,b_i}|\alpha\rangle \tag{2.14}$$

$$W_j = \frac{1}{Z}\frac{\beta^{n\pm1} (M-(n\pm1))!}{M!}\langle\alpha|\prod_{i=1}^{M} H_{a_i,b_i}|\alpha\rangle \tag{2.15}$$

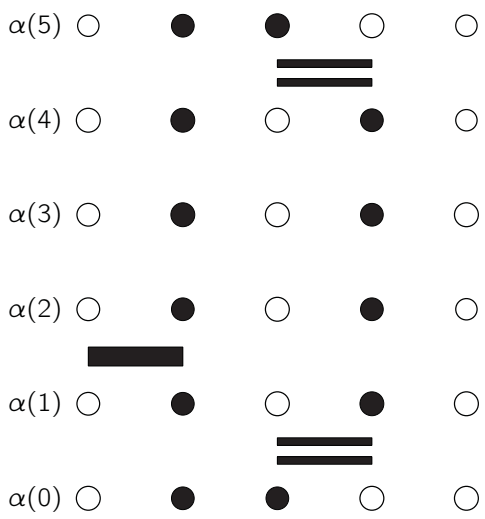

Figure 2.2: Expanded 5-site spin S=1/2 chain up to maximum order of $n = 6$ with one diagonal H_{1,b_0}, two off-diagonal H_{2,b_2} and the rest of the expansion filled up with $\mathbb{1}$-operators. Solid (empty) circles stand for spin up (down), consequently solid bars donate diagonal operators, double bars off-diagonal ones.

depending on whether we insert $(+)$ or remove $(-)$ a diagonal operator. With those weights, the probability to *insert* an operator into the expansion at expansion position p and random bond b_i reads

$$P\left([0, b_i] \to [1, b_i]\right) = \min\left(1, \frac{N_b \beta \langle \alpha(p)|H_{1,b}|\alpha(p)\rangle}{M - n}\right), \tag{2.16}$$

where the factor N_b stems from the N_b possibilities to replace a $\mathbb{1}$-operator by a diagonal operator at any empty expansion order position p. Note that, given a perfect implementation, the processing time of any given problem should scale only *linear* in system size, inverse temperature and diagonal matrix elements of the Hamiltonian (e.g. applied magnetic fields for the Heisenberg model). In other words: the defining key-strengths of the QMC are condensed in equation (2.16)!

To complete the *diagonal update* section, eqns. (2.14) and (2.15) yield

$$P\left([1, b_i] \to [0, b_i]\right) = \min\left(1, \frac{M - n + 1}{N_b \beta \langle \alpha(p)|H_{1,b}|\alpha(p)\rangle}\right). \tag{2.17}$$

for the Metropolis probabilities to *remove* a diagonal operator at position (p, b_i).

In the implementation of the algorithm, a loop from initial state $|\alpha(0)\rangle$ to $|\alpha(M)\rangle$ is performed and each slice of the expansion order is checked for the presence of any

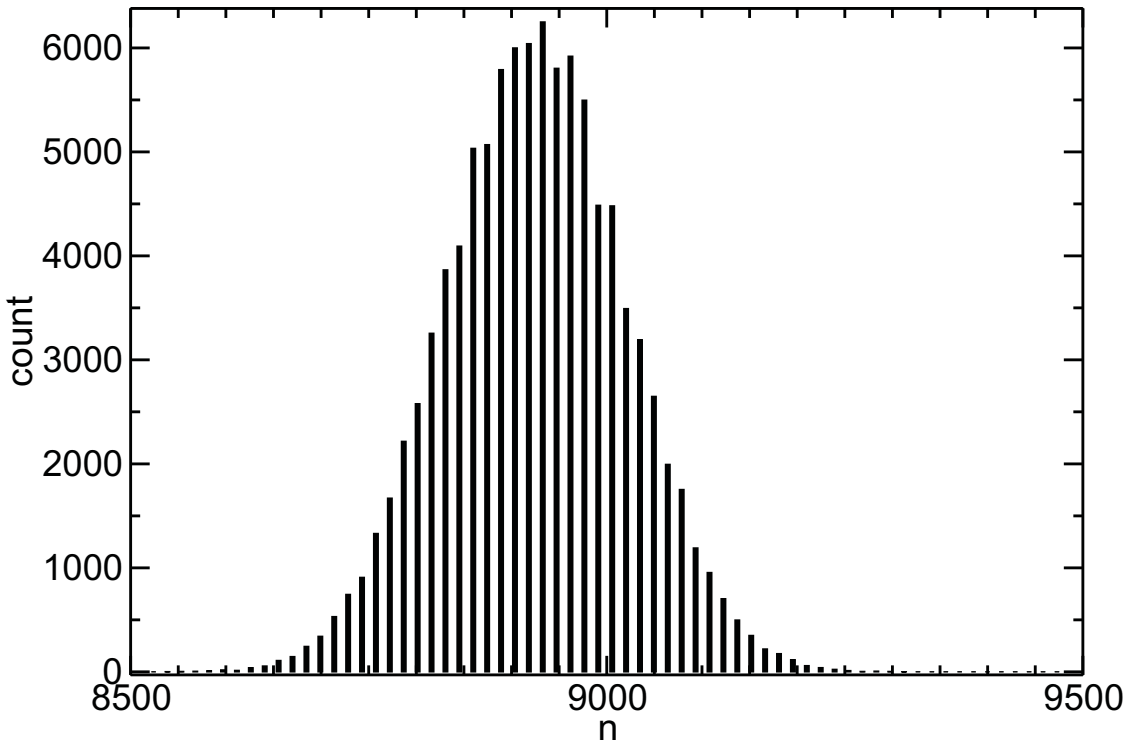

Figure 2.3: Histogram of the expansion order of a QMC run for a spin S=1/2 chain with 100 sites at $T/J = 0.01$. The cutoff during thermalization was adjusted to be $M = 13000$, typically $1.2 - 1.5 \times n_{\mathrm{max}}$ in order to avoid possible cutoff effects.

non-unit operator. If a diagonal one is found, roll for removal with probability given by (2.17), reducing the expansion order $n \to n-1$ eventually. If there is no operator, roll for insertion according to (2.16) with a new expansion order $n \to n+1$ on a successful roll. Finally, in the case of an off-diagonal operator, move on to the next slice without any changes.

Looking at the probabilities to insert/remove an operator, it is now also comprehensible, that at large enough M there will be a balance of inserting and removing operators which ultimately leads to a gaussian distribution of the average number of operators $\langle n \rangle$ in the expansion (see Fig. 2.3). Therefore one has to choose the cutoff M carefully in an equilibration phase in order to avoid cropping the distribution of n which in return justifies the truncation of the expansion in (2.12).

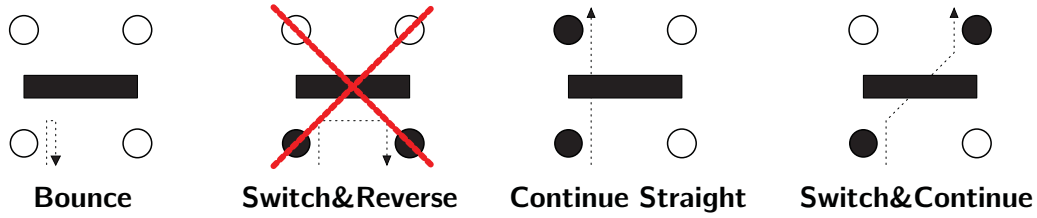

Figure 2.4: Illustration of the four possible ways through an example operator of a Heisenberg spin S=1/2 system. Solid circles stand for spin down, open circles stand for spin up which means the initial operator is one with both "incoming" and "outgoing" spins pointing up. As illustrated, the *bounce* process leaves an operator untouched and exits through the entry spin. *Switch and reverse*, as shown second, is not among the valid choices, since the new configuration does not exist. *Continue straight* leaves the diagonal operator a diagonal operator, but with one spin pointing up and one pointing down. Finally the last choice *switch and continue* changes the initial diagonal operator into an off-diagonal operator (S^+S^- operation).

2.3.2 Loop update

After introduction of the *diagonal update* with operator string length sampling $[0, b_i] \leftrightarrow [1, b_i]$, a second so called loop update is required for changes of the kind $[1, b_i] \leftrightarrow [2, b_i]$ which, in combination with a state update of free spins, should deplete the whole Hilbert space of the system. It is important to note that, while the *diagonal update* is not susceptible to critical system parameters, the *loop update* is. To overcome efficiency problems with large autocorrelation times, the *loop update* is designed as a cluster update and its basic idea is explained in a few words: pick a random position in the expansion and insert a discontinuity $S^{\pm}S^{\mp}$, depending on the spin state at that particular position. Now let the "head" or "tail" of that discontinuity move in one direction, while spins get flipped on its path. Upon meeting any kind of non-unit operator, there are four ways to traverse as illustrated in Fig. 2.4:

1. **Bounce**: leaves operator untouched and undoes changes that have been made on the way to the operator

2. **Switch and reverse**: changes diagonal into off-diagonal operators and vice versa

3. **Continue straight**: leaves diagonal/off-diagonal operators

4. **Switch and continue**: changes diagonal into off-diagonal operators and vice versa.

Both ways which include switching the real-space coordinate perform the desired sampling $[1, b_i] \leftrightarrow [2, b_i]$, the other ways leave the operator type untouched[2]. After this kind of directed random-walk through the expansion, where the traverse-probabilities through operators are again given by a Metropolis scheme as will be explained in the next subsection, the "head" and "tail" of the discontinuity will eventually meet and "heal" out. A new configuration has been created and, owing to its cluster character, it is a very efficient update even at critical system parameters.
An algorithmic side note at this point: typically one performs more than just one of those loops to reduce autocorrelation times between a full QMC-update (diagonal and consecutive loop update). A well working rule of thumb is, that on average a full loop update should reach every operator at least once which in praxis means that about 20 up to 1000 loops per diagonal update are performed. Parameters such as the average number of loops N_l or the cutoff M are adjusted in an equilibration phase and remain unchanged for measurements of observables to prevent biasing results.

2.3.3 Directed loop and generalization to spin S

In the last subsection, the loop update's general working principle was presented. This subsection will account for the implementation details such as traverse probabilities through operators and the algorithmic generalizations of spin S.

Traverse probabilities through operators need to fulfill detailed balance (2.3) and ergodicity (2.2). While ergodicity can be proven for the loop update, it is detailed balance that sets up the equations for the correct probabilities of the four possible ways in Fig. 2.4:

$$W_c P(c, e, x) = W_{c'} P(c', x, e). \tag{2.18}$$

Here, W_c is the local weight of the operator before traversing, $W_{c'}$ the weight after traversing, $P(c, e, x)$ the probability to enter at entry spin $e \in 0, 1, 2, 3$ and exit the operator at exit spin $x \in 0, 1, 2, 3$.

[2] Continue straight changes the operator, but not the type as in diagonal/off-diagonal.

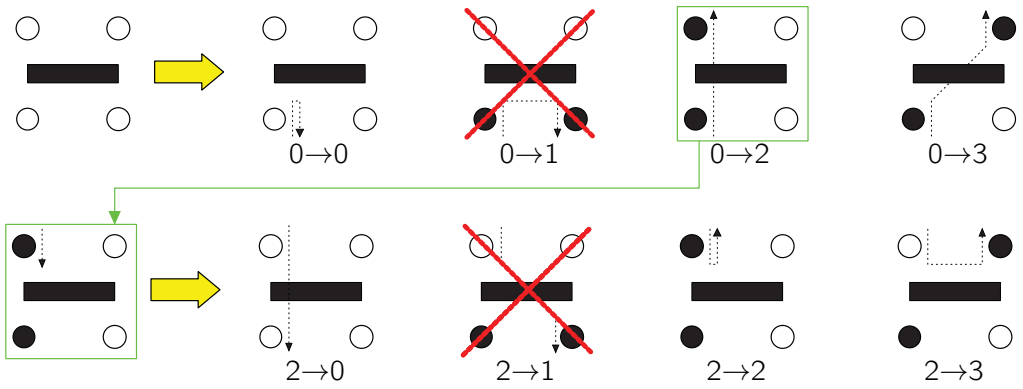

Figure 2.5: Illustration of detailed balance for the Heatbath-solution. Entering the initial Operator with weight W_c (two spins up) at spin $e = 0$ and leaving it at spin $x = 2$ leads to the same Heatbath-denominator as by entering the newly created operator with weight $W_{c_{e,x}}$ at spin $e' = 2$ and leaving at exit spin $x' = 0$.

Since the loop has to exit at any leg, there is a second equation given by

$$\sum_{x=0}^{3} P(c, e, x) = 1. \tag{2.19}$$

Equation (2.18) and (2.19) combined form a set of equations called *directed loop* equations. A very simple solution is given by the *Heatbath* traverse probabilities

$$P(c, e, x) = \frac{W_{c_{e,x}}}{\sum_{x=0}^{3} W_{c_{e,x}}}, \tag{2.20}$$

where $W_{c_{e,x}}$ are the weights of the newly created operators by entering at spin e and leaving at spin x. That the Heatbath-solution (2.20) fulfills the directed loop equations is easily shown. For (2.18) we find

$$\begin{aligned} W_c P(c, e, x) &= W_c \frac{W_{c'}}{\sum_{x=0}^{3} W_{c_{e,x}}} \\ &= W_{c'} \frac{W_c}{\sum_{x=0}^{3} W_{c_{e,x}}} \\ &= W_{c'} P(c', x, e). \end{aligned}$$

To comprehend the last line, note that by entering the newly created operator $W_{c'} = W_{c_{e,x}}$ at its former exit spin x leads to the same denominator in eqn. (2.20) as by entering the initial operator W_c at its entry spin e (see Fig. 2.5).

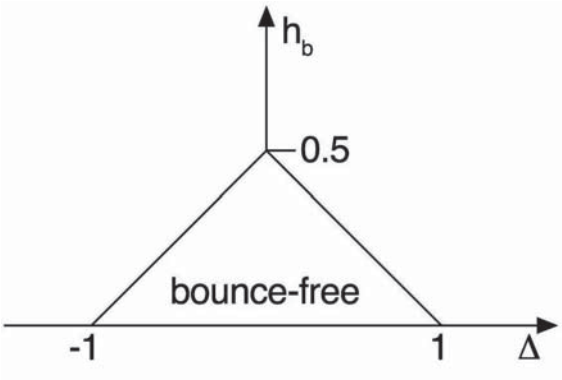

Figure 2.6: Algorithmic phase-diagram showing bounce-free solutions for the spin S=1/2 Heisenberg model.

As for (2.18) we immediately find eqn. (2.19) fulfilled:

$$\sum_{x=0}^{3} P(c,e,x) = \frac{\sum_{x=0}^{3} W_{c_{e,x}}}{\sum_{x=0}^{3} W_{c_{e,x}}} = 1.$$

The heatbath solution is a particularly simple way to set up the probability tables for all traverse ways through all types of operators in the system. Nevertheless it represents just *one* solution in the more general framework of the directed loop equations (2.18) and (2.19). A reason to take a closer look at a more optimized probability set is motivated by bounce-probabilities. Bounces are always valid choices when a loop arrives at an operator and choosing to bounce means that a loop will be partially undone – a very unfavorable behavior since CPU time for creating and undoing changes is wasted in such a case.
To create a more advanced set of probabilities, one can set up all directed loop equations and optimize the solution in regard to minimum bounce probabilities. By doing this one can achieve whole parameter regions of the Hamiltonian, where bounce-free solutions exist (see Fig. 2.6). In my algorithm, the solution is found by the use of a free linear programming solver "lpsolve" [53].

To get an idea about the complexity of the equation system, I hereby present some typical examples:

1. Spin S=1/2 Heisenberg, 4 diagonal and 2 off-diagonal operators, number of detailed balance equations: $192N_b$, number of bounce probabilities to minimize: $12N_b$

2. Spin S=1 Heisenberg, 9 diagonal and 8 off-diagonal operators, number of detailed balance equations: $1088N_b$, number of bounce probabilities to minimize: $68N_b$

3. Spin S=3/2 Heisenberg, 16 diagonal and 18 off-diagonal operators, number of detailed balance equations: $3264N_b$, number of bounce probabilities to minimize: $204N_b$

4. Spin S=2 Heisenberg, 25 diagonal and 32 off-diagonal operators, number of detailed balance equations: $7296N_b$, number of bounce probabilities to minimize: $456N_b$

5. Spin S=5/2 Heisenberg, 36 diagonal and 50 off-diagonal operators, number of detailed balance equations: $13760N_b$, number of bounce probabilities to minimize: $860N_b$

Given numbers stem from the formula $4S \times$ [# of operators] $\times$ [# of entry spins] $\times$ [# of exit spins] $\times$ [# of bonds]. In this formula, $4S$ accounts for the different types of the loop update. While for $S = 1/2$, only spin-flips $\Delta m = \pm 1$ are allowed, there are $4S$ so called *loop colors* possible in spin S systems. In practice this means that, at the starting point of a loop, one has to choose randomly among the allowed loop colors. In practice this also means, that loops with $|\Delta m| > 1$ are unfavorable, since generally less traverse probabilities through operators are allowed (= non-zero). Since one of the allowed ways will always be bounce (even though minimized by the linear programming solver), the relative weight of bounces increase for such loops.
Partially there are very interesting workarounds for such problems, such as for example for the spin S=1 model, where $\Delta m = \pm 2$ bounce probabilities can be *maximized* to be the only allowed way [54]. What appears to be contra-productive on first sight, allows to leave out loops of the color $\Delta m = \pm 2$ completely, since the update is deterministic and will end after immediately bouncing back to the starting position without changing anything in the system.

The improvements by "tuning" traverse probabilities in the general directed loop framework are visible most of all at low temperatures when the amount of operators in the

system becomes larger and more operators are reached within a single random walk. Autocorrelation times decrease substantially [50] and less loop updates are required to visit each operator at least once on average.

2.4 Observables

It is ever-surprising how close the QMC actually resembles experiments. Simulations are performed at finite temperatures and in the thermodynamic limit, observables are "measured" during runtime and, just like any real experiment, the QMC quantities are subject to errors – statistical errors in this case. Due to the $1/\sqrt{N}$ behavior of the standard deviation σ

$$\sigma = \sqrt{\frac{1}{N}\sum_{i=1}^{N}(A_{c_i} - \bar{A})^2}, \tag{2.21}$$

simulation runtimes have to be approximately quadrupled in order to achieve double accuracy of any observable A.

This section is divided into three subsections. Firstly, there is an introduction on how static quantities are measured within the formalism of the SSE. Among them standard quantities such as susceptibility, magnetization, energy, specific heat and correlation functions.
Secondly, measurements of dynamic quantities will be explained in detail. The main focus here lies on the longitudinal and transverse dynamic structure factor, which can be related both, to dynamic and static quantities. Overall measuring such an observable is quite involved and post-processing of QMC data is required to create a basis for comparisons with experimental data.
This section is finally closed by a short discussion about error propagation.

2.4.1 Static quantities

In the latest version of the algorithm, the following static quantities are measured each update:

- magnetization $M(q) = \frac{1}{N}\sum_m e^{iqm} S^z_m$
- energy E

- longitudinal susceptibility $\chi^{zz}(q)$
- specific heat C
- static longitudinal real space correlations $C^{zz}(r_i, r_j) = \langle S^z_{r_i} S^z_{r_j} \rangle$
- static longitudinal structure factor $S^{zz}(q) = \frac{1}{N^2} \sum_{r_i, r_j} e^{iq(r_i - r_j)} C^{zz}(r_i, r_j)$.

Furthermore, there are a few other implemented static observables such as various *transverse* quantities (susceptibility, correlations, structure factors), which follow from Kubo-integrals of dynamic measurements. The way to obtain those is a subset of the next section and will be left out at this point.

To deduct a few quantities on the list above, basic thermodynamics are required. Starting with the magnetization M, which is given by the derivative

$$M = -\frac{\partial F}{\partial B} \tag{2.22}$$

of the free energy

$$F = -\frac{1}{\beta} \ln Z$$

where Z is the partition function given in (2.9) with Hamiltonian (1.2).
Equation (2.22) yields

$$M = \frac{1}{\beta Z} g\mu_B \beta \mathrm{Tr}\left[S^z e^{-\beta H}\right] = g\mu_B \langle S^z \rangle = \frac{g\mu_B}{N} \sum_{i=1}^{N} \langle \alpha(0) | S^z_i | \alpha(0) \rangle.$$

Hence the measurement in the SSE formalism requires a simple measurement of the S^z quantum number in $|\alpha(0)\rangle$, which is particularly easy in a code working in the S^z-basis.

The static uniform susceptibility χ is connected to the magnetization by

$$\chi = \frac{\partial M}{\partial B},$$

which leads to

$$\begin{aligned} \chi &= -\frac{g^2 \mu_B^2 \beta}{Z^2} \left(\mathrm{Tr}\left[S^z e^{-\beta H}\right]\right)^2 + \frac{g^2 \mu_B^2 \beta}{Z} \mathrm{Tr}\left[(S^z)^2 e^{-\beta H}\right] \\ &= g^2 \mu_B^2 \beta \left(\langle (S^z)^2 \rangle - \langle S^z \rangle^2\right). \end{aligned}$$

Consequently the susceptibility is measured alongside with the magnetization and its square.

In a system without outer field B, the inner Energy E is given by

$$E = \frac{1}{Z}\mathrm{Tr}\left[He^{-\beta H}\right] = 3\langle S_i^z S_{i+1}^z\rangle, \tag{2.23}$$

which means the nearest neighbor correlations need to be averaged over all QMC steps.

Just as the susceptibility, the specific heat is a second derivative of the grand potential

$$\begin{aligned} C &= k_B\beta^2\frac{\partial E}{\partial\beta} && (2.24)\\ &= k_B\beta^2\left(\langle E^2\rangle - \langle E\rangle^2\right). && (2.25)\end{aligned}$$

and thus it is a measure for the fluctuations of the inner energy. An important note at this point: the difference of two squared numbers in combination with the pre-factor β^2 makes the specific heat a statistically very unpleasant quantity, in particular for low temperatures. In practice, extremely high numerical effort is required to achieve sufficiently low relative errors for non-gapped systems.

For both, energy and specific heat, there exist so called *improved estimators*. Such estimators are algorithm-adapted measurements which are very fast or simple to perform and often yield improvements regarding statistics, autocorrelations times or the like.
In the case of the inner energy (and also the specific heat), one finds an improved estimator by starting at the series expansion of the partition function, which is connected with the inner energy by

$$E = -\frac{\partial}{\partial\beta}\ln Z.$$

With (2.12), the energy is given by the remarkably simple expression

$$E = -\frac{1}{Z}\frac{\partial}{\partial\beta}\left(\sum_{S_M}\frac{(-\beta)^n(M-n)!}{M!}\mathrm{Tr}\left[\prod_{i=1}^{M}H_{a_i,b_i}\right]\right) = \frac{1}{\beta}\langle n\rangle. \tag{2.26}$$

Evaluating (2.24) again in the formalism of (2.26), one ends up at a very similar expression for the specific heat

$$C = \langle n^2\rangle - \langle n\rangle^2 - \langle n\rangle. \tag{2.27}$$

Finally, there are longitudinal correlations $C^{zz}(r_i, r_j)$ and their q-space fourier-transform $S^{zz}(q)$ (longitudinal static structure factor). Just as the magnetization or susceptibility,

correlations are measured in the initial state $|\alpha(0)\rangle$, but to improve the statistical quality, an averaging over all M slices of the expansion order, so called *cyclic averaging*, is beneficial[3]:

$$\langle S^z_{r_i} S^z_{r_j} \rangle = \frac{1}{M} \sum_{p=0}^{M-1} \langle \alpha(p) | S^z_{r_i} S^z_{r_j} | \alpha(p) \rangle. \tag{2.28}$$

2.4.2 Dynamic quantities

The measurement of longitudinal and in particular transverse dynamic correlation functions is probably among the most involved quantities to obtain by a QMC method. While static quantities *only* require operations on $|\alpha(0)\rangle$ (with optional statistic improvements by averaging over all slices), dynamic quantities need informations about the full expanded system, which is not only far more complicated conceptually, but also slows down the algorithm considerably.

The motivation to look at dynamic correlations is given by experiments such as inelastic neutron scattering (INS) or nuclear magnetic resonance (NMR). Both experiments can be directly related to the dynamic structure factor (DSF) – in the case of INS, the scattering rates per solid angle and energy are directly proportional to

$$\frac{d\sigma^2}{d\Omega d\omega} \propto S^{\mu\nu}(q, \omega),$$

where $S^{\mu\nu}(q, \omega)$ is the space and time fourier-transform of the real-time correlation function

$$S^{\mu\nu}(q, \omega) = \sum_r \int_{-\infty}^{\infty} dt e^{-i(\omega t - qr)} \langle S^\mu_r(t) S^\nu_0(0) \rangle \tag{2.29}$$

and $\mu\nu \in \{zz, xx\}$. At zero magnetic field, longitudinal and transverse correlations are equal due to SU(2) invariance of the model but once a magnetic field is applied, a superposition of $S^{zz}(q, \omega)$ and $S^{xx}(q, \omega)$ is measured. To resolve those quantities further, polarized neutrons have to be used in experiments.

The NMR measures the relaxation of precessing nuclei spins – the so called nuclear spin-lattice relaxation time $1/T_1$, which refers to the mean time of an individual spin to return to its thermal equilibrium state after being flipped in an external field. This

[3] It is not beneficial for the magnetization measurement (which consequently includes the susceptibility), since the Hamiltonian preserves the spin ($[H, M] = 0$) and therefore every slice of the expansion just yields the exact same value for M.

quantity can also be directly related to the dynamic structure factor by a summation over all q-vectors, weighted with the hyperfine coupling form factor $A(q)$, evaluated at the NMR resonance frequency ω_R

$$1/T_1 \propto \sum_q A(q) S^{+-}(q, \omega_R), \tag{2.30}$$

which is equivalent to performing the limit $\omega_R \to 0$ in relation to typical coupling constants[4].
In other words: the dynamic structure factor is one of the most desirable quantities of a quantum spin system and it does not only contain all spectral information (which gives direct access to static quantities via sum-rules), but it is also the key-quantity for comparisons with more involved experimental methods.

In order to calculate the dynamic structure factor, real time correlation functions with time evolution in the Heisenberg picture

$$\langle S^{\mu}_{r_1}(t) S^{\nu}_{r_2}(0) \rangle = \frac{1}{Z} \mathrm{Tr} \left[e^{itH} S^{\mu}_{r_1} e^{-itH} S^{\nu}_{r_2} e^{-\beta H} \right] \tag{2.31}$$

need to be evaluated. Unfortunately, a direct evaluation of (2.31) by expanding the exponential functions in the SSE formalism (following steps (2.9) to (2.12)) is hindered by the heavy oscillating character of $e^{\pm itH}$ which leads to convergence problems when translating discrete QMC slices into time (simply replace "τ" by "it" in eqn. 2.34). A workaround is available by performing a Wick-rotation $it \to \tau$ and calculate (2.31) in *imaginary* time instead in order to transform the heavily oscillating exponential functions into exponentially decaying ones. Two questions remain: how to obtain imaginary time correlation functions within the SSE and, even more importantly, how to get back to the real axis in the end? The first question will be answered in the consecutive paragraphs, however the analytic continuation to the real axis will require a section of its own and will be discussed in depth in section 2.5.

To translate the expectation value for the imaginary version of (2.31) into SSE notation,

[4] Assuming $\omega_R \approx 10^9$ and $J \approx 1\mathrm{K}$ one finds $\hbar\omega_R/J \leq 10^{-2}$

the exponential functions are expanded

$$\begin{aligned}\langle S^{\mu}_{r_1}(\tau)S^{\nu}_{r_2}(0)\rangle &= \frac{1}{Z}\sum_{\alpha}\langle\alpha|\sum_{n=0}^{\infty}\frac{(\tau-\beta)^n}{n!}H^n S^{\mu}_{r_1}\sum_{m=0}^{\infty}\frac{(-\tau)^m}{m!}H^m S^{\nu}_{r_2}|\alpha\rangle \qquad (2.32)\\ &= \frac{1}{Z}\sum_{\alpha}\sum_{n=0}^{\infty}\sum_{m=0}^{n}\frac{(\tau-\beta)^{n-m}(-\tau)^m}{(n-m)!m!}\langle\alpha|H^{n-m}S^{\mu}_{r_1}H^m S^{\nu}_{r_2}|\alpha\rangle\\ &= \frac{1}{Z}\sum_{\alpha}\sum_{n=0}^{\infty}\sum_{S_n}\sum_{m=0}^{n}\frac{(\tau-\beta)^{n-m}(-\tau)^m}{(n-m)!m!}\\ &\quad\times\langle\alpha|\prod_{l=m+1}^{n}H_{a_l,b_l}S^{\mu}_{r_1}\prod_{k=1}^{m}H_{a_k,b_k}S^{\nu}_{r_2}|\alpha\rangle \qquad (2.33)\end{aligned}$$

In the case of $\mu\nu = zz$ (diagonal), one can extract the eigenvalues $S^z_{r_i}|\alpha(p)\rangle = S^z_{r_i}(p)|\alpha(p)\rangle$

$$\begin{aligned}\langle S^{z}_{r_1}(\tau)S^{z}_{r_2}(0)\rangle &= \frac{1}{Z}\sum_{\alpha}\sum_{n=0}^{\infty}\sum_{S_n}\frac{(-\beta)^n}{n!}\langle\alpha|\prod_{l=1}^{n}H_{a_l,b_l}|\alpha\rangle\\ &\quad\times\sum_{m=0}^{n}\frac{(\tau-\beta)^{n-m}(-\tau)^m n!}{(-\beta)^n(n-m)!m!}S^z_{r_i}(m)S^z_{r_j}(0).\end{aligned}$$

The partition function Z cancels out and the final result after truncation of the sum to M in the fixed string representation (see (2.12)) reads

$$\langle S^{z}_{r_1}(\tau)S^{z}_{r_2}(0)\rangle = \sum_{m=0}^{M}\binom{M}{m}\left(\frac{\tau}{\beta}\right)^m\left(1-\frac{\tau}{\beta}\right)^{M-m}\frac{1}{M}\sum_{p=0}^{M-1}S^z_{r_1}(m+p)S^z_{r_2}(p). \qquad (2.34)$$

with optional, but recommended cyclic averaging (compare with (2.28)).

With this conversion, the discrete expansion slices of the SSE are linked to continuous imaginary time via a binomial distribution which obviously has to hold for transverse correlations as well. Note, that working in a fixed string representation has the huge advantage of fixed binomial coefficients for the whole simulation at each temperature. This means that, instead of measuring in imaginary time, we can now "measure" correlations of states between each of the M slices, average over sufficient updates and convert to imaginary time through eqn. (2.34).

For diagonal operators, this measurement is very simple and can be performed in each diagonal update just as the averaging of equal-time correlation functions in (2.28). For

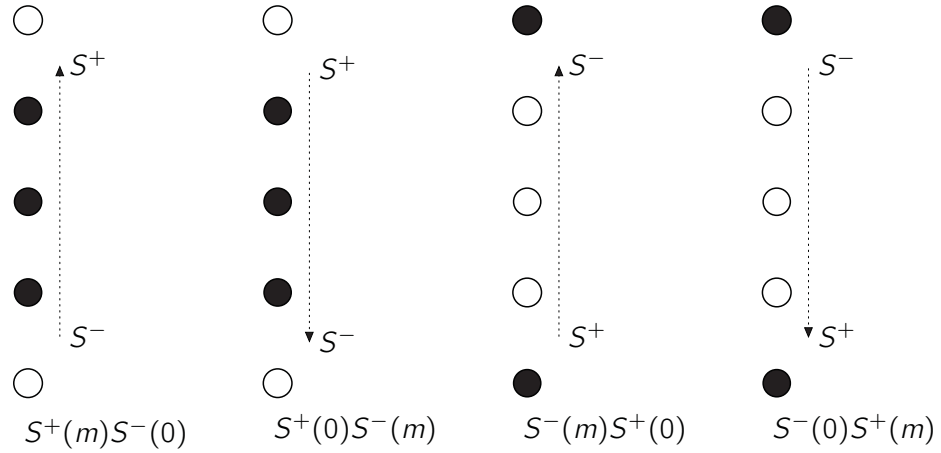

Figure 2.7: Illustration of the four possible cases of inserting a pair of S^+S^-/S^-S^+ with the head, respectively tail performing the directed random walk. Solid circles stand for spin down, open circles stand for spin up as in previous pictures.

off-diagonal operators, this is however a highly non-trivial task since, on the one hand, inserting a pair of raising and lowering operators needs to preserve detailed balance and, on the other hand, the process has to sample over all distances in space and expansion order.
Luckily, both requirements are already fulfilled in the loop update – thus it is obviously a good idea to measure correlations of the kind $\langle S^{\pm}_{r_1}(\tau)S^{\mp}_{r_2}(0)\rangle$ directly in the loop building process.

One can convince oneself quickly by permutations within the trace of eqn. (2.33), that

$$S^+_{r_1}(m)S^-_{r_2}(0) = S^-_{r_2}(M-m)S^+_{r_1}(0)$$

and likewise

$$\langle S^+_{r_1}(\tau)S^-_{r_2}(0)\rangle = \langle S^-_{r_2}(\beta-\tau)S^+_{r_1}(0)\rangle.$$

Furthermore we know that

$$\langle S^x_{r_1}(\tau)S^x_{r_2}(0)\rangle = \frac{1}{2}\left(\langle S^+_{r_1}(\tau)S^-_{r_2}(0)\rangle + \langle S^-_{r_1}(\tau)S^+_{r_2}(0)\rangle\right).$$

Consequently, in order to acquire *any* transverse correlation function it is sufficient to know either $\mu\nu = +-$ or $\mu\nu = -+$.

The actual recording process needs some considerations which will be explained in depth in the following paragraphs now. Given is a system of N spins of magnitude S with

a maximum expansion order M without restrictions to zero magnetic field. The first step in the loop building process is the random choice of a coordinate (r, m) with $r \in \{0, \ldots, N-1\}$ and $m \in \{0, \ldots, M\}$. Adjacent, the eigenvalue $S_r^z(m)$ at position (r, m) is evaluated, and a loop color is chosen given by the possible options in regard to the eigenvalue. Only if the color corresponds to spin-flips $|\Delta m| = 1$, correlation function during the loops construction can be measured, otherwise a loop update is performed without measuring. At this point there are four distinct cases (also see Fig. 2.7):

1. insertion of S^+S^-, S^+ moves up

2. insertion of S^+S^-, S^- moves down

3. insertion of S^-S^+, S^- moves up

4. insertion of S^-S^+, S^+ moves down

Case 1: The spin configuration allows the insertion of a S^+S^--discontinuity and the random number generator decides that S^+ moves up. All future measurements are performed relative to the starting position, assuming a translationally invariant system. That means during the random walk through the system, measurements of the type

$$S_r^+(m)S_0^-(0) = \langle\tilde{\alpha}(m)|S_r^+|\alpha(m)\rangle\langle\tilde{\alpha}(0)|S_0^-|\alpha(0)\rangle$$

are recorded.
A small but nevertheless important detail has to be taken into account: periodic boundaries in time. Once the loop reaches $S_r^+(M)S_0^-(0)$, we find by permutation of the matrix element in eqn. (2.33)

$$\begin{aligned} \langle\alpha|S_r^+H^MS_0^-|\alpha\rangle &= \langle\alpha|H^MS_0^-S_r^+|\alpha\rangle & (2.35)\\ &= \langle\alpha|H^MS_r^+S_0^-|\alpha\rangle, \quad r \neq 0, & (2.36)\end{aligned}$$

that means normal periodic boundaries $S_r^+(M)S_0^-(0) = S_r^+(0)S_0^-(0)$ apply for $r \neq 0$. For $r = 0$ however the loop is obviously closed, but the distinction between closing by moving up or closing by moving down has an important consequence: the final measurement $S_r^+(0)S_0^-(0)$ has to be left out in the case of the loop closing by moving up, but it must be included if the loop closes by moving down. This is not a particular feature of case 1, but a general feature, since $S_r^+(0)S_0^-(0)$ will never commute at the

point where the loop closes. Thus it is important to note, that for *all* cases, the final step may only be recorded, when the loop closes in the configuration which was originally inserted into the system.

Case 2: The spin configuration allows the insertion of a S^+S^--discontinuity and the random number generator decides that S^- moves down. With the loop construction, measurements of the type

$$S_0^+(0)S_r^-(m) \tag{2.37}$$

can be performed. Since correlation functions can only depend on the relative distances in space and time and the system is M-periodic, eqn. (2.37) can be rewritten to

$$\begin{aligned} S_0^+(0)S_r^-(m) &= S_0^+(-m)S_r^-(0) \\ &= S_r^+(M-m)S_0^-(0). \end{aligned}$$

That means even though the S^--tail moves around in the system, S^+S^- correlations can be measured by a simple re-numeration $m \to M - m$ of the slices.

Case 3: The spin configuration allows the insertion of a S^-S^+-discontinuity and the random number generator decides that S^- moves up. Correlations of the kind

$$S_r^-(m)S_0^+(0)$$

are recorded during loop construction. This expression can again be rewritten with the arguments of relative distance and permutation (compare eqn. (2.36))

$$\langle\alpha|H^{M-m}S_r^-H^mS_0^+|\alpha\rangle = \langle\alpha|H^mS_0^+H^{M-m}S_r^-|\alpha\rangle,$$

which leads to the measured quantity

$$S_r^-(m)S_0^+(0) = S_r^+(M-m)S_0^-(0)$$

(see also case 2).

Case 4: The spin configuration allows the insertion of a S^-S^+-discontinuity and the random number generator decides that S^+ moves down. Correlations of the kind

$$S_0^-(0)S_r^+(m)$$

can be measured. With the typical arguments of relative distance and permutation, one shows

$$\begin{aligned} S_0^-(0)S_r^+(m) &= S_0^-(-m)S_r^+(0) \\ &= S_0^-(M-m)S_r^+(0) \\ &= S_r^+(m)S_0^-(0), \end{aligned}$$

which equals the measurement of Case 1.

One important addition to the measurement of transverse correlation function has to be made for nonzero magnetic fields. While the imaginary time correlations are mirror-symmetric in time around the point $m = M/2$ for zero field, this symmetry is lost in the case of finite magnetic fields with the consequence that

$$S_0^\pm(M)S_0^\mp(0) \neq S_0^\pm(0)S_0^\mp(0), \quad \forall B > 0 \tag{2.38}$$

is not given by symmetry anymore. Unfortunately, this quantity is required for the $m \to \tau$ conversion and it is also needed to deduct other correlation functions (e.g. $-+, xx$ from $+-$). In the special case of $S = 1/2$, the knowledge about $S_0^z(0)S_0^z(0) = S_0^x(0)S_0^x(0) = 1/4$ allows to construct

$$\begin{aligned} 1/4 &= S_0^x(0)S_0^x(0) \\ &= \frac{1}{2}\left(S_0^+(0)S_0^-(0) + S_0^-(0)S_0^+(0)\right) \\ &= \frac{1}{2}\left(S_0^+(0)S_0^-(0) + S_0^+(M)S_0^-(0)\right) \\ \Leftrightarrow 1/2 - S_0^+(0)S_0^-(0) &= S_0^+(M)S_0^-(0). \end{aligned}$$

For general spin S and magnetic field $B > 0$ however, $S_0^\pm(M)S_0^\mp(0)$ has to be evaluated separately during the loop. Following case 1 till 4 we find that, whenever a $+-$ measurement is forbidden due to non-commutativity (at the very start or end of a loop), one can measure the $-+$ quantity $S_0^-(0)S_0^+(0) = S_0^+(M)S_0^-(0)$ instead, which turns out to be missing piece for the τ-conversion (2.34).

As a final note, there also exists an improved estimator for measurements of diagonal correlations such as $S_r^z(m)S_0^z(0)$, following classical cluster Monte Carlo estimators: since all spins on a loop are flipped it follows, that in a sum of "before" and "after" measurement, spins on the loop have zero correlation with the rest of the spins in the expanded system, whereas loop-spins are fully correlated. In other words: while recording transverse correlation functions by following the head or tail of the loop and

counting up the number of visits of each coordinate (r, m), the longitudinal correlations can be acquired by applying a modulo 2 operation to the transverse correlations.
However, a problem arises in the general spin S case and finite magnetic fields: the loop can heal out by arriving at the starting position in two ways. Returning the way the loop has taken at loop start essentially removes the starting position from the loop and makes a measurement relative to the initial coordinate (r, m) impossible by following the simple "modulo 2" operation. In this case, high numerical effort has to be used to track all correlations of all spins among each other on the same loop retroactively, which most likely does not outweigh the statistical quality gain over a direct measurement in the diagonal loop update. For the particular case $S = 1/2$ and zero magnetic field, the directed loop equations lead to a deterministic loop update that prevents the loop from closing in a way where it would remove its own starting position. Ironically, transverse and longitudinal correlations are equal due to SU(2) symmetry in this case, making either of the measurements obsolete.

2.4.3 Errors

As the final section dealing with the QMC algorithm, error handling will be explained. The statistical mean error estimation in eqn. (2.4) needs to take into account, that subsequent configurations $c_1, c_2, \ldots, c_M$ and consequently subsequent measurements $A(i)$ of a quantity $\langle A \rangle$ are always correlated. The quantity that reflects the degree of correlation is the (normalized) autocorrelation function

$$C_A(t) := \frac{\langle A(i)A(i+t)\rangle - \langle A(i)\rangle\langle A(i+t)\rangle}{\langle A(i)A(i)\rangle - \langle A(i)\rangle\langle A(i)\rangle}, \tag{2.39}$$

which typically decays exponentially ($\propto e^{-t/\tau}$) at large t. This leads to the definition of the exponential autocorrelation time

$$\tau_{\text{exp}} = \limsup_{t\to\infty} \frac{t}{-\ln|C_A(t)|}. \tag{2.40}$$

Taking a look at the variance $\sigma^2(A)$ of a quantity A now, one finds that

$$\begin{aligned}\sigma^2(A) &= \frac{1}{M^2}\sum_{i,j=1}^{M}\left(\langle A(i)A(j)\rangle - \langle A(i)\rangle\langle A(j)\rangle\right)\\ &= \frac{1}{M^2}\sum_{i,j=1}^{M} C_A(i-j)\left(\langle A^2\rangle - \langle A\rangle^2\right)\\ &= \frac{1}{M}\sum_{t=-(M1)}^{M-1}\left(1-\frac{|t|}{M}\right)C_A(t)\left(\langle A^2\rangle - \langle A\rangle^2\right)\end{aligned}$$

which, with the definition of an integrated autocorrelation time

$$\tau_{\text{int}} = \frac{1}{2}\sum_{t=-\infty}^{\infty} C_A(t) = \frac{1}{2} + \sum_{t=1}^{\infty} C_A(t),$$

reads

$$\sigma^2(A) = \frac{1}{M}\left(\langle A^2\rangle - \langle A\rangle^2\right)2\tau_{\text{int}}. \tag{2.41}$$

This means due to the correlation of data, the effective number of measurements is by a factor of $2\tau_{\text{int}}$ smaller than the real number of measurements which underlines the great importance of efficient creation of independent configurations by Monte Carlo algorithms.

To extract reliable data from QMC it is crucial to estimate errors as correct as possible. The general strategy is based on so called *binning* of the data into k subsets of length $L = M/k$. If those subsets have a length that is larger than the integrated autocorrelation time, then the averaged quantities within those data blocks

$$A_b := \frac{1}{L}\sum_{i=(b-1)*L+1}^{bL} A(i), \quad b = 1,\ldots,k \tag{2.42}$$

are statistically independent and they form the correct variance

$$\sigma^2(A) := \frac{1}{k-1}\sum_{b=1}^{k}\left(A_b - \bar{A}\right)^2, \quad \bar{A} = \frac{1}{N}\sum_{i=1}^{N} A(i). \tag{2.43}$$

While *binning* is perfectly viable for linear quantities (energy, susceptibility, magnetization, ...), it does not take into account error propagation of non-linear quantities such

as the specific heat. A more suited method in is the *Jackknife*-procedure in that case. The basic idea behind the jackknife error estimator is a *resampling* of the data sets by creating k subsets out of the k bins with length $L = M/k$ by leaving out one bin at each time. Calculating the average

$$\bar{A}_{av} = \frac{1}{k} \sum_{i \in \text{subset}} \bar{A}_i, \quad \bar{A}_i = \frac{1}{L} \sum_{j \in \text{bin}_i} A(j)$$

over the k subsets which, combined with $\bar{A}_0 = \frac{1}{M} \sum_{i=1}^{M} A(i)$ of the complete set, is a set of $k+1$ averages, backed up by a large amount of measurements each.
In the Jackknife algorithm, the final average is now given by

$$\bar{A} = \bar{A}_0 - (k-1) \left(\bar{A}_{av} - \bar{A}_0 \right) \tag{2.44}$$

with a variance

$$\sigma^2(A) = \frac{k-1}{k} \sum_{i=1}^{k} \left(\bar{A}_i^2 - \bar{A}_{av}^2 \right) \tag{2.45}$$

The advantage of this method is an automatic error propagation of non-linear quantities, resulting in a bias $(k-1)\left(\bar{A}_{av} - \bar{A}_0\right)$ of the binning average $\bar{A}_0$. For linear quantities, Jackknife and simple binning are identical.

2.5 Maximum Entropy

In subsection 2.4.2 it has been shown that the *SSE* is capable of extracting dynamic correlation functions, however, the highly oscillating character of the time development operators $e^{\pm itH}$ in the *SSE*-formalism forces a Wick-rotation $it \to \tau$ to imaginary time where the time development operators become diffusive functions. This chapter will provide the bridge between experimentally relevant quantities such as the dynamic structure factor, T_1-relaxation rates and the imaginary time correlation functions of subsection 2.4.2.

2.5.1 The continuation problem

In order to connect the imaginary plane $\langle S^{\mu}_{r_i}(\tau) S^{\nu}_{r_j}(0) \rangle$ with the real axis in form of e.g. the dynamic structure factor, we start with the imaginary time Greens function

$$G_{AB}(\tau) = -\langle T_\tau A(\tau) B(0) \rangle. \tag{2.46}$$

Here A, B stand for $S^{\pm,z}$ and T_τ is the imaginary time ordering operator. Expanding (2.46) in a full eigensystem $\{|n\rangle\}$ with $H|n\rangle = E_n|n\rangle$ one finds $G_{AB}(\tau)$ to be β-periodic:

$$G_{AB}(\tau) = \frac{1}{Z}\sum_{n,m}\langle n|A|m\rangle\langle m|B|n\rangle e^{-\tau(E_m-E_n)}e^{-\beta E_n} = G_{AB}(\tau+\beta). \tag{2.47}$$

Consequently, one can express $G_{AB}(\tau)$ through a discrete Fourier-transform

$$G_{AB}(\tau) = \frac{1}{\beta}\sum_{\omega_n} e^{-i\omega_n\tau}\tilde{G}_{AB}(i\omega_n) \tag{2.48}$$

with coefficients given by

$$\tilde{G}_{AB}(i\omega_n) = \int_0^\beta d\tau e^{i\omega_n\tau}G_{AB}(\tau). \tag{2.49}$$

The so called *Matsubara-frequencies* ω_n are given by $\omega_n = (2n+1)\pi/\beta$ for fermions, respectively $\omega_n = 2n\pi/\beta$ for bosons with $n \in \mathbb{N}$.
Combining eqn. (2.47) and (2.49) links $\tilde{G}_{AB}(i\omega_n)$ to the spectral function $\chi''_{AB}(\omega)$

$$\begin{aligned}
\tilde{G}_{AB}(i\omega_n) &= -\int_0^\beta d\tau e^{i\omega_n\tau}\frac{1}{Z}\sum_{n,m}\langle n|A|m\rangle\langle m|B|n\rangle e^{-\tau(E_m-E_n)}e^{-\beta E_n} &(2.50)\\
&= \frac{1}{Z}\sum_{n,m}\langle n|A|m\rangle\langle m|B|n\rangle\frac{1-e^{\beta(E_n-E_m)}}{i\omega+E_n-E_m}e^{-\beta E_n} &(2.51)\\
&= \int_{-\infty}^{\infty} d\omega\frac{\chi''_{AB}(\omega)}{i\omega_n-\omega} &(2.52)
\end{aligned}$$

with

$$\chi''_{AB}(\omega,q) = \frac{1}{Z}\sum_{n,m}\langle n|A(q)|m\rangle\langle m|B(-q)|n\rangle\delta(\omega+E_n-E_m)(1-e^{\beta(E_n-E_m)})e^{-\beta E_n}. \tag{2.53}$$

This quantity is directly related to the dynamic structure factor

$$\begin{aligned}
S_{AB}(\omega,q) &= \frac{1}{Z}\sum_{i,j}e^{-q(r_i-r_j)}\int_{-\infty}^{\infty}e^{i\omega t}\langle A_{r_i}(t)B_{r_j}(t)\rangle &(2.54)\\
&= \frac{1}{Z}\sum_{n,m}\langle n|A(q)|m\rangle\langle m|B(-q)|n\rangle\delta(\omega+E_n-E_m)e^{-\beta E_n} &(2.55)
\end{aligned}$$

by a comparison with eqn. (2.53):

$$\chi''_{AB}(\omega,q) = (1-e^{-\beta\omega})S_{AB}(\omega,q). \tag{2.56}$$

This is the so called *fluctuation-dissipation theorem*, which, in combination with eqn. (2.52) and insertion into eqn. (2.47), provides the wanted link of QMC-data and dynamic structure factor

$$G_{AB}(\tau, q) = \frac{1}{\beta} \sum_{\omega_n} \int_{-\infty}^{\infty} d\omega \frac{1 - e^{-\beta\omega}}{i\omega_n - \omega} S_{AB}(\omega, q). \tag{2.57}$$

In a final step, the Matsubara sum is carried out by rewriting the sum into a contour-integral in the complex plane with poles at the Matsubara-frequencies in order to use *Cauchy's residue theorem*. This yields the simple equation

$$G_{AB}(\tau, q) = \int_{-\infty}^{\infty} d\omega e^{-\tau\omega} S_{AB}(\omega, q) \tag{2.58}$$

which, in the case of $S_{AB}(q, \omega)$ with $AB \in \{S^z S^z, S^x S^x\}$ can be further simplified by looking at the symmetries of eqn. (2.55):

$$\begin{aligned} S_{AB}(q, -\omega) &= \frac{1}{Z} \sum_{n,m} \langle n|A(q)|m\rangle\langle m|B(-q)|\rangle \delta(-\omega + E_n - E_m) e^{-\beta E_n} && (2.59)\\ &= \frac{1}{Z} \sum_{m,n} \langle n|B(-q)|m\rangle\langle m|A(q)|n\rangle \delta(-\omega + E_m - E_n) e^{-\beta(E_n+\omega)} && (2.60)\\ &= e^{-\beta\omega} S_{BA}(q, \omega). && (2.61) \end{aligned}$$

Inserting this result into eqn. (2.58) yields a new kernel with new integration borders

$$G_{AB}(\tau, q) = \int_0^{\infty} d\omega (e^{-\tau\omega} + e^{-(\beta-\tau)\omega}) S_{AB}(\omega, q), \quad AB \in \{S^z S^z, S^x S^x\} \tag{2.62}$$

In the numerical implementation of (2.58) and (2.62), $G_{AB}(\tau, q)$ is a vector $\mathbf{G} = (G_1, \ldots G_{N_\tau})$, the spectrum a vector $\mathbf{A} = (A_1, \ldots A_{N_\omega})$ and finally the kernel K_{ij} an $N_\tau \times N_\omega$ matrix. Several issues hinder the simple inversion of K in order to get $\mathbf{A} = K^{-1}\mathbf{G}$. Firstly, a solution is not unique due to $N_\omega > N_\tau$ with N_τ being of the order of 10 while N_ω is typically chosen to be of the order of 10^3 for a smooth ω-resolution. Secondly, a direct inversion of the kernel involves singular numerical values which, multiplied with error-prone QMC data, often results in high-frequent noise without any connection to the real spectrum. Over the course of this thesis, three different versions were implemented to invert eqn. (2.58) – from a "quick and dirty" direct inversion-test in form of the singular value decomposition (SVD) over the Meshkov-algorithm [55] which transforms the inversion-problem onto the minimization of a vector up to a Maximum Entropy method, tailored specifically to deal with correlated and noisy data (Bryan-Algorithm) [56].

2.5.2 Singular value decomposition

The most simple and straightforward way of inverting eqn. (2.58) utilizes the so called singular value decomposition (SVD), a tool of the linear algebra to factorize real or complex rectangular matrices of the form

$$K = U\Sigma V^* \tag{2.63}$$

where K is the $N_\tau \times N_\omega$ transformation kernel, U a unitary square matrix of dimensions $N_\tau \times N_\tau$, Σ a $N_\tau \times N_\omega$ diagonal matrix and V^* the conjugate-transpose of the unitary $N_\omega \times N_\omega$ matrix V. For our real-valued kernel K we have $U^{-1} = U^T$ and $V^* = V^T = V^{-1}$ with only real eigenvalues in Σ.
Applied to the inversion problem, the SVD yields for the dynamic structure factor

$$A_i = \sum_{j=1}^{N_\omega} \sum_{k=1}^{N_\tau} V_{ij} \sigma_j^{-1} U_{jk}^T G_k \tag{2.64}$$

In our implementation the SVD is performed by the `LAPACK` subroutine `DGESV` [57]. A straightforward approach to carry out the sums in eqn. (2.64) is likely to fail, since the eigenvalues σ_j in Σ vary among 30 orders of magnitude and applied to QMC data simply do not yield any useful results. Instead, one can truncate the eigenvalues to the N_c most dominant ones, typically with $N_c < 10$, leading to

$$A_i = \sum_{j=1}^{N_c} \sum_{k=1}^{N_\tau} V_{ij} \sigma_j^{-1} U_{jk}^T G_k. \tag{2.65}$$

This truncation is a very special case of a more general set of filter functions which help to regularize eqn. (2.64), see Tikhonov regularization [58] for a review. However, we did not explore filter details further after a few SVD continuation tests, one of them shown in Fig. 2.8: displayed is the autocorrelation time of a spin S=1/2 dimer system at $T = 0.25J$ – a system that can easily be treated analytically and its results are well understood with hand-waving arguments: at high temperatures, the spin barely sees his neighboring spin and it performs a thermally driven random-walk, leading to dominant intensity at $\omega = 0$ and its vicinity. Upon cooling, the neighbor-interaction becomes dominant and the spin starts precessing in the field of its neighbor, leading to high intensity of the autocorrelation function at its larmor-frequency $\omega/J = 1$. While static and dynamic quantities are accessibly analytically, it is also a system that allows for extremely high numerical accuracy with the QMC owing to its small size – an ideal test subject for an analytic continuation. Our imaginary time source data in the inset of Fig. 2.8 has a relative error of 10^{-6} which can be regarded as very high

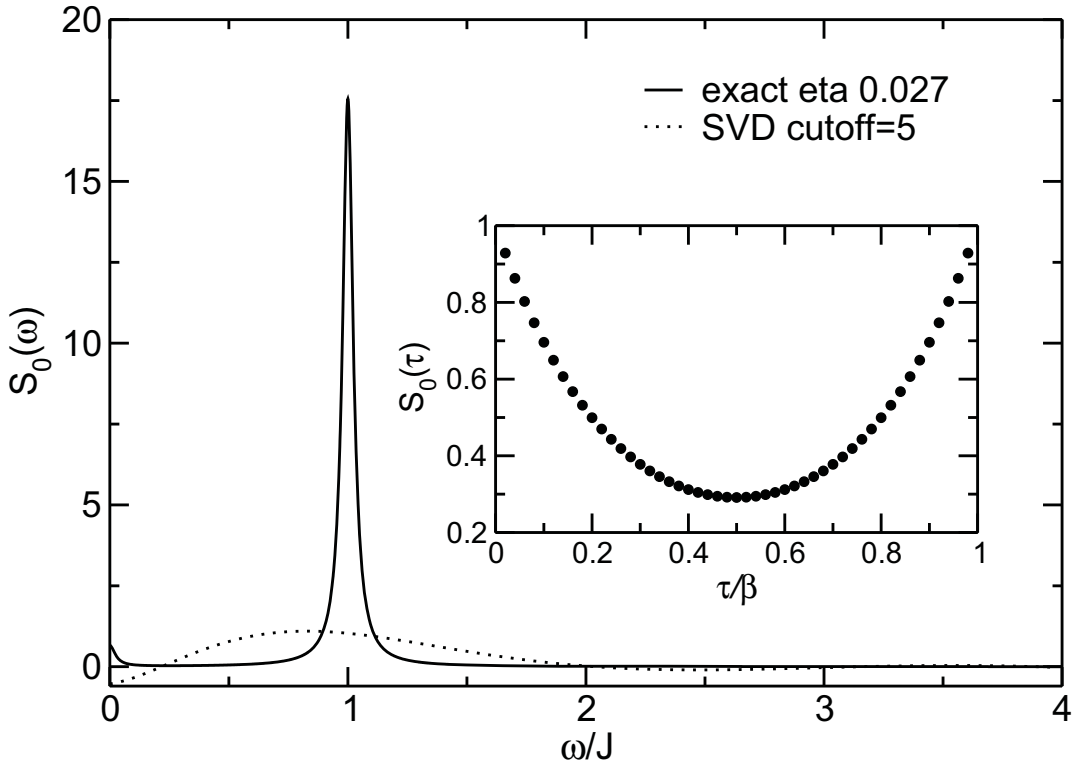

Figure 2.8: Autocorrelation function of a dimer spin system at T/J=0.25. The solid line is the exact result from diagonalizing the Hamiltonian, the dashed line is the result from imaginary time QMC-data (shown in the inset), which was fed into a straight forward inversion of eqn. (2.62) by singular value decomposition (see eqn. (2.65)). The results are poor at best.

accuracy. Despite the excellent statistical quality it is pretty obvious, that the SVD in this brute force approach with $N_c = 5$ does not yield any useful spectral properties – the larmor-frequency peak of the analytic results is barely visible and at a wrong position, the spectral intensity drops below zero at times and already at slightly larger $N_c > 7$ the spectrum becomes completely distorted by high-frequency oscillations with strong intensity, orders of magnitudes higher than the analytic results. This test scenario clearly shows that a straightforward SVD is not a viable way to perform the analytic continuation.

2.5.3 Regularization – the Maximum Entropy formalism

In the last subsection it has become very clear, that the ill-posed inversion problem of eqns. (2.58) and (2.62) needs more advanced ways of regularization, eventually even asks for additional input to find the solution that resembles the true spectrum **A** most. Since **G** of the inversion problem is the result of a measurement it can be interpreted as a realization of a gaussian distributed random variable with the exact value as the mean and a width that reflects the statistical error of the QMC. One can then use statistical reasoning to find an expression for the distribution of $P[\mathbf{A}|\mathbf{G}]$ of observing **A** when **G** has already occurred. The final spectrum would then read as

$$\bar{\mathbf{A}} = \int \mathbf{A} P[\mathbf{A}|\mathbf{G}] d\mathbf{A}. \tag{2.66}$$

To simplify things for later numerical application, one approximates the mean of our spectrum to be the value at the distribution's maximum

$$\bar{\mathbf{A}} = \max_{\mathrm{A}} P[\mathbf{A}|\mathbf{G}]. \tag{2.67}$$

In order to calculate the conditional probability $P[\mathbf{A}|\mathbf{G}]$ (also called *posterior probability*), one makes use of Bayes theorem

$$P[\mathbf{A}|\mathbf{G}] = \frac{P[\mathbf{G}|\mathbf{A}]P[\mathbf{A}|I]}{P[\mathbf{G}|I]} \tag{2.68}$$

with the *likelihood* $P[\mathbf{G}|\mathbf{A}]$ of the observation **G** for a given **A** and the *prior probability* $P[\mathbf{A}|I]$ of the spectrum, given any prior information I one might have. Examples for this are positivity or even analytical behavior of the spectrum. Finally there is the so called *evidence* $P[\mathbf{G}|I]$ which functions as a normalization and has no effect on the outcome of the spectrum, hence can be disregarded for the analytic continuation problem.

Likelihood Function Under the assumption of Gaussian-distributed QMC-data **G**, the choice of the likelihood function $P[\mathbf{G}|\mathbf{A}]$ is given by

$$P[\mathbf{G}|\mathbf{A}] = \mathrm{norm}^{-1} e^{-\chi^2/2}, \quad \chi^2 = \sum_{i,j=1}^{N_\tau} \left(G_i - \tilde{G}_i\right) C_{ij}^{-1} \left(G_j - \tilde{G}_j\right) \tag{2.69}$$

with $\tilde{G}_i$ obtained through the original integral equation (2.58,2.62) of the spectral trial data in its discretized form with finite step-width $\Delta\omega$

$$\tilde{G}_i = \sum_{k=1}^{N_\omega} K_{ik} A_k \Delta\omega. \tag{2.70}$$

C_{ij} is the so called covariance matrix of M repeated measurements

$$C_{ij} = \frac{1}{M(M-1)} \sum_{k=1}^{M} (G_i^{(k)} - \bar{G}_i)(G_j^{(k)} - \bar{G}_j) \tag{2.71}$$

and $G_i^{(k)}$ stands for the k-th measurement of the i-th entry in $\mathbf{G}$ with an M-averaged value of $\bar{G}_i$.
Perfectly uncorrelated data (see Fig. 2.9 and caption) would leave all off-diagonal entries of eqn. (2.71) zero with the variance σ_i^2 on its diagonal and in such a case, χ^2 in eqn. (2.74) simplifies to

$$\chi^2 = \sum_{i=1}^{N_\tau} \left(\frac{G_i - \tilde{G}_i}{\sigma_i} \right)^2 . \tag{2.72}$$

In other words: χ^2 is the least square measure of integral transformed trial spectrum to the imaginary QMC data, weighted by its variance.

Prior Probability Following [59], the fundamental principle of maximum entropy suggests the so called *entropic prior* to be

$$P[\mathbf{A}|I] = \text{norm}^{-1} e^{\alpha S}, \quad S = \Delta\omega \sum_{i=1}^{N_\omega} \left(A_i - m_i - A_i \ln \frac{A_i}{m_i} \right) \tag{2.73}$$

as most uninformative and unbiased prior. S is an entropic measure very similar to the Shannon entropy and $\mathbf{m}$ a reference distribution of rank N_ω (default model), holding all information one might have about the spectrum.[5] An uninformed default model is typically flat and positive, ideally adjusted in height to match the zeroth moment of $\mathbf{A}$ if that information is available through sum-rules for example (see subsection 4.2.6).

Posterior Probability Connecting eqns. (2.69) and (2.73) through (2.68) yields

$$P[\mathbf{A}|\mathbf{G}] = \text{norm}^{-1} e^{\alpha S - \chi^2/2} \tag{2.74}$$

for the form of the posterior distribution. This equation is maximized for

$$\min \left(\chi^2/2 - \alpha S \right) \tag{2.75}$$

[5] Note that S stands for the entropy here and *only* here. For chapter 3 onwards, S will refer to the spin magnitude again.

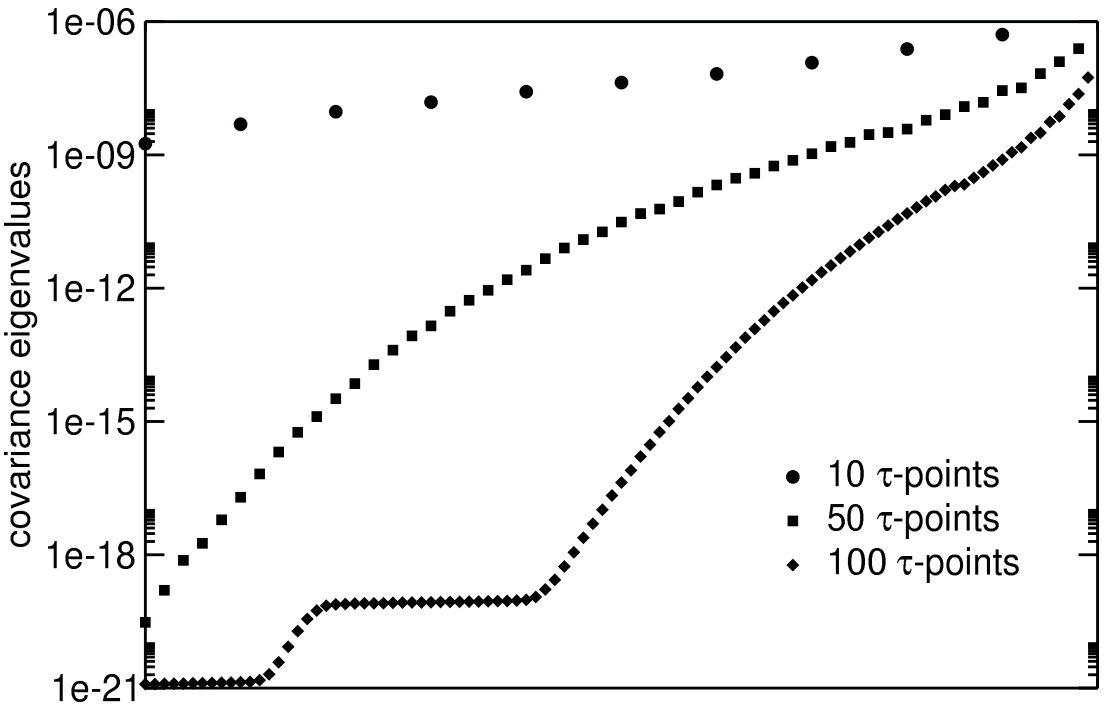

Figure 2.9: This plot shows the results of diagonalizing the covariance matrix of eqn. (2.71). The system is a single dimer system, introduced in Fig. 2.8. Due to its small size ($N = 2$) and comparably high temperatures $\beta = 4$, the corresponding maximum order M of the expansion is very small ($M = 200$), since it scales linear with N and M. This means an extraction of too many τ-points inevitably leads to correlations among the data points. This behavior is clearly shown in the plot, where the extraction of more than 10 τ-points already leads to spurious eigenvalues after diagonalizing the covariance matrix. On the other hand the extraction of only a handful of τ-points shows eigenvalues of the covariance similar to the diagonal elementals of the undiagonalized covariance matrix – a consequence of extremely small off-diagonal matrix elements $C_{ij}, i \neq j$. In other words: using only the diagonal covariance entries in the determination of χ^2 in eqn. 2.72 is justified, as long as the QMC data is not over-sampled through extraction of too many τ-points.

and we find the choice of the spectrum to be a competition between the least square functional χ^2 and the proximity to the default model through the entropy, driven by the choice of the regularization parameter α. For large α, the final solution will resemble the default model, for small α it will give in to the data constraints. Therefore the correct choice of α is of great importance.

The correct α – historic maximum entropy To close the discussion of the maximum entropy method, we describe how statistical arguments can be used to derive criteria for the correct choice of the regularization parameter. In the so called *historic maximum entropy* [60], the solution is found when

$$\chi^2(\mathbf{A}_\alpha) = \sum_{i=1}^{N_\tau} \left(\frac{G_i - \tilde{G}_i(\mathbf{A}_\alpha)}{\sigma_i} \right)^2 = N_\tau. \tag{2.76}$$

This choice is easily understood: the correct value for α is given, when the trial spectrum matches the original imaginary time data up to the standard deviation – a very reasonable criteria since, for smaller α, the data quality is in principle not sufficient to justify a closer fit. More sophisticated arguments are used in the so called *classic* maximum entropy.

The correct α – classic maximum entropy Here, α is treated as a parameter in the solution-space and the posterior probability in eqn. (2.68) gets expanded to $P[\alpha, \mathbf{A}|\mathbf{G}, \mathbf{m}]$, which means we now maximize $P[\alpha, \mathbf{A}|\mathbf{G}, \mathbf{m}]$ with respect to $\mathbf{A}$ and simultaneously the posterior probability $P[\alpha|\mathbf{G}]$ with respect to α (this probability should not depend on the default model $\mathbf{m}$). To find $P[\alpha|\mathbf{G}]$, we again utilize Bayes' theorem

$$\begin{aligned} P[\alpha, \mathbf{A}|\mathbf{G}, \mathbf{m}] &= P[\alpha, \mathbf{A}, \mathbf{G}|\mathbf{m}]/P[\mathbf{G}] && (2.77)\\ &= P[\mathbf{G}|\mathrm{S}]P[\mathbf{A}|\alpha, \mathbf{m}]P[\alpha]/P[\mathbf{G}|\mathbf{m}] && (2.78)\\ &\propto P[\alpha]e^{\alpha S - \chi^2/2}, && (2.79) \end{aligned}$$

where we annihilated some obvious independencies of the default model $\mathbf{m}$ or α, e.g. $P[\mathbf{G}|\mathbf{A}, \alpha, \mathbf{m}] = P[\mathbf{G}|\mathbf{A}]$. $P[\alpha]$ is typically chosen as constant or as the so called *Jeffrey's prior* $P[\alpha] \propto 1/\alpha$ which makes $P[\alpha]$ 'scale-free' and therefore as uninformed as possible [56, 61, 62]. Following the same references one arrives at the posterior probability for α by integration over $\mathbf{A}$ which yields:

$$\begin{aligned} P[\alpha|\mathbf{G}, \mathbf{m}] &\propto P[\alpha] \int e^{\alpha S - \chi^2/2} M(\mathbf{A}) d^{N_\omega}\mathbf{A} && (2.80)\\ &\propto P[\alpha] \prod_{i=1}^{N_\omega} \left(\frac{\alpha}{\alpha + \lambda_i} \right)^{\frac{1}{2}} e^{\alpha S - \chi^2/2}. && (2.81) \end{aligned}$$

Here $\{\lambda_i\}$ are the eigenvalues of $\mathrm{diag}\{\mathbf{A}\}\nabla\nabla\frac{1}{2}\chi^2\mathrm{diag}\{\mathbf{A}\}$ with the measure $M(\mathbf{A}) = \prod_{i=1}^{N_\omega} \frac{1}{\sqrt{A_i}}$.

The sealing argument for classical maximum entropy is now to assume that $P[\alpha|\mathbf{G},\mathbf{m}]$ is sharply peaked at $\hat{\alpha}$, yielding a result for the spectrum by

$$\begin{aligned}\langle\mathbf{A}\rangle &= \int \mathbf{A}P[\alpha,\mathbf{A}|\mathbf{G},\mathbf{m}]d\alpha d^{N_\omega}\mathbf{A} &(2.82)\\ &= \int \mathbf{A}_\alpha P[\mathbf{A}|\mathbf{G},\alpha,\mathbf{m}]P[\alpha|\mathbf{G}]d\alpha d^{N_\omega}\mathbf{A} &(2.83)\\ &\approx \int \mathbf{A}P[\mathbf{A}|\mathbf{G},\hat{\alpha},\mathbf{m}]d^{N_\omega}\mathbf{A} &(2.84)\\ &\approx \mathbf{A}_{\hat{\alpha}}. &(2.85)\end{aligned}$$

The maximum of $P[\alpha|\mathbf{G}]$ is easily determined by its partial derivative of eqn. (2.81) with respect to α. For this purpose we look at the logarithm of $P[\alpha|\mathbf{G}]$

$$\frac{\partial \log P[\alpha|\mathbf{G}]}{\partial\alpha} = 0 \tag{2.86}$$

and find

$$-2\hat{\alpha}S(\mathbf{A}_{\hat{\alpha}},\mathbf{m}) = \sum_{i=1}^{N_\omega}\frac{\lambda_i}{\hat{\alpha}+\lambda_i} \tag{2.87}$$

as the determining equation for $\hat{\alpha}$.

The correct α – Bryan maximum entropy Unlike *historic* and *classic* maximum entropy which determined their solution by selecting *one* particular α, *Bryan's* approach actually calculates the full posterior probability distribution (2.78) and forms the final spectrum as weighted average over a whole range of spectra $\mathbf{A}_\alpha$ with α typically $\in \{0.001,\ldots 10^7\}$:

$$\begin{aligned}\langle\mathbf{A}\rangle &= \int \mathbf{A}P[\mathbf{A}|\mathbf{G},\alpha,\mathbf{m}]P[\alpha|\mathbf{G}]d\alpha d^{N_\omega}\mathbf{A} &(2.88)\\ &= \int_{\alpha_{\min}}^{\alpha_{\max}} \mathbf{A}_\alpha P[\alpha|\mathbf{G}]d\alpha. &(2.89)\end{aligned}$$

The classic approach makes sense whenever the distribution is sharply peaked. However, depending on the quality of the QMC-data, this is not necessarily fulfilled (see Fig. 2.10, Fig. 2.11 and Fig. 2.12 with captions).
In Fig. 2.10 we show continuation results on $S(q=\pi,\omega)$ of a four-spin ring with 10^5, respectively 10^7 sweeps. The resulting spectra look very similar, however the lesser data quality spectrum is slightly smoother. In the inset $P[\alpha|\mathbf{G}]$ is shown. Clearly the function is far from being sharply peaked and the shift to higher α with lesser data

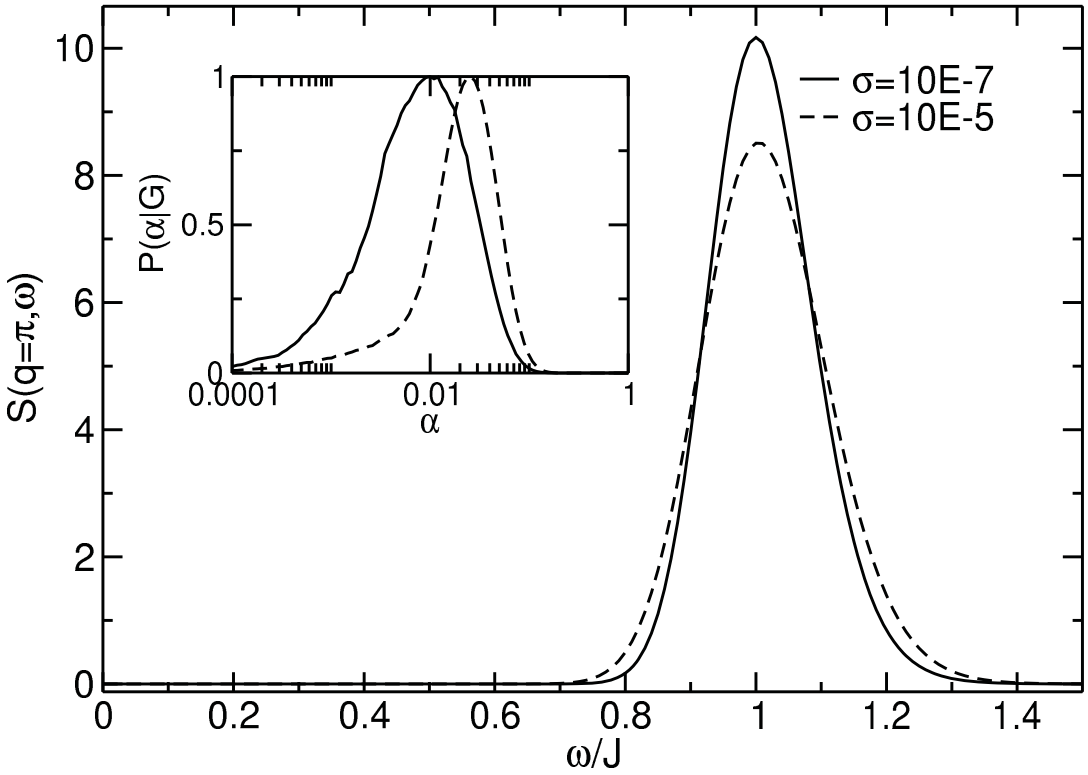

Figure 2.10: This figure shows the effect of statistical errors on the quality of the analytic continuation, in this case $S(q = \pi, \omega)$ of a N=4 spin S=1/2 Heisenberg chain with sweeps of 10^5 and 10^7. Clearly the maximum gets less and less pronounced and less sharp the more the statistical quality is reduced. Exemplarily two posterior probabilities for α are shown in the inset which makes very clear, that the classic assumption of a sharply peaked distribution is not always true, seeing that the distribution is nonzero over four orders of magnitude. However, the spectrum hardly changes shape in the region of the nonzero posterior distribution (see also Fig. 2.11 and Fig. 2.12), leading to relatively similar results of classic and Bryan maximum entropy.

quality explains the smoother spectrum in the main plot.
In Fig. 2.11 we contrast the three different choices of α at the example of the dynamic structure factor $S^{zz}(q = \pi/2, \omega)$ for a Heisenberg S=1/2 chain with 128 spins at $T/J = 0.25$. Obviously, historic, classic and Bryan show *very* similar results, even though the cutoff $\hat{\alpha}$ and the maximum of $P[\alpha|\mathbf{G}]$ varies over four orders of magnitude (see inset). Such stability in the solution indicates very high data quality (low errors, minimum correlation). Note how nicely the transition from default model (for very large α) up to the final spectrum (for very low α) is portrayed by the grey alpha scan lines

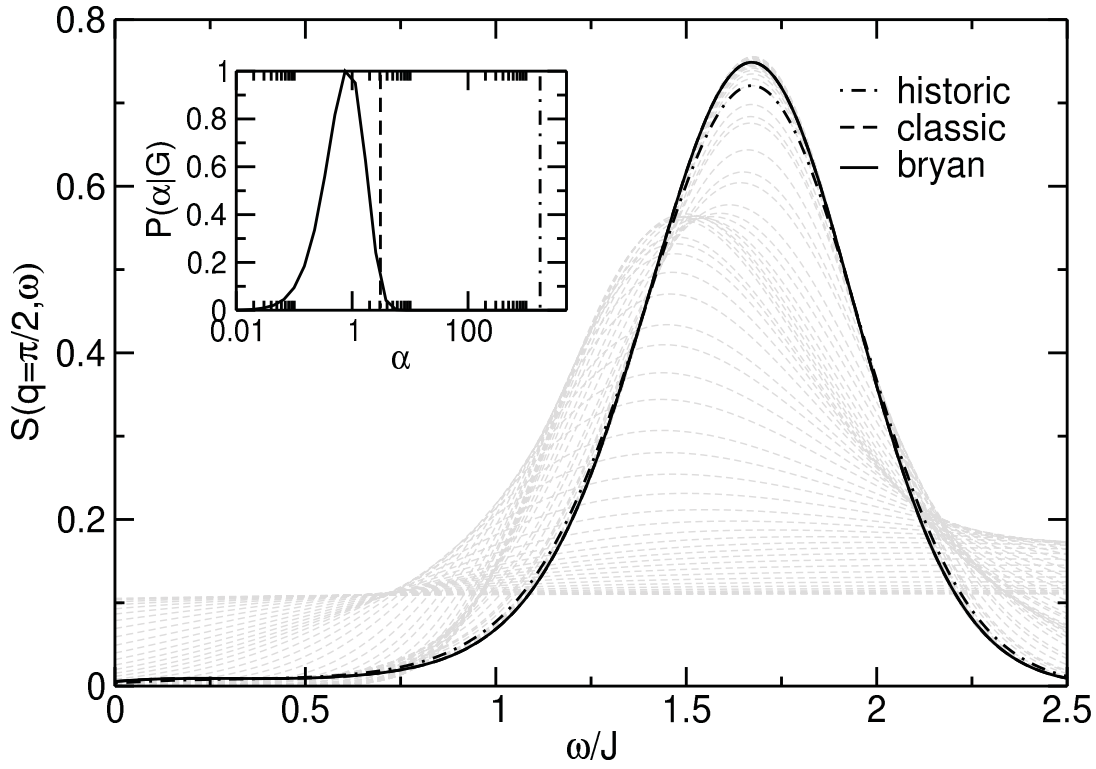

Figure 2.11: Shown in this plot are the resulting trial spectra of a scan over the regularization parameter α, coming from $\alpha = 10^9$ with a trial spectrum relatively close to the flat default model, down to $\alpha = 10^{-4}$ with a probably over-fitted trial spectrum. Obviously, historic, classic and Bryan maximum entropy yield very similar results which speaks for the imaginary time QMC data quality. Nevertheless we find, that the choice of the regularization parameter changes over several orders of magnitude from $\alpha_{\text{historic}} = 3000$ over $\alpha_{\text{classic}} = 3$ down to the distribution with maximum around $\alpha = 1$. The continued data shown is the dynamic structure factor of a spin S=1/2 Heisenberg chain with N=128 sites at wave vector $q = \pi/2$ and temperature $T/J = 0.25$.

$(10^7 > \alpha > 10^{-4})$.

Finally in Fig. 2.12 we present continuation results for the autocorrelation function $S_0(\omega)$ of the dimer at $T/J = 0.25$, first introduced in Fig. 2.8. The underlying τ-data is highly correlated due to the very small expansion orders, leading to less reliable and stable continuations. As a consequence, historic, classic and Bryan strongly differ in sharpness, however the correct maximum position is found by all three choices of α.

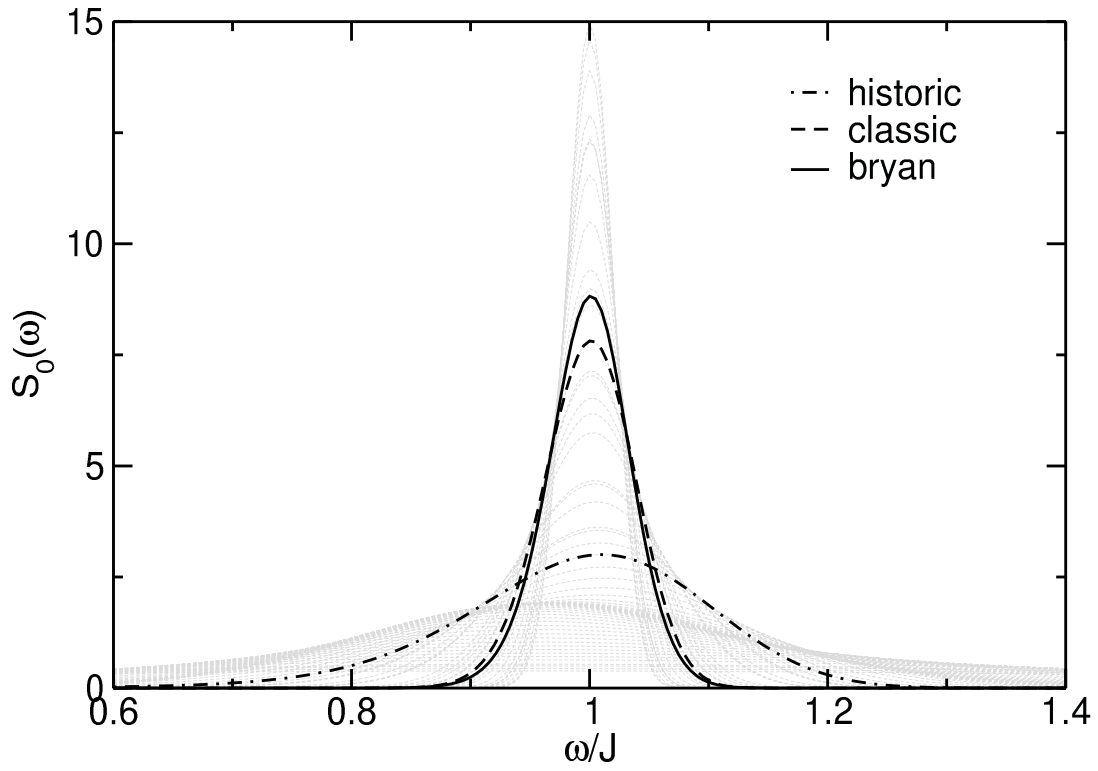

Figure 2.12: Shown ins this plot are again resulting trial spectra of a scan over the regularization parameter α, coming from $\alpha = 10^7$ down to $\alpha = 10^{-4}$ of the dimer autocorrelation function introduced first in Fig. 2.8. This time the historic maximum entropy solution is clearly less sharp in comparison to classic and Bryan's solution despite the extremely good data quality.

2.5.4 Meshkov-Algorithm

After the discussion of the maximum entropy formalism and the extended discussion about the choice of the regularization parameter, the remaining issue is the algorithmic realization of the minimization procedure of the maximum entropy functional given in eqn. (2.75). One should keep in mind that finding the minimum in a 200+ dimensional variable space is not trivial and two tested realizations will be given. One of them is an algorithm given by Meshkov in 1994 [55] which reduces the minimization problem onto finding the minimum of a quadratic functional with linear constraints, also known as *non negative least square* (NNLS) problem. The other is the algorithm of Skilling and Bryan [56], which works in principle with standard Newton-iterations, however in a highly reduced and optimized variable space, which makes the algorithm

extremely fast and relatively stable despite the high dimensionality of the solution vector.

Meshkov's algorithm starts from a series expansion of the entropy (eqn. (2.73)) up to second order in $\mathbf{A}$ around a positive function $\mathbf{f} = \{f_1, f_2, \ldots, f_{N_\omega}\}$, leading to:

$$\begin{aligned} \alpha S &= \alpha \sum_{i=1}^{N_\omega} \left[m_i - A_i + A_i \ln\left(\frac{A_i}{m_i}\right) \right] \Delta\omega && (2.90) \\ &\approx \alpha \sum_{i=1}^{N_\omega} \left[m_i + \frac{f_i}{2} - A_i + A_i \ln\left(\frac{f_i}{m_i}\right) + \frac{A_i^2}{2f_i} \right] \Delta\omega && (2.91) \\ &= R(\mathbf{f}|\mathbf{A}). && (2.92) \end{aligned}$$

If this positive vector $\mathbf{f}$ is chosen as the true minimum $\langle \mathbf{A} \rangle$ of the non-quadratic MaxEnt-functional eqn. (2.75) then it should also give the minimum of the quadratic functional in eqn. (2.91). Following [55] further, the process of finding the minimum (under the constraint of a positive $\mathbf{A}$) is chosen as a recursive determination of the vector $\mathbf{f}$

$$\mathbf{A}^{(n+1)} = \min_{A_i \geq 0 \forall i} \left[\chi^2(\mathbf{A})/2 + R(\mathbf{f}^{(n)}|\mathbf{A}) \right] \tag{2.93}$$

where $\mathbf{f}^{(n)}$ is designed with a memory of the old solution

$$\mathbf{f}^{(n)} = \eta \mathbf{A}^{(n-1)} + (1-\eta)\mathbf{A}^{(n)}, \quad \mathbf{A}^{(0)} = \mathbf{A}^{(1)} = \mathbf{m} \tag{2.94}$$

in order to stabilize the iterations. The rate of convergence is controlled by the parameter $0 < \eta < 1$ and we went with Meshkov's suggested value of $\eta = 0.3$ for guaranteed stability.

In each iteration process, the quadratic functional of N_ω variables

$$F(\mathbf{A}) = \frac{1}{2} \sum_{i=1}^{N_\tau} \left(\frac{G_i - \Delta\omega \sum_{j=1}^{N_\omega} K_{ij} A_j}{\sigma_i} \right)^2 + \alpha \Delta\omega \sum_{j=1}^{N_\omega} \left\{ A_j \left[\ln\left(\frac{A_j^{(n)}}{m_j}\right) - 1 \right] + \frac{A_j^2}{2A_j^{(n)}} \right\} \tag{2.95}$$

has to be minimized under N_ω linear constraints $A_i \geq 0$. Equation (2.95) can be rewritten in the form of a series expansion up to quadratic order in $\mathbf{A}$ (higher order terms were neglected)

$$F(\mathbf{A}) = -\sum_{j=1}^{N_\omega} F_j'(\mathbf{A}^{(n)}) A_j + \frac{1}{2} \sum_{i,j=1}^{N_\omega} F_{ij}'' A_i A_j + \text{const} \tag{2.96}$$

where

$$F'_j(\mathbf{A}^{(n)}) = \Delta\omega \sum_{i=1}^{N_\tau} \sigma_i^{-2} G_i K_{ij} - \alpha\Delta\omega \left[\ln\left(A_j^{(n)}/m_j\right) - 1\right] \tag{2.97}$$

$$F''_{ij} = \Delta\omega^2 \sum_{l=1}^{N_\tau} \sigma_l^{-2} K_{li} K_{lj} + \alpha\Delta\omega \frac{\delta_{ij}}{A_j^{(n)}}. \tag{2.98}$$

Upon diagonalizing F''_{ij} in eqn. (2.98) with the orthogonal transformation matrix U_{ij}

$$F''_{ij} = \sum_{l=1}^{N_\omega} \phi_l U_{il} U_{jl}, \tag{2.99}$$

one can substitute

$$A_i = \sum_{j=1}^{N_\omega} U_{ij} \frac{1}{\sqrt{\phi_j}} (\bar{\psi}_j + \psi_j), \quad \bar{\psi}_j = \frac{1}{\sqrt{\phi_j}} \sum_{l=1}^{N_\omega} U_{lj} F'_l(\mathbf{A}^{(n)}) \tag{2.100}$$

which simplifies the minimization of eqn. (2.95) to a standard Least Distance Programming (LDP) problem of finding a vector with minimal norm

$$||\psi||^2 = \sum_{i=1}^{N_\omega} \psi_i^2 \tag{2.101}$$

under N_ω linear constraints

$$\sum_{j=1}^{N_\omega} \frac{1}{\sqrt{\phi_j}} U_{ij} \psi_j \geq -\sum_{j=1}^{N_\omega} \frac{1}{\sqrt{\phi_j}} U_{ij} \bar{\psi}_j. \tag{2.102}$$

As a summary for the Meshkov algorithm: The non-linear MaxEnt functional is expanded around a memory function into a quadratic form, whose minimization yields the new spectrum in recursive iterations with a memory-parameter η to stabilize the algorithm. Each minimization of the quadratic functional in respect to $\mathbf{A}$ is reduced to a LDP problem and can be even further reduced to a non-negative least square (NNLS) problem with N_ω linear constraints. During each iteration, a matrix-diagonalization of dimension $N_\omega \times N_\omega$ and one LDP minimization has to be performed – both steps that scale with the spectral resolution in a non-linear fashion which turned out to be very unfavorable for useful resolutions, in particular in direct comparison with Bryan's algorithm which will be given in the next subsection. Continuation and runtime results of both algorithms will be given subsequently.

2.5.5 Bryan-Algorithm

While Meshkov's algorithm [55] works on expanding the MaxEnt-functional in eqn. (2.75) up to quadratic order in **A**, Bryan's algorithm [56] works on the full functional by finding the minimum over its gradient in regard to **A**. For the entropy (eqn. (2.73)), this yields

$$(\nabla S)_j = \frac{\partial}{\partial A_j} \sum_{i=1}^{N_\omega} \left[A_i - m_i - A_i \ln\left(\frac{A_i}{m_i}\right)\right] = -\ln\left(\frac{A_j}{m_j}\right). \tag{2.103}$$

Likewise we calculate the gradient of the least square measure in eqn. (2.72)

$$\nabla \frac{1}{2}\chi^2 = \frac{1}{2} K^T \frac{\partial \chi^2(\mathbf{G}, \tilde{G})}{\partial \tilde{G}}, \quad \tilde{G} = K\mathbf{A}. \tag{2.104}$$

Now, one can apply the singular value decomposition of the kernel (see eqn. (2.63))

$$\nabla \frac{1}{2}\chi^2 = \frac{1}{2} U \Sigma V^T \frac{\partial \chi^2(\mathbf{G}, \tilde{G})}{\partial \tilde{G}}. \tag{2.105}$$

and put the two equations together

$$-\alpha \ln\left(\frac{\mathbf{A}}{\mathbf{m}}\right) = \frac{1}{2} U^{(c)} \Sigma^{(c)} (V^{(c)})^T \frac{\partial \chi^2(\mathbf{G}, \tilde{G})}{\partial \tilde{G}} \tag{2.106}$$

where the index $^{(c)}$ means a reduction to the N_c largest eigenvalues of Σ which considerably shrinks the computational effort of matrix operations in the algorithm, but most of all allows for a reduced number of search variables by a smart decomposition of **A** through

$$A_j = m_j \exp\left[\sum_{i=1}^{N_c} U_{ji}^{(c)} u_i\right]. \tag{2.107}$$

By this transformation two things are achieved. Firstly, the spectrum **A** is bound to be positive at all times and secondly, the N_ω search directions of the minimization have been reduced to down to the N_c most efficient ones, which obviously only depend on the kernel, or in a further step, only on the number of extracted τ-points and the inverse temperature β. This reduction to $\mathbf{u} = \{u_1, u_2, \ldots u_{N_c}\}$, as will become clear during the comparison of Meshkov and Bryan, allows for a high gain of speed and a convenient independence of the desired spectral resolution which limits Meshkov's algorithm in its current form.
Applying this transformation to eqn. (2.106) yields

$$-\alpha U^{(c)} \mathbf{u} = \frac{1}{2} U^{(c)} \Sigma^{(c)} (V^{(c)})^T \frac{\partial \chi^2(\mathbf{G}, \tilde{G})}{\partial \tilde{G}}. \tag{2.108}$$

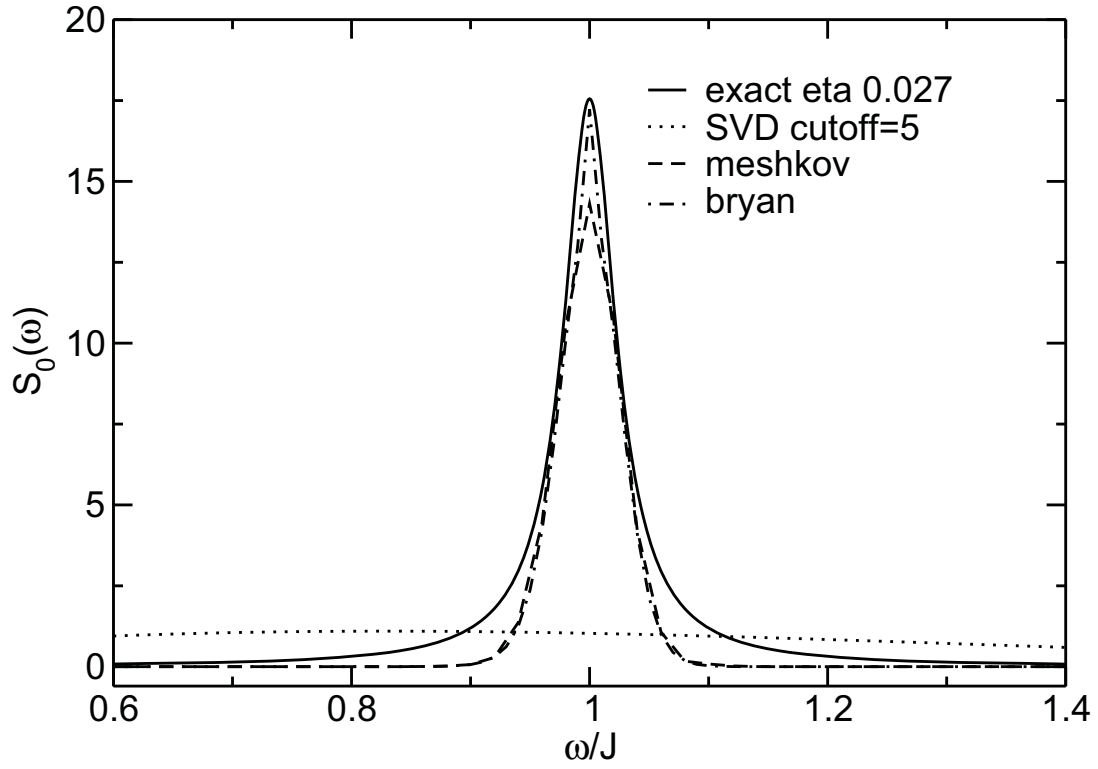

Figure 2.13: Direct comparison of SVD, Meshkov's and Bryan's MaxEnt algorithms on a dimer system at $T/J = 0.25$. While SVD is far off the exact spectrum, Meshkov and Bryan are basically giving equally good results, just with a large difference in runtime in favor of Bryan's algorithm (see Tab. 2.1).

Due to the orthogonality of U, the equation simplifies further to

$$-\alpha\mathbf{u} = \frac{1}{2}\Sigma^{(c)}(V^{(c)})^T\frac{\partial\chi^2(\mathbf{G},\tilde{G})}{\partial\tilde{G}} = \mathbf{g} \tag{2.109}$$

which is taken as basic equation for standard Newton-iterations

$$\mathbf{g}(\mathbf{u}^{(\mathrm{n})}) + \alpha\mathbf{u}^{(\mathrm{n})} + \left(\mathbf{g}'(\mathbf{u}^{(\mathrm{n})}) + \alpha 1\right)\delta\mathbf{u} \approx 0, \quad \mathbf{u}^{(n+1)} = \mathbf{u}^{(n)} + \delta\mathbf{u}. \tag{2.110}$$

For that purpose, $\mathbf{g}'$ must be evaluated

$$\frac{\partial\mathbf{g}}{\partial\mathbf{u}} = \frac{1}{2}\Sigma V^T\frac{\partial^2\chi^2(\mathbf{G},\tilde{\mathbf{G}})}{\partial\tilde{\mathbf{G}}^2}\frac{\partial\tilde{\mathbf{G}}}{\partial\mathbf{A}}\frac{\partial\mathbf{A}}{\partial\mathbf{u}} \tag{2.111}$$

$$= \frac{1}{2}\Sigma V^T\frac{\partial^2\chi^2(\mathbf{G},\tilde{\mathbf{G}})}{\partial\tilde{\mathbf{G}}^2}V\Sigma U^T\mathrm{diag}\{\mathbf{A}\}U \tag{2.112}$$

$$= MD \tag{2.113}$$

Resolution	Meshkov	Bryan
50	12sec	2sec
100	27sec	2sec
200	128sec	2sec
400	1550sec	3sec

Table 2.1: Run-time comparison of Meshkov's and Bryan's MaxEnt-algorithms.

with

$$M = \frac{1}{2}\Sigma V^T \frac{\partial^2 \chi^2(\mathbf{G}, \tilde{\mathbf{G}})}{\partial \tilde{\mathbf{G}}^2} V\Sigma \tag{2.114}$$

and $D = U^T \mathrm{diag}\{\mathbf{A}\}U$. Substituting in eqn. (2.110) finally leads to the simple equation

$$(\alpha 1 + MD)\delta\mathbf{u} = -\alpha\mathbf{u} - \mathbf{g} \tag{2.115}$$

which is solved with respect to $\delta\mathbf{u}$ by simple matrix inversion

$$\delta\mathbf{u} = -(\alpha 1 + MD)^{-1}(\alpha\mathbf{u} + \mathbf{g}), \tag{2.116}$$

performed by `LAPACK` routines `DGETRF` and `DGETRI` in our implementation.

To imposed a certain control on the increment $\delta\mathbf{u}$ we thresholded it with the ratio $\frac{||\delta u||}{||u||}$. Whenever the changes exceed a certain fraction of the norm $||\mathbf{u}||$, the changes were renormalized through

$$u_i = \xi \frac{||\mathbf{u}||}{||\delta\mathbf{u}||} \tag{2.117}$$

by a ξ of choice, in our case typically $\xi = 0.1$.

2.5.6 Conclusion

For both algorithms we used the same convergence criteria suggested by Touchette/Poulin [63]

$$\frac{\left[\frac{1}{2}\chi_n^2 - \alpha S_n\right] - \left[\frac{1}{2}\chi_{n-1}^2 - \alpha S_{n-1}\right]}{\left[\frac{1}{2}\chi_n^2 - \alpha S_n\right]} < \epsilon \tag{2.118}$$

with an epsilon which was chosen to be 10^{-8} in all performed continuations. Both algorithms also used identical regularization parameters as described in subsection (2.5.3).

Results for the already introduced continuation of the dimer autocorrelation function are shown in Fig. 2.13. Clearly, both algorithms match the exact spectrum very well with an $\eta = 0.027$ in the artificially broadened δ-functions $\delta_\eta(x) = \frac{1}{\pi}\frac{\eta}{\eta^2+x^2}$ of eqn. (2.55). However, the runtime of Meshkov's and Bryan's algorithm differ by a large margin due to completely different scaling. While Meshkov becomes increasingly slower with resolution increase, Bryan's algorithm proves to be more or less unaffected owing to the smart choice of search directions (see Tab. 2.1).

Chapter 3

Static properties of low dimensional quantum magnets

In this chapter, results of my thesis will be presented in three main sections. Each section is relatively independent and materials, experiments and theoretical motivation will therefore be given in each particular section. Nevertheless I would like to give a short overview at this point to prepare for the upcoming results.

In Section 3.1, we investigate the spin driven transition between quantum and classical behavior of isotropic Heisenberg quantum spin *chains* by means of the static susceptibility. Apart from that comparison, we fit our results with a Padé-fit to provide an analytic expression of our data and assess the fit quality my comparing to previous fit attempts.

In the next section 3.2, we move from chains to two-dimensional systems by introducing an interchain coupling to form n-leg ladders, which are known to exhibit a gapful excitation spectrum for n even. For the spin S=1 two-leg ladder, we perform parameter scans of the rung and leg coupling constants as well as the single-ion anisotropy, following the pioneering work of Todo *et al.* on this particularly interesting system with the gapful limits of Haldane chain and dimer. We analyze our results in terms of susceptibility and magnetization and show that the system may be driven into a gapless phase for certain ratios of rung/leg coupling parameters and a weak easy-plane anisotropy. Furthermore, we compare our parameter studies to an assumed spin S=1 ladder material and clarify the strength of the coupling constants in the thermodynamic limit by means of the experimental susceptibility and magnetization.

While both preceding sections increased the Hilbert space by stretching the system size into the thermodynamic limit, we look at small molecular magnets with large spin magnitude motivated by experiments predominantly performed by Waldmann *et al.* in the last section. Our particular interest was driven by a Mn-$[3 \times 3]$-grid system of nine spin S=5/2. This system can be regarded as an eight-site ring of spins with the center spin coupled to four ring spins via center-spin coupling. Such systems are of great interest for various technical applications, among them the realization of a Qbit by quantum tunneling of the Néel vector. We analyzed the susceptibility, magnetization and (staggered) static structure factors of the system as function of center-spin coupling and single-ion anisotropy with adjacent comparison to experimental results of the susceptibility in order to clear up contradicting publications about the coupling constants.

To understand the general layout of this chapter, note that all three sections are unified by combining investigations of purely *static* QMC observables while chapter 4 will deal predominantly with *dynamic* properties of quantum spin systems.

3.1 Spin S chains – searching the classical limit

Two decades ago, Haldane's conjecture [19] divided the spectral properties of antiferromagnetic spin chain into integer and non-integer spin magnitudes. Experiments [64–68] and involved methods like the Bethe-Ansatz, exact diagonalization, DMRG and QMC-methods shed light onto the two very different systems and lead to detailed knowledge about the inherent physics. The scientific focus was on S=$\frac{1}{2}$ and S=1 systems while higher spins systems suffered from exponentially increased numerical effort and/or lack of compounds. With the synthesis of molecular magnets the transition metal ions in non-magnetic ligand-surroundings, (e.g. Pyrimidine or Pyrazine [69]) offer experimental access to a wide range of low dimensional materials for integer (Ni, Fe) and non-integer spins (Cu, Co, Mn). Among those systems we highlight the long-neglected $(C_4H_4N_2)(NO_3)_2$ (CuPzN, S=1/2) [70–72] which will be subject of our studies on $1/T_1$-relaxation rates in chapter 4. In addition to the relatively new way of designing materials, there exist plenty of oxide or chloride based materials by now, e.g. $SrCuO_2$ (S=1/2) [73], Sr_2CuO_3 (S=1/2) [74], $Cu(C_6H_5CO_2)_2$ (copper benzoate, S=1/2) [75], $Ni(C_2HZ_8N_2)_2NO_2ClO_4$ (NENP, S=1) [66, 67, 76–78], $CsNiCl_3$ (S=1) [79–82], Y_2BaNiO_5 (S=1) [83], $Ni(C_5D_{14}N_2)_2N_3(PF_6)$ (NDMAP, S=1) [84–88], $CsVCl_3$ (S=3/2) [89, 90], $(C_{10}H_8N_2)MnCl_3$ (S=2) [91], and $(CH_3)_4NMnCl_3$ (TMMC, S=5/2) [92, 93]. Their thermodynamic properties are well described by the Heisenberg-Hamiltonian (eqn. (1.2)) which can be studied in a variety of approximations/limits such as the asymptotic spin wave approach [94–96], series-expansions in powers of 1/T [97, 98], in the Ising-limit for highly anisotropic coupling ($\Delta \to \infty$) [99–101] or in the classical limit $S \to \infty$ for large spins [27].
In this section we want to focus on the latter which is known to yield analytic closed expressions for thermodynamic quantities as pointed out by Fisher [27]. The shortcomings of the classical limit should be visible at low temperatures where quantum fluctuations are dominant in respect to thermal fluctuations. To study the validity of the classical approach, we use Fisher's expression for the susceptibility in comparison with QMC data for S=$\{\frac{1}{2}, 1, \frac{3}{2}, 2, \frac{5}{2}\}$ chains to qualitatively follow the crossover from pure quantum to classical regime as a function of temperature and spin. Since the QMC covers those spin quantum numbers which refer to the most common ionization states of transition metal atoms in molecular magnets, we will additionally give Padé-approximations to our susceptibilities and compare with widely used fit-approaches [102, 103].

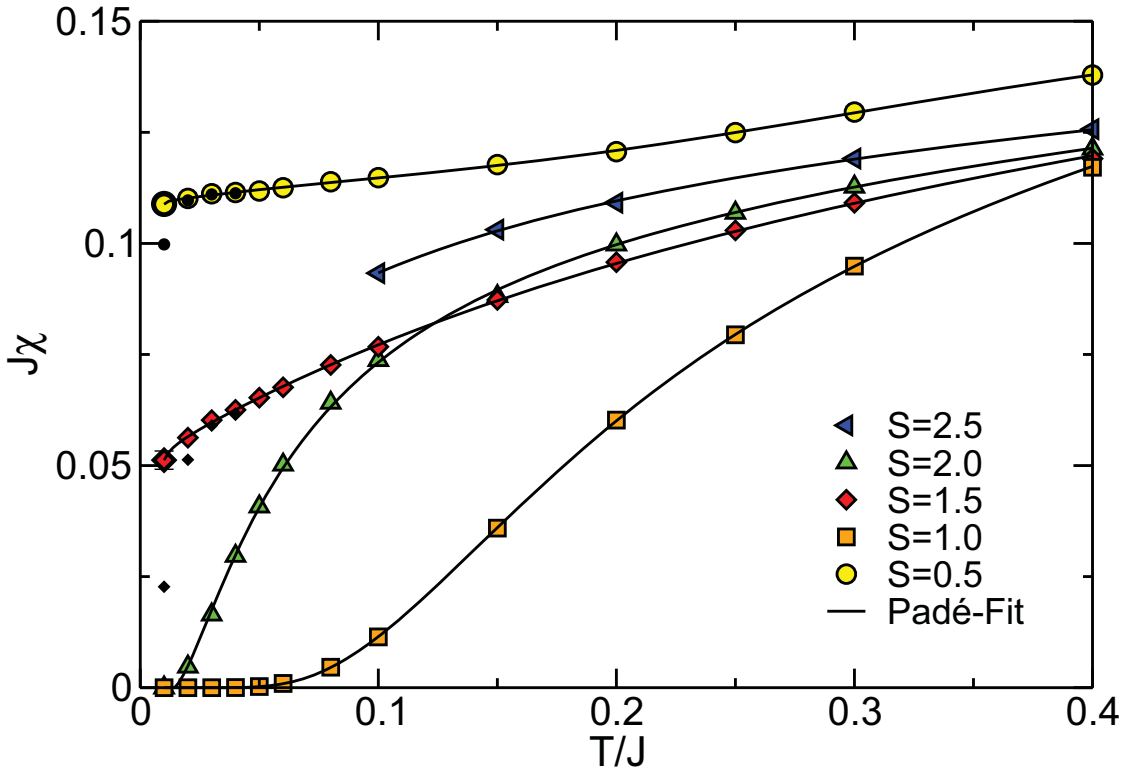

Figure 3.1: Low temperature region of QMC-susceptibilities for Spin-$\{\frac{1}{2}, 1, \frac{3}{2}, 2, \frac{5}{2}\}$ Heisenberg-chains of 512 sites (colored symbols). Black small foregrounded symbols denote systemsizes of 256, respectively 768 (large backgrounded symbols) sites to check the thermodynamic limit for β=100. Statistical errors are only shown when they exceeded the symbol-size. The solid lines are Padé-approximations to the QMC data.

3.1.1 Magnetic susceptibilities

In Fig. 3.1 we present the low temperature results of the susceptibilities for S = $\{\frac{1}{2}, 1, \frac{3}{2}, 2, \frac{5}{2}\}$ and systemsizes up to 768 sites. The finite-size analysis shows that 512 sites can be considered as the thermodynamic limit for all calculations. Statistical errors are not shown in the plots unless they exceed the symbol-sizes. The typical order of the error is 10^{-5} for high and 10^{-3} for low temperatures. In the case S=$\frac{5}{2}$ the errors at low temperature are not negligible anymore. This is due to the extremely large Hilbert space of $(2S+1)^{768}$ which contains 10^{366} times more configurations than the corresponding S=$\frac{1}{2}$ system. To sample such a large Hilbert space sufficiently, great numerical effort with long runtimes are a consequence which is why we restricted ourselves to a maximum of β=10 for S=$\frac{5}{2}$.

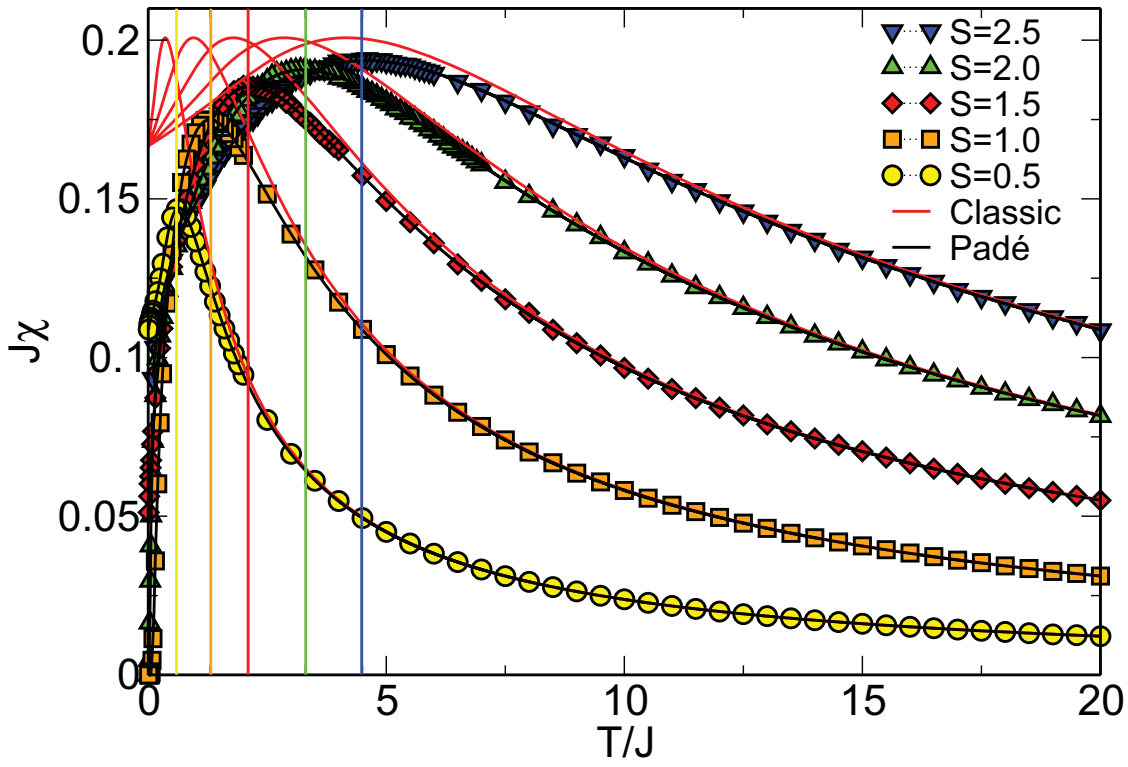

Figure 3.2: QMC-susceptibilities (symbols) with their Padé-fit (black solid lines) in comparison with classical results (red solid lines) as a function of T/J. The colored lines mark the maximum position of the QMC data.

Looking at the low temperature regime $T/J \ll 1$, we find the two different characteristics of integer and non-integer spin chains. The former (S=1, 2) show exponentially activated behavior of the susceptibility with energy excitation gap $\Delta_{S=1} \approx 0.410(3)$ and $\Delta_{S=2} \approx 0.08(1)$ which was extracted by fitting $\chi \sim e^{-\Delta/T}$ to the low-temperature region of our data. The latter (S=$\frac{1}{2}$, $\frac{3}{2}$, $\frac{5}{2}$) are known to have a gapless excitation spectrum leading to finite susceptibilities at T=0, which is consistent with the low-temperature behavior shown by S=$\frac{1}{2}$ and S=$\frac{3}{2}$ in Fig. 3.1. Similarly we expect a finite susceptibility for S=$\frac{5}{2}$ as well although it is not clearly approved by the data since we restricted ourselves to T≥0.1J.

Fig. 3.2 shows the QMC-susceptibilities in direct comparison with results for the classical Heisenberg model from Fisher [27]. His expression for the magnetic susceptibility reads

$$\chi = \frac{g^2 S(S+1)\mu_B^2}{3kT} \frac{1+u}{1-u} \tag{3.1}$$

with

$$u = \coth\left[\frac{JS(S+1)}{kT}\right] - \frac{kT}{JS(S+1)} \tag{3.2}$$

which can be obtained by taking the limit $S \to \infty$ of the Heisenberg-model. As can be seen, eqn. (3.1) and (3.2) perfectly match the QMC data at high temperatures. For low temperatures instead, we find strong differences owing to the onset of quantum effects. In contrast to integer-spin QMC results at T=0, we find a constant finite susceptibility ($\chi|_{T=0} = \frac{g^2}{6|J|}$) for each spin magnitude. However, there is spin-depending convergence of classical and quantum mechanical results concerning the position of the maxima. While we find a 46% maximum position deviation for spin S=$\frac{1}{2}$, it is only 9% for the highest spin S=$\frac{5}{2}$.

3.1.2 Padé-fits

For an analytic description of the numerical QMC results as a function of temperature/coupling we use the following general expression to fit χ in the temperature region $0.01 \leq k_B T/J \leq 20$, respectively $0.1 \leq k_B T/J \leq 20$ for S=$\frac{5}{2}$:

$$\chi(x) = e^{-\Delta/x}\frac{S(S+1)}{3x}P_k^l(x) \tag{3.3}$$

$$P_m^n(x) = \frac{1 + \sum_{n=1}^{l} A_n x^{-n}}{1 + \sum_{m=1}^{k} B_m x^{-m}} \tag{3.4}$$

where

$$x = \frac{k_B T}{|J|}. \tag{3.5}$$

The orders of the Padé approximant $P_k^l(x)$ are determined by the low temperature behavior of χ. For S=$\frac{1}{2}$ the susceptibility $\chi|_{T=0}$ has the finite value of 0.101322 [104], requiring k=l+1 and Δ=0. For this case, Klümper et al. gave very accurate fits ($\sim 10^{-7}$) to numerical Bethe-Ansatz data [102] – an accuracy we cant achieve due to the intrinsic statistical errors of the SSE data ($10^{-5} athighupto \to 10^{-3}$ for lowest temperatures and largest Hilbert space). Similar behavior from higher non-integer spins suggests the same Padé-setup for S=$\frac{3}{2}$, $\frac{5}{2}$.

For integer-spin chains the approximations need to reflect the finite spin gap $\Delta \neq 0$ and the exponential suppression of the susceptibility. Numerical results for the gap of S=1 and S=2 chains are $\Delta_{S=1} \simeq 0.4105$ (DMRG, [105]) and $\Delta_{S=2} \simeq 0.0876$ (DMRG, [106]). However, we are using Δ as a free fit-parameter to gain better overall fit-results to our data. Therefore we need to point out that Δ for S=1 and S=2 must

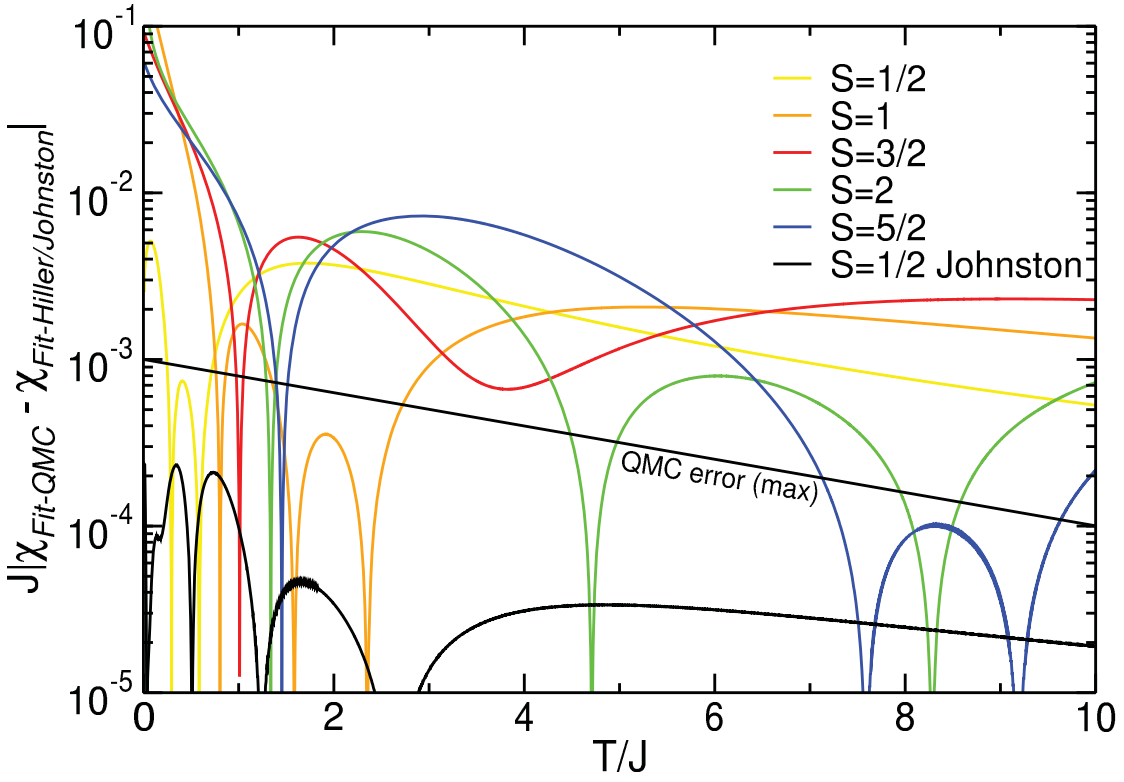

Figure 3.3: Absolute differences of the two different Padé-approximations for the susceptibilities. The solid line is a comparison of our data and a high-accuracy fit (error $\approx 10^{-7}$) to Bethe-Ansatz data from Klümper et al. [102].

S	Δ	A_0	A_1	A_2	A_3	B_0	B_1	B_2	B_3	B_4
$\frac{1}{2}$	-	0.01069	0.06901	0.03924	-0.0003	0.5001	0.37725	0.07918	0.09097	-0.0008
1	0.46024	93.2513	1987.5	22.2623	410.805	93.1356	2093.27	1663.99	2336.51	-
$\frac{3}{2}$	-	0.03832	0.83126	0.09970	-0.00095	2.529	4.86816	4.3319	2.57636	-0.02273
2	0.03550	1.00386	5.13266	6.85929	-0.11084	4.95696	18.9541	34.3336	116.45	-
$\frac{5}{2}$	-	3.13943	8.02237	-10.5702	-0.23443	9.38686	33.6076	221.48	-220.366	-18.4252

Table 3.1: Fit-coefficients of eqn. (3.3) to numerical QMC-data for isotropic antiferromagnetic Heisenberg chains with S=$\frac{1}{2}$, 1, $\frac{3}{2}$, 2, $\frac{5}{2}$.

not necessarily match the numerical results of $\Delta_{S=1}$ and $\Delta_{S=2}$. Furthermore we choose the order k=l for integer spins to achieve asymptotic decay of the high temperature susceptibility proportional to 1/T. The Padé-coefficients of eqn. (3.3) are given in Tab. 3.1 for $S = 1/2, 1, 3/2, 2, 5/2$.

For the case $S = \frac{1}{2}$, Johnston et al. have already presented fits to Bethe-Ansatz data in 2000 [7]. We use their Padé-approximation as a reference-fit for S=$\frac{1}{2}$ and find good

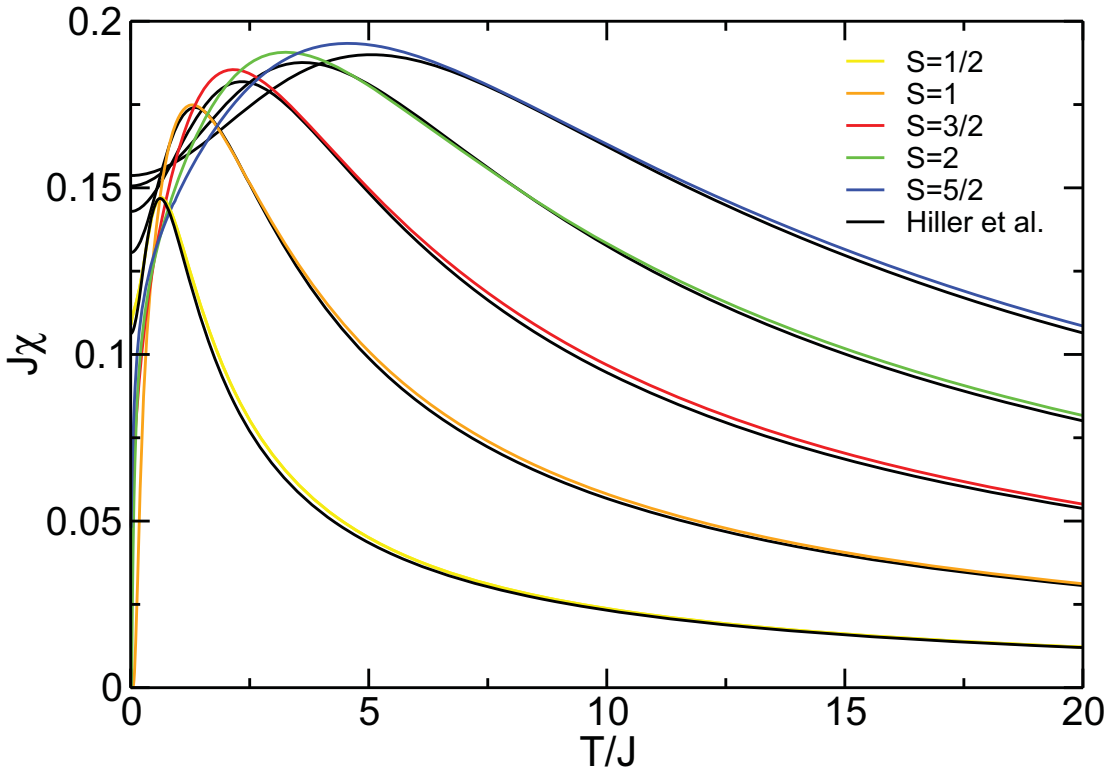

Figure 3.4: Padé-fits to QMC-susceptibilities (colored lines) and to Weng-data (black lines) by Hiller et al. [103] for different spins (S=$\frac{1}{2}$, 1, $\frac{3}{2}$, 2, $\frac{5}{2}$) as a function of T/J.

agreement within the statistical QMC errors (see Fig. 3.3). For high temperatures the deviations are of the order 10^{-5}, for temperatures smaller than the coupling we find differences up to 10^{-4}.
Finally we compare our fits with a widely used Padé-approximation from Hiller et al. [103]:

$$\chi = \frac{Ng^2\mu_B^2}{kT}\left[A + Bx^{-2}\right]\left[1 + Cx^{-1} + Dx^{-3}\right]^{-1}. \tag{3.6}$$

The coefficients were fitted to numerical data from Weng [107] who used exact diagonalization to extrapolate susceptibilities of small systems ($N < 10$) with even and odd number of sites to the thermodynamic limit.

For the Curie-like region ($\chi \sim 1/T$) we find an overall fair agreement with the fits to QMC data (see Fig. 3.4). Nevertheless the deviations up to 5% are surprising compared to former Padé-fits to Weng-data for S=1 [108]. Lower temperatures reflect the fact that Hiller et al. fitted to data which is dominated by large finite-size errors. While

the fit for S=$\frac{1}{2}$ shows an overall correct low temperature behavior of the susceptibility[1] with a maximum deviation of 5×10^{-3} (see Fig. 3.4), we find stronger deviations for larger spins. In particular the exponentially activated susceptibility of integer spin chains is not described by the original extrapolation data and therefore neither by the fit. For larger spins we also find the susceptibility-maximum to deviate stronger from the QMC results. While the maximum-position for S=$\frac{1}{2}$ is 3% lower than that of the QMC, it is already 10% higher for S=2 and S=$\frac{5}{2}$.

3.1.3 Conclusion

We used the Stochastic Series Expansion to calculate susceptibilities for S = $\left\{\frac{1}{2}, 1, \frac{3}{2}, 2, \frac{5}{2}\right\}$ Heisenberg chains in the thermodynamic limit. A comparison with classical data in the limit $S \to \infty$ shows fundamentally different behavior at low temperatures for all spins. We find large differences for the positions of the susceptibility-maxima which are however decreasing with increasing spin magnitude. A Padé-approximation of the QMC-data has been given and we have shown those approximations to match with high-accuracy spin S=1/2 Bethe-ansatz results from Johnston et al. within statistical errors. For larger spin magnitudes $S > 1/2$, we have shown our Padé-approximations to considerably improve widely used Padé-fits from Hiller *et al.*. This improvement pertains both, to the high, and more pronounced to the low-temperature region.

[1] Of course the fit can not take logarithmic corrections into account which were introduced in 1994 [109].

3.2 Spin S=1 ladder system

Coming from the preceding chapter about spin chains, we saw that even-site half-integer Heisenberg spin chains with uniform nearest neighbor exchange coupling form a spin singlet ground state with gapless excitations. Introducing an additional inter-chain magnetic exchange coupling between adjacent spin chains the so-called n-leg spin ladders are formed. These have been discussed very intensively for the S=1/2 case since even-n compared to odd-n exhibit completely different ground state properties [110, 111]. In particular for even-leg ladders a non-magnetic spin-liquid ground state with a finite energy gap is found [112].

For S=1, already for a single antiferromagnetic chain, the ground state is well described by the AKLT ansatz ([113]) with a finite energy gap as proposed by Haldane [19] and several experimental realizations are known [114]. Only very little is known about the ground state and excitations of a S=1 two-leg spin ladder. From bosonization studies [115, 116] and quantum Monte-Carlo simulations [117] a continuous crossover from the Haldane spin gap state to the case of antiferromagnetic dimers, which also shows a spin excitation gap, is predicted.

Experimentally the situation is complicated by the fact that most S=1 systems (usually based on high spin Ni(II) transition metal ions) show a strong axial crystal field anisotropy D which modifies the ground state of the spin system [118].

In this part of the thesis, which has been partially published in [28], we focus on a Heisenberg S=1 two-leg spin ladder with variable intra-chain (J) and inter-chain coupling K for different single-ion anisotropies as an extension to [117]. Todo *et al.* have shown in large scale QMC calculations that in the crossover of Haldane chain ($J = 1$, $K = 0$, spin gap $\Delta = 0.41J$) to Dimer ($J = 0$, $K = 1$, $\Delta = J$) the excitation gap gets smaller by up to one order of magnitude with respect to uncoupled dimers/chains. We will show, that the system may even become gapless with the introduction of an easy-plane anisotropy D by adding $H_{\text{ion}} = D\sum_i (S_i^z)^2$ as used in eqn. (1.2). Here, positive D yields an easy-plane anisotropy, negative D an easy-axis anisotropy for a spin on each site.

Our interest has been driven by recent experiments by C. Mennerich *et al.* on the Ni(II) based material $Na_2Ni_2(C_2O_4)_3(H_2O)_2$ (see Fig. 3.5), which include static susceptibility, high-field magnetization and high-field high-frequency ESR measurements. As preview to a detailed discussion in subsection 3.2.1 we find, that the structurally nearly isotropic S=1 spin ladder is magnetically very well described by isolated spin dimers with an antiferromagnetic exchange of $J = 43$ K on the rungs and a large easy-plane anisotropy of $D = 11.5$ K. While the size of the anisotropy was determined by ESR, its sign stems

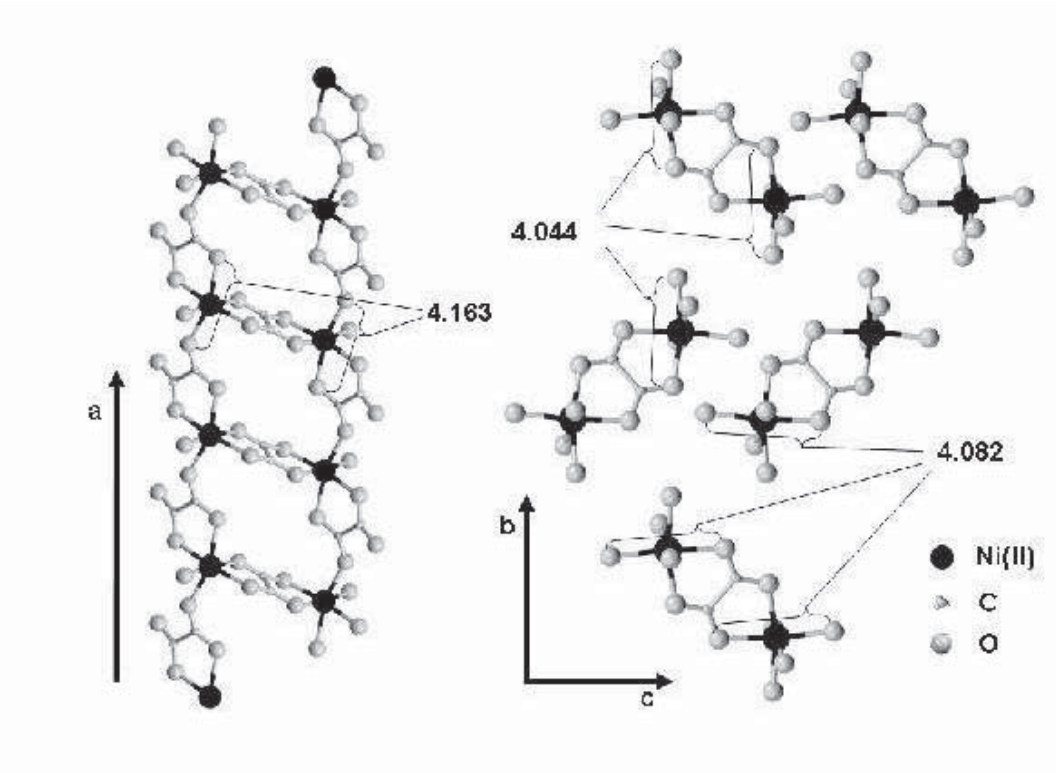

Figure 3.5: Crystal structure of $Na_2Ni_2(C_2O_4)_3(H_2O)_2$. For clarity, Na and H atoms are not shown. The numbers indicate the distance (in Å) between opposing oxygen atoms on the distorted NiO_6 octahedra which are tilted by 17 degree with respect to the a axis.

from comparing a dimer model to high-field magnetization results. Its calculated field dependence shows successive level crossings of higher spin states ($S = 1, 2$) with the ground state up to full polarization. This is confirmed by experimental magnetization data which provides direct evidence for a magnetic field induced switching of the S=0 ground state to an S=1 state at $B_{c_1} \approx 30\,\mathrm{T}$ and to S=2 at $B_{c_2} \approx 60\,\mathrm{T}$.

3.2.1 Magnetic susceptibility

First we look at the magnetic susceptibility as function of rung- (J) and leg- (K) coupling for fixed easy-plane single-ion anisotropy $D = 11.5K = 0.27J$ at experimentally accessible temperatures down to $\beta \leq 10$. A careful finite size scaling analysis has been performed and the thermodynamic limit is reached with $2x200$ sites for these comparably high temperatures. This is in agreement with existing results for

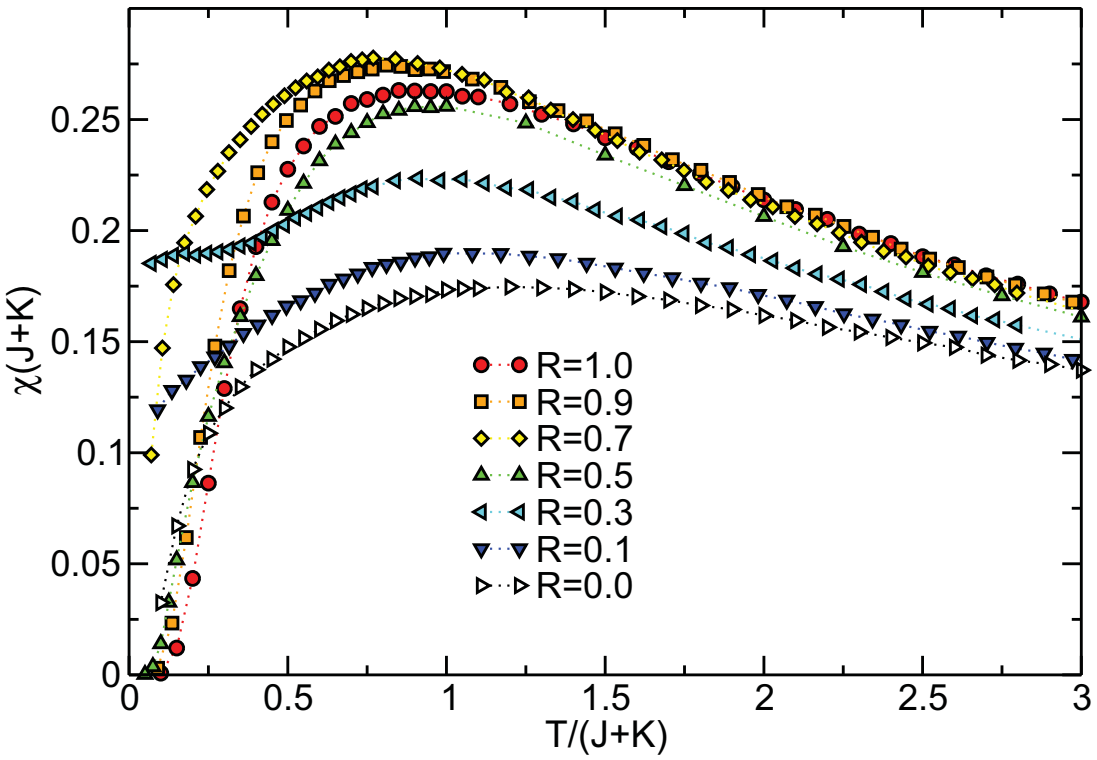

Figure 3.6: Scaled static susceptibility for the two-leg spin $S = 1$ ladder for an easy-plane anisotropy $D = 0.27J$ (taken from ESR measurements on $Na_2Ni_2(C_2O_4)_3(H_2O)_2$) as function of a scaled temperature $T/(J+K)$ for different ratios of $R = K/(J+K) \in \{0.0, 0.1, 0.3, 0.5, 0.7, 0.9, 1.0\}$.

$D = 0$ [117]. Fig. 3.6 shows the scaled static susceptibility $\chi(J+K)$ as function of scaled temperature $\tilde{T} = T/(J+K)$ for different ratios $R = \frac{K}{J+K}$ between uncoupled dimers ($R = 1$) and two uncoupled Haldane chains ($R = 0$). Both limiting cases are well studied and the static susceptibility is expected to vanish exponentially at low temperatures $\chi \propto e^{-\Delta/T}$ with $\Delta = 1$ for the dimer and $\Delta \approx 0.41050(2)$ for the Haldane chain [105]. The region of intermediate R for $\tilde{T} < 0.5$ however displays a significant change of shape for the susceptibility as function of R. Firstly we find a noticeable increase of the broad maximum upon R-decrease as already mentioned by Todo *et al.*. Upon further decrease $R \leq 0.5$, the susceptibility is suppressed again even below its value at $R = 1$. Secondly we find a strong suppression of the spin gap up to the point $R < 0.5$ where it is not clear anymore if the system is still gapful. Finally we find a shoulder structure for $R = 0.3$ which is an indication for the second energy scale in the system, introduced by the two different coupling constants. Such shoulders are also expected for other ratios of R with finite J, K, however they are not dominant enough

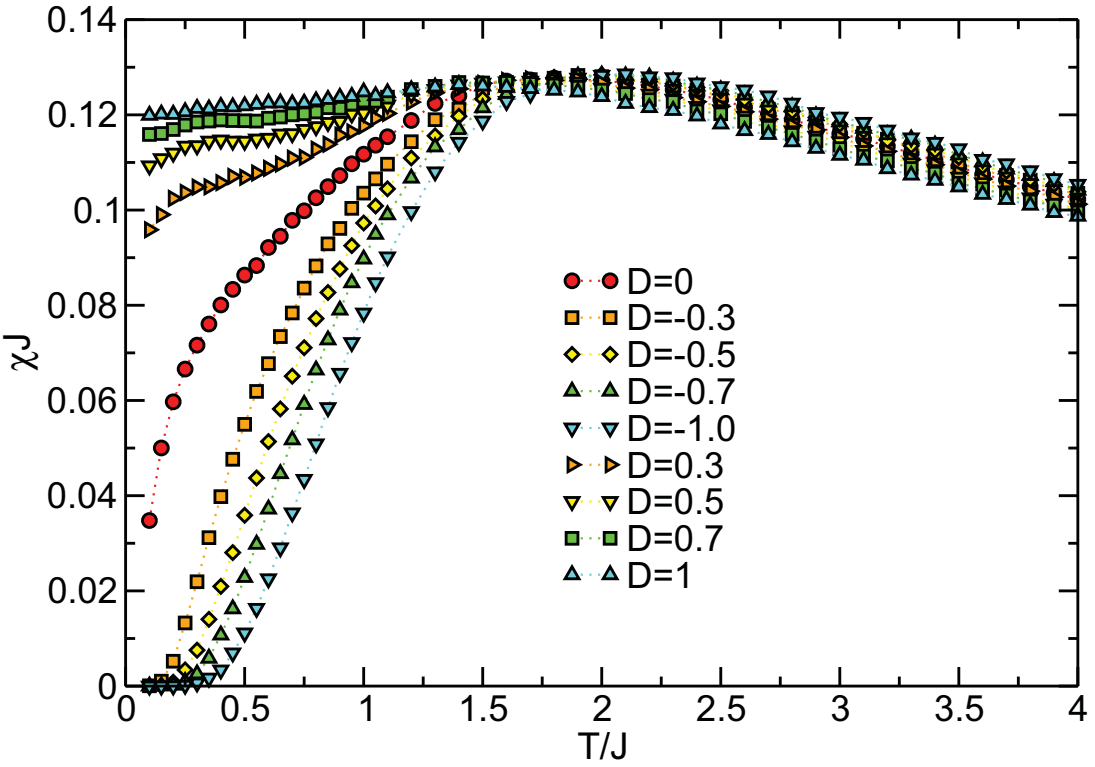

Figure 3.7: Static susceptibility for $J = K = 1$ as function of temperature for different single-ion anisotropies $D \in \{-1.0, -0.7, -0.5, -0.3, 0.0, 0.3, 0.5, 0.7, 1.0\}$.

to be directly observable in the QMC results. In direct comparison with data at $D = 0$ from Todo *et al.* we would like to point out the significant difference for intermediate $0.5 \geq R \geq 0.1$. This region coincides with a region where the spin gap is shown to be $\Delta \leq 0.1J$ and we believe that a finite easy-plane anisotropy closes the small gap completely.

To elaborate on the influence of the single-ion anisotropy, we performed QMC calculations for the susceptibility (see Fig. 3.8) at very low temperatures $0.001 \leq T/J \leq 0.1$ with system sizes up to $N = 512x2$ and $R = 0.3$ as the parameter featuring the smallest spin gap for $D = 0$. By fitting exponentially activated behavior $\chi \approx Ae^{-\Delta/T}$, we find $\Delta_{D=-0.1} \approx 0.440$ and $\Delta_{D=0} \approx 0.069$ for our data. These values can be regarded as upper boundaries to the true zero temperature gap with an uncertainty introduced by the fitting procedure, which overestimates the gap depending on the upper cutoff temperature of the fit. In this respect, the value at $D = 0$ is perfectly in line with the value $\Delta_{D=0} = 0.06476(4)$ of the second-moment [119] given by [117]. For the easy-plane anisotropy $D = 0.1$, the susceptibility is still finite even at lowest

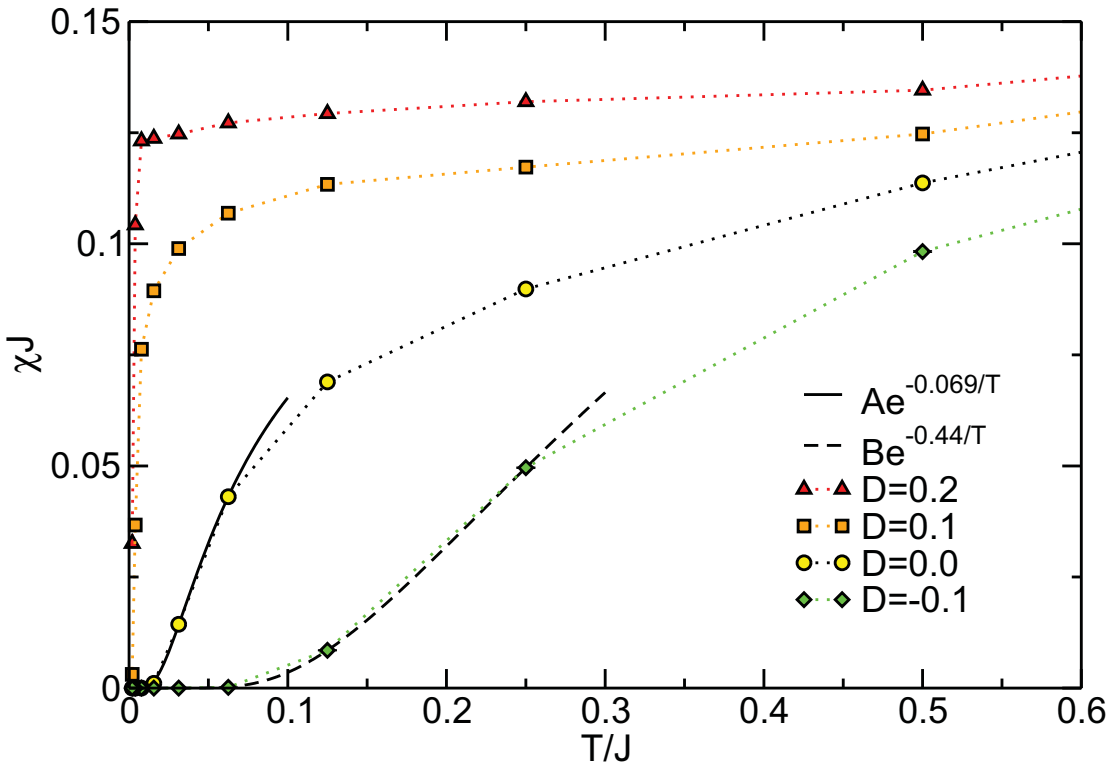

Figure 3.8: Low-temperature susceptibility of the ladder system for $R = 0.3$ and three different anisotropies $D \in \{-0.1, 0, 0.1\}$. Error bars are within symbol size. For $D = 0, -0.1$, exponential fits were performed to extract the spin gap.

elevated temperatures. Obviously, such a small and positive value of D already drives the system into a gapless excitation spectrum.

Finally we want to compare our susceptibility with experimental results published in [28]. Taking into account the two different topologies of exchange pathways, one can assume a magnetic interaction J along the rungs which is stronger than the magnetic interaction K along the legs. In the limit of $J >> K$ this leads to an isolated dimer picture where each dimer consists of two S=1 spins on the rungs of the ladder. Since all Ni-ions on a ladder are crystallographically equivalent they share the same size and orientation of the single-ion anisotropy D. Hence, we produced results close to the dimer limit with an easy-plane anisotropy $D = 11.5K = 0.27J$ extracted from ESR measurements and fitted the experimental data to QMC results. It should be noted, that the scaled experimental dataset appreciably depends on the g-factor (in the range of 2.2 to 2.25). Nevertheless, all possible fits lead to a value of $R \approx 0.95 - 1.00$ for total magnetic exchange strengths between 43 K ($R = 1$) and 45 K ($R = 0.95$). The

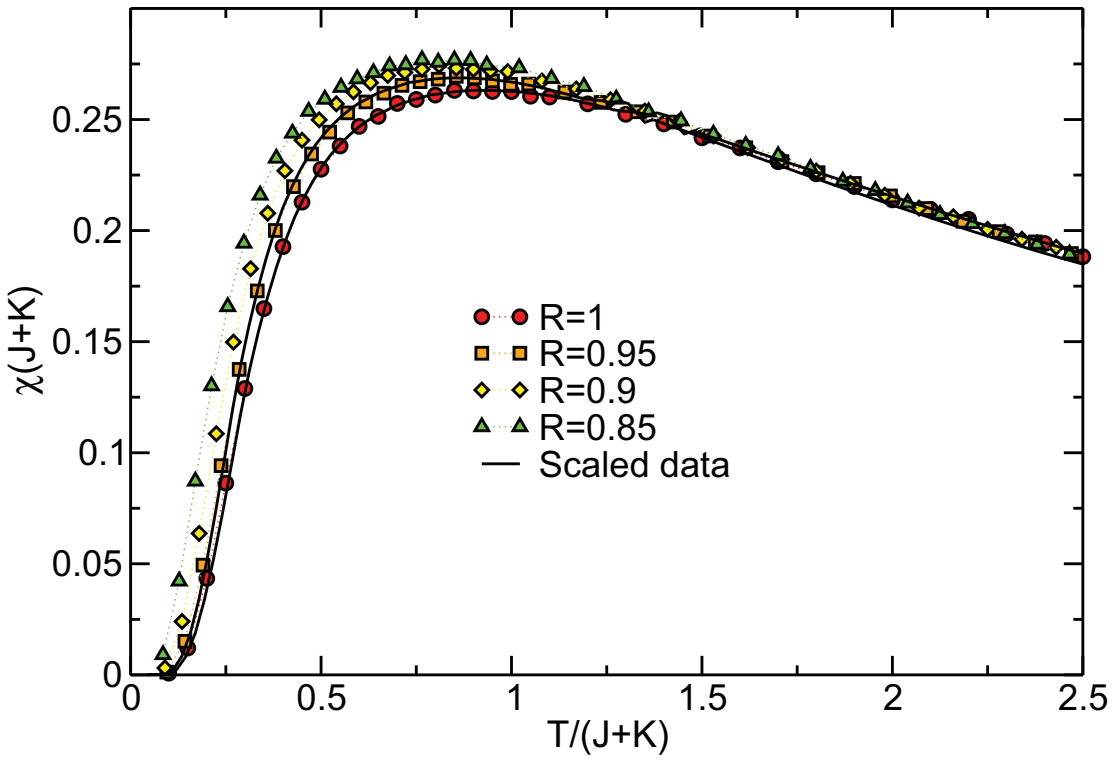

Figure 3.9: Comparison of experimental susceptibility versus (J+K)-scaled QMC results with $D = 11.5K = 0.27J$ and different ratios $R \in \{0.85, 0.9, 0.95, 1.0\}$. A g-factor of $g = 2.23$ was used.

solid line in Fig. 3.9 shows the best result of the fit using a total coupling constant $J{+}K = 45$ K, a g-factor $g = 2.23$, a temperature independent term of 0.0085 μ_B/dimer and a Curie constant of 0.0045 μ_BK/dimer. A comparison with the QMC data in the low temperature regime of $T/(J + K)\leq 1.5$ yields a value of R=0.95, which results in an intradimer coupling of $J = 42.75$ K and an interdimer coupling of $K = 2.25$ K.

3.2.2 High-field magnetization

Similarly to the susceptibility, we performed calculations for the magnetization M at corresponding temperatures of high-field magnetization experiments on powder samples, which were carried out in pulsed fields up to 55T.

As can be seen from the energy diagram of the spin states of the spin ladder (Fig. 3.10)

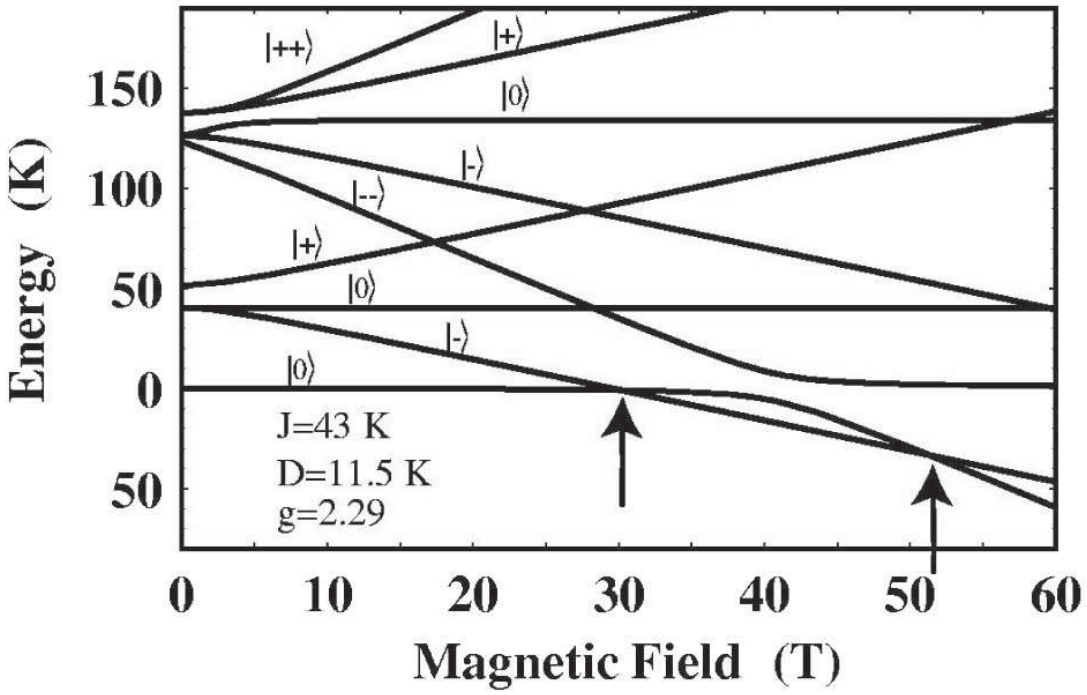

Figure 3.10: Breit-Rabi diagram of a S=1 dimer model with single-ion anisotropy $D = 11.5K = 0.27J$, calculated for the magnetic field applied perpendicular to the z-axis: the triplet S=1 and the quintet S=2 are well separated from the S=0 ground state by an activation energy of roughly $J = 43$K. Both multiplets exhibit a zero field splitting due to crystal field anisotropy. Note the ground state level crossings around 30 and 53T

in the approximation of a single dimer with a single-ion anisotropy D=11.5K, the splitting of the states in a magnetic field yields a level crossing of the ground state with the lowest triplet state $|-\rangle$ at a field B_{C1} and a second level crossing of the $|-\rangle$ state with the $|--\rangle$ quintet state at field B_{C2} with $B_{C1} < B_{C2}$. This leads to a step-like behavior for the high field magnetization. If the field is applied along the z-axis, the critical field B_{C1} can be estimated using the equation $B_{C1} = (J - D/3)/(g\mu_B/k_B)$, depending strongly on the sign of D. For a field perpendicular to the local anisotropy axis, a negative D (leading to higher critical fields for $B \parallel z$) pushes the critical field to lower fields and vice versa for a positive D. Since for measurements on powder samples, the perpendicular situation dominates the spectrum of the spin states, the field dependent magnetization can give a clear indication for the sign of the anisotropy D – in our case for a positive $D = 11.5$K. With this fixed easy-plane anisotropy, we performed an R-scan at the lowest accessible experimental temperatures $T = 1.47K = 0.034J$,

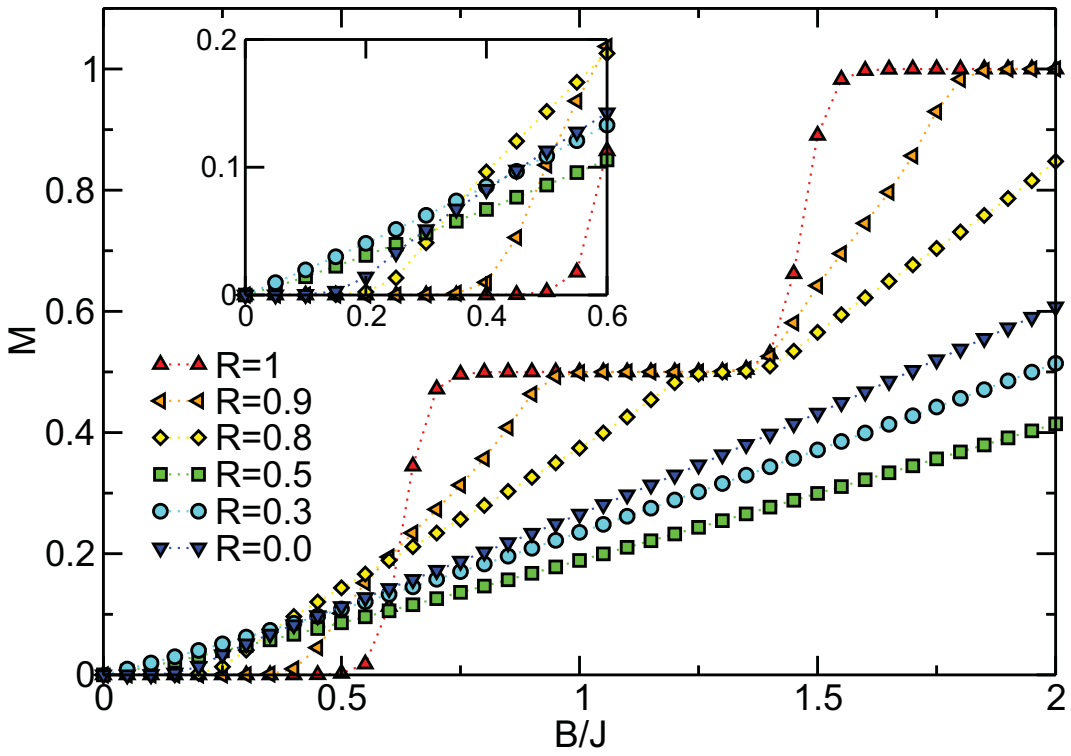

Figure 3.11: Field dependent magnetization for different ratios $1 \geq R \geq 0$ and $D = 0.27J$ of the S=1 ladder system at the temperature $T = 0.034J$.

depicted in Fig. 3.11 with the inset showing the low-field behavior.

It is apparent, that already a small inter-dimer coupling smears the magnetization step structure and decreases the length of the $M = 0.5$ plateau. For a coupling ratio $R \leq 0.7$ and for temperature above $T = 0.034J$, plateaus in the calculated magnetization profile are absent. The low-temperature inset reveals the expected variation of the gap in R in accordance with our susceptibility calculations: for $R \geq 0.7$ we still find a clear spin gap, indicated by $M = 0$. At lower ratios $0.7 \geq R \geq 0.3$ gaps are not visible anymore. Note that this however is no clear indication for a vanishing gap due to the relatively high temperatures. Finally for the pure Haldane system, we again find a magnetization profile which is consistent with a gapped excitation spectrum.

The calculations for R=1, 0.95 and 0.9 are compared with the measured data in Fig. 3.12. The data was scaled by setting the magnetization at $B_{ex} = 40$ T to $M = 0.5$ and using a value $J+K \approx 43$ K. A variation of $J+K$ mainly shifts the position of the step and does not affect the broadening of the step. The QMC calculations show a broadening of the magnetization step for decreasing R, i.e. increasing magnetic exchange strength

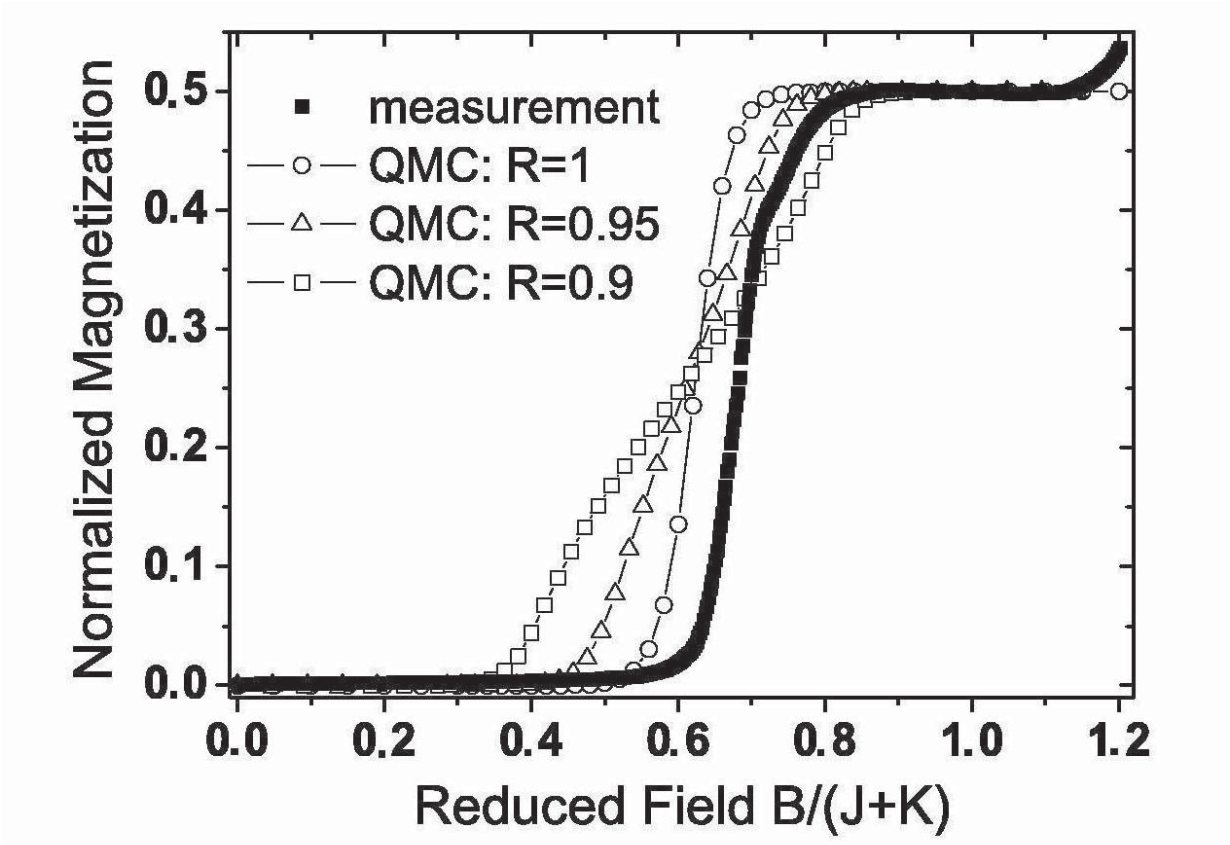

Figure 3.12: QMC calculations of the field dependent magnetization for different ratios of R with $D/J = 0.27$. Open circles: $R = 1$, open triangles: $R = 0.95$, open squares:$R = 0.9$. The calculations were done for a reduced temperature $T/J = 0.034$, corresponding to $J + K = 43$K and $T = 1.47$K. The solid squares are the normalized measurements scaled with $J + K = 43$K.

along the legs of the ladder. The QMC calculations are possible only for B parallel to the anisotropy axis up to now. Therefore, comparing with the measurements on powder samples one has to consider that the magnetization step in the experimental data set is additionally broadened by the averaged presence of the axial anisotropy D. Therefore, the step of the appropriate QMC calculation has to be sharper than the measurement performed on a powder sample. For this reason, the experimental data is in agreement only with the calculation for $R = 1$, i.e. the uncoupled dimer model.

3.2.3 Conclusion

We have shown QMC data for the susceptibility and the magnetization of a spin S=1 ladder system with different ratios of rung and leg coupling, limited by Haldane-chain and uncoupled dimers, for various single-ion anisotropies. It turns out that a small easy-plane anisotropy drives the system from a gapped to a gapless excitation spectrum which we have shown for the particular ratio $R = 0.3$ within the thermodynamic limit. It is to be expected that small easy-plane anisotropies will act similarly for other ratios R. For the experimental comparison we conclude that although the Ni(II) ions form a structural ladder, a model of isolated dimers on the rungs describes the susceptibility very well with an upper limit of 5 % interdimer exchange coupling by fitting a different susceptibility temperature region. The analysis of the temperature dependent susceptibility and magnetization data leads to a magnetic exchange constant of $J = 43$ K along the rungs of the ladder with a single-ion anisotropy $D = 11.5$ K.

3.3 Spin S grid systems

To close the chapter of static QMC applications, we utilize our method in a very different context as compared to the preceding sections. The ability of the QMC to deal with a large Hilbert space has so far mainly been used to scale up system sizes into the thermodynamic limit. In this section however, we look at particularly small grid systems with large spin magnitudes S=5/2 which increase the Hilbert space beyond the scope of exact diagonalization techniques. Such systems can be realized in molecular nano-magnets which are compounds with magnetic metal ions linked by organic ligands to form well defined magnetic nano-clusters. A prominent example which has driven numerous scientific effort is the Mn_{12} molecule ($Mn_{12}O_{12}(OAc)_{16}(H_2O)_4$, see Fig. 3.3 (b)) with review articles documenting the physical, chemical and technological implications of such materials [120–127]. This molecule exhibits slow relaxation of the magnetization, with a relaxation time of about one month at 2 K which makes it an ideal storage for 1 bit of information while at the same time being orders of magnitude smaller than nanoparticles of conventional ferromagnets. This, and the observation of quantum tunneling of the magnetization in the presence of a single-ion anisotropy, were identified to be of purely molecular origin which lead to an enormous growth in the field of molecular magnets.
In this section we report on another molecular magnet which is Mn_9(2POAP-2H)$_6(ClO_4)_6 \cdot 3.57MeCN{\cdot}H_2O$, the so called Mn-[3 × 3] grid (see Fig. 3.3 (a)). The system can be described by a Hamiltonian consisting of a ring of eight spins coupled by J_r and a center-spin coupled to the edge spins of the ring by J_c with single-ion anisotropies D_r, D_c working separately on ring- and center-spin.

Due to the very large dimensions of the Hilbert space (10077696) this material has so far only been described in terms of an effective Hamiltonian in which spin operators of corners and edges were combined to sublattice spin operators $\mathbf{S}_\mathrm{A}$, $\mathbf{S}_\mathrm{B}$ with $S_A = S_B = 4 \times 5/2$ [30]. Parameters extracted from inelastic neutron scattering measurements [128] suggest $J_r = J_c = J = 5$K (antiferromagnetic) and $D_r = D_c = D = 0.14$K (easy-plane anisotropy), while previous fit attempts based on susceptibility measurements assumed the center spin as essentially uncoupled [29].

3.3.1 The effect of center-spin coupling

To shed light on the consequences of the parameters J_c, J_r, D we performed parameter studies of the full [3 × 3] grid system Hamiltonian as function of single-ion anisotropy D and center-spin coupling J_c. The latter will be discussed in the following paragraphs, the single-ion anisotropy is subject of the next subsection.

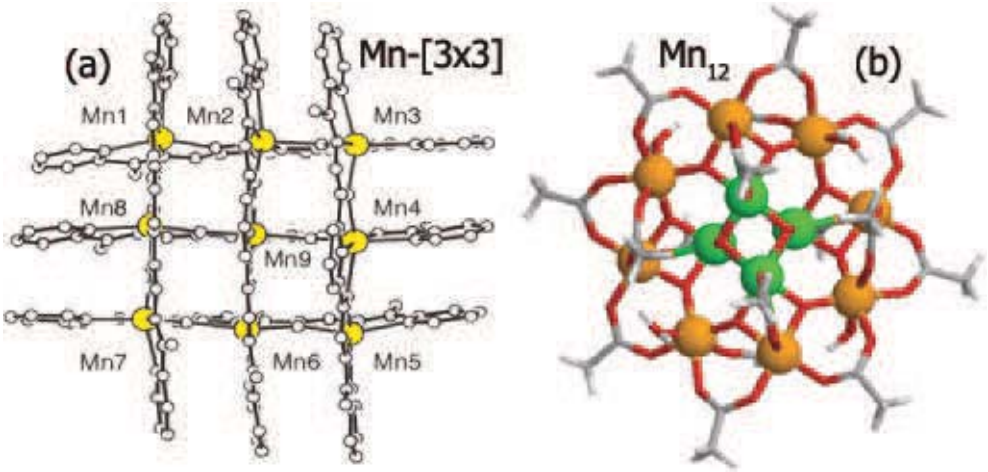

Figure 3.13: (a) Structural representation of the cation $[Mn_9\text{-}(2POAP\text{-}2H)_6]^{6+}$ and (b) of the Mn_{12} molecular magnet $Mn_{12}O_{12}(OAc)_{16}(H_2O)_4$.

Susceptibility In Fig. 3.14 we present results for the susceptibility as function of center-spin coupling $0 \leq J_c \leq 1$. We find several effects – firstly we find classical Curie behavior for the high-temperature region as indicated by a straight line in the log-log plot ($\rightarrow \chi \propto 1/T$). The same behaviour is found at low temperatures as second observation. This comes as expected, since we examine a system with an odd number of spins, leading to a macroscopic total spin $S = \sum_{i=1}^{9} S_i^z$. The latter will act as an effective free spin as long as no single-ion anisotropy is present. The transition between a weakly and a strongly coupled center-spin appears to be smooth for all temperatures, as also shown in the low-temperature inset of Fig. 3.14. The dominant effect of decreasing J_c is a slightly enhanced susceptibility in the temperature region $1 \leq T/J_r \leq 10$. This effects pertains beyond the trivial scaling factor $\chi(2J_r + J_c)/3$ and $3T/(2J_r + J_c)$ given by the 2:1 ratio of ring- to center-bonds. In order to pronounce the effect on the susceptibility upon variation of J_c in Fig. 3.15, we depicted the susceptibility with respect to J_r.

Ergodicity It is interesting to note the relatively large QMC errors for the susceptibility at low temperatures (not visible in Fig. 3.14 as consequence of the utilized scales). To elucidate on that issue, we present temperature dependent magnetization data for three different coupling ratios $J_c/J_r \in \{0.0, 0.5, 1.0\}$ at zero field (see Fig. 3.15). What we find is, that at temperatures below $T/J_r < 0.1$, QMC errors increase substantially by orders of magnitude. This is a direct consequence of the macroscopic total spin of the

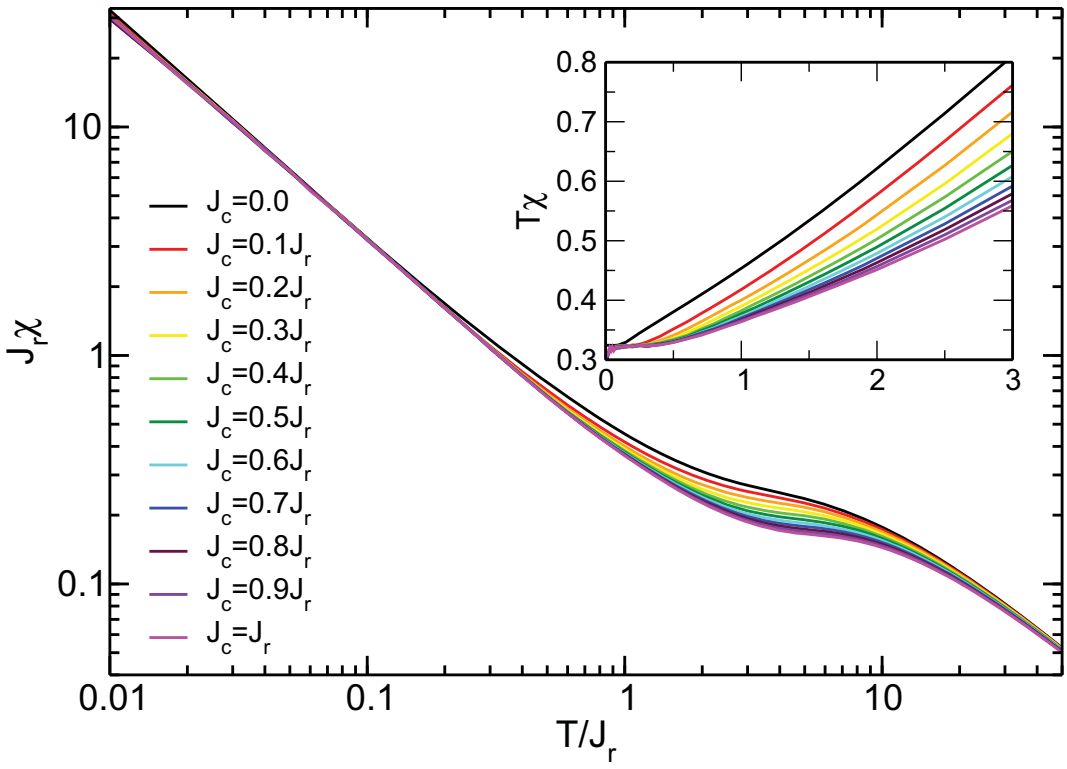

Figure 3.14: Susceptibility for the spin S=5/2 [3 × 3] grid system with $D = 0$ as function of temperature and center-spin coupling J_c in units of the ring-coupling J_r. The main plot shows a double logarithmic scale corresponding to the expected free spin Curie behavior which is clearly visible in the high- and in the low-temperature regime. The inset shows $T\chi$ in the low temperature region. QMC errors are within line-width of the plots.

system, which has to be sampled efficiently to result in a zero total magnetization for zero magnetic field. This sampling however requires an extensive amount of Monte-Carlo sweeps since the Hilbert space is extremely large and a tunneling of the Néel vector $S \rightarrow -S$ has to cross an energy barrier of intermediate higher energy states which is lowered by an easy-plane ($D > 0$), respectively heightened further by an easy-axis anisotropy ($D < 0$). To ensure ergodicity of the QMC we paid close attention to the zero-field magnetization as an ergodicity probe for all presented data – any deviations from $M = 0$ outside the standard deviation indicates ergodicity loss[2].

[2]Note that the converse argument does not hold – we cannot deduce preserved ergodicity by $M = 0$.

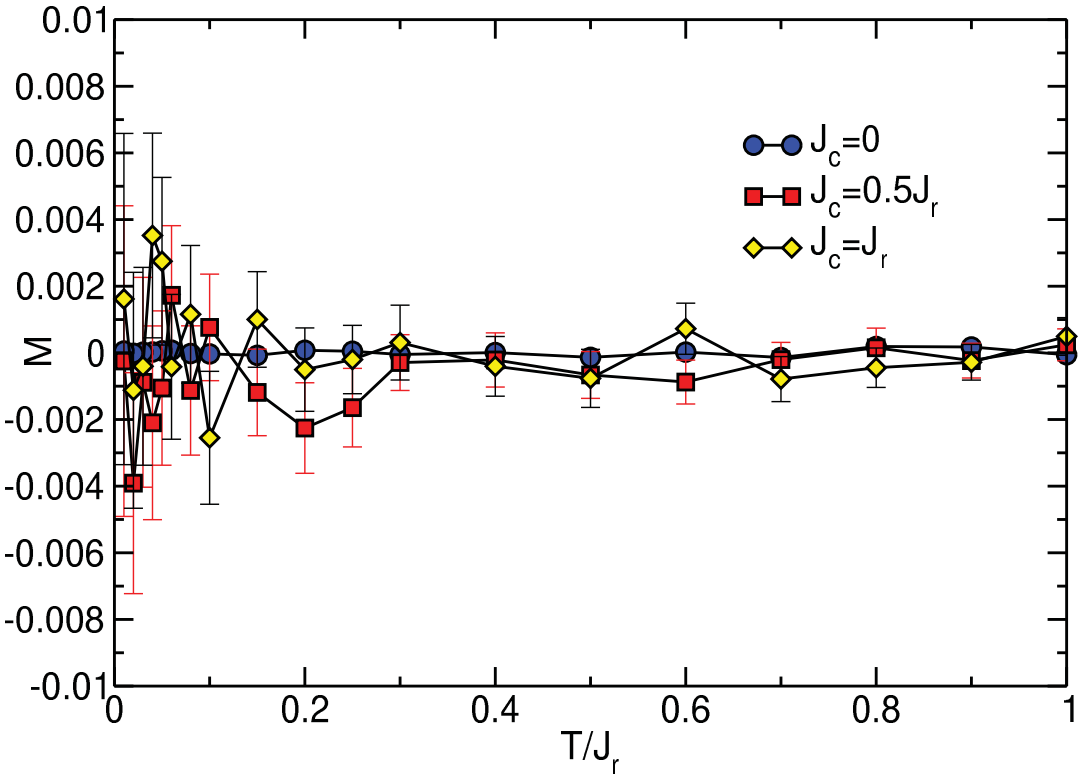

Figure 3.15: Magnetization for the spin S=5/2 [3 × 3] grid system with $D = 0$ as function of temperature and center-spin coupling $J_c/J_r \in \{0.0, 0.5, 1.0\}$. Note the strong increase of the error at low temperatures, reflecting the enormous Hilbert space which brings the algorithm to a point where ergodicity might not be ensured anymore.

3.3.2 The effect of single-ion anisotropy

After the rather subtle effect of center-spin coupling on the spin susceptibility, we now focus on the effect of a single-ion anisotropy D.

Susceptibility In Fig. 3.16 we show $T\chi$ as function of temperature and six different single-ion anisotropies $D \in \{-0.3, -0.2, -0.1, 0.1, 0.2, 0.3\}$ in comparison to the reference value of $D = 0$. The results support our expectation, that even a small single-ion anisotropy has a large impact on the system due to the large spin magnitude which enters the anisotropy contribution to the Hamiltonian quadratically. In comparison to the reference data at $D = 0$ we find two dominant effects – a large spin gap for the susceptibility with easy-axis anisotropy $D < 0$ in contrast to the Curie-like plateau of

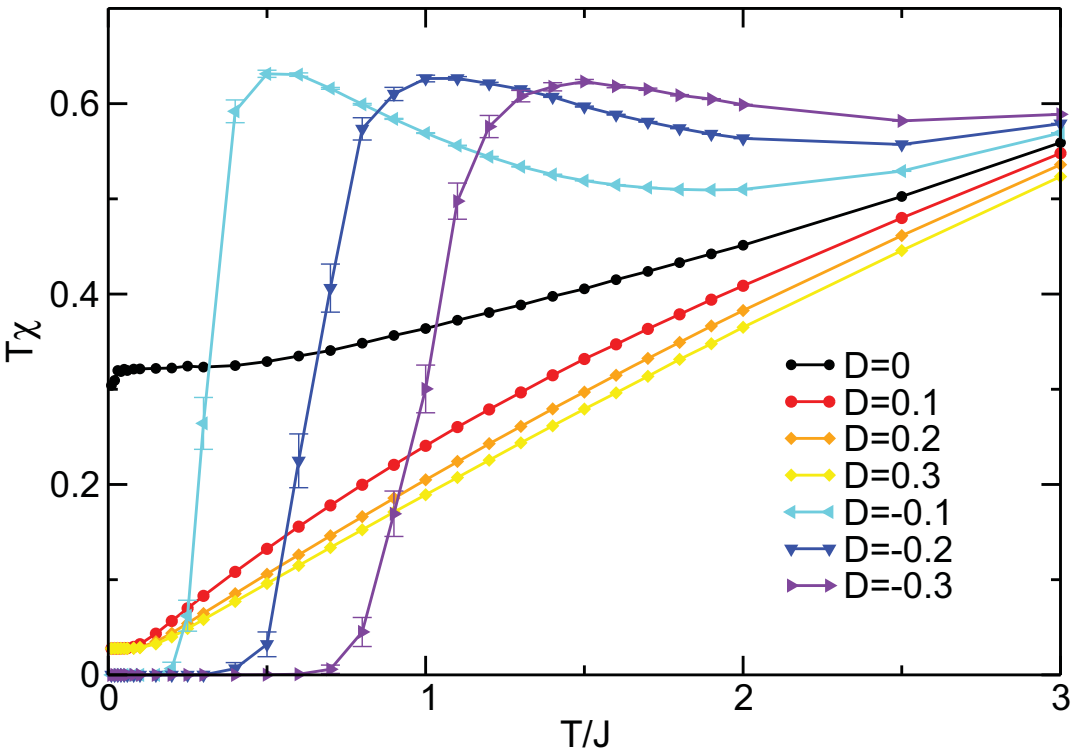

Figure 3.16: Susceptibility for the spin S=5/2 [3 × 3] grid system with $|D/J| \in \{0.0, 0.1, 0.2, 0.3\}$ as function of temperature for $J_c = J_r = J$. We find Curie behavior for easy-plane and a large spin gap for easy-axis anisotropy. The QMC-errors (if not shown) are within symbol size.

the easy-plane datasets (note that $T\chi$ is shown). Both effects are fairly easy to understand: on the one hand, a small easy-axis anisotropy immediately leads to a strong energy contribution whenever the individual spin z-component is large. This drives the system into a high total spin state $S = 5/2$, nearly independent of the magnitude of D. In contrast to that, already a small easy-plane anisotropy forces each spin into its lowest z-state, leading to a total spin of $S = 1/2$. This effect also appears to be relatively independent of the magnitude of D.

Ergodicity Again, we notice comparably large errors of the susceptibility for $0.25 \leq T/J \leq 1$ and easy-axis anisotropy. A look at temperature dependent magnetization data as function of single-ion anisotropy $D \in \{-0.3, 0, 0.3\}$ (see Fig. 3.17) indicates, that the QMC seems to produces a reliable error for all three choices of D, since the magnetization is zero within QMC error bars. For an easy-axis anisotropy however, the error is nearly one order of magnitude larger than for the $D = 0$ and $D = 0.3$ results

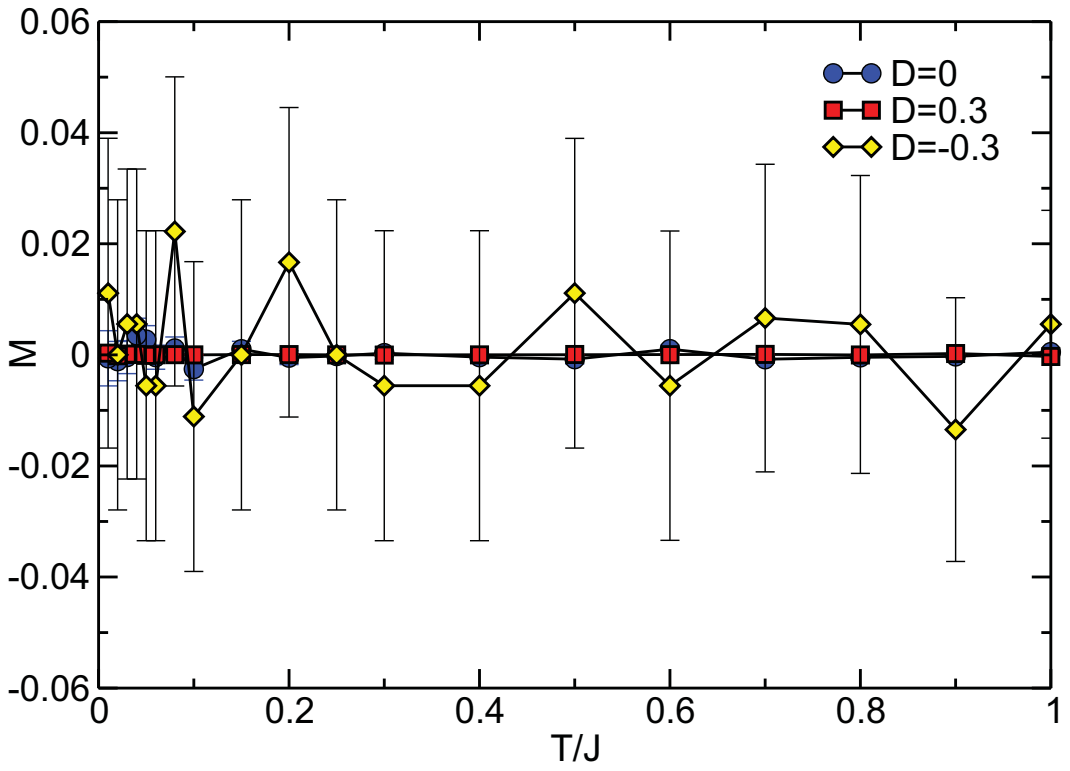

Figure 3.17: Magnetization for the spin S=5/2 [3 × 3]-grid system with $|D/J| \in \{0.0, 0.3\}$ as function of temperature with $J_c = J_r = J$. In the case of strong easy-axis anisotropy we find an increase of the statistical errors up to one order of magnitude compared to $D = 0.0$. However, $\langle M \rangle = 0$ is still fulfilled owing to independent parallel computing of observables to ensure ergodicity.

in the displayed temperature region $0.01 \leq T/J \leq 1$. This can be explained by the additional tunnel barrier introduced by the easy-axis choice of D, which complicates the tunneling $S \to -S$ of the energetically equivalent total spin states.

These obvious sampling complications can in principle be countered by parallel tempering [129]. For our results however, parallel computing of 100+ independent systems running on different CPUs seemed sufficient to extract reliable information.

Static Structure Factor To support our arguments for the susceptibility shown in Fig. 3.16 with total spin z-component state $S = 1/2$ for $D > 0$ and $S = 5/2$ for $D < 0$, we present the static structure factor at $q = 0$ (Fig. 3.18) and $q = \pi$ (Fig. 3.19). Starting with $S(q = 0)$, we find that, independent of the magnitude of D, the

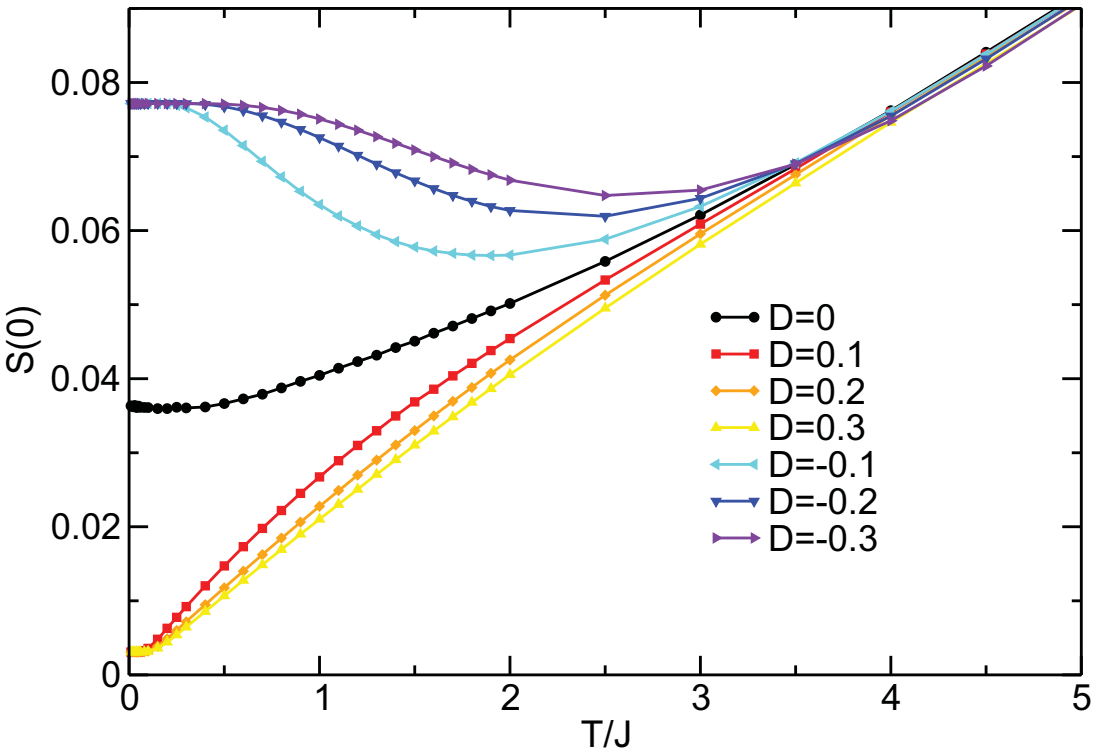

Figure 3.18: Static structure factor $S(0)$ as function of temperature for seven different single-ion anisotropies $|D/J| \in \{0.0, 0.1, 0.2, 0.3\}$ with $J_c = J_r = J$. QMC-errors are within symbol size.

zero-temperature limit of $D < 0$ and $D > 0$ is always the same. In the case of an easy-plane anisotropy $D > 0$ we find $S(0)|_{D>0} \approx 0.0030864198(3)$ which agrees up to 8 digits with the results of a classical Néel state of a 3×3 spin $S = 1/2$ system $S(q = 0)_{\text{classic}} = \frac{1}{9^2}\frac{1}{4} = 0.00308642$. On the other hand we find $S(q = 0)|_{D<0} \approx 0.077160494(4)$ for the zero-temperature limit of the static structure factor with easy-axis anisotropy $D < 0$. The corresponding classical result of a $[3 \times 3]$ grid with spin $S = 5/2$ in perfect Néel order is $S(q = 0)_{\text{classic}} = \frac{1}{9^2}\frac{25}{4} = 0.0771605$. This means at zero temperature for any single-ion anisotropy, the system becomes *immediately* well described by a purely classical Néel-state with either maximized ($D < 0$) or minimized ($D > 0$) z-components.

If we follow the same classical argument for the staggered static structure factor $S(\pi)$ shown in Fig. 3.19, we find a zero-temperature limit of $S(\pi)_{D=0.3} \approx 0.6505(2)$ and $S(\pi)_{D=-0.3} \approx 0.1257(4)$ for the largest $D \in \{0.3, -0.3\}$. The corresponding classical results read $\frac{1}{9}\frac{1}{4} = 0.69444$ and $\frac{1}{9}\frac{25}{4} = 0.02777$. While the classical description fits the easy-axis anisotropy reasonably well, we find a much larger staggered structure factor

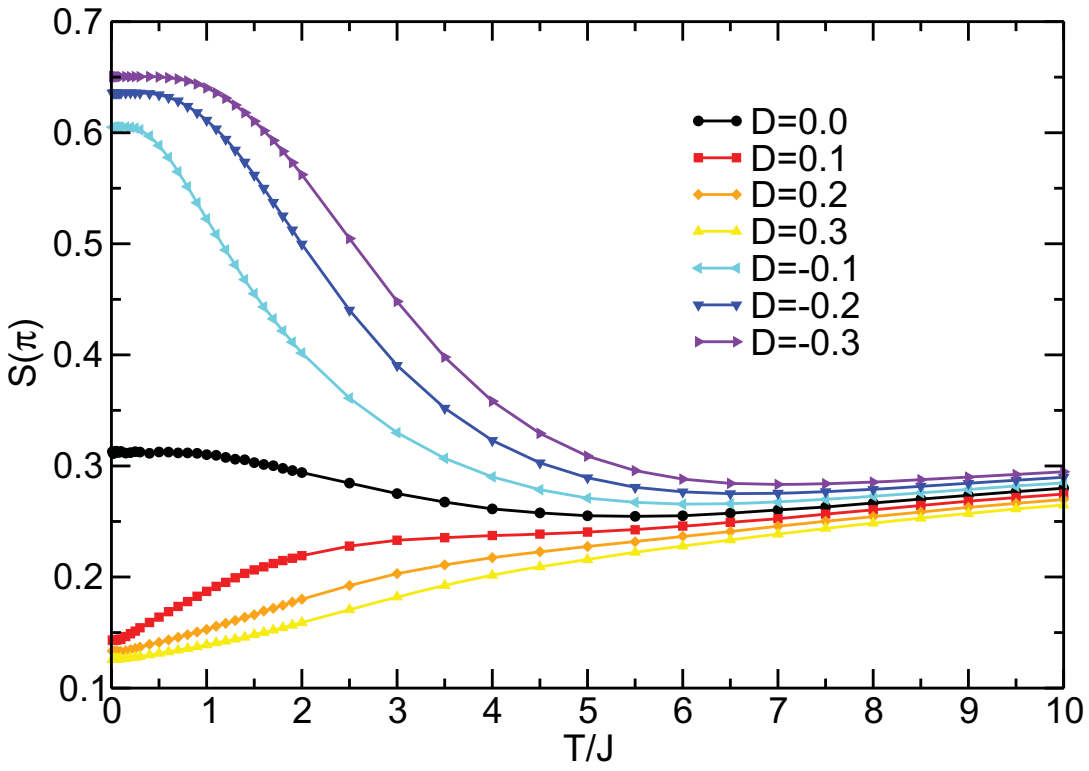

Figure 3.19: Staggered structure factor $S(\pi)$ as function of temperature for seven different single-ion anisotropies $|D/J| \in \{0.0, 0.1, 0.2, 0.3\}$ with $J_c = J_r = J$. QMC-errors are within symbol size.

for the easy-plane anisotropy $D = 0.3$ in comparison to classical results.

Magnetization We finally present results for the magnetization M of the grid system as function of applied magnetic field B and single-ion anisotropy D at temperatures $T/J \in \{0.1, 0.01\}$ (see Fig. 3.20). From previous results of the susceptibility and the static structure factor it is clear, that the effects of a small ion-anisotropy should lead to very different magnetization profiles as function of B and D. On the one hand we learnt that the system aligns immediately around the z-axis with a high spin z-state for $D < 0$. This should result into the initial polarization of a total spin $S = 5/2$, followed by a series of $\Delta S = 1$ level crossings for larger B. On the other hand we know that the system orients in-plane with a minimum spin z-state for $D > 0$ which should lead to an initial polarization of a total spin $S = 1/2$ with adjacent $\Delta S = 1$ level crossings.
Those expectations are matched perfectly in Fig. 3.20 (note that M is normalized by the system size $N = 9$). Beyond these expected observations it is interesting to note the

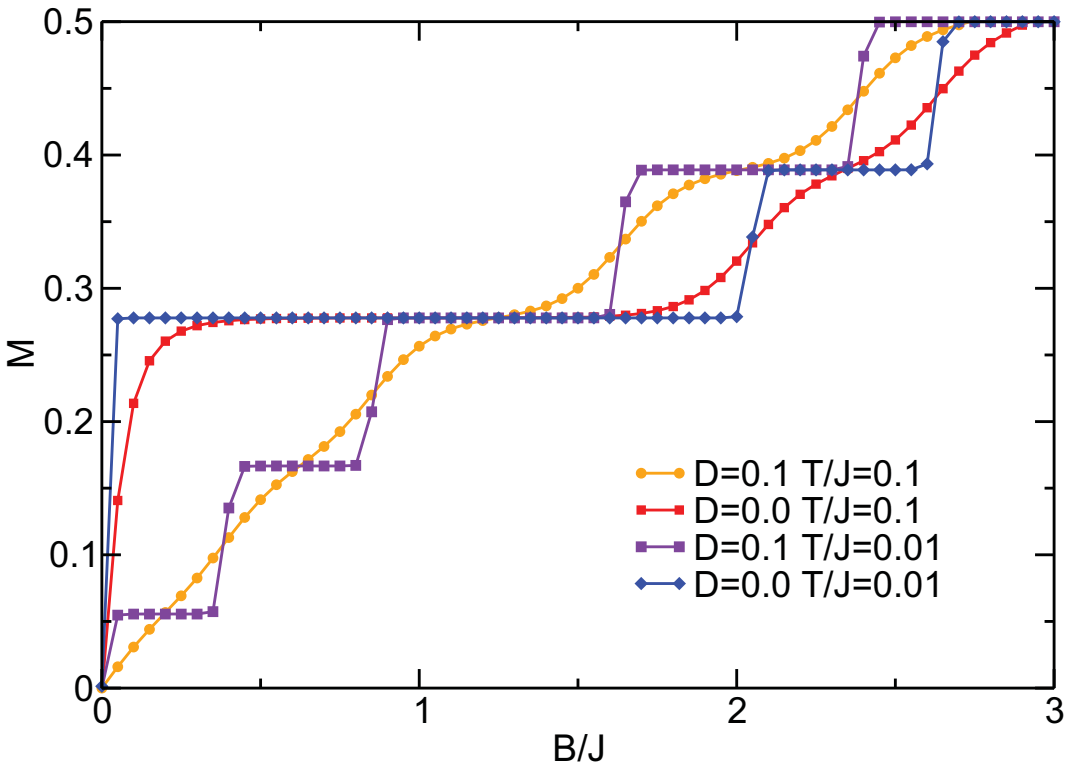

Figure 3.20: Magnetization M of the $[3\times3]$-grid system as function of applied magnetic field B and for three different single-ion anisotropies $|D| \in \{0.0, 0.1\}$ in units of $J_r = J_c = J$. QMC-errors are within symbol size.

particularly long plateau of the data for $D = 0$ in contrast to the considerably smaller plateaus for the spin $S = 1/2$, $3/2$ and $5/2+$ transitions in the case of $D = 0.1$. The effect of temperature is merely a weakening of the step-structure. No results are shown for the easy-axis anisotropy $D < 0$ since the QMC showed clear signs of ergodicity problems, stemming from the large tunnel barrier between total spin $S = \pm5/2$ state which lead to extremely large errors bars with questionable validity.

3.3.3 Comparison to experimental data

In this final subsection we compare our results to experimental data on Mn-$[3\times3]$ [29]. Our focus for comparisons is set on the susceptibility since magnetization measurements are again (as for the ladder system discussed in subsection 3.2) only available as powder-average. So far the susceptibility of Mn-$[3\times3]$ has been interpreted by coupling constants $J_r = 5.5$K and $J_c = 0$ [29]. Two years later an INS study found the parame-

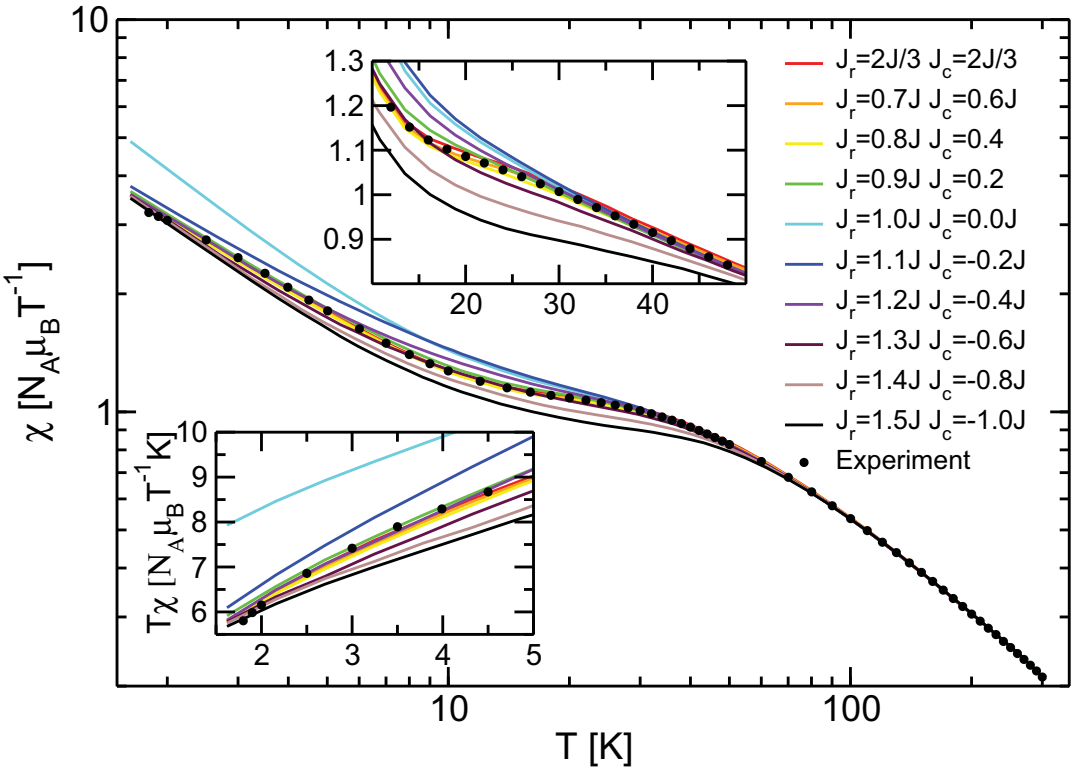

Figure 3.21: Comparison of QMC data with experimental susceptibility of the $[3 \times 3]$-grid system with parameters $D = 0.07$K and $J = 5.4$K for different ratios of J_r, J_c while preserving the high-temperature limit of the QMC data through 1:2 changes on $J_r : J_c$ which is dictated by the bond ratios. Obviously all shown ratios even with ferromagnetic center-spin coupling lead to satisfying high-temperature ($T > 50$K) description of the grid system. In the intermediate regime (upper panel), only ratios $1/2 < J_r/|J_c| < 2$ still display an acceptable description of the data while for the low-temperature regime the best fit supports $J_r \approx J_c$.

ters $J_r = J_c \approx 5$K with an easy-plane anisotropy $D = 0.14$K to be the best description of the spectral features. Obviously a thorough study with the full Hamiltonian would be helpful to clarify the basic parameters of the system.

In Fig. 3.21 we present our results for the the susceptibility for different parameters J_r, J_c in units $J = 5.4$K with a weak easy-plane anisotropy $D = 0.013J = 0.07$K. At high temperatures ($T > 50$K, main panel Fig. 3.21), we find all our trial parameters to be a valid description of the experimental susceptibility as long as the coupling constants J_r:J_c obey 1:2 step changes. Those step changes are dictated by the bond ratio of eight ring bonds versus four center spin bonds. In contrast to that, the intermediate region ($10K < T < 50$, upper panel) pins the ratio to be $2 \geq J_r/J_c \geq 1$ and clearly excludes

the choice $J_r = 5.5$K and $J_c = 0$ of [29]. The lowest temperature region finally shows best agreement with $J_r = J_c$, supporting [128]. However, we suspect that the marginal differences displayed in the susceptibility for all ratios $2 \geq J_r/J_c \geq 1$ can be lifted by small variations of D in the low-temperature limit.

3.3.4 Conclusion

We presented QMC data for the susceptibility, magnetization and (staggered) static structure factor of a Mn-[3×3] grid system with large spin $S = 5/2$. First we systematically studied center-spin coupling dependency $J_c \in \{0.0, \ldots, J_r\}$ and found enhanced susceptibility in the region $1 \leq T/J_r \leq 10$ upon decreasing J_c. The transition between $J_c = 0$ and $J_c = 1$ was shown to be smooth with no signs of fundamental changes in the underlying physics. Much stronger impact than the center-spin coupling has been found by applying small single-ion anisotropies. The effect of applied easy-plane anisotropies was shown to be consistent with an Ising-like low-z state description with a total spin $S = 1/2$ while the system immediately favors an Ising-like high-z state with a total spin $S = 5/2$ for any applied easy-axis anisotropy. Both effects have been documented by the (staggered) dynamic structure factor, which showed classical Néel ordering upon $|D| > 0$ for the $T \to 0$ limit. For the easy-plane anisotropy $D > 0$ the low-z state was also proven in the magnetization data in the initial polarization of the total spin $S = 1/2$, followed by level crossings of $S = 3/2, 5/2, \ldots$ with increasing magnetic field. This however was not possible for the easy-axis anisotropy, since our QMC algorithm showed clear signs of ergodicity problems due to the large tunnel barrier of the total spin introduced by relatively small easy-axis anisotropies.
We finalized our investigation on the [3×3] grid system with a comparison of QMC vs. experimental susceptibility on Mn-[3×3] [29] with the conclusion that, even though there is a wide choice of parameters fitting the high temperature region, the low temperature exchange couplings J_r, J_c need to be within $2 \geq J_r/J_c \geq 1$ in combination with a small easy-plane anisotropy $D = 0.07$K. This result contradicts early fits on an effective model Hamiltonian [29] and it supports later INS studies [128] on this issue.

Chapter 4

Dynamic properties of 1D quantum magnets

In this section, dynamic properties of spin chains will be discussed, contrasting the zero-field spinon-continuum of the isotropic spin S=1/2 Heisenberg chain with the sharp magnon-excitations of the Haldane chain as function of temperature and magnetic field. This very broad context is carried in the case of spin S=1/2 by numerous high- ($SrCuO_2$ [73] ($J/k_B \approx 2600$K), Sr_2CuO_3 [74, 130, 131] ($J/k_B \approx 2200$K)) and low-J ($Cu(C_4H_4N_2)(NO_3)_2$ [132] ($J/k_B \approx 10.7$K)) materials. Methods for non-static quantities are typically high resolution spectroscopy methods such as inelastic neutron scattering (INS) [133], high-field nuclear magnetic resonance (NMR) [31, 134–136], muon spin-resonance (μSR) [137], but also magnetic transport measurements accessible through heat transport [138, 139]. The key-quantities to look at from an experimental point of view are the dynamic structure factor $S^{\alpha\beta}(\omega, q)$ which is directly proportional to the neutron scattering cross section of INS experiments, and its q-integration at the NMR resonance frequency, which corresponds to the $1/T_1$-relaxation rate of an NMR experiment (see eqn. (2.30)).

From a theory point of view, the dynamics of the Heisenberg chain is still a challenging subject for various methods and, in the case of finite fields in combination with finite temperatures, results are completely absent. It is generally accepted that spin excitations of the spin S=1/2 chain fractionalize into multi-spinon states, which span an energy continuum [140, 141]. At zero temperatures, numerical analysis of these excitations has been carried out in many studies using exact diagonalization (ED) of finite AFHCs, see eg. refs. [142–144], including the effects of B and Δ, as well as by dynamic variants of the DMRG [145, 146]. In principle, also BA allows to determine

dynamic correlation functions, however calculating the corresponding matrix elements is highly non-trivial and progress has been made only recently. By now analytic expressions for dynamic spin correlation functions are available for the two- [147–149] and the four-spinon sector [150–153] at $\Delta = 1$, $B = 0$ and $T = 0$. In addition, determinant approaches [154, 155] allow for numerical treatment of two- [156–158] and many-spinon [159, 160] states of the XXZ chain in finite magnetic fields at $T = 0$. Finally, mapping to field theory in the continuum limit [161] has been used to study the small-q behavior of the longitudinal dynamic structure factor in the gapless regime [68, 162–164].

At finite temperatures, the dynamic correlation functions of the AFHC remain an open issue. The dynamic structure factor $S^{\alpha\beta}(q,\omega)$ has been studied by complete ED of small systems [165, 166] in the context of spin diffusion, see [138, 167] and refs. therein. However, such analysis is limited by finite size effects to $k_B T \gtrsim J$. Recently, finite temperature real-time auto- and next-nearest neighbor correlation functions have been accessed by DMRG methods [39, 168]. However, the time range of such calculations is limited, as the spectrum of the reduced density matrix used to truncate the Hilbert space becomes dense. In this respect QMC remains a key tool to evaluate $S^{\alpha\beta}(q,\omega)$ for system sizes which are close to the thermodynamic limit, over the complete Brillouin zone and at finite temperatures with the limitations set primarily by the analytic continuation of imaginary-time data [169]. QMC analysis of $S^{\alpha\beta}(q,\omega)$ has been carried out for $B = 0$ [170–172], results for $B \neq 0$, however, are lacking.

A very interesting aspect of the spin S=1/2 chain is the field driven quantum critical point (QCP) at saturation field B_c. Following the pioneering analysis of spin chains [173–175] and spin ladders [25] in external magnetic fields, Bose-Einstein condensation of hard-core bosons has been related to some phase transitions in quantum magnets which stem from the level-crossing of elementary triplet excitations with the ground state at a critical external magnetic field. Such field induced QCPs have been under intense scrutiny for three and quasi-two dimensional spin $S = 1/2$ dimer systems, i.e. $TlCuCl_3$ [24, 176–178] and $BaCuSi_2O_6$ [179], for S=1/2 ladder materials $Cu_2(C_5H_12N_2)_2Cl_4$ [180] and $(C_5H_{12}N)_2CuBr_4$ [181, 182], for the S=1 Haldane chain $Ni(C_5H_{14}N_2)_2N_3(PF_6)$ [68], for the coupled-chain compound $NiCl_2$-4SC$(NH_2)_2$ (DTN) [183, 184] with S=1, as well as for the effective S=1 system $(CH_3)_2CHNH_3CuCl_3$ [185, 186]. All of the latter materials feature a gapful zero-field state with the lowest triplet branch condensing as the field is *increased*. However, a similar scenario can be realized in the AFHC upon *decreasing* the field through the critical value for complete polarization. Intriguing NMR experiments have been performed by

Hannes Kühne *et al.* [31] which lead to a comparison of their experimental and our theoretical $1/T_1$ relaxation rates in the vicinity of the QCP presented in subsection 4.1.3.

In contrast to that, the dynamics of the Haldane chain will be discussed in section (4.2), following similar discussions for spin S=1/2 in section 4.1 and 4.1.3 which means we focus mainly on dynamic structure factors and resulting NMR rates as function of temperature and magnetic field to connect to section 4.1. In contrast to the half-integer spin chain, the spin excitations of the Haldane chain are gapped [19]. Furthermore, most of the spectral weight is combined into a sharp S=1 one-magnon branch [187–189] in contrast to the broad energy continuum of the spin S=1/2 chain. Even though the spectral properties are very different for spin S=1/2 and Haldane chain in *zero* field, the latter can be described by a Luttinger liquid once the spin gap is closed by the first critical field B_{c_1} [161, 173, 190].

The Haldane system found many experimental realizations in multiple materials $Ni(C_2H_8N_2)_2NO_2(ClO_4)$ (NENP) [66, 67, 76–78], $CsNiCl_3$ [79–82, 191], $Ni(C_5D_{14}N_2)_2N_3(PF_6)$ (NDMAP) [84–88], $Ni(C_5H_{14}N_2)_2N_3(ClO_4)$ (NDMAZ) [192], $AgVP_2P_6$ [193] and $CsNiCl_3$ [194, 195]. Additionally, various spin S=1/2 two-leg ladder materials $TlCuCl_3$ [24, 196, 197], $(C_4H_{12}N_2)Cu_2Cl_6$ (PHCC) [198] and $(C_5H_{12}N)_2CuBr_4$ [199, 200] were found to display dynamics very similar to that of the Haldane chain and they have been studied extensively in the context of magnon-fractionalization in the Luttinger liquid phase as already mentioned.

From a theoretical point of view, the dynamic properties are framed by field theory approaches, most prominently the non-linear σ-model (NLσM) [201–203], Tsevlik's three coupled Majorana fermions [203, 204] and the bosonic Landau-Ginzburg model [173, 174, 203]. Such analyses are typically valid in the limits of low energy near the zone boundary and/or center. Beyond field theory approaches, only very few other methods are available. Several QMC [171, 188, 205, 206] and first tDMRG results [207] for the dynamic structure factor exist, however none at finite magnetic fields even though particularly the field dependence of the Haldane dynamics yields rich properties.

After analysis of the dynamic structure factors and the $1/T_1$ rate (in 4.1.3), we treat the subject of finite temperature spin diffusion for the SU(2) symmetric point $\Delta = 1$ in section 4.3, where up to present time contradicting results exist. Spin transport in the Heisenberg chain is directly related to carrier transport in 1D correlated spinless fermion systems, via the Jordan-Wigner transformation, and therefore is of great interest in a broader context. Linear response theory [167] shows the zero momentum, frequency dependent spin conductivity $\sigma'(\omega) = D\delta(\omega) + \sigma'_{reg}(\omega)$ to consist of the Drude weight

D and a regular spectrum $\sigma'_{reg}(\omega)$. This Drude weight has been under intense scrutiny for more than two decades. However, no generally accepted picture has emerged. A nonzero Drude weight would imply *dissipationless* transport in a correlated system [208], despite the fact that the z-component of the spin current j and Hamiltonian H do not commute $[j, H] \neq 0$ for the XXZ model. Very recently, spin diffusion has been conjectured to govern the low-frequency spectrum of the regular conductivity [32], based on real-time transfer matrix renormalization group (tTMRG) and a perturbative analysis using bosonization. The latter provides for an approximate expression for the Fourier transform of the retarded spin-susceptibility $\chi_{ret}(q,t) = i\Theta(t)\langle[S^z_q(t), S^z_{-q}]\rangle$, a quantity we relate directly to QMC results free of any MaxEnt procedure for a high-precision comparison in subsection (4.3).

4.1 Dynamic structure factors of the spin 1/2 Heisenberg chain

In this section we will present results for the transverse and longitudinal dynamic structure factor at finite temperatures, in the range of $T = J/20 \ldots J$ and magnetic fields below and above the saturation field B_c. Furthermore we extract relaxation rates to document the QCP of the system upon approaching the saturation field in comparison to experiments performed by H. Kühne *et al.* on the material CuPzN. We conclude our results with a sum-rule consistency check of our analytic continuations.
All QMC calculations refer to systems with 128 sites, typically with one billion Monte-Carlo updates (one diagonal and sufficient [50] loop updates), distributed over 1000 bins. Only 50-100 τ-points were extracted for each temperature in order to prevent over-sampling of the relatively short expansion orders at elevated temperatures close to $T = J$. An indication for over-sampling is given by diagonalizing the covariance matrix which exhibits vanishing eigenvalues in case of statistically dependent data.

4.1.1 Longitudinal dynamic structure factor $S^{zz}(q, \omega)$

In Fig. 4.1 and 4.2 we show the longitudinal dynamic structure factor both, as a 3D and a contour plot for two different temperatures $T = \{J, J/4\}$ and three different magnetic fields $B = \{0, B_c/2, B_c\}$. The solid lines displayed in the contour plots for $B < B_c$ refer to the upper and lower boundaries of the two-spinon spectrum as obtained from BA selection rules [142]. For zero magnetic field they enclose a region which, within two-spinon calculations, contains about 73% of the zero temperature spectral weight [148]. We will now focus on each of the magnetic fields separately.

The case $B = 0$ At zero magnetic field and high temperatures, i.e. Figs. 4.1a) and 4.2a), we find a strong broadening of spectral features. While the region of finite spectral weight remains bounded from above by $J\pi \sin|q/2|$ [141], significant weight appears below the lower two-spinon boundary $\frac{\pi J}{2} \sin|q|$ set by de Cloizeaux-Pearson [140]. Most noteworthy, high spectral weight occurs for $q, \omega \to 0$. This intensity is related to spin conservation which dominates the long wave-length dynamics in the quasi-classical regime $k_B T \gg J$. The question whether the long wave-length spin dynamics in the AFHC can be described by spin *diffusion* is a long-standing issue with no final answer as of today, however we will present strong indications for a diffusive transport channel in section 4.3. For a recent review on the present status and related references we refer to [138].

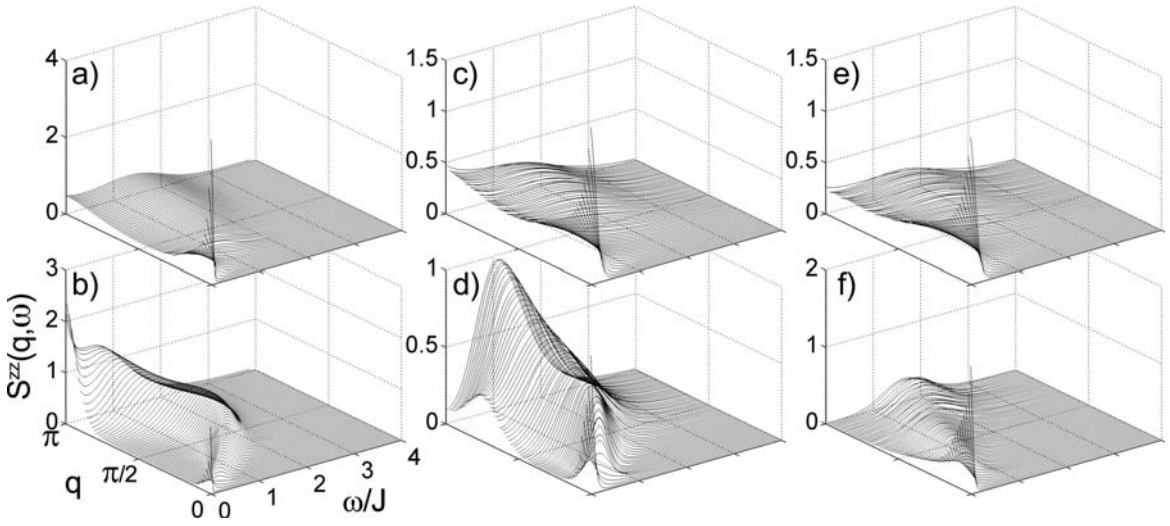

Figure 4.1: 3D plot of the longitudinal dynamic structure factor by QMC + MaxEnt as function of frequency ω and wave vector q. Temperatures and magnetic fields in units J: a) T=1 and B=0, b) T=0.25 and B=0, c) T=1 and B=1, d) T=0.25 and B=1, e) T=1 and B=2 and f) T=0.25 and B=2.

Unfortunately QMC is too sensitive to the default model for the MaxEnt continuation in the small-q, ω regime [171] to elucidate the issue of spin-diffusion on the real axis. Yet, we would like to mention agreement of our results regarding the frequency-transformed autocorrelation function $S_0^{zz}(\omega)$, i.e. the q-integrated dynamic structure factor (not shown here) with previous QMC, performed at $B = 0$, high temperature series expansion [172] and TMRG [168]. These results exhibit a $\omega^{-0.3\ldots-0.4}$-divergent behavior which bears resemblance to the phenomenological approaches by Bloembergen [210] and de Gennes [211] who predicted $\omega^{-1/2}$.

Next we consider lower temperatures, i.e. $T = J/4$. As is obvious from Figs. 4.1b) and 4.2b), spectral weight is removed from the long wave-length regime in this case. Both figures demonstrate that most of the spectral weight is confined within the two-spinon boundaries with however still an appreciable intensity below the lower boundary. This is consistent with findings reported in [171]. In contrast to $T = J$ we find a strongly enhanced spectral weight at $q = \pi$ owing to the increase of the antiferromagnetic correlation length [212] which is consistent with the autocorrelation function reported in ref. [168].

In the limit $(q, \omega) \to (\pi, 0)$ we find indications for diverging behavior of $S^{zz}(\pi, \omega)$ with decreasing temperatures. This is shown in more detail in Fig. 4.3, scanning a wide

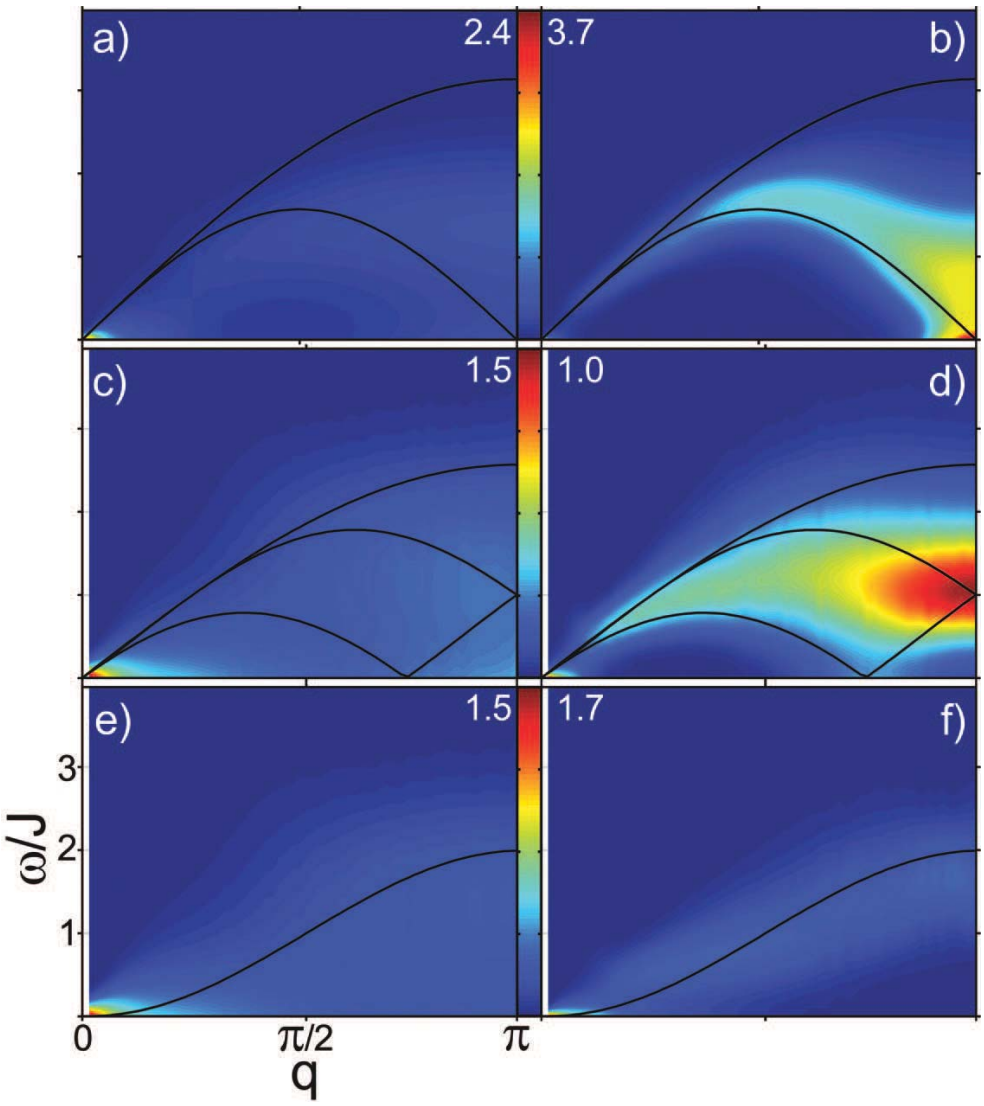

Figure 4.2: Contour plot of the longitudinal dynamic structure factor as function of frequency ω and wave vector q. Temperatures and magnetic fields in units of J: a) T=1 and B=0, b) T=0.25 and B=0, c) T=1 and B=1, d) T=0.25 and B=1, e) T=1 and B=2 and f) T=0.25 and B=2. For $B < B_c$ the solid lines are zero temperature excitation boundaries by the Müller-ansatz [142] while at critical fields the exact zero temperature $1 - \cos(q)$ dispersion [209] is shown.

range of temperatures from $T = J$ to $T = J/20$. As can be seen, the spectrum consists of an upturn for $\omega \to 0$ and a peak at finite ω. The latter peak shifts to lower energies while gaining sharpness as $T \to 0$. For $T \to 0$, Fig. 4.3 suggests that the peak will

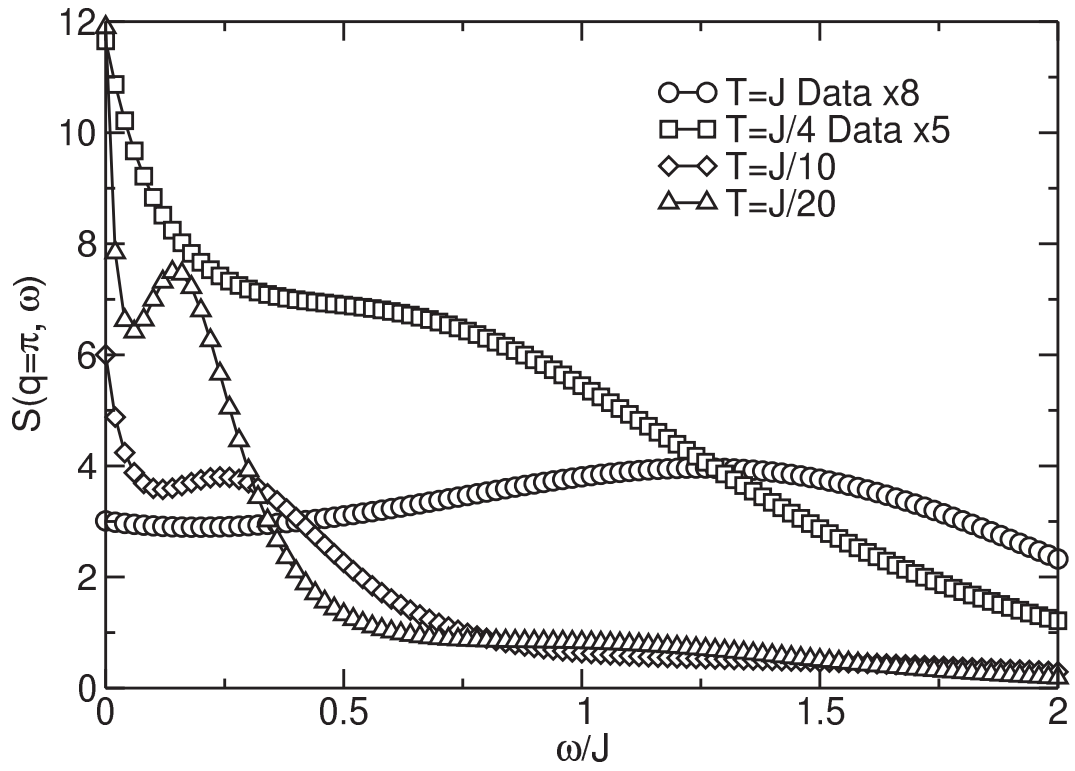

Figure 4.3: Zero-field dynamic structure factor at $q = \pi$ for four different temperatures (in units of J) $\{1, 0.25, 0.1, 0.05\}$. As the temperature decreases we find an increased divergent behavior for $\omega \to 0$ as predicted by two-spinon calculations. In addition there is a low frequency peak which shifts to lower energies while steadily gaining sharpness. Note that the dataset for $T = 1$ and for $T = 0.25$ was multiplied by a factor of eight, respectively five for illustrative reasons.

merge with the zero-ω upturn to form a single divergence at $\omega \to 0$, as predicted by two-spinon calculations at $T = 0$ which lead to $S^{zz}(\pi, \omega) \sim \omega^{-1}$ [142]. A similar peak at finite ω was observed also in ref. [171]. However, smaller system sizes in that case, i.e. $N = 32$, render the zero-ω upturn into a shoulder only. Biasing the default model by several sum-rules, it was shown in ref. [171], that $S^{zz}(\pi, \omega)$ on 32-site systems could be obtained with only a single peak at finite ω. Recent SSE-QMC on 128-site systems at $B = 0$ show only a single rounded maximum, centered at $\omega = 0$ [172]. While all these findings are consistent with the formation of a zero-ω divergence as $T \to 0$, they show that the details of the low-ω spectrum are subject to details of the MaxEnt approach.

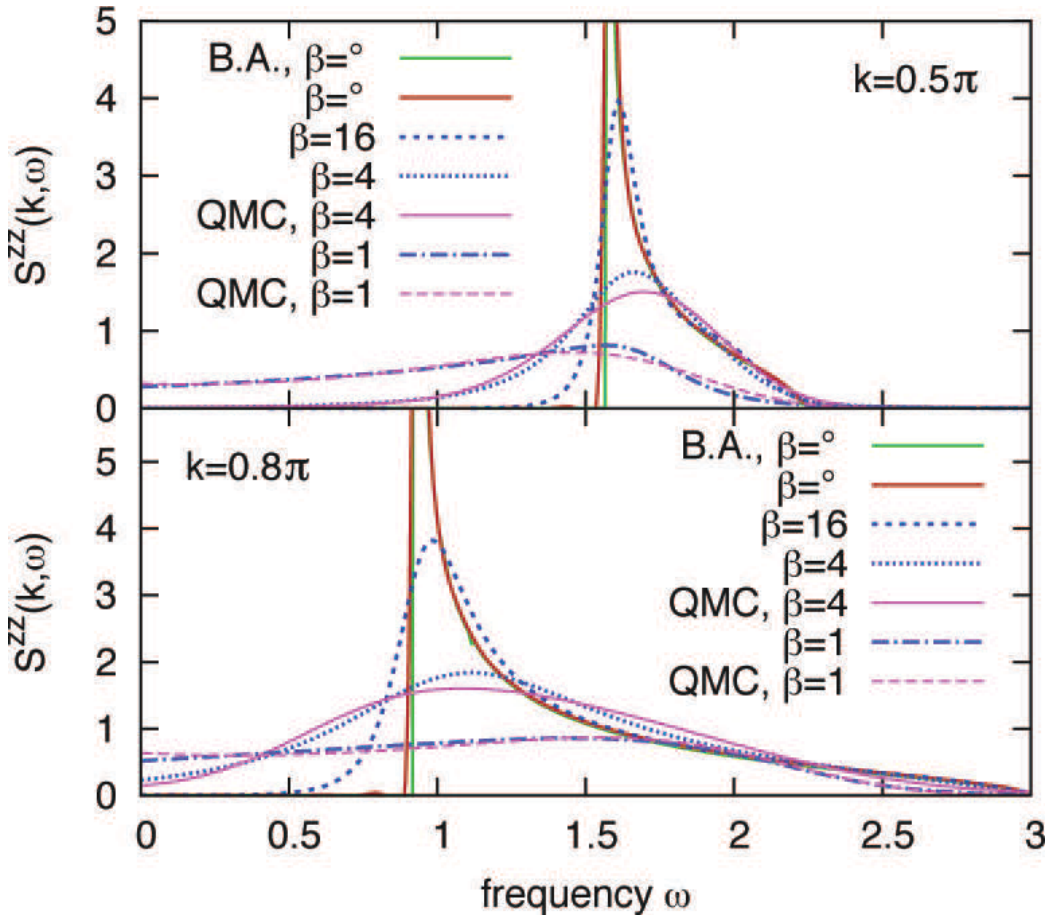

Figure 4.4: Zero-field dynamic structure factor calculated by finite-temperature t-DMRG [40] in comparison to QMC + MaxEnt at two different wave vectors $q \in \{\pi/2, 0.8\pi\}$ at T/J=0.25 (picture published in [40].

Later studies of this subject, motivated by recent DMRG results [40, 41], showed that analytic continuations employing the *informed*[1] kernel $K = e^{-\tau\omega} + e^{-(\beta-\tau)\omega}$ (eqn. (2.62)) in the finite interval $[0, \omega_c]$, with ω_c being the cutoff-frequency, are not necessarily favorable over analytic continuations over the symmetric frequency interval $[-\omega_c, \omega_c]$ using the *uninformed* kernel $K = e^{-\tau\omega}$ (eqn. (2.58)). Partially this strikes as a surprise since the informed kernel has, despite prior knowledge about the spectrum, also a much smaller dynamic range $[1, e^{-\beta\omega_c}]$ compared to $[e^{\beta\omega_c}, e^{-\beta\omega_c}]$ of the uninformed kernel. Therefore its inversion is much more robust to QMC errors

[1] The *informed* kernel contains prior information about the spectrum – in this case the spectral property $S(q, -\omega) = e^{-\beta\omega} S(q, \omega)$.

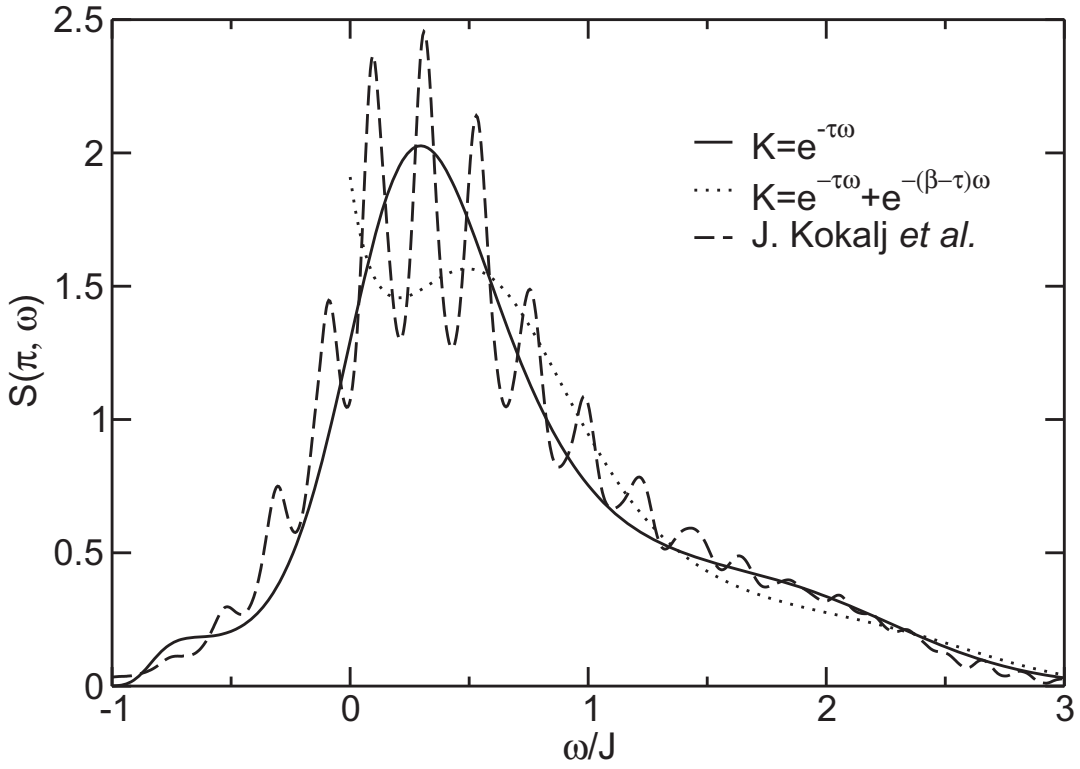

Figure 4.5: Zero-field dynamic structure factor calculated by FTD-DMRG [41] in comparison with QMC + MaxEnt at $q = \pi$ and T/J=0.25.

from a numerical point of view. However, the $\omega \to 0$ behavior shown in Fig. 4.3 can be traced down to cutoff-effects of the integral transform – a well-known phenomenon of Fourier transforms. In our case, whenever there is finite spectral weight at the cutoff frequency, an upturn was found in our spectra – less pronounced for small spectral weight and more pronounced for strong spectral weight such as displayed at wave vectors near the zone boundary $q \to \pi$.

To showcase the effect of weak cutoff effects we present Fig. 4.4, which stems from a cooperation with T. Barthel on the spin S=1/2 dynamic structure factor at finite temperatures, calculated by t-DMRG and published in [40]. In this figure, results of our QMC were used to support a newly developed t-DMRG method with very satisfying agreement in the frequency dependent spectra for several selected wave vectors. However, note the small upturn at $\omega \to 0$ for $\beta = 1$ of the QMC results, which is a hint for a weak cutoff effect due to small spectral weight at the lower integration interval border of the *informed* kernel continuation. In contrast to that, no differences can be found

in the τ-data comparisons of t-DMRG and QMC – a clear indication that the small differences on the real axis are only subject to the analytic continuation procedure.
A showcase for stronger cutoff effects is presented in Fig. 4.5, where $q = \pi$ QMC data is compared to very recent FTD-DMRG at $q = \pi$ [41]. Here we clearly see the impact of the cutoff in a direct comparison of the informed kernel with $[0, \omega_c]$ integration interval versus the uninformed kernel with $[-\omega_c, \omega_c]$ integration interval. This effect has to be taken very serious for comparisons with NMR relaxation rates, which typically have resonance frequencies in the limit $\omega \to 0$.

The case $B = B_c/2$ Figs. 4.1,4.2 c) and d) depict the longitudinal structure factor at half of the critical field. The impact of a finite magnetic field is fourfold. First, at zero momentum the longitudinal structure factor is proportional to the square of the field-induced magnetization at zero frequency, i.e. $S^{zz}(q = 0, \omega) \sim \langle S^z \rangle^2 \delta(\omega)$. To focus on the remaining spectrum, we have chosen to skip the single wave vector $q = 0$ in all 3D, as well as contour plots of $S^{zz}(q, \omega)$ for $B \neq 0$. Second, longitudinal excitations with $q \neq 0$ will have decreasing matrix elements with increasing magnetic field. This is consistent with the evolution of the overall scale in Fig. 4.1 a)-e) and b)-f). Third, longitudinal spin-excitations at the zone boundary are energetically unfavorable in a magnetic field. In fact, at low temperatures a gap can be observed at $q = \pi$, which is proportional to the magnetic field [142] (see Fig. 4.2d)). Finally, a soft mode occurs at an incommensurable wave vector $q_s = \pi(1 - 2\langle S^z \rangle)$ (see Fig. 4.2d)). This can be understood in terms of the Jordan-Wigner fermionic description of the AFHC [213–215], where S^z_q is related to the fermion density and the magnetic field plays the role of a chemical potential driving incommensurability. This finding is consistent with ref. [142], with interacting spin-wave calculation [216] as well as with finite system diagonalization [217]. The role of temperature is evident. At high temperatures, i.e. $T = J$ in Fig. 4.2c), $S^{zz}(q, \omega)$ is rather featureless and extends clearly beyond the boundaries set by the two-spinon continuum. This changes as the temperature is lowered to $T = J/4$ (Fig. 4.2d)), where the spectrum is far more confined to within the dCP boundaries and displays more pronounced features. In particular, the weight is enhanced as $(q, \omega) \to (\pi, J)$.

The case $B = B_c$ For $B \geq B_c$ and $T = 0$, the statistical operator of the AFHC is pure and corresponds to the fully polarized state, i.e. $S^{zz}(q, \omega) = N(1/4)\, \delta_{q,0}\, \delta(\omega)$. Additional finite spectral weight for $q, \omega \neq 0$ will occur only for $T > 0$. To observe this we have again removed the wave vector $q = 0$ from Figs. 4.1,4.2 e), f), which are at the critical field. Indeed, on lowering the temperature from panel e) to panel f) in Fig. 4.1, the remaining total spectral weight decreases. Apart from this the higher

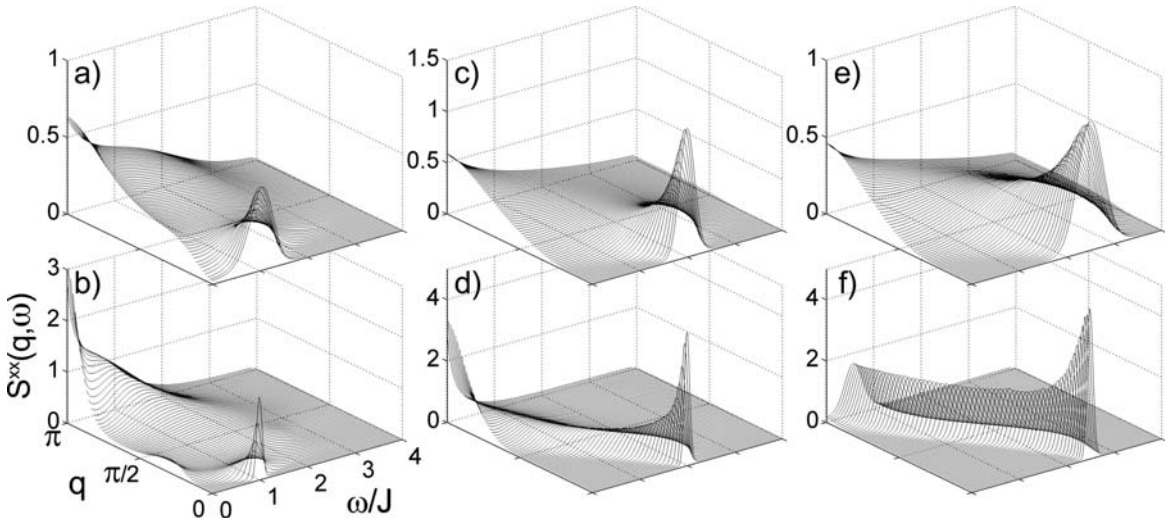

Figure 4.6: Transverse dynamic structure factor by QMC + MaxEnt as function of frequency ω and wave vector q. Temperature and magnetic field in units of J: a) T=1 and B=1, b) T=0.25 and B=1, c) T=1 and B=2, d) T=0.25 and B=2, e) T=1 and B=2.5 and f) T=0.25 and B=2.5.

temperature spectrum is rather featureless, while the lower temperature spectrum clearly resembles the exact zero temperature dispersion of $1-\cos(q)$ [209] (see Fig. 4.2f)). This excitation has a constant spectral weight $2\pi/N$ for $q \neq 0$ and vanishes in the thermodynamic limit.

4.1.2 Transverse dynamic structure factor $S^{xx}(q,\omega)$

In Fig. 4.6 and 4.7 we show the transverse dynamic structure factor as 3D and as contour plots for identical temperatures $T/J = \{1, 0.25\}$ as for the longitudinal dynamic structure factor, however for a different range of magnetic fields $B/J = \{1, 2, 2.5\}$. For vanishing magnetic field we refer to Figs. 4.1,4.2 a), b) for $S^{xx}(q,\omega)$ which is identical to $S^{zz}(q,\omega)$ at $B = 0$ due to $SU(2)$ invariance.

The case $B = B_c/2$ First, we note that the results for $S^{xx}(q,\omega)$ in Figs. 4.6,4.7 a) and b) are clearly different from those for $S^{zz}(q,\omega)$ in Figs. 4.1,4.2 c) and d) at identical magnetic fields. This is to be expected, since the application of a finite magnetic field breaks the $SU(2)$ invariance of the AFHC. Second, long wave-length transverse spin-excitations will experience the Zeeman energy due to the magnetic field, which leads to

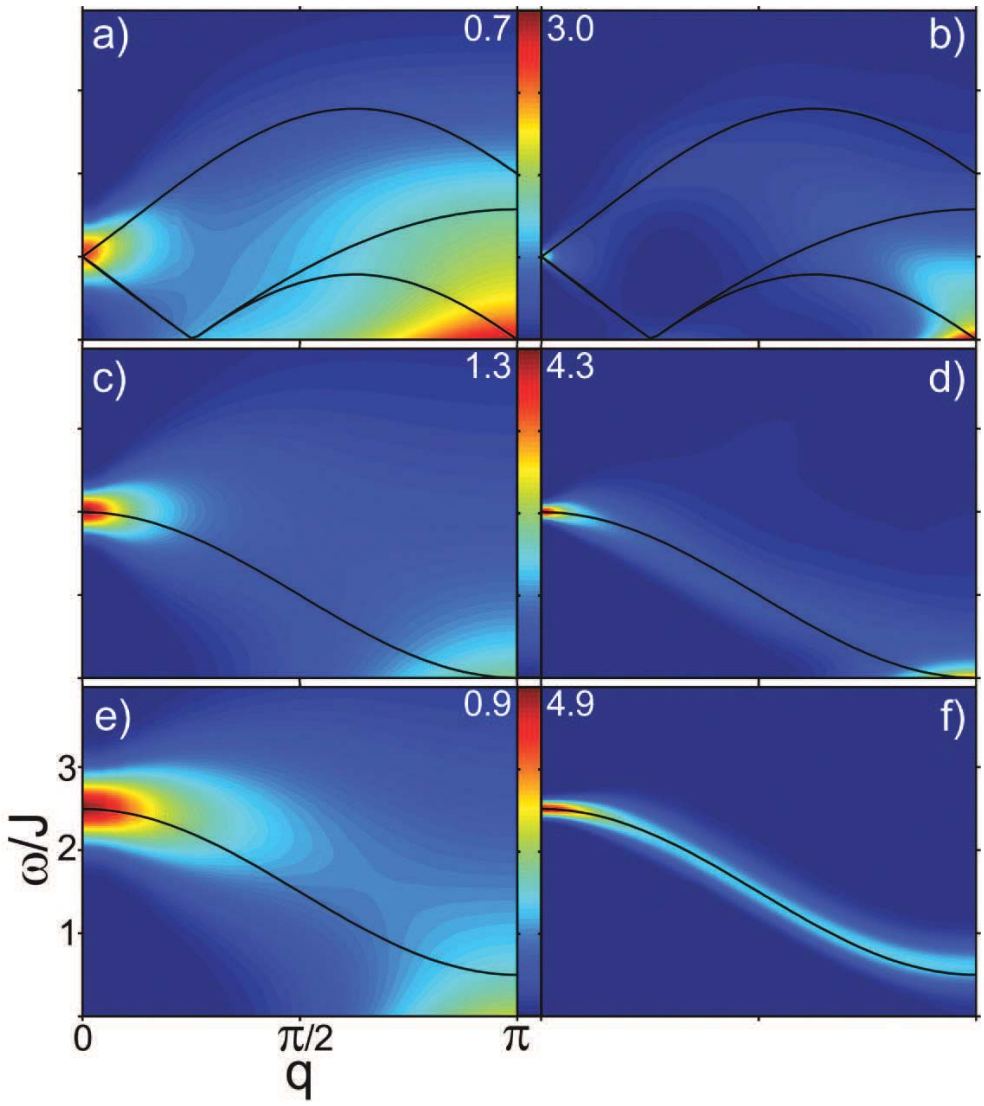

Figure 4.7: Transverse dynamic structure factor by QMC + MaxEnt as function of frequency ω and wave vector q in a contour plot. For parameter details see text or Fig. 4.6. The solid lines for half critical field a) and b) are zero temperature excitation boundaries of different BA selection rules (see [142]). For $B \geq B_c$ the one-magnon cosine dispersion is shown.

a spin gap of size B/J at $q = 0$. This has to be contrasted against the gap at $q = \pi$ in $S^{zz}(q, \omega)$ at finite fields in Figs. 4.1,4.2 d). Third, and as for the longitudinal case, a field driven zero mode at $q = q_s$ can be seen in 4.2 a), b) – with a rather low intensity as $T \to 0$. In contrast to the longitudinal case, this mode develops out of the zone

center and moves to the zone boundary with $q_s = 2\pi\langle S^z\rangle$ [142, 218, 219].

Even though it can be misleading to compare MaxEnt data based on different QMC data sets quantitatively due to the underlying different statistic quality, we notice enhanced spectral weight near the zone boundary in Fig. 4.6b) compared to zero magnetic field in Fig. 4.1b), which means that a weak uniform field strengthens the antiferromagnetic order in the transverse structure factor. This effect was also observed in [142] for small fields and by Karbach *et al.* for the static structure factors [220].

The case $B \geq B_c$ At intermediate fields selection rules [142] allow for a fairly complex distribution of spectral weight as is also obvious from the solid lines in Figs. 4.7a) and b). In contrast to this, above the saturation field and at low temperatures, a straightforward picture emerges (see Fig. 4.6,4.7 d) and f)). In this regime and for $T \to 0$ the system is fully polarized. In that case the elementary excitations are non-interacting ferromagnetic one-magnon states, leading to a dispersion $E(k) = J\cos(k) + B$ in the transverse structure factor, with a momentum-independent spectral weight [142]. For finite T, we find that this picture is modified in two ways. First, significant thermal broadening occurs, which as e.g. in Fig. 4.7e), at $B = 2.5$ and $T = J$ can lead to a complete closure of the zone boundary spin gap. Second, and as can be seen in Figs. 4.6 d) and f), there is a substantial wave vector dependence of the spectral weight in the cosine-signature of the one-magnon state. The latter can be explained by elementary one-magnon states being excited in a polarized background which contains thermal fluctuations. For this purpose we expand the spectral function $\chi''(q,\omega)$ of the polarized system into numbers of excited magnons with a hard-core repulsion. Because of $S^{xx}(q,\omega) = \frac{1}{2}(S^{+-}(q,\omega) + S^{-+}(q,\omega))$ and $S^{+-}(q,\omega) = e^{-\beta\omega}S^{-+}(q,\omega)$, it is sufficient to look at either $+-$ or $-+$ contributions to understand the wave vector dependence.

$$\begin{aligned}
\chi''^{+-}(q,\omega) &= (1 - e^{-\beta\omega})S^{+-}(q,\omega) \\
&= \frac{1}{Z\pi}\mathrm{Im}\left[\sum_{l,m}|\langle l|S_q^-|m\rangle|^2\frac{e^{-\beta E_m} - e^{-\beta E_l}}{(\omega + i0^+) - E_m + E_l}\right] \\
&\approx \frac{1}{Z\pi}\mathrm{Im}\left[|\langle 0|S_q^-|1\rangle|^2\frac{e^{-\beta E_1} - e^{-\beta E_0}}{(\omega + i0^+) - E_1 + E_0}\right. \\
&\qquad \left. + |\langle 1|S_q^-|2\rangle|^2\frac{e^{-\beta E_2} - e^{-\beta E_1}}{(\omega + i0^+) - E_2 + E_1} + \ldots\right] \qquad (4.1)
\end{aligned}$$

The first term of the sum in eqn. (4.1) is known to have no q-dependence [142], so any non-constant spectral weight distribution must be hidden in higher magnon excitations.

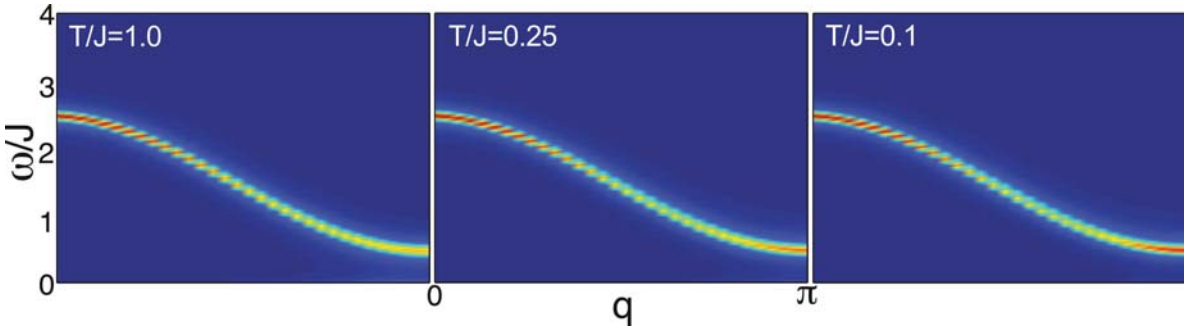

Figure 4.8: Two magnon contribution to the spectral weight of the expansion in eqn. 4.1 for a 64-site system at $B/J = 2.5$ and three different temperatures $T/J \in [0.1, 0.25, 1]$. The weight increase for the QMC at $q \to 0$ can be explained fairly well (compare with Fig. 4.7). However, we can not find the weight increase at the zone boundary for lower temperatures in our QMC data.

In Fig. 4.8 we show the contributions of *two* magnons $(l, m) = (1, 2)$. This figure clearly demonstrates the weight increase for $q \to 0$ at finite temperatures and interestingly, the largest dependence on q is displayed for the lowest temperature for which the spectral weight also increases at the zone boundary.

Finally, we emphasize the difference in the evolution of the overall spectral weight, contrasting longitudinal versus transverse excitations. While in Fig. 4.1 the weight of the excitations decreases with increasing field, this is not so in Fig. 4.6.

Figs. 4.6 and 4.7 bear a close resemblance to the concept of field-induced Bose-Einstein condensation of triplets, which has been under intense scrutiny for several quantum spin-systems recently [24, 68, 176–186]. These systems feature a gapful *zero-field* state with the lowest triplet branch 'condensing' as the field is *increased*. For the AFHC, this scenario is reversed, i.e. *decreasing* the field through the critical value for complete polarization B_c, the magnons condense at $q = \pi$ and the system switches from a gapful state to a Luttinger liquid of deconfined spinons. Obviously, the latter does not represent a true gauge-symmetry broken state, since (i) 1D-correlation functions decay algebraically and (ii) the magnons above B_c are constrained by a hard-core repulsion [25, 173–175].

As the temperature is lowered, the thermal smearing of the approximately quadratic dispersion at $q = \pi$ for $B = B_c$ is reduced, see Figs. 4.7 c) to d). For the momentum-integrated structure factor this will lead to a critical increase of the density of states at $\omega = 0$ as temperature is lowered. This is something we will discuss in detail in the next subsection.

4.1.3 T_1-relaxation rate of the spin 1/2 Heisenberg chain

To tie up to the results of the DSF in the last subsection, we now want to discuss the behavior of the nuclear spin-lattice relaxation rate T_1^{-1}, which measures the spin fluctuations at the nuclear Larmor frequency ω_n [221] given in eqn. 2.30 and repeated for convenience:

$$\frac{1}{T_1} \propto \sum_q \sum_{\beta=x,y,z} (A^2_{x\beta}(q) + A^2_{y\beta}(q)) \cdot \int_{-\infty}^{\infty} \langle S^\beta(q,t) S^\beta(-q,0)\rangle e^{-i\omega_n t} dt \tag{4.2}$$

$$= \sum_q (F^\perp(q) S^\perp(q,\omega_n) + F^z(q) S^z(q,\omega_n)). \tag{4.3}$$

Here, $F^\perp(q)$ and $F^z(q)$ are the geometrical form factors and $S^\perp(q,\omega)$ and $S^z(q,\omega)$ are the transverse and longitudinal dynamical structure factors of the electronic spin system. $A^{\alpha\beta}$ with $\alpha,\beta = x,y,z$ are the components of the hyperfine coupling tensor $\underline{\mathbf{A}}(q)$. This tensor mixes transverse with longitudinal contributions to the T_1 rate. With sample orientation however, one can minimize longitudinal contributions by measuring in the principle coordinate system of the tensor, which reduces the NMR rate to transverse contributions only. In the following we will assume that only transverse fluctuations contribute to the T_1 relaxation rate. Furthermore we will take into account only the on-site coupling $A(r) \approx A_0\delta(r)$, i.e. the real space form factor is reduced to the autocorrelation function at the NMR frequency ω_n. This means that the T_1 relaxation rate can be written as:

$$1/T_1 \approx \sum_q A_0 S^\perp(q,\omega_n) \tag{4.4}$$

$$= S_0^\perp(q,\omega_n). \tag{4.5}$$

For the MaxEnt procedure, we tested both ways to determine the relaxation rates – on the one hand direct continuation of the autocorrelation function versus the DSF resolved for all available wave-vectors with subsequent integration. Both procedures produced very similar results, however the fully q-resolved QMC data seems to produce more features in comparison with the simple continuation of the autocorrelation function. This is to be expected, seeing that the MaxEnt has generally problems with resolving rich structures while e.g. single peaks are typically captured very well. We therefore adopt the q-integrated T_1 as the most accurate one, following similar results of [172].

There are three interesting aspects shown in Fig. 4.9. Firstly, and as central result of this plot, we find a diverging NMR rate at $B \approx B_c$ which is very suggestive of

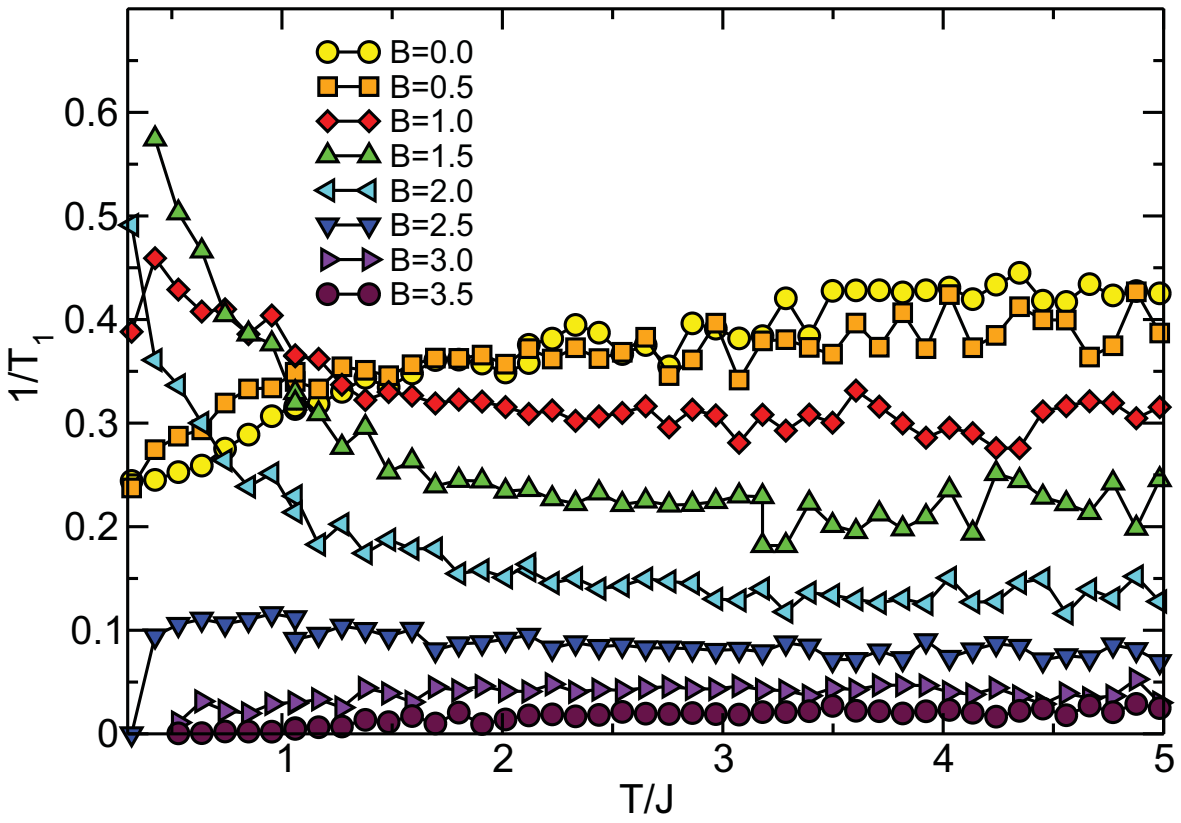

Figure 4.9: Temperature and field dependent transverse $1/T_1$ relaxation rates with fields $B \in \{0.0, 0.5, 1.0, 1.5, 2.0, 2.5, 3.0, 3.5\}$ in units of J. Each point in this plot is a constant form factor q-integration over the full transverse DSF as displayed in Fig. 4.7. The scattering of the points gives a rough estimate of the average error - typically within 10-20% of the absolute scale.

critical scattering as $T \to 0$. As T increases, the van-Hove singularity in the DOS at B_c is smeared, leading to the decrease in T_1^{-1} (compare with Fig. 4.7). Secondly we observe a weak temperature dependence in the classical regime $k_B T \gg J$ with a rate decrease with increasing fields, which is indicative of an excitation spectrum dominated by spin-diffusion modes from $q = 0$. Finally, we observe the spin gap to open for $B > B_c$ at sufficiently low temperatures. This results in an exponentially decreasing relaxation $1/T_1 \propto exp(-(B-B_c)/k_B T)$, which is visible in a drop of the rate.

For comparisons with NMR experiments, H. Kühne *et al.* provided excellent data on the spin S=1/2 chain material copper pyrazine dinitrate $Cu(C_4H_4N_2)(NO_3)_2$ (CuPzN) (see

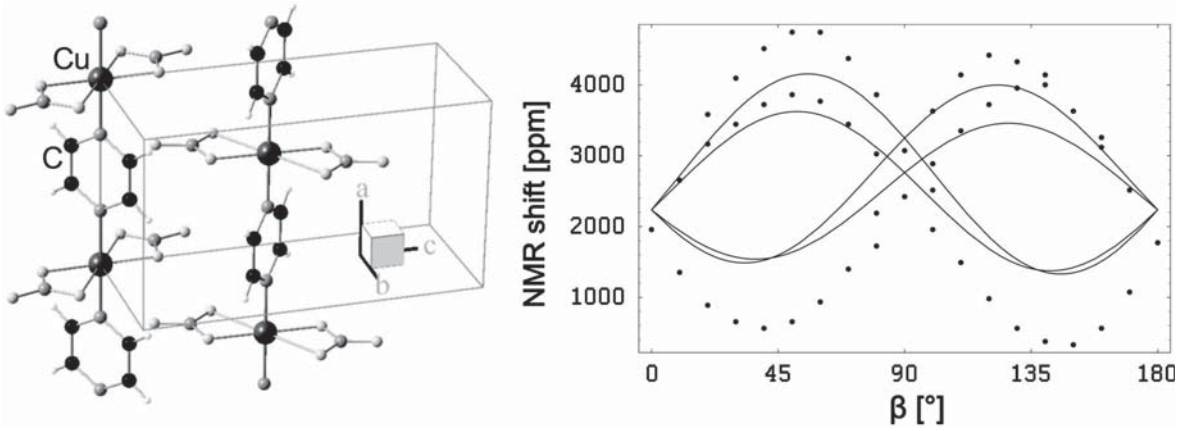

Figure 4.10: Left: Crystal structure of CuPzN. Right: NMR center shift δ of spectral lines versus β compared with a simulation of the local magnetic field.

Fig. 4.10) [31]. This copper compound with pyrazine-ring spacers is a molecular magnet with only 10.7K intra-chain coupling and three orders of magnitude lower inter-chain coupling, resulting in a critical field of only 14.9T. It has been characterized by inelastic neutron scattering, muon-spin relaxation, magnetothermal transport, specific heat and magnetization measurements [133, 222–224] and all of these studies are consistent with a description of CuPzN in terms of the AFHC.

In CuPzN the ^{13}C-nuclei used as a probe for the NMR experiment are coupled to the magnetic moments of the Cu(II) electrons via isotropic hyperfine coupling, mediating only *transverse* spin fluctuations, and anisotropic dipolar coupling, mediating *transverse and longitudinal* spin fluctuations [225]. Consequently, to compare with our transverse $1/T_1$-rates, the dipolar contribution to $\underline{\mathbf{A}}(q)$ has to be minimized. This minimum was found for the orientation $\beta = 50^\circ$ via a study of the angular dependence of the NMR shift $\delta = (\omega_n - \gamma B_0)/\gamma B_0$ (see Fig. 4.10) [136].

To gauge the experimental results to theory, we compared the Knight shift for a fixed orientation of the external field

$$\delta(T) = A(0) \cdot \frac{M(T)}{B}$$

with QMC magnetization results (see Fig. 4.11). The scaling factor $A(0)$ was determined to be $A(0) = 0.101\mathrm{T}/\mu_B$ by a least-squares fit of the 2 T data sets. For 2 T there is excellent agreement between theory and experiment, both showing a broad maximum around 6.5 K, reflecting the onset of antiferromagnetic correlations. At 13.8

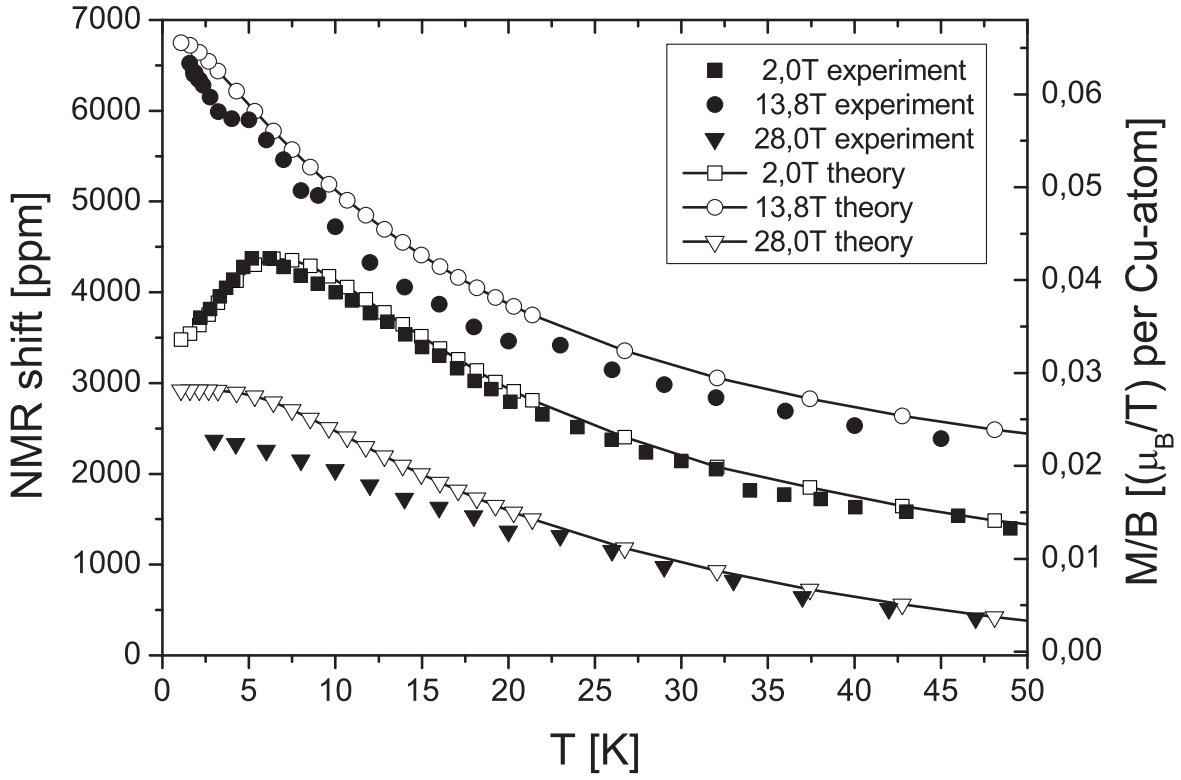

Figure 4.11: Comparison of temperature dependent NMR shift δ with magnetization data calculated by QMC. For clarity, an offset has been added to the data at 13.8 T (+1000 ppm to NMR shift and 0.0099 (μ_B/T) to calculated magnetization) and 28 T (-1000 ppm and -0.0099 (μ_B/T), respectively). The QMC errors are within symbol size. All solid lines are a guide to the eye.

T, slightly below the saturation field, both data sets show monotonous increase towards saturation with decreasing temperature. The kink near 5 K in the experimental data is due to the proximity of the boiling point of liquid Helium. At 28 T, theory and experiment deviate below 20 K. An rf heating of the sample can be excluded since the conditions of the CPMG pulse-sequence were carefully adjusted.

To achieve best comparison results with the NMR rate in the experiment, we allowed a tuning of the form factors in eqn. (4.3) beyond the purely constant on-site contribution. Fig. 4.10 (left) shows that the NMR site, i.e. the carbon nucleus, is located asymmetrically between two Cu(II)-ions. We extended results shown in Fig. 4.9 by a next-nearest neighbor contribution to the form factor $A(r) = [A_0\delta(r) + A_1\delta(r-a)]$,

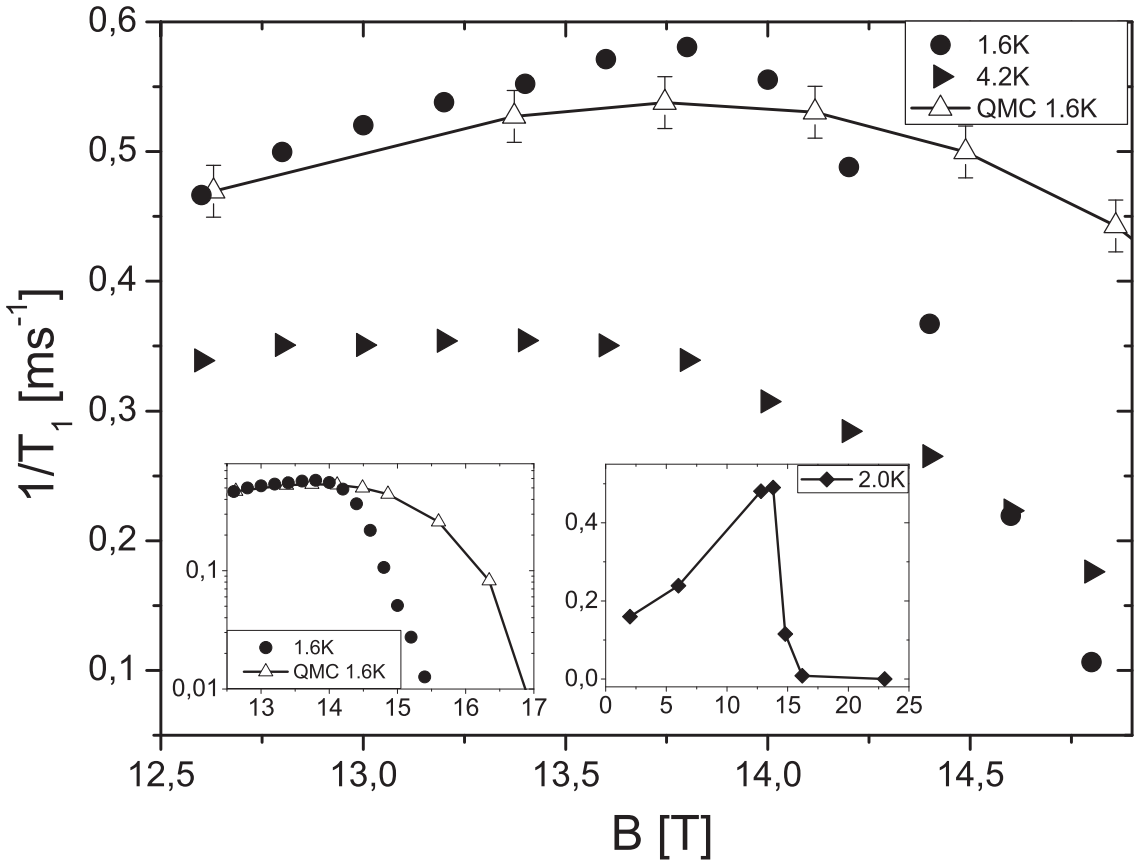

Figure 4.12: Field dependence of the nuclear spin-lattice relaxation rate of ^{13}C in the critical regime. Left inset: The log-scale plot demonstrates the linear opening of the spin gap with field. Right inset: The full scale plot highlights the maximum of $T_1^{-1}(B)$ near the T=0 K critical field. All solid lines are a guide to the eye.

where a is the lattice constant and $A_{0,1}$ parameterize the hyperfine coupling between the nucleus and its nearest copper moments. This leads to a transverse relaxation rate of

$$\frac{1}{T_1} = A_0^2 \left[(1+R^2)S_\perp(0,\omega) + 2RS_\perp(1,\omega)\right]|_{\omega\to 0} \tag{4.6}$$

where $S_\perp(r = 0(1), \omega)$ are the real-space transverse spin correlation functions at a distance $r = 0(1)$.

In Fig. 4.12 we compare the observed NMR rate with the QMC results versus magnetic field in the quantum regime $k_B T \ll J$, with $T = 1.6$ K. The QMC data is shown for $R = 0$ and a "best-fit" normalization A_0 assigned at 2 T and high temperatures. The similarity between theory and experiment is remarkable. For both we find a pronounced

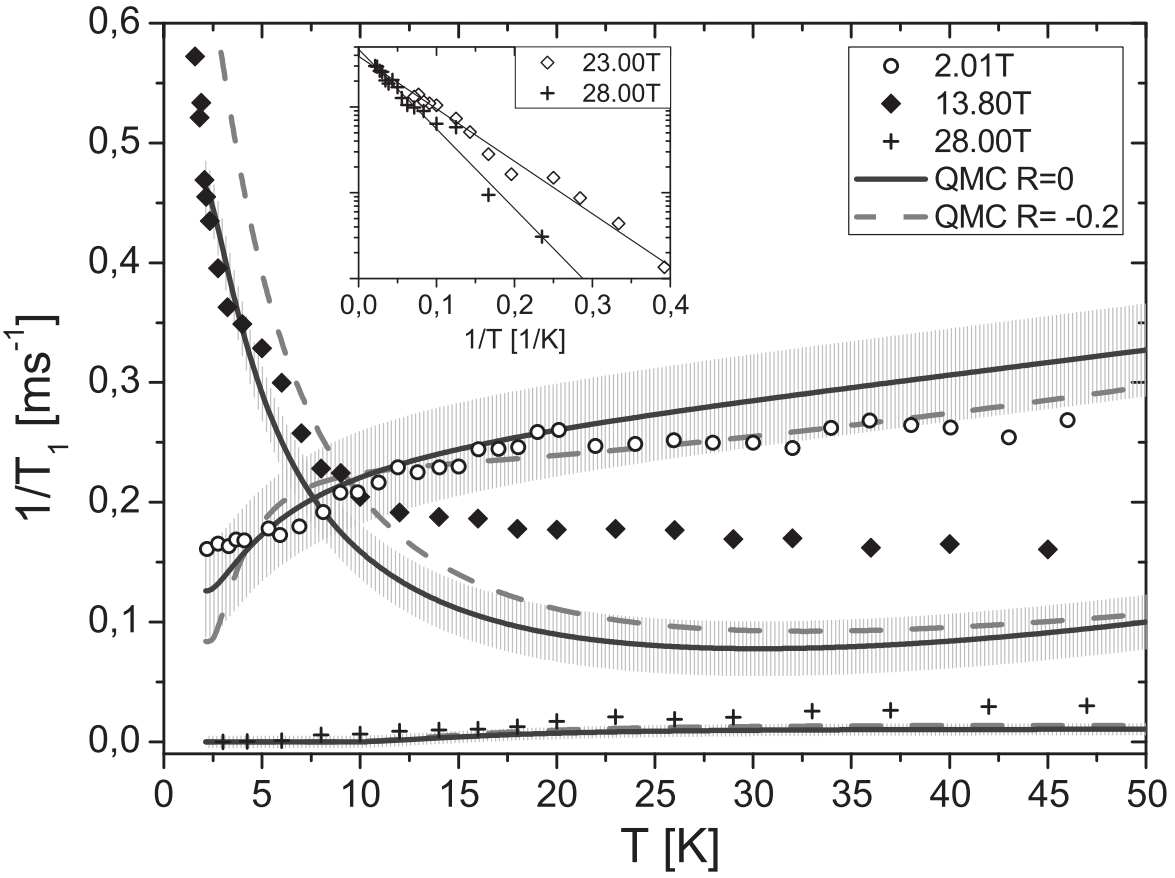

Figure 4.13: Temperature dependence of the nuclear spin-lattice relaxation rate of ^{13}C for different external fields. The solid QMC data lines are each polynomial fits to 50 analytic continuations of a 128 site system and the error-tube was chosen to contain all data points within a range of 2 σ (compare fluctuations with Fig. 4.9). The log-scale inset shows the exponential decrease of $1/T_1$ with $1/T$ above B_c.

maximum of $T_1^{-1}(B)$ at $B = 13.8$ T shifting to lower fields with increasing temperature. To interpret these results, note that in the fully polarized state for $B > B_c$, single magnons are exact eigenstates with a dispersion of

$$E_>(k) = J\cos(k) + g\mu_B B \ , \tag{4.7}$$

$E_>(k)$ displays a field-driven excitation gap of $g\mu_B B - J$ leading to an exponential decrease of $T_1^{-1}(B)$ at fixed T and for $B > B_c$ (also compare with Fig. 4.7 e) $\rightarrow$ f)). This can be seen for both, NMR and QMC, on the log-scale left inset in Fig. 4.12. The rates calculated by QMC display a broader maximum than the measured data, but drop with the same slope for fields above 16 T. We emphasize that this deviation between

NMR-data and QMC is confined to low temperatures $T \lesssim 6$ K and to a limited range of fields 15 T $\lesssim B \lesssim$ 17 T which can be seen from the log-scale of the left inset. At $B = B_c$ the dispersion touches the zero at $k = \pi/2$ (see Fig. 4.7 d)) with a *quadratic* momentum dependence yielding a van-Hove type of critical DOS. This leads to the maximum in T_1^{-1}, tending to diverge as $T \to 0$. For both, NMR experiment and QMC, the maximum in Fig. 4.12 occurs at $\tilde{B}_c \approx 13.8$ T, which is slightly less than the saturation field of $B_c = 14.9$ T for the magnetization. Most likely this downshift is a finite temperature effect of excitations populating the gap. In the Luttinger liquid for $B < B_c$ the low-energy spinon excitations have a field-dependent *linear* dispersion, yielding a finite, yet reduced NMR rate.

In Fig. 4.13 we finally compare our QMC T_1^{-1} rates with selected experimentally observed ones versus temperature for three fields, i.e. above, at, and below $\tilde{B}_c$. As for the field dependence, the agreement between theory and experiment is very good. Inclusion of next nearest neighbor hyperfine couplings, i.e. R= -0.2, can slightly improve this agreement at high temperatures, but decreases the agreement at low temperatures.

In conclusion, by a complementary analysis of experiment and theory for the low frequency spin-spectrum of the AFHC CuPzN, as probed by the NMR T_1^{-1} rate as well as by the Knight shift, we have provided clear evidence for critical dynamics close to a field-induced QCP. Both, theory and experiment are in good agreement and show a pronounced maximum in T_1^{-1} in the vicinity of the saturation field, which tends to diverge as $T \to 0$. Moreover, good agreement between theory and experiment is also found for the magnetization versus temperature and field, except for a low-T deviation at 28 T, yet to be explored. Our findings may be of interest in the context of other field-induced QCPs as eg. in $TlCuCl_3$ [24, 176–178] or $BaCuSi_2O_6$ [179].

4.1.4 Sum rules

Sum rules have been used extensively for the AFHC to evaluate the contribution of two- and four-spinon excitations to the spectral weight of the dynamic structure factor at T=0 [148, 152, 153, 226]. For the present work sum rules can be applied to assess the quality of the analytic continuation. We will focus on the sum rules for the static structure factor $S^{\alpha\beta}(q)$ and the static susceptibility $\chi^{\alpha\beta}(q)$, obtained by integral transforming the dynamic structure factor [227]

$$S^{\alpha\beta}(q) = \frac{1}{\pi}\int_0^\infty d\omega (1 + e^{-\beta\omega}) S^{\alpha\beta}(q,\omega) \tag{4.8}$$

$$\chi^{\alpha\beta}(q) = \frac{2}{\pi}\int_0^\infty d\omega\, \omega^{-1}(1 - e^{-\beta\omega}) S^{\alpha\beta}(q,\omega). \tag{4.9}$$

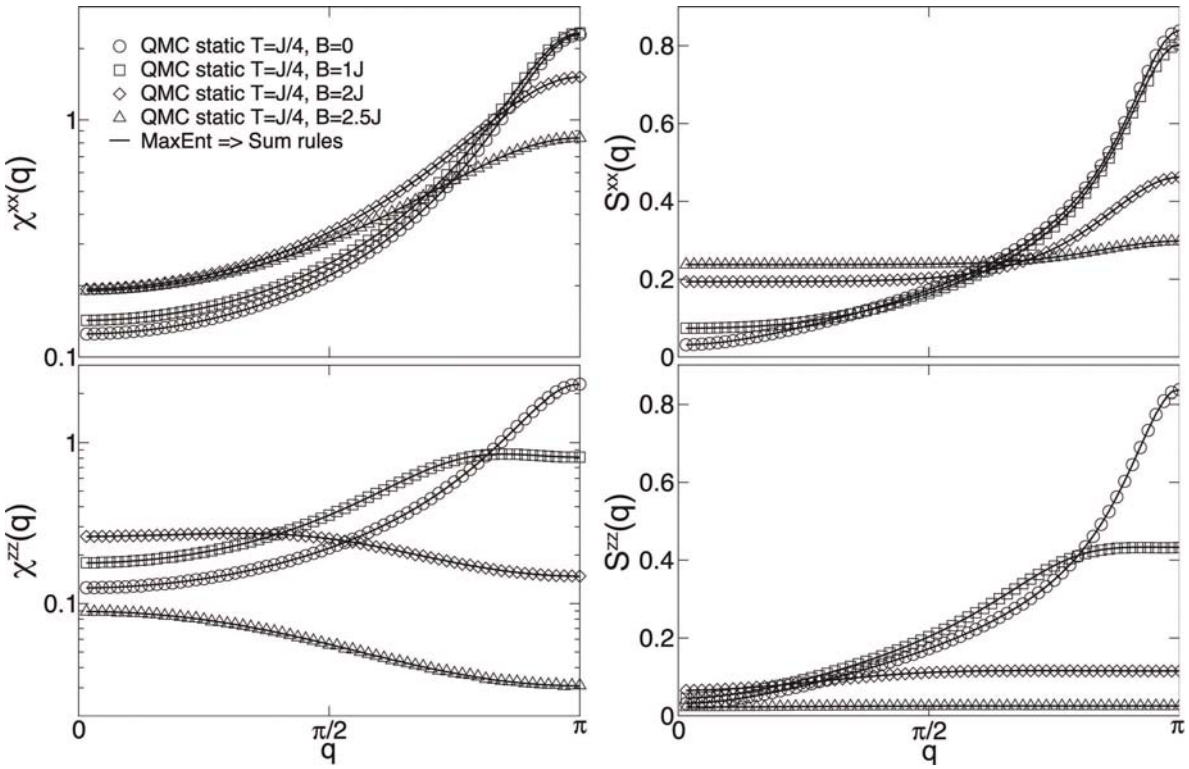

Figure 4.14: Comparison of transverse and longitudinal static susceptibility/structure factor (symbols) and sum rules (lines) for T=J/4 and four different magnetic fields $B/J = \{0, 1, 2, 2.5\}$ (from top to bottom). All sum rule results are within the error bars of the static quantities which are within symbol size.

While $S^{\alpha\beta}(q,\omega)$ on the right-hand side of eqns. (4.8) and (4.9) involve MaxEnt-data, the static structure factor $S^{\alpha\beta}(q)$ in eqn. (4.8) is calculated from a real-space Fourier transform of the equal-time correlation functions and the static susceptibility $\chi^{\alpha\beta}(q)$ in eqn. (4.9) can be evaluated by the Kubo integral

$$\chi^{\alpha\beta}(q) = \sum_r e^{iqr} \int_0^\beta d\tau \left\langle S_r^\alpha(\tau) S_0^\beta(0) \right\rangle . \tag{4.10}$$

of the imaginary time QMC-data. I.e. both, $S^{\alpha\beta}(q)$ and $\chi^{\alpha\beta}(q)$ are obtained from QMC-data which is *independent* from the MaxEnt continuation. In particular the static susceptibility should provide for a clear consistency check regarding the low energy features in the zero field dynamic structure factor at $k = \pi$ as shown in Fig. 4.3.

In Fig. 4.14 we compare the left- and right-hand sides of eqns. (4.8) and (4.9) both, for the longitudinal and transverse components, i.e. $\alpha\beta = zz$ and $\alpha\beta = xx$. First,

we emphasize that the numerical values for $S^{zz}(0)$, $S^{zz}(\pi)$, $\chi^{zz}(0)$ and $\chi^{zz}(\pi)$ which we have obtained at zero magnetic field are consistent with those reported in refs. [172, 212] and corroborate the parameters of scaling relations [172]

$$S^{zz}(\pi) = D_s \ln(T_s/T)^{\frac{3}{2}}, \quad D_s = 0.094(1), \quad T_S = 18.3(5)$$

$$\chi^{zz}(\pi) = \frac{D_\chi}{T} \ln(T_\chi/T)^{\frac{1}{2}}, \quad D_\chi = 0.32(1), \quad T_\chi = 5.9(2)$$

for $T = J/4$. Second, Fig. 4.14 proves an excellent agreement of QMC data involving analytic continuation to that free of the MaxEnt procedure. We have found this agreement for all temperatures and all fields investigated, including those not depicted here. All differences lie within the error bars of the static quantities which is remarkable, given that the typical MaxEnt error is estimated to be ∼10-20% [172]. We note that we have performed this sum-rule check for various MaxEnt procedures, i.e. historic, classic and bryan and found the same level of agreement.

4.1.5 Conclusion

In conclusion, using MaxEnt continuation of QMC results, we have analyzed the evolution of transverse and longitudinal spin excitations of an AFHC with 128 sites at finite temperatures and magnetic fields up to and above the saturation field. Our results are consistent with and complement similar studies using small system ED and zero-temperature BA. In particular we have detailed the difference between longitudinal and transverse excitation as a function of the magnetic field and temperature, highlighting the occurrence of incommensurate zero-modes and the field induced magnon 'condensation' at the saturation field. The latter has been studied in further detail by means of the $1/T_1$-relaxation rate. In this context, we compared our data to NMR-experiments on CuPzN by Kühne *et al.* and found good agreement for both, the diverging relaxation rate for $T \to 0$ due to triplets crossing the ground state as well as the shifting of the rate's maximum to lower fields with increasing temperatures [31]. A comparison of Knight shift and magnetization data rounds up the conclusion of a good description of CuPzN by a purely spin S=1/2 Heisenberg chain.

Several open questions remain. While the issue of spin-diffusion has been out of reach in this section, future analysis might improve the resolution of the MaxEnt in order to access the line-shapes at small q. This also pertains to the form of the low-ω spectrum of the zero-field dynamic structure factor at $q = \pi$. Finally it will be interesting to perform similar calculations for various generalizations of the AFHC including anisotropy and disorder.

4.2 Dynamic structure factors of the Haldane chain

In this section we will present dynamic properties of the Haldane chain with focus on transverse structure factor, evolution of the Haldane-gap and T_1-relaxation rates at finite temperatures $1/10 \leq T/J \leq 1$ and magnetic fields $0 \leq B \leq B_{c_2}$. As strong contrast to the gapless *continuum* of spinons in the spin S=1/2 case, the Haldane dynamics in zero field are dominated by a sharp magnon dispersion. However, upon closing the gap by a magnetic field $B \geq B_{c_1}$, both systems can be described as a Luttinger liquid with incommensurate Fermi wave vectors and similar critical dynamic properties beyond the saturation field B_{c_2}. We conclude this section again with a sum-rule consistency check of our data. As for the spin S=1/2 chains of the previous section, also the calculations for the spin S=1 chains of this section were done for 128 sites. Technically we again performed up to one billion Monte-Carlo updates, distributed over 1000 bins with only 50-100 τ-points prevent over-sampling of the relatively short expansion orders at elevated temperatures close to $T = J$. As usual, an indication for over-sampling is given by diagonalizing the covariance matrix which exhibits vanishing eigenvalues in case of statistically dependent data.

4.2.1 Temperature dependence of the transverse DSF

Figure 4.15 shows temperature dependent contour plots with $T \in \{J/10, J/4, J/2, J\}$ of the transverse dynamic structure factor in zero magnetic fields with insets of the DSF normalized by its static results. Unlike the spinon *continuum* of the S=1/2 Heisenberg chain ([228] and ref. therein), we find a sharp, symmetric mode at $\pi/3 \leq q \leq \pi$ with the Haldane gap [19] of $\Delta = 0.41J$ at $q = \pi$, supported my numerical [187–189] and numerous experimental results on $CsNiCl_3$ [79–82, 191], NENP [66, 67, 76–78] and $AgVP_2P_6$ [193].

Going to lower wave vectors $0 \leq q \leq \pi/3$ at $T/J = 0.1$ we find strongly suppressed spectral weight, resembling the static structure factor's q-dependence in a single-mode approximation (SMA) $S(q) \propto q^2$ which is related to the dynamic structure factor by sum rules (eqn. (4.8)). Additionally the line shapes become increasingly asymmetric for longer wavelengths which is subject of recent experimental studies on $CsNiCl_3$ [194, 195, 198] and will be discussed in more detail in the next subsection on the basis of Fig. 4.17. In the limit of $q \to 0$ we find finite weight of intra-band excitations owing to finite temperatures. For the lowest temperature, those excitations are essentially zero in respect to the absolute scale 160 of the contour plot. However, the insets

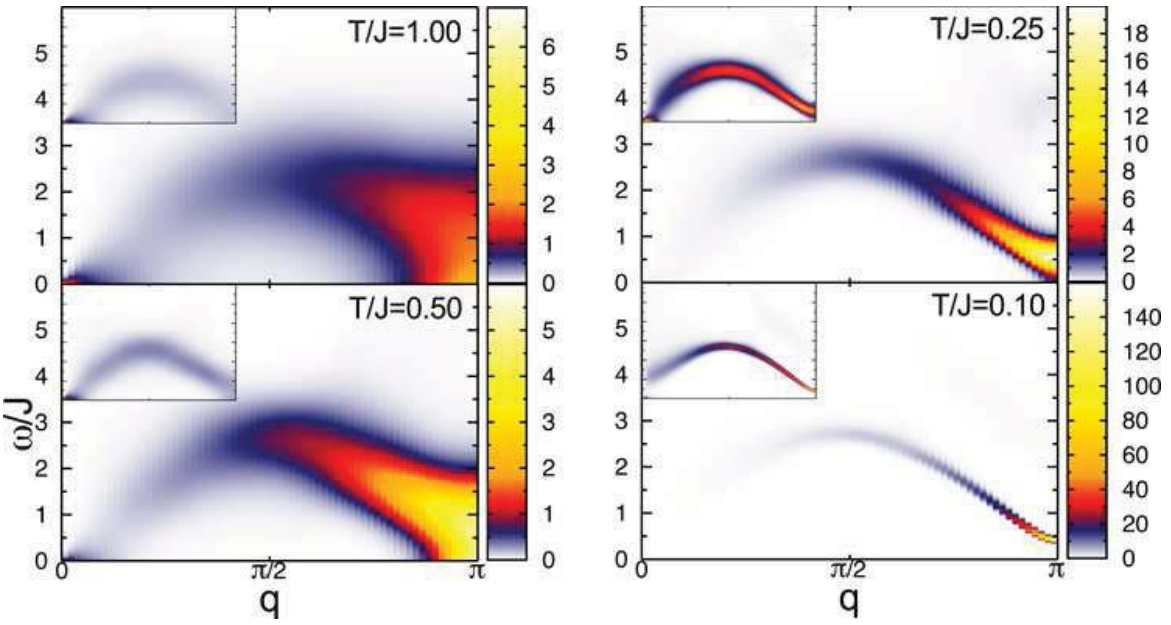

Figure 4.15: Contour plots of the dynamic structure factor $S^{xx}(q,\omega)$ for four different temperatures $T \in \{J/10, J/4, J/2, J\}$ and zero magnetic field with insets showing the normalized quantity $S^{xx}(q,\omega)/S^{xx}(q,t=0)$. At lowest temperatures, a sharp single mode with the Haldane-gap $\Delta = 0.41J$ at $q = \pi$ as key-signature of the S=1 Heisenberg chain is shown. Its spectral weight decays for $q < \pi/3$ into multi magnon excitations (see Fig. 4.17) with an ω-integrated weight-scale given by the behavior of the static structure factor $S(q) \propto q^2$. For higher temperatures, the gap closes and $S(q,\omega)$ becomes a smooth continuum as already known from previous calculations on the S=1/2 chain [228].

of Fig. 4.15, Fig. 4.22 (and also Fig. 4.23 to some extent) clearly shows the finite weight which is rapidly increasing with temperatures due to widening of the linewidth.

In parallel with the growth of the intra-band excitation weight, we notice the closing of the Haldane-gap when the temperature is increased. Already at $T = J/4$ the sharp magnon mode has broadened enough to close the gap at $q = \pi$. This trend, combined with steady weight increase at long wavelength and $\omega \to 0$, continues and finally leads to a smooth continuum for $T/J = 1.0$, resembling of what is known from earlier work on spin S=1/2 chains in the limit of high temperatures [172, 228].

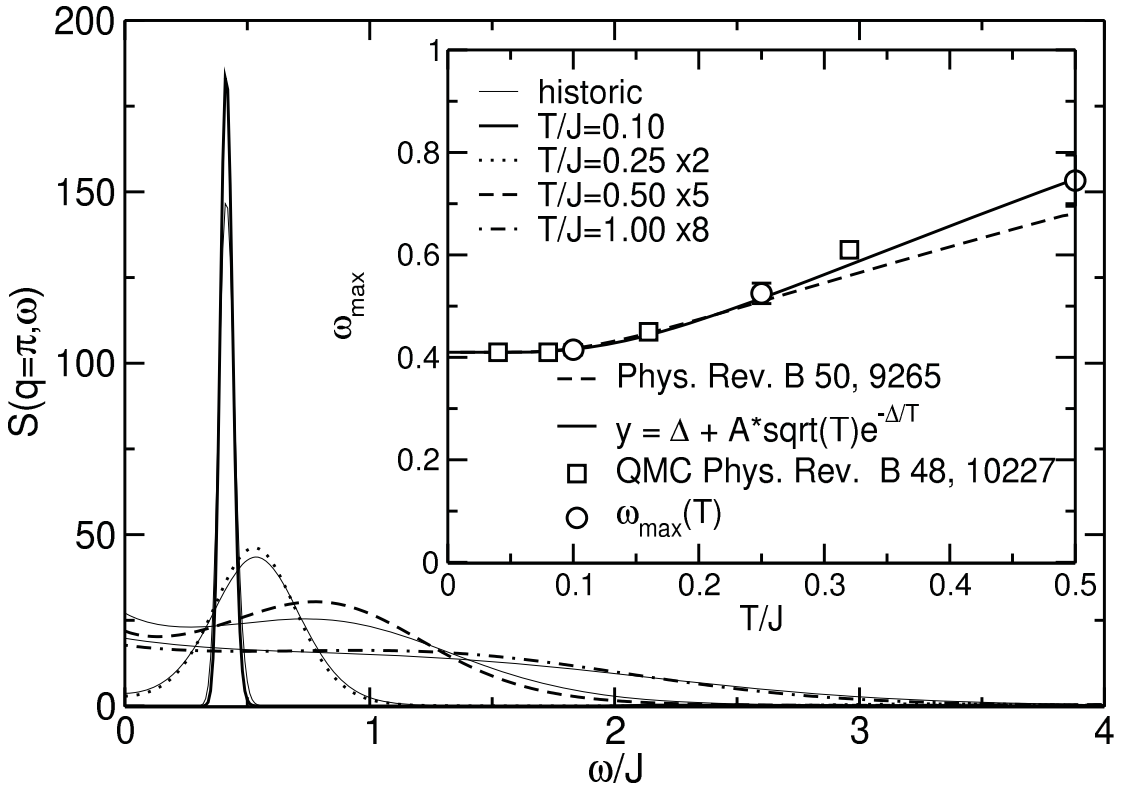

Figure 4.16: Shown here is the temperature dependence of the transverse dynamic structure factor at $q = \pi$. The inset shows the position of the peak which agrees well with other QMC results [171]. A direct comparison to the temperature dependence of the massive triple mode of a NLσM calculation (self consistent solution in [202], not the given low-temperature approximation) agrees well at lower temperatures and slightly deviates at higher temperatures. Above $T/J > 0.5$ the peak position seems to be not observable anymore, matching previous QMC findings and experimental results [66, 171].

4.2.2 Temperature dependence of the gap $\Delta(T)$

The temperature dependence of the gap has been observed in experiments on $CsNiCl_3$ [80] and NENP [66], and discussed from a theoretical point of view by NLσM studies [202] and QMC calculations [171, 205]. The NLσM suggests an exponentially activated low temperature behavior of the form

$$\Delta(T) \approx \Delta(0) + \sqrt{2\pi\Delta(0)T}\, e^{-\Delta(0)/T}, \quad T/\Delta(0) \to 0. \tag{4.11}$$

Our results for the dynamic structure factor $S(\pi, \omega)$ and its maximum position are presented in Fig. 4.16. For low temperatures $T/J = 0.1$ we find a sharp, symmetric mode at exactly $\omega/J = \Delta$, which displays strong broadening with respect to increase of temperature. Additionally the peak position shifts to higher energies which can be understood as an increasing gapsize of the massive triplet mode in the picture of the NLσM. At $T/J = 0.5$ the maximum in the QMC is hardly noticeable anymore (in agreement with experiments [66]) and due to its weak curvature, the positional error introduced by the MaxEnt is not negligible anymore (compare Bryan vs. historic solutions). However, our results for the maximum positions (inset Fig. 4.16) agree very well with results reported by Deisz *et al.* [171] and the fit (solid line, inset) supports exponential behavior. A comparison of our data with eqn. (4.11) showed strong deviations and we must question the validity of this low-temperature approximation at the temperatures relevant for this work. Taking one step back, we solved the general gap-equation in [202] for each temperature numerically and the results displayed satisfying agreement within the QMC error bars given by the differences of Bryan and historic continuations shown in the main frame of Fig. 4.16. We like to add, that the gap-size of the triplet branch in the NLσM is not necessarily equal to the maximum position of the spectrum at finite temperatures.

4.2.3 Low-q behavior

Recently the DSF has been studied in the region of long to intermediate wave vector, i.e. $0 < q < \pi/3$ [194, 198, 229]. For these wave vectors it is believed that the one magnon excitation decays into a continuum of multi-magnon modes. Due to its low intensity, detecting this continuum by INS is challenging and has been achieved only recently [194]. The NLσM predicts, that the triplet spectrum at $q = 0$ is gapped by twice the Haldane gap Δ. This can be understood in terms of the lower bound of the two-particle continuum at q=0 formed from two one-magnon states at $q = \pi, -\pi$. This has been confirmed by tDMRG calculations performed last year [207]. Considering MaxEnt of QMC results, spin conservation renders the observation of spectral weight at finite frequencies complicated as $q \to 0$. However, already at $q = \pi/64$ we find non-zero spectral weight at finite frequencies. This spectrum is show in Fig. 4.17 and Fig. 4.18. It displays a double peak structure, with the low-energy peak located almost exactly at 2Δ. As the wave vector is increased, the double-peak structure shifts to higher energies. This shift is consistent with the predictions of the NLσM on the lower threshold ω_{th} and the position ω_{max} of the lower maximum at zero temperature [201]. To the best of our knowledge, the maximum, visible at higher energies of approximately $\omega = 2J$, has not been reported in the literature yet. We speculate that it originates from

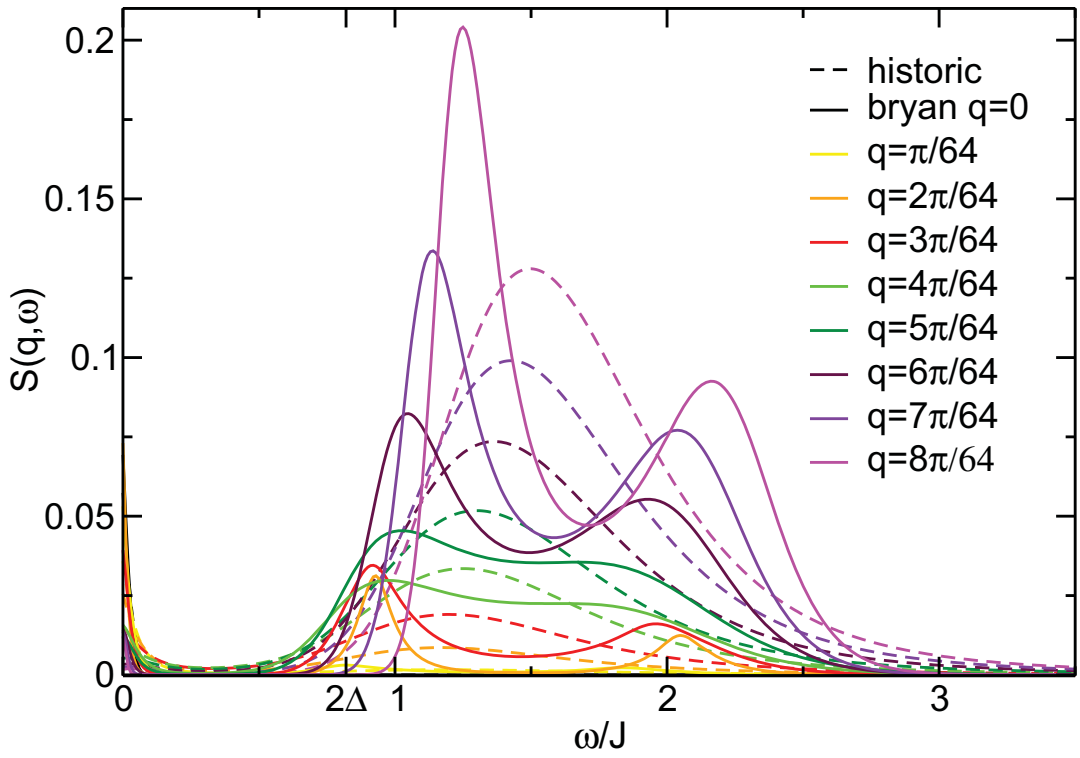

Figure 4.17: Low-q behavior at $T/J = 0.1$ for wave vectors $0 \leq q \leq \pi/8$. The solid lines are Bryan MaxEnt results, the dashed lines are the corresponding historic results. Obviously the historic approach cannot resolve a double peak structure while Bryan does. This is most probably related to the relative error of τ-data, which increases for long wavelengths as described in the text. A bigger relative error leads to large regularization parameter cutoffs with the consequence of generally smooth spectral results.

higher order multi-magnon excitations. In the context of this secondary peak we would like to point out that within the present calculation the *absolute* error of the QMC data on the τ-axis is 10^{-6}, which is very small. However, the *relative* error increases by orders of magnitude as $q \to 0$, since the static structure factor $S(q)$ scales as $\propto q^2$, which implies small absolute numbers for the DSF $S(q, \tau)$ also. This leads to a very sensitive response to the choice of the regularization parameter α at long wavelengths and as a consequence, historic, classic and Bryan MaxEnt results are clearly distinguishable in this q-region. In direct comparison to Deisz *et al.* [171] and S. V. Meshkov [206], our historic MaxEnt (the least ambitious choice of α) in Fig. 4.17 resembles their presented data very well.

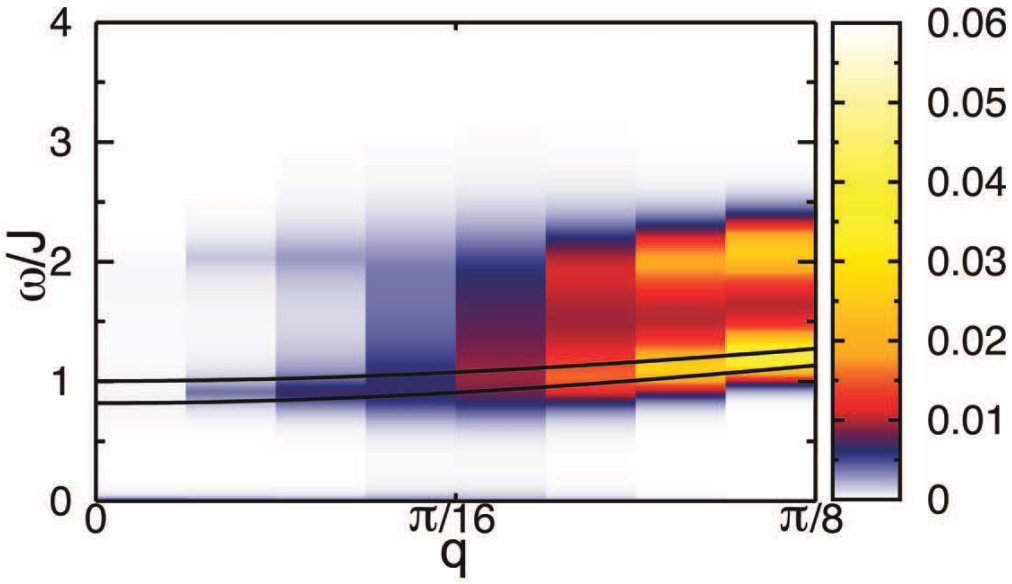

Figure 4.18: Same parameter region as Fig. 4.17 in a contour plot. The two solid lines are taken from a NLσM approach [201] and denote the lower threshold for spectral weight at $T = 0$ (lower solid line), respectively the maximum position of the spectral weight (upper solid line).

4.2.4 Field dependence of the transverse DSF

In this subsection we discuss the field dependence of the transverse dynamic structure factor $S^{xx}(q, \omega)$. A magnetic field closes the Haldane-gap linearly $\Delta(B) = \Delta(0) - B$ [173] by level-crossing of the lower triplet branch with the ground state at the first critical field B_{c_1}. Results of $S^{xx}(q, \omega)$ for this field interval $0 < B \leq B_{c_1}$ will be given in Fig. 4.19. We detail the field dependence of the gap in Fig. 4.20 and exemplarily resolve into $S^{+-}(\pi, \omega)$ and $S^{-+}(\pi, \omega)$ contributions at field $B/J = 0.2$. Beyond the first critical field, we present results for $S^{xx}(q, \omega)$ in the gapless Luttinger liquid phase $B_{c_1} \leq B \leq B_{c_2}$ in Fig. 4.21. This regime has been highlighted very recently by INS experiments on magnon fractionalization of a spin ladder systems [199, 200].

The case $0 < B < B_{c_1}$: Figure 4.19 shows results for the transverse DSF at temperatures $T/J = 0.1$ and magnetic fields $B/J \in \{0.1, 0.2, 0.3, 0.4\}$. Several effects occur as function of the applied field: firstly we find that a gap opens linearly at $q = 0$ with respect to the field due to the Zeeman energy (visible in the insets normalized by the static structure factor). Secondly, there is a broadening of the sharp zero field

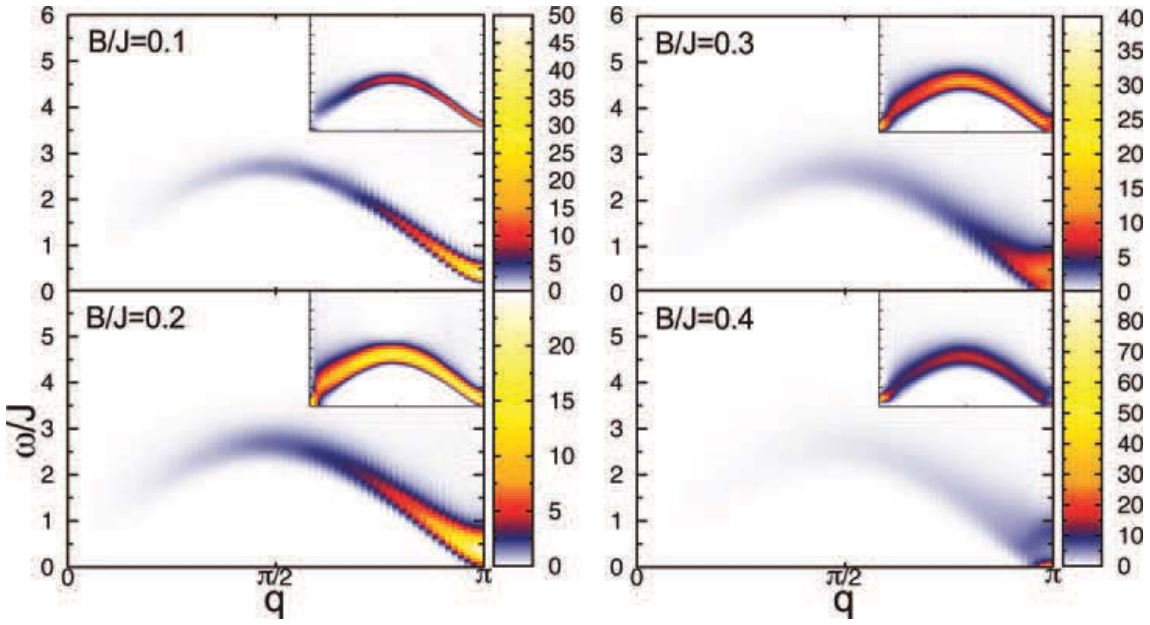

Figure 4.19: Results for the transverse DSF at $T/J = 0.1$ for four different magnetic fields (in units of J) $B \in \{0.1, 0.2, 0.3, 0.4\}$ with corresponding normalized insets by its static structure factor. Coming from zero magnetic field, the +- and -+ branch move towards lower, respectively higher energy, leading to a widening of the spectrum at the zone boundary while at the same time a gap opens at $q = 0$ linearly with the applied field. Close to the critical field $B = 0.4J$ (last panel), the system's groundstate fills with gapless excitations, leading to a high density of states and a high absolute scale.

magnon dispersion with increasing fields near the zone boundary due to the splitting of the triplet excitations. This is emphasized in Fig. 4.20 (and inset), where the peak structure is exemplarily resolved into $S^{+-}(\pi, \omega)$ and $S^{-+}(\pi, \omega)$ contributions for the case $B/J = 0.2$. The inset clearly shows the linear opening, respectively closing of the triplet branches with the applied field in agreement with [173, 203]. Small deviations from the linear behavior are most likely finite temperature or continuation effects.

Thirdly we find, that the major contribution to the total spectral weight can be found at short wave lengths. This is even more emphasized in Fig. 4.23 where $S^{xx}(q, \omega \to 0)$ data is displayed for finite fields at $T/J = 0.1$. Such concentration of spectral weight in the direct vicinity of $q \to \pi$ yields a T_1-relaxation rate which is largely independent of the form factor choice as long as short wavelengths are probed. Therefore a purely on-site form factor $A(r) \approx A_0\delta(r)$ as in the spin S=1/2 case would be well founded in order to compare with NMR experiments. Finally it is interesting to note, that the absolute scale of Fig. 4.15 starts to decrease coming from zero fields due to the splitting

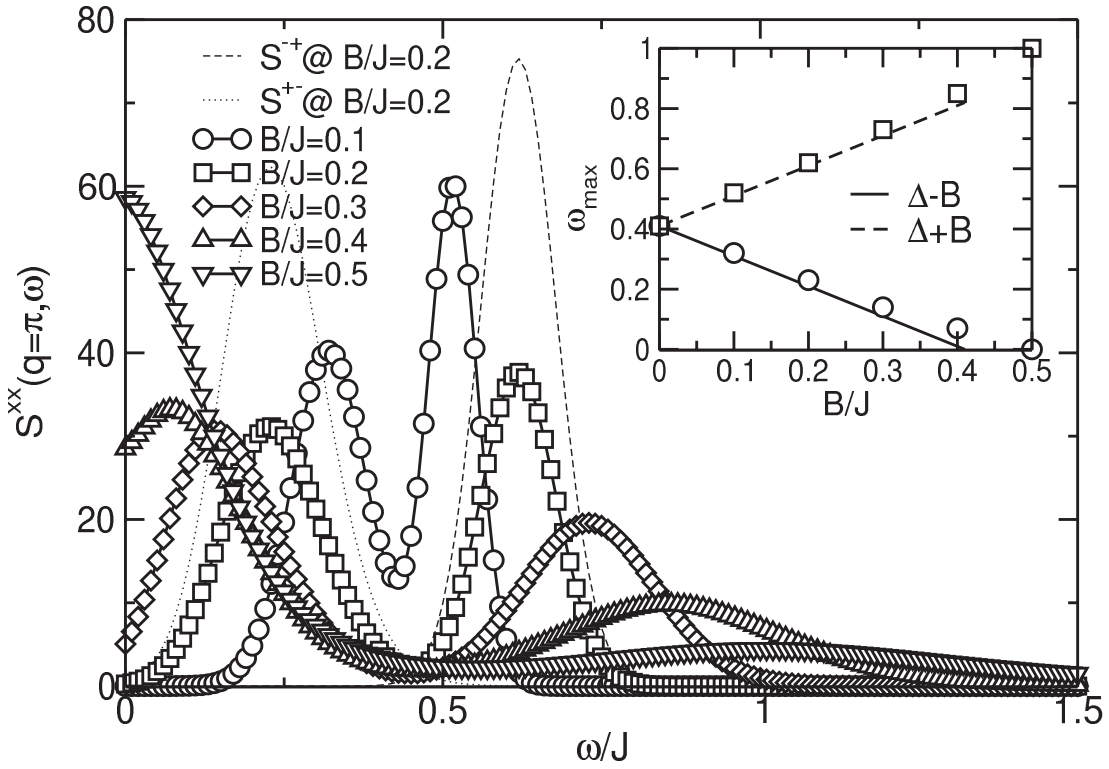

Figure 4.20: Shown here is the field dependence of the gap at $T/J = 0.1$ for five different magnetic fields ranging from $B/J \in \{0.1, 0.2, 0.3, 0.4, 0.5\}$. We find that the sharply peaked one magnon line at $\omega/J = 0.41$ for zero field (see Fig. 4.16 is broken up into the two splitting triplet branches at finite fields. The linear closing, respectively opening of +- and -+ contributions are exemplarily shown for $B/J = 0.2$ and the maximum positions of $S^{+-}(\pi, \omega)$ and $S^{-+}(\pi, \omega)$ are presented in the inset.

of the triple excitations. Near the critical field $B_{c_1} = \Delta$ it starts to increase strongly again, since the ground state of the spin chain fills with gapless excitations, leading to a high density of states at $q = \pi$. Beyond the critical field at $B/J = 0.5$, the absolute scale decreases again (not depicted).

The case $B_{c_1} \leq B \leq B_{c_2}$: Once the lower triplet branch crosses the ground state of the Haldane-chain, the system becomes gapless and can be described by a sea of interacting fermions. Such a system is known as Luttinger liquid which has been analyzed in regard to the Haldane-chain in some detail [26, 173, 174, 203, 204, 231]. In the context of magnon fractionalization there exist numerous and, in some cases,

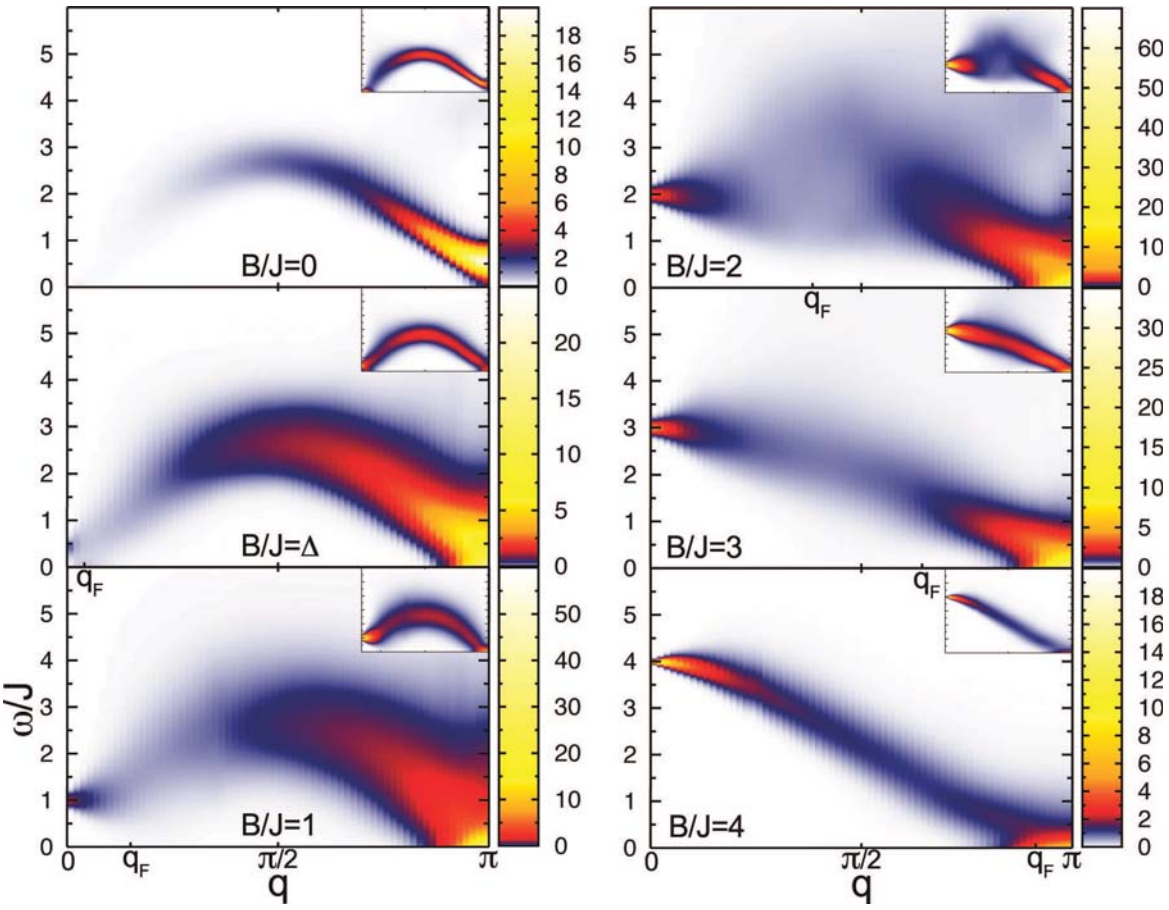

Figure 4.21: Results for the transverse DSF at $T/J = 0.25$ for six different magnetic fields $B/J \in \{0, \Delta, 1, 2, 3, 4\}$, normalized by the static structure factor in the corresponding insets. q_F stands for the incommensurate Fermi wave vector of the Luttinger liquid regime given by recent field theory predictions [230].

very recent results of ESR and INS on the Haldane chains NDMAP [68, 84–87, 232], NDMAZ [192] and on a spin S=1/2 ladder material $TlCuCl_3$ [24, 199, 200].
Fig. 4.21 shows our QMC results for the transverse DSF in this intermediate magnetic field regime at a temperature $T/J = 0.25$ for five different magnetic fields $B \in \{B_{c_1}, B_{c_2}/4, B_{c_2}/2, 3B_{c_2}/4, B_{c_2}\}$.

Following the trend of Fig. 4.19, the gap at $q = 0$ keeps opening linearly with the applied magnetic field. It should be noted that the weight of the low-q regime is steadily increasing with increasing fields, matching the behavior of the static structure factor $S^{xx}(q)$ [142, 220], which is coupled to the DSF by sum rules (see section 4.2.6).

At wave vectors near the zone boundary the system remains gapless, and, as already known from spin S=1/2 chain calculations [142, 220, 228], small magnetic fields initially lead to an increase of the transverse spectral weight at the antiferromagnetic wave vector. For magnetic fields beyond $B_{c_2}/2$, the absolute scale decreases and the weight shifts from $q = \pi$ to $q = 0$ with relatively low weight at intermediate wave vectors. This behavior matches earlier results on the spin S=1/2 chain [228] very well. However, for the intermediate field and wave vector region we find weight extending nearly over the whole displayed frequency interval in contrast to results of the spin S=1/2 chain. Much less pronounced than for the S=1/2 system is the expected weight at the incommensurate Fermi wave vector q_F, moving from $q = 0$ to $q = \pi$ by $q_F = \pi\langle S^z\rangle$ [230] as predicted by field theory results of Tvselik's Majorana fermion theory [204]. While at low magnetic fields, we find clear indications of finite spectral weight at q_F, it becomes increasingly harder to spot at fields $B \geq B_{c_2}/2$.
At the upper critical field B_{c_2} one finds a coherent picture of S=1/2 and S=1 again as the spectrum becomes a magnon cosine dispersion with increased weight at $q = 0$ and $q = \pi$ due to finite temperatures (see Fig. 4.8). At zero temperatures one would expect an cosine dispersion with constant spectral weight, which finally becomes gapped for fields $B > B_{c_2}$ (not displayed here).

4.2.5 NMR rates

There exist numerous measurements of NMR T_1^{-1}-relaxation rates on $AgVp_2S_6$ [235, 236] and on NENP [237–239] where two major effects have been observed – the most basic effect of temperature and magnetic field in the region $0 \leq B \leq B_{c_1}$ is the linear closing of the Haldane-gap, which generally leads to an exponentially activated relaxation rate $1/T_1 \propto e^{-(\Delta - B)/T}$. As the second major effect, the rate initially decreases with $1/T_1 \propto B^{-1/2}$ into a global minimum [235, 239], which was remarkably well explained by results of Yamamoto *et al.* [234] (modified spin-wave theory) and Damle *et al.* [233] (semiclassical picture). Unfortunately, this effect has to be considered as beyond the scope of this work due to the coarse field and temperature resolution. In addition to our resolution with respect to field, the effect is also very small compared to the absolute scale of the spectrum (see $q \to 0$ versus $q \to \pi$ contributions in Fig. 4.23).

To access the NMR-rate by QMC we integrate over the wave vectors at the NMR resonance frequency

$$1/T_1 \propto \sum_q A_0 S^{\perp}(q, \omega \to 0) \tag{4.12}$$

where we implicate that the hyperfine coupling tensor $A^{\alpha\beta}(q)$, $\alpha, \beta \in \{x, y, z\}$ does

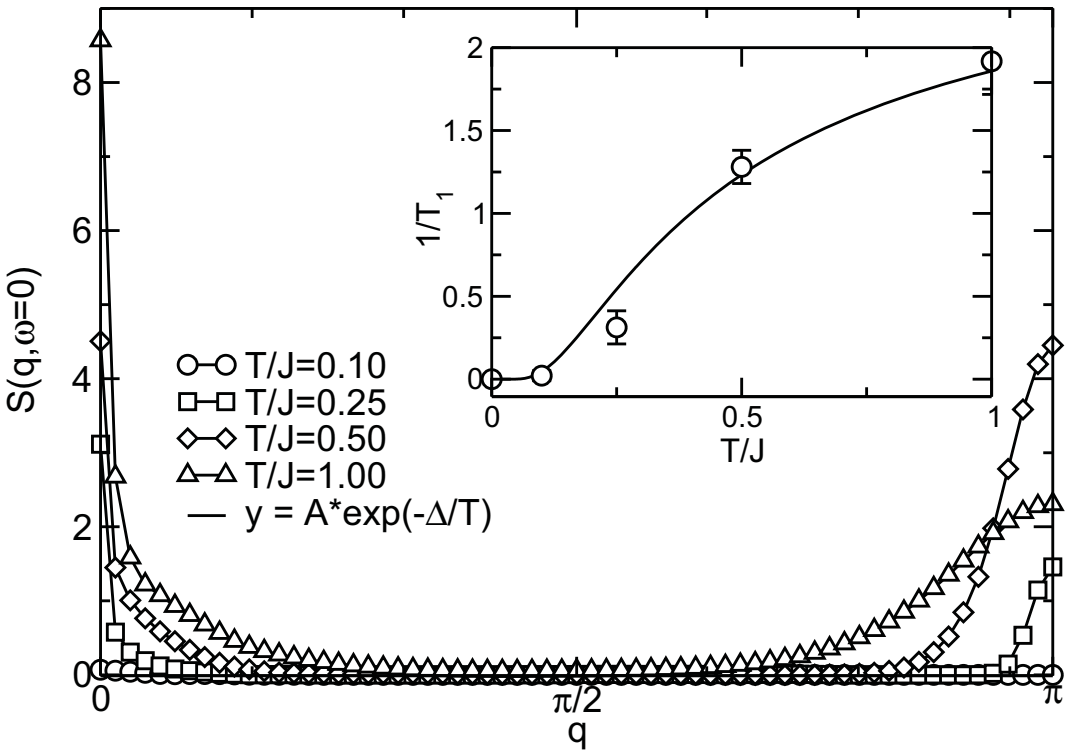

Figure 4.22: Temperature dependence of the transverse dynamic structure factor at $\omega \to 0$. The inset shows the T_1-relaxation rate with constant form factor for temperatures $T/J \in \{1.0.0.5, 0.25, 0.1\}$ and an error bar estimated by Bryan (most advanced) versus historic (least ambitious) MaxEnt approach. The strong weight increase with temperatures at the zone center due to diffusive behavior and the zone boundary due to closing of the Haldane-gap drives the rate into exponentially activated behavior $1/T_1 \propto e^{-\Delta/T}$ in agreement with other theories [233, 234].

not mediate longitudinal spin fluctuations which can be achieved my measuring in the principle coordinate system. Following up our findings of subsection 4.2.4 that the most dominant contribution to NMR rates stems solely from the direct vicinity of $q = \pi$, we consider a constant $A(q) \to A_0$ (on-site relaxation only). This is justified in a sense that the form of $A(q)$ can be chosen without noticeable impact on the relaxation rates as long as short wavelengths are probed.

In Fig. 4.22 and Fig. 4.23 we present QMC results for the temperature and field dependence of the transverse DSF at the NMR resonance frequency $S(q, \omega \to 0)$. Starting with Fig. 4.22, we find negligible weight for $T/J = 0.1$ at all wave vectors. On the one hand the gap at $q = \pi$ is still open at such low temperatures, on the

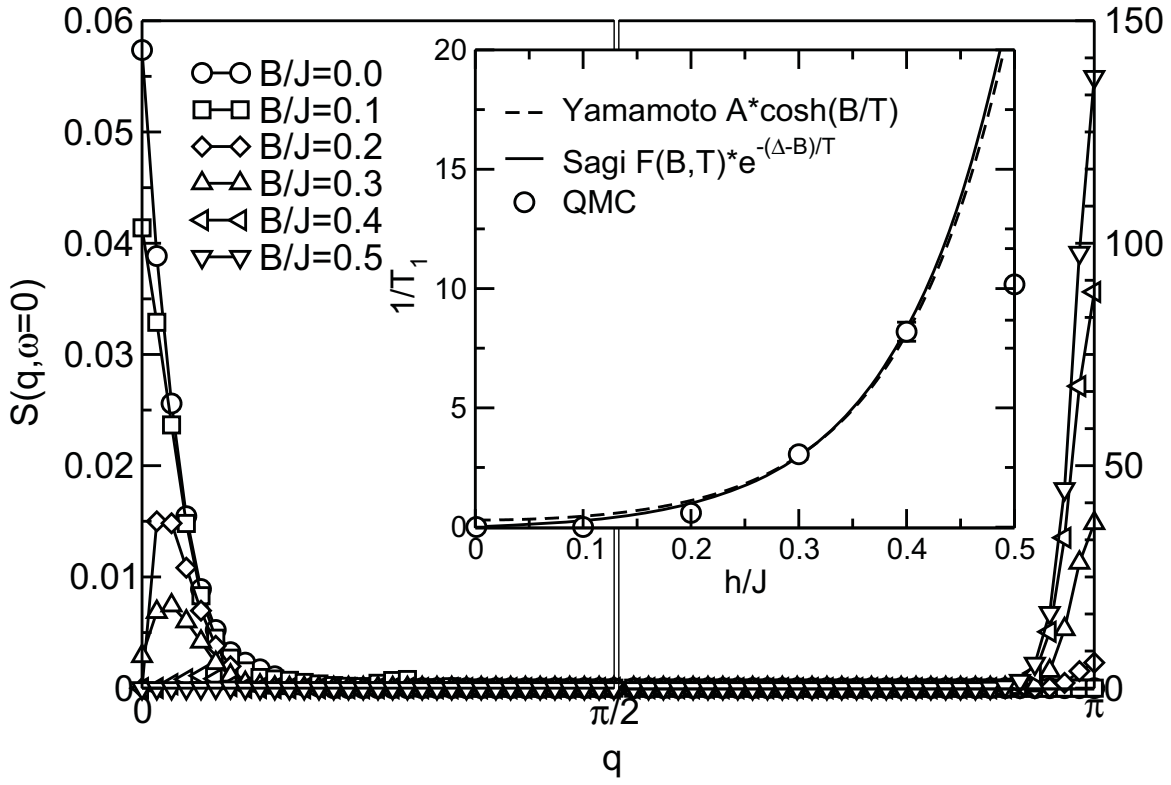

Figure 4.23: Field dependence of the transverse dynamic structure factor at $\omega \to 0$ and the resulting T_1-relaxation rate in the inset. Error bars are as in the preceding picture estimated by Bryan versus historic MaxEnt procedure. Again we find exponentially activated behavior. Unlike experiments [235, 239] however, we cannot spot the initial $1/\sqrt{B}$ decrease of the rate, since its contributions stemming from the zone center [234] are just too small at elevated temperatures $T/J = 0.1$ and fields (note the cut of the q-scan data into separate scales) to be picked up in our coarse field resolution. At higher temperatures this behavior becomes more pronounced due to strongly enhanced spectral weight at the zone center and therefore should become detectable by QMC.

other hand the magnon linewidth allows for only a negligible amount of intra-band excitations, leading to a low $q = 0$ contribution as well. Further warming increases weight at both q-positions while widening the q-interval with finite weight noticeably. Interestingly, at the highest temperatures $T/J = 1$, absolute weight at $q = \pi$ is decreasing compared to lower temperatures $T/J = 0.5$ due to thermal fluctuations, instead the thermally activated spectral weight spreads over a much larger q-region. The behavior described in $S(q, \omega \to 0)$ translates into the $1/T_1$ relaxation rate by eqn. (4.12) in the inset of Fig. 4.22. At the lowest temperatures the system is

gapped and relaxation cannot take place, resulting in a close to zero $1/T_1$ with only minor contributions stemming from $q \to 0$. Increasing the temperature exponentially activates the relaxation rate proportional to $1/T_1 \propto Ae^{-\Delta/T}$ [202, 234, 240] which was used to fit the displayed four data points within their errors estimated by comparing Bryan versus historic regularization parameter choices.

For the field dependence displayed in Fig. 4.23, a similar exponentially activated relaxation rate is expected [234, 240], however the underlying wave vector dependency is fundamentally different as indicated by the two different scales in Fig. 4.23. While the spectrum at $q \to 0$ becomes immediately gapped at B_{c_1} due to the Zeeman energy (as visible in Fig. 4.19), the Haldane-gap at $q = \pi$ gets linearly closed by S^{+-} processes (see Fig. 4.20), leading to a strong increase of spectral weight with fields close to the lower critical field B_{c_1}. As shown in the inset, the $1/T_1$ relaxation rate reflects this strong increase with exponentially activated behavior which is solely driven by zone boundary excitations. Comparisons with $Ae^{-(\Delta-B)/T}$, respectively by expressions from Yamamoto *et al.* [234] and Sagi *et al.* [240] confirm this. Beyond the closing of the gap the system reaches the Luttinger liquid regime as mentioned in the preceding subsection and the relaxation rate loses its exponential growth. A similar exponential behavior of the rate should be visible at the upper critical field B_{c_2} as a consequence of magnon condensation which has been presented in earlier calculations and verified experimentally on the spin S=1/2 chain [31].

4.2.6 Sum rules

As in section 4.1.4, we assess the quality of the analytic continuation by sum rules for the static structure factor $S^{\alpha\beta}(q)$ and the static susceptibility $\chi^{\alpha\beta}(q)$, following eqn. (4.8) and (4.9) and repeated here for convenience:

$$S^{\alpha\beta}(q) = \frac{1}{\pi}\int_0^\infty d\omega(1+e^{-\beta\omega})S^{\alpha\beta}(q,\omega) \tag{4.13}$$

$$\chi^{\alpha\beta}(q) = \frac{2}{\pi}\int_0^\infty d\omega\,\omega^{-1}(1-e^{-\beta\omega})S^{\alpha\beta}(q,\omega). \tag{4.14}$$

While $S^{\alpha\beta}(q,\omega)$ on the right-hand side of eqns. (4.13) and (4.14) involve MaxEnt-data, the static structure factor $S^{\alpha\beta}(q)$ and static susceptibility $\chi^{\alpha\beta}(q)$ can be evaluated directly by the QMC.

In Fig. 4.24 we compare the left- and right-hand sides of eqns. (4.13) and (4.14) for the transverse components $\alpha\beta = xx$ and find excellent agreement (even on a logarithmic

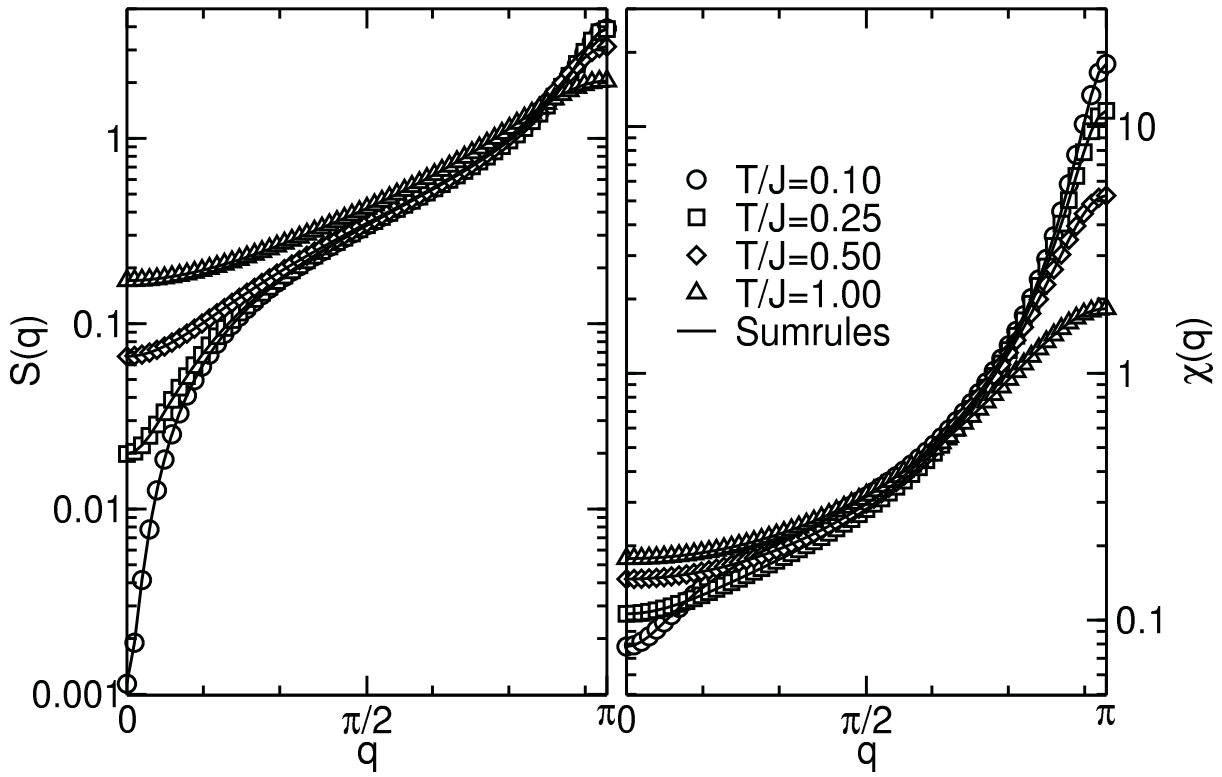

Figure 4.24: Sumrules for four different Temperatures $T/J \in \{0.1, 0.25, 0.5, 1.0\}$. Static structure factor and static susceptibility obtained by QMC free of the MaxEnt procedure in direct comparison to the integral equations on the DSF (4.8, 4.9) given in the text. Static results $\chi(\pi)$ and $S(\pi)$ are in agreement with static QMC results by Kim *et al.* [212].

scale) of QMC data involving analytic continuation to that free of the MaxEnt procedure for the static structure factors and static susceptibility. This agreement persists for all temperatures, wave vectors and also for field dependent data not displayed here.

4.2.7 Conclusion

In conclusion, using MaxEnt continuation of QMC results, we analyzed the transverse spin fluctuations of a Haldane chain with 128 sites as function of finite temperatures $0.1 \leq T/J \leq 1$ and finite magnetic fields $0 \leq B \leq B_{c_2}$. Our temperature dependent results are consistent with previous QMC results and field-theories with the latter also being complemented by our results for fields below the Luttinger liquid phase $0 \leq B \leq$

B_{c_1}. A direct comparison with field-theories was given for the T_1-relaxation rate and for the maximum position of the structure factor at zone center and zone boundary as the accessible limits of field theory approaches. We show that the limits $q \to 0$ and $q \to \pi$ are in fact well founded for low temperatures, as low-frequency spectral contributions to the relaxation rate stem for the most part from those wave vectors and their direct vicinity. We confirm the picture of two π-magnon excitations as lowest energy boundary in the low-q region and resolve a yet unseen double-peak structure of higher-magnon contributions. For the evaluated temperature $T/J = 0.1$ we document the condensation of magnons in the dynamic structure factor and the relaxation rate as in the spin S=1/2 chain, although this time we linearly close the gap upon *increasing* the magnetic field. Beyond the first critical field, we show results of the transverse dynamic structure factor in the Luttinger liquid regime $B_{c_1} \leq B \leq B_{c_2}$ and find hints of incommensurate Fermi wave vectors as in previous studies on the spin S=1/2 chain. We finalize our results again with a sum-rule consistency check which proves excellent agreement with the zeroth-momentum static structure factor and the low-frequency probing sum-rule for the static susceptibility. Again our results may be of high-relevance to INS experiments and help to understand the spectral evolution and contribution to the NMR experiments.

While we overall showed good agreement with field theory results for $0 \leq B \leq B_{c_1}$, open questions remain for the Luttinger liquid phase where we hope to achieve better continuation results to clearly identify Fermi wave vectors. Furthermore our data quality for the longitudinal dynamic structure factor needs to be improved in order to yield a better basis for the MaxEnt. Finally, similar calculations for single-ion anisotropy and eventually disorder are highly desirable since most Haldane chains exhibit anisotropies due to orbital quenching.

4.3 Hydrodynamic limit for the spin dynamics of the Heisenberg chain

In the last section, the issue of spin diffusion for the spin S=1/2 Heisenberg chain has been out of reach due to the numerical difficulties with the analytic continuation to the real axis. In this section, we propose a method to circumvent the continuation by working directly on the imaginary time axis.

To get started, we look at the linear response theory [167], which shows the zero momentum, frequency dependent spin conductivity

$$\sigma'(\omega) = D\delta(\omega) + \sigma'_{reg}(\omega) \tag{4.15}$$

to consist of the Drude weight

$$D = \frac{\beta}{N} \sum_{\substack{m,n \\ E_m = E_n}} e^{-\beta E_m} |\langle m|j|n\rangle|^2 \tag{4.16}$$

and a regular spectrum

$$\sigma'_{reg}(\omega) = \frac{1 - e^{-\beta\omega}}{\omega} \frac{1}{N} \sum_{\substack{m,n \\ E_m \neq E_n}} \left[e^{-\beta E_m} |\langle m|j|n\rangle|^2 \delta(\omega - E_n + E_m) \right] \tag{4.17}$$

where $j = j_{q=0}$ is the z-component of the spin current with $j_q = (i\Delta J/2) \sum_l e^{(-iql)} (S^-_l S^+_{l+1} - S^+_l S^-_{l+1})$ and m, n are the eigenstates with energies $E_{m,n}$.

For the Drude peak no generally accepted picture has emerged yet, since a nonzero Drude weight would imply dissipationless transport in a correlated system [208], despite $[j, H] \neq 0$ for the XXZ model. Here we give a brief summary regarding the status of this issue and refer to [138] and refs. therein for a more extensive summary. At $T = 0$ and in the massless regime $|\Delta| < 1$ of the XXZ chain, the zero temperature Drude weight is known to be finite [241]. At $T \neq 0$, Bethe-Ansatz (BA) calculations arrive at contradictory results regarding the temperature dependence of $D(T)$ [242–244]. The same holds for the question whether $D(T > 0)$ is finite or not at the $SU(2)$ symmetric point $\Delta = 1$ [242, 243]. Recent numerical studies using QMC [245, 246], exact diagonalization (ED) at zero [167, 247–249], as well as finite magnetic fields [250], and master equations [251, 252] are consistent with $D \neq 0$ for $|\Delta| \leq 1$ and $T \geq 0$, supporting a ballistic contribution to the conductivity at finite temperatures. Recent time-dependent density-matrix renormalization group (tDMRG) studies have given evidence for ballistic spin dynamics for $|\Delta| \leq 1$ in the out-of-equilibrium case [253].

The regular finite-frequency contribution $\sigma'_{reg}(\omega)$ has been considered by ED studies [254, 255], which however leave many open issues. Very recently, spin diffusion has been conjectured to govern the low-frequency spectrum of the regular conductivity [32], based on real-time transfer matrix renormalization group (tTMRG) and a perturbative analysis using bosonization. The latter provides for an approximate expression for the Fourier transform of the retarded spin-susceptibility $\chi_{ret}(q,t) = i\Theta(t)\langle[S^z_q(t), S^z_{-q}]\rangle$ which reads

$$\chi_{ret}(q,\omega) = -\frac{Kvq^2}{2\pi}\frac{1}{\omega^2 - v^2q^2 - \Pi_{ret}(q,\omega)} , \tag{4.18}$$

with

$$\Pi_{ret}(q,\omega) \approx -2i\gamma_B\omega - b\omega^2 + cv^2q^2 , \tag{4.19}$$

where at $\Delta = 1$, $K = 1 + g/2 + g^2/4 + g^3/8$, $v = \pi/2$ (see e.g. [7]), $2\gamma_B = \pi g^2 T$, $b = g^2/4 - g^3(3 - 8\pi^2/3)/32 + \sqrt{3}T^2/\pi$, and $c = g^2/4 - 3g^3/32 - \sqrt{3}T^2/\pi$ have been obtained by perturbative expansions (PE) at $T \ll J$ [32] in powers of the running coupling constant $1/g + \ln(g)/2 = \ln\left(\sqrt{\pi/2}\exp(G + 1/4)/T\right)$ and $G \approx 0.577216\ldots$ is Euler's constant [256].

Some remarks are in order. First, for $\omega \ll \gamma$, eqn. (4.18) displays a diffusion pole with a diffusion constant $\Gamma = (1 + c)v^2/(\pi g^2 T)$. I.e. within this approximation the spin dynamics of the Heisenberg chain would allow for a plain hydrodynamic limit. Second, eqns. (4.18) and (4.19) do not incorporate the finite width of the spectral function $\chi''(q,\omega) = Im[\chi_{ret}(q,\omega)]/\pi$ at $T = 0$, which is dominantly set by the two-spinon continuum. However, at $q/\pi \ll 1$ the latter width is of order $\pi J q^3/16$, which for those wave vectors and temperatures which we will be interested in is negligible against γ_B. Third, for any finite momentum $q \neq 0$, the isothermal susceptibility $\chi_q = \int_{-\infty}^{\infty} d\omega \chi''(q,\omega)/\omega$ obtained from eqn. (4.18) is identical to the isolated susceptibility $\chi_{ret}(q,0) = \int_{-\infty}^{\infty} d\omega \chi''(q,\omega)/(\omega - i0^+)$, since $\chi''(q \neq 0, \omega \to 0) \propto \omega$. Therefore $\chi_q = K/(2\pi v(1 + c))$. Furthermore, the isothermal susceptibility of the Heisenberg model is a continuous function of q. Its limiting value $\lim_{q\to 0}\chi_q = \chi_0$ at zero momentum is known from thermodynamic Bethe Ansatz (TBA) [7, 256]. Therefore

$$\frac{K/(2\pi)}{v(1+c)} = \chi_0 \approx \frac{1}{\pi^2}(1 - \frac{g}{2} + \frac{3g^3}{32} + \frac{\sqrt{3}T^2}{\pi}) = \chi_{PE} , \tag{4.20}$$

should be satisfied, where χ_{PE} is a known PE of the TBA result [7, 256] and which is consistent with the parameters listed following eqn. (4.19)

The spectral function $\chi''(q,\omega)$ is related to $\sigma'_{reg}(\omega)$ by means of the lattice version of the continuity equation $\partial_t S^z_q = (1 - e^{-iq})j_q$ through

$$\sigma'_{reg}(\omega) = \lim_{q\to 0}\frac{\omega}{q^2}\chi''(q,\omega) . \tag{4.21}$$

Therefore, the spectrum of the regular part of the optical conductivity can be deduced from eqns. (4.18) and (4.19).

The main goal of this section is to analyze, to which extent eqns. (4.18) and (4.19) are consistent with QMC calculations. The significance of such comparison is with the regular part of the spin conductivity. It will *not* clarify the size of the Drude weight, as any discrepancy arising may be due to partial spectral weight transfer into a Drude weight. Furthermore, we focus on the isotropic point $\Delta = 1$, which may be different from the anisotropic case. To begin, we note, that eqns. (4.18) and (4.19) approximate the on-shell part of the spectrum for $|\omega \pm vq| \ll T$. Yet, similar to the comparison with tTMRG in eqns. (C2) and (C3) of ref. [32], we will assume them to be valid for all ω. Furthermore, χ_q is known to monotonously increase for the Heisenberg model as $q \to \pi/2$. However, $\chi_q = K/(2\pi v(1+c))$ from bosonization is momentum independent. Therefore, a momentum dependence $K \to K_q$, $v \to v_q$ – albeit weak at $q \ll 1$ – is to be allowed for, when matching up eqns. (4.18) and (4.19) with QMC.

We perform the comparison to QMC by transforming $\chi_{ret}(q,\omega)$ onto the imaginary time axis

$$\begin{aligned} \chi(q,\tau) &= 2\sum_{n=0}^{\infty} \cos(\omega_n \tau)\chi(q,\omega_n) - \chi(q,0) \\ \chi(q,\omega_n) &= \frac{K_q v_q q^2/(2\pi)}{(1+b)\omega_n^2 + (1+c)v_q^2 q^2 + 2\gamma_q|\omega_n|} \end{aligned} \tag{4.22}$$

The main point is, that a corresponding $\chi_{QMC}(q,\tau)$ can be obtained directly from QMC, following preceding work employing the stochastic series expansion method [228]. This involves only the statistical error, which is well controlled. Uncontrolled sources of error, due to e.g. transformations to real or Matsubara frequencies, do not occur. $\chi(q,\tau)$ is gauged against $\chi_{QMC}(q,\tau)$ by fitting K_q, v_q, and γ_q at *small* momentum, while retaining b and c as given by bosonization. This is justified, because the latter two constants do not enlarge the space of fitting-parameter, as any modification of them can be absorbed into a renormalization of K_q, v_q, and γ_q. Regarding the temperature range, we confine ourselves to $T/J \leq 0.25$. This is motivated by the PE to $O(g^3, T^2)$ for thermodynamic properties to agree rather well with QMC results up to $T/J \lesssim 0.1$ [7], while for $T \gtrsim 0.25$ the PE starts to fail significantly.

Fig. 4.25 shows the result of the comparison of QMC with eqn. (4.22) for the smallest non-zero wave vector $q = \pi/64$ of a 128-site system for two temperatures $T/J = 0.1$ and 0.25 allowing for three different choices of γ_q, namely (i) $\gamma_{q,QMC}$ as optimized by fitting, (ii) γ_B taken from the bosonization, and finally (iii) $\gamma_q = 0$ forced to be zero [257]. The upper panel b) of this figure clearly demonstrates, that QMC is inconsistent with $\gamma_q = 0$ and that increasing γ_q above zero improves the quality of the fit. In

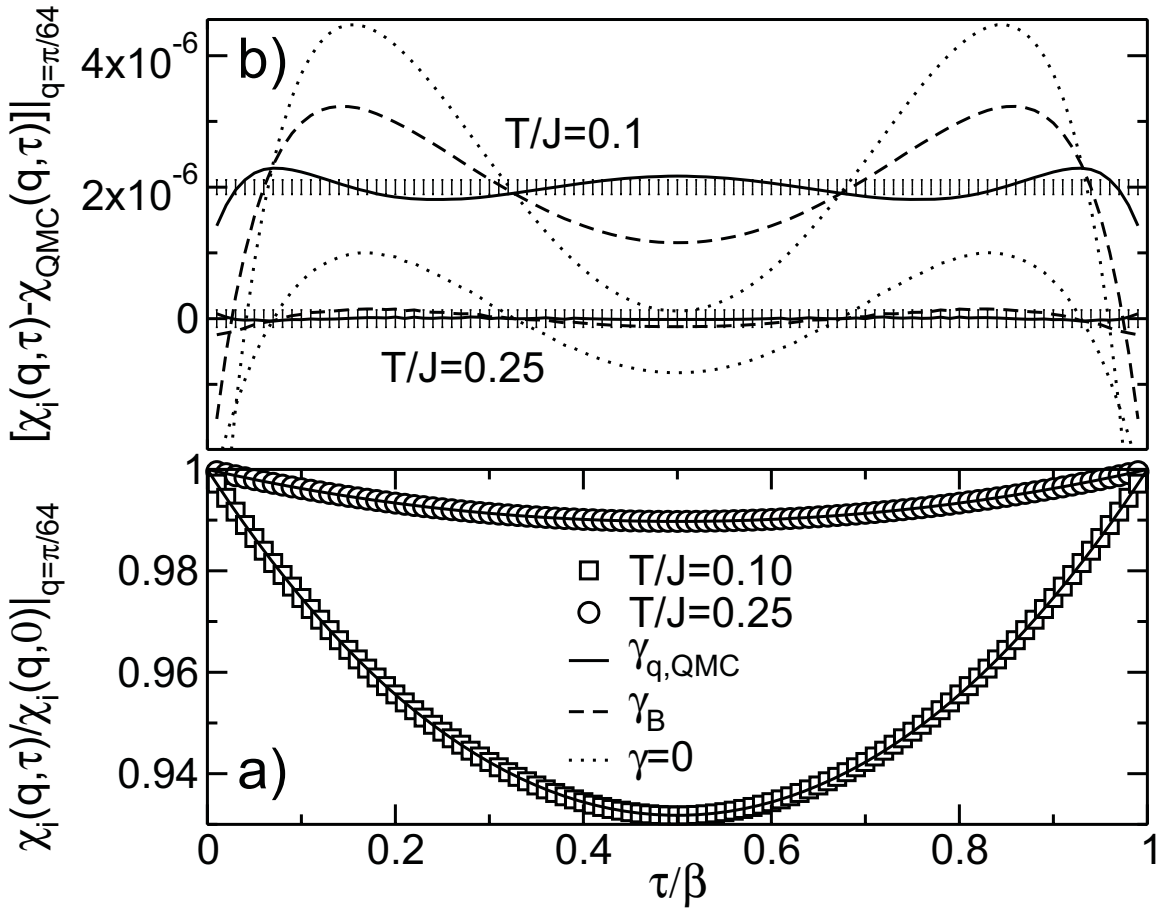

Figure 4.25: Imaginary-time susceptibility $\chi_{QMC}(q,\tau)$ at $q = \pi/64$ on 128 sites, for two temperatures T, fitted to $\chi(q,\tau)$ from eqn. (4.22) (lines) in three ways, namely: $\gamma_{q,QMC}$ optimized (solid), γ_B taken from ref. [32] (dashed), and γ forced to zero (dotted). The index 'i' on the y-axis refers to $\chi(q,\tau)$ from eqn. (4.22) for the lines in panels a) and b) as well as to QMC for the symbols in panel a). Panel a) Global behavior of $\chi_{QMC}(q,\tau)/\chi_{QMC}(q,0)$ for $T/J = 0.1$ (QMC, squares) and 0.25 (QMC, circles). In this panel the three fits (lines) are indistinguishable on the scale of the plot. Panel b) Error 2σ of $\chi_{QMC}(q,\tau)$ for each τ evaluated (error bars) and difference $\chi(q,\tau) - \chi_{QMC}(q,\tau)$ between QMC and the three fits (lines). 2σ for the QMC data is $O(10^{-7})$. Plots corresponding to $T/J = 0.1$ have been shifted by 2×10^{-6}.

particular the best fit, i.e. for $\gamma_{q,QMC}$, is identical within the standard deviation 2σ (error bar) to QMC for almost all $\tau \in [0,\beta]$ at both temperatures. Yet, we find $\gamma_{q,QMC} > \gamma_B$, and moreover there are *systematic* oscillatory deviations. While the latter seem a subdominant effect, which could be due to the on-shell approximation

in eqns. (4.18) and (4.19), these deviations may also indicate relevant corrections to diffusion and should be investigated in future studies. We emphasize the vertical scale on panel b) of Fig. 4.25 which demonstrates that high-precision QMC is mandatory for the present analysis. Fig. 4.25 is a central result of this section. It shows that QMC is consistent with a dynamic structure factor of the isotropic antiferromagnetic Heisenberg chain which is approximately diffusive at intermediate temperatures in the long wave-length limit with a diffusion kernel $(1+c)v^2/(2\gamma_{q,QMC})$. Any momentum dependence of $\gamma_{q,QMC}$, to be discussed later, implies corrections to this diffusion. Next, and to further support our approach, we will also discuss the Luttinger parameters we find.

In table 4.1 we compare the parameters obtained from the fit to QMC with results from TBA, PE and tTMRG. This table shows, that $\chi_{q,QMC} = K_q/(2\pi v_q(1+c))$ at $q = \pi/64$ is in excellent agreement with the isothermal susceptibility at $q = 0$ from the TBA for *both* temperatures which we have studied. This result should not be confused with the well known agreement between static QMC and TBA for the isothermal susceptibility [7], but rather it is a satisfying consistency check for our approach. In fact, fitting the imaginary-time transform of an *approximate* $\chi(q,\omega)$, i.e. eqn. (4.18), to QMC could require values for K_q, v_q, and γ_q which deviate from exactly known values for these quantities on a scale which is unrelated to the error 2σ of the QMC. As will be shown later the variation of K_q and v_q with momentum is very weak as $q \ll 1$, i.e. we expect no relevant change for $\chi_{q,QMC}$ as $q \to 0$. Yet we are tempted to point out, that $\chi_{q=\pi/64,QMC}$ in table 4.1 is barely larger than χ_0, which is consistent with the momentum dependence for the exact χ_q. The fact that $\chi_{q,QMC}/\chi_{PE} > 1$ and is increasing as T increases, evidences that χ_{PE} on the l.h.s. of eqn. (4.20) increasingly underestimates the TBA result as T increases beyond $T/J \gtrsim 0.1$. In Fig. 4.25 we have shown, that $\gamma_{q,QMC} \neq \gamma_B$. Yet, table 4.1 demonstrates that $\gamma_{q,QMC}$ and γ_B are comparable to within factors of order 2. Most important, the relaxation rate $\gamma_{q,QMC}$ we find is much larger than the width of the two-spinon continuum, yet, very small compared to temperature $\gamma_{q,QMC} \ll T$. We note, that fits to tTMRG [32] at $T/J = 0.2$, lead to $\gamma_{tTMRG}/\gamma_B \approx 0.64$.

T/J	$\chi_{q,QMC}/\chi_0$	$\chi_{q,QMC}/\chi_{PE}$	γ_B[32]	γ_{tTMRG}[32]	$\gamma_{q,QMC}$
0.1	1.0005	1.0032	0.0096		0.0191
0.25	1.0005	1.0248	0.0440		0.0511
0.2			0.0297	0.0190	

Table 4.1: Columns 2 and 3: Comparison of $\chi_{q,QMC} = K_q/(2\pi v_q(1+c))$ from QMC at $q = \pi/64$ with χ_0 from TBA [258] and χ_{PE} from the l.h.s. of eqn. (4.20). Columns 4, 5, and 6 display γ from bosonization, tTMRG, and QMC.

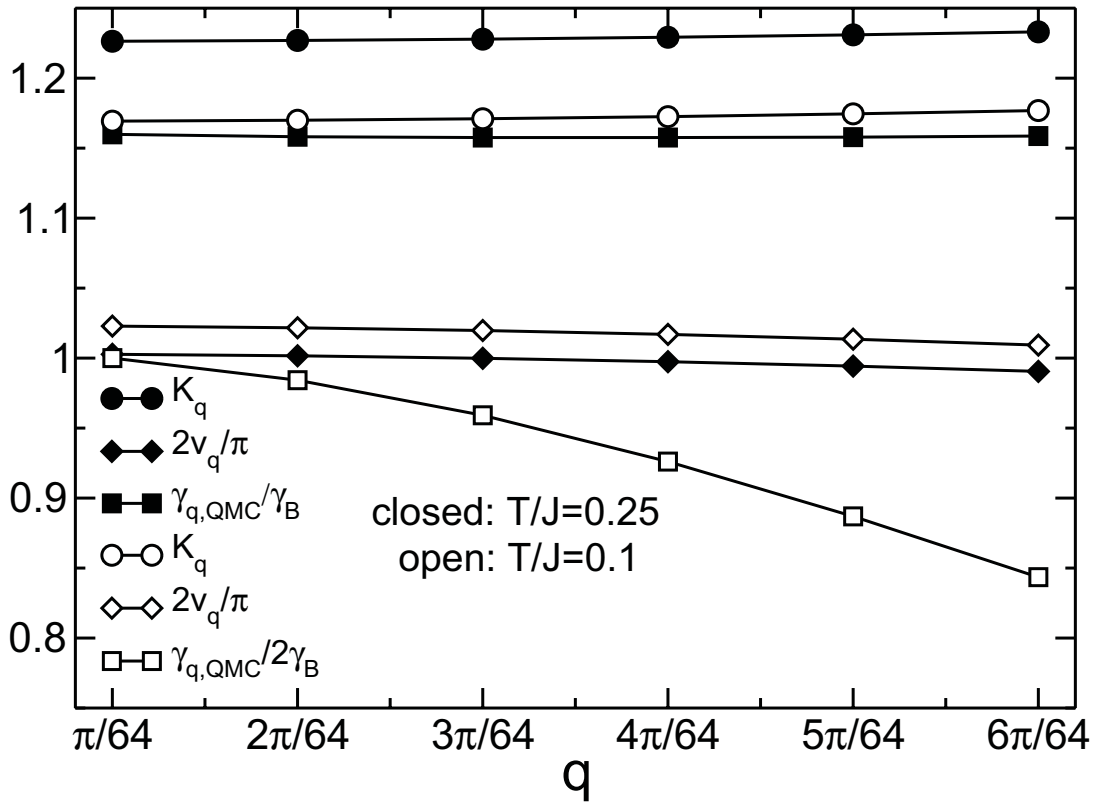

Figure 4.26: Momentum dependence of the renormalized Luttinger parameter K_q, spinon velocity v_q, and scattering rate $\gamma_{q,QMC}/\gamma_B$ for the first non-zero six momenta on a 128 site system for two temperatures $T/J = 0.1$ (white symbols) and 0.25 (black symbols). Note that $\gamma_{q,QMC}/\gamma_B$ for $T = 0.1$ has been *scaled by 2* to fit into the plot.

Next we discuss the momentum dependence. Fig. 4.26 displays all three fit parameters K_q, v_q and $\gamma_{q,QMC}$ versus the first six non-zero momenta and the two temperatures $T/J = 0.1$ and 0.25 which have also been considered in Fig. 4.26. v_q and $\gamma_{q,QMC}$ have been normalized to their values given by bosonization, i.e. $\pi/2$ and γ_B. Obviously all momentum variations are very smooth and rather weak. As can be seen from this figure, most of the renormalization of the ratio K_q/v_q from its bare value of $2/\pi$ stems from $K_q > 1$. The spinon velocity v_q deviates slightly from $\pi/2$, however only to within $O(1\%)$. As discussed in the previous paragraph, this is necessary to obtain an optimum fit of the QMC to the approximation eqn. (4.22) and does *not* imply that QMC is at variance with the bare spinon velocity. K_q displays a very weak upward curvature, while v_q shows a small downward curvature. The latter can be understood in terms of the $O(q^3)$ corrections to the linear on-shell dispersion $\omega(q)$ which are not contained in bosonization. The combined momentum dependence of K_q/v_q leads to

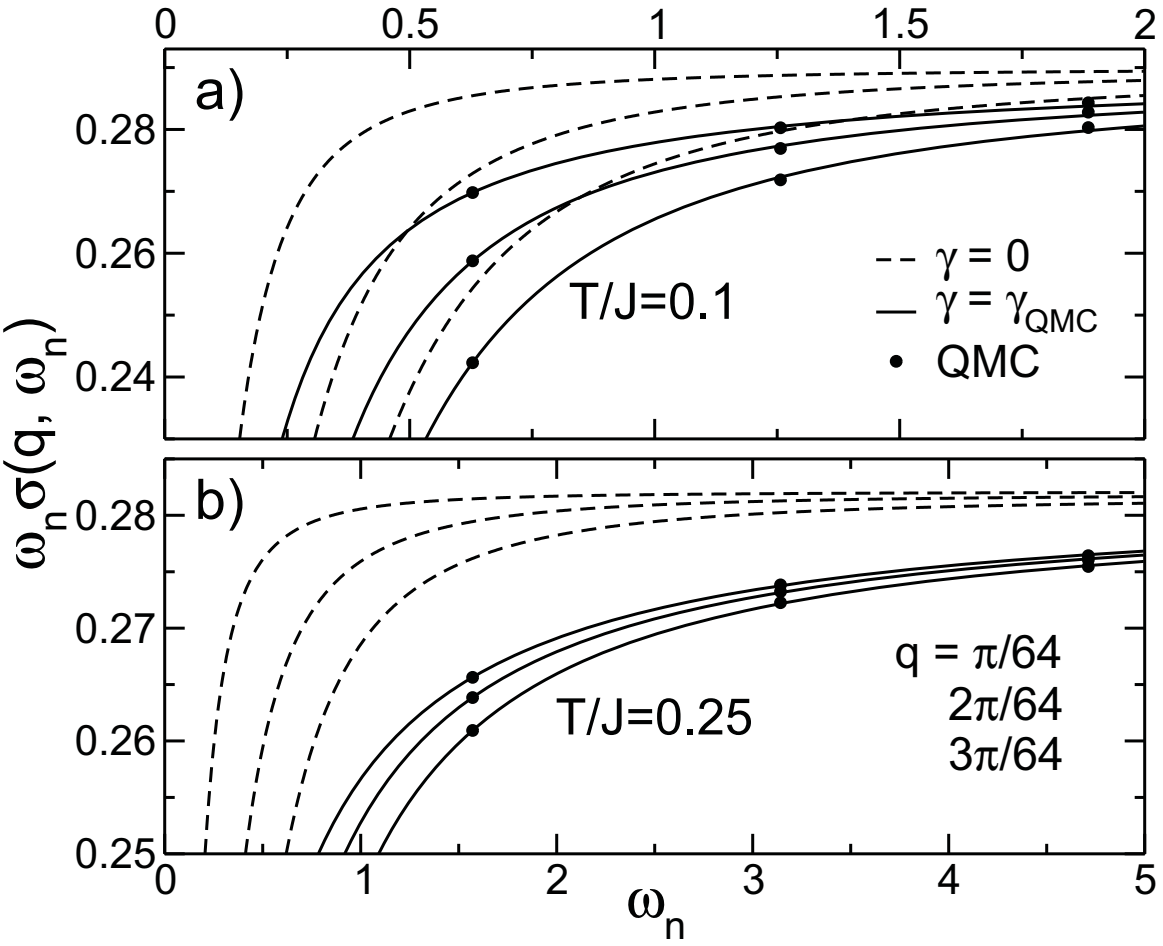

Figure 4.27: $\omega_n \sigma_{QMC}(q, \omega_n)$ from QMC for the first three non-zero Matsubara frequencies $\omega_n = 2\pi n T$ and wave vectors $q = n\pi/64$, with $n = 1, 2$, and 3 as compared to $\omega_n^2 \chi(q, \omega_n)/q^2$ using eqn. (4.22) with $\gamma = 0$ (dashed) and $\gamma = \gamma_{q,QMC}$ (solid) on a 128 site system for a) $T/J = 0.1$ and b) 0.25. (See text regarding statistical error.)

the expected increase of the static susceptibility with q. Finally, $\gamma_{q,QMC}/\gamma_B$ also displays a weak momentum dependence which is larger for $T/J = 0.1$. The latter may signal the onset of finite size effects. In fact, $\gamma_{q,QMC} \neq 0$ implies a length scale l of order $O(v/(2\gamma_{q,QMC}))$ for the regular current relaxation. l is less than the system size for both temperatures studied. Yet, $128/l \approx 9$ for $T/J = 0.25$ and and $128/l \approx 3$ for $T/J = 0.1$. With momentum dependence, γ as extracted from a real-space quantity [32] will differ from that obtained by QMC at fixed small momenta.

While the preceding has been exact up to the statistical error of the QMC, we would like to conclude this section by speculating on the line-shape of the regular part of the

conductivity on the imaginary frequency axis at $\omega_n = 2\pi nT$. In principle this requires a careful analysis of the error introduced by the Fourier transform $\chi_{QMC}(q,\omega_n) = \int_0^{1/T} \exp(i\omega_n\tau)\chi_{QMC}(q,\tau)d\tau$. This error will increase as ω_n increases. Here we refrain from analyzing this, since our goal is merely to demonstrate to which extend our QMC data discriminates between a conductivity with $\gamma = 0$ and one with $\gamma = \gamma_{q,QMC} \neq 0$. To this end Fig. 4.27 displays $\omega_n \sigma_{QMC}(q,\omega_n) = \omega_n^2 \chi_{QMC}(q,\omega_n)/q^2$ as compared to $\omega_n \sigma(q,\omega_n) = \omega_n^2 \chi(q,\omega_n)/q^2$ with $\chi(q,\omega_n)$ taken from eqn. (4.22) and with $\gamma = 0$ or $\gamma = \gamma_{q,QMC}$. Without any further ado, this figure clearly demonstrates that $\gamma = 0$ in $\sigma(q,\omega_n)$ from eqn. (4.21) and (4.22) is inconsistent with our QMC which however agrees very well with $\sigma(q,\omega_n)$ for $\gamma = \gamma_{q,QMC}$ [2]. This implies that QMC is consistent with a Drude type of behavior of the frequency dependence of the regular conductivity with a relaxation rate $2\gamma_{q,QMC}$. While future studies, may focus on finite size scaling, to perform the limit of $q \to 0$, as required in eqn. (4.21), this is beyond the scope of the present analysis.

Conclusion In conclusion QMC is consistent with spin dynamics of the isotropic 1D Heisenberg antiferromagnet which is primarily diffusive in the long wave-length limit and at intermediate temperatures, implying a *regular* part of the spin conductivity with a finite relaxation rate $\gamma \ll T$. This corroborates recent findings by bosonization and tTMRG. Our analysis does not allow conclusions on the pending open questions on the Drude weight at $\Delta = 1$, yet based on the numerical evidence for $D(T > 0) > 0$, our findings may open up the intriguing possibility of a finite temperature dynamical spin conductivity of the isotropic Heisenberg model which comprises of both, a finite Drude weight and a regular part with a very large mean free path at low temperatures. Future analysis should focus on the relevance of corrections beyond the on-shell approximation, on the case $\Delta < 1$, and on higher temperatures $T \gtrsim J$.

[2] For a different QMC approach, not suited to clarify the role of γ in $\sigma(q,\omega_n)$ see ref. [32]

Chapter 5

Conclusion

In my thesis, static and dynamic properties of low-dimensional spin models were studied by means of a state of the art QMC method (SSE). As one among many numerical algorithms (e.g. DMRG, ED), the QMC proved to be a very flexible and high-performance tool with access to dynamic correlation functions at finite temperatures and finite magnetic fields within the thermodynamic limit[1]. After detailed introduction of the QMC's basic implementation, I provided yet unpublished information about the measurement of transverse (and longitudinal) imaginary time correlation functions for the spin S Heisenberg model. In addition to that, complications of the analytic continuation to the real axis were explained and two common Maximum Entropy algorithms (Bryan and Meshkov) introduced briefly. In my thesis, both algorithms have been implemented and contrasted in regard to their performance and quality of the continuation, clearly favoring Bryan's method which is a standard least square algorithm based on Newton iterations with however *highly* optimized search directions in the multi-dimensional solution space.

As far as physics are concerned, we have shown published and unpublished results on very different low-dimensional Heisenberg spin systems with very different static and dynamic properties. Among them essentially zero-dimensional grid systems, critical half-integer spin chains and gapped spin liquids such as integer spin chains and ladder systems. In chapter 4, we focused entirely on static observables, starting with susceptibilities of quantum spin chains with variable spin magnitude $S \in \{1/2, 1, 3/2, 2, 5/2\}$

[1] Only very recent developments based on DMRG [40, 41] offered first finite temperature results on the spectrum of the spin S=1/2 Heisenberg chain in the thermodynamic limit outside finite size dominated ED, two- and four-spinon results by Bethe ansatz and QMC. Both methods proved consistency with our results published earlier in [228].

in comparison to classical $S \to \infty$ results by Fisher. After a finite size analysis of our results for temperatures down to $0.01 \leq T/J$, we found that, regarding the maximum position of the susceptibility and its low-temperature behavior, even for largest evaluated spins the deviations from classical results were still significant. To provide analytical access to our data, we performed Padé-fits and compared our results to high-accuracy Bethe-ansatz data for spin S=1/2. For spins of larger magnitude, our fits suggests improvements of commonly used fit formulas available in literature.

With the addition of an interchain-coupling, we analyzed a spin S=1 two-leg ladder system as function of leg/rung-coupling and single-ion anisotropy next. The predominant effect of variable rung/leg-coupling is a strong weakening of the spin gap in the intermediate regime, even though a two-leg ladder, uncoupled dimers as well as uncoupled Haldane chains show a *large* gap. With an additional easy-plane anisotropy the gap was lifted completely, resulting in a finite susceptibility down to $T/J = 0.001$ within the thermodynamic limit. After this surprising result, we turned to experimental data by Mennerich *et al.* of the Ni(II) two-leg ladder material $Na_2Ni_2(C_2O_4)_3(H_2O)_2$. With the extraction of coupling constants as well as single-ion anisotropies for experimental susceptibility and high-field magnetization data, we confirmed the picture of weakly-coupled dimers with a small easy-plane anisotropy which however is not enough to close the spin gap of the system [28].

Coming from systems in the thermodynamic limit in the previous two sections, we investigated thermodynamical properties of an essentially zero-dimensional Mn-[3×3]-grid system with large spin S=5/2 as function of center-spin and ring-coupling as well as the single-ion anisotropy D in the final section of chapter 4. While the effect of center-spin coupling is marginal (ultimately due to an odd total number of spins) with largest (albeit small) impact in the intermediate temperature region $1 \leq T/J \leq 10$, the response even to small single-ion anisotropies was significant. In fact, magnetization as well as (staggered) static structure factor agree on an Ising-like picture in the case of easy-plane *and* easy-axis anisotropies with a minimum- respectively maximum-z state of total spin S=1/2 in the case of easy-plane and S=5/2 in the case of easy-axis anisotropy. This becomes obvious in the low-temperature limit of the structure factor compared to results of a classical Neél state and in the step signature of the magnetization, showing the initial polarization of a spin S=1/2, respectively S=5/2 with adjacent $\Delta S = 1$ excitations. This strong impact of even small $|D|$ is a direct consequence of the large spin magnitude entering the Hamiltonian as square. In an attempt to fit the three parameters center-, ring-coupling and single-ion anisotropy J_c, J_r, D of the Mn-based material by means of the experimental

susceptibility provided by O. Waldmann, we narrowed the center- to ring-coupling ratio down to $2 \geq J_r/J_c \geq 1$ in combination with a small easy-plane anisotropy D=0.07K. Furthermore our magnetization data showed the expected level crossing of higher total spin S states with the ground state, leading to a step-like magnetization profile which qualitatively explained observed periodic oscillations in magneto-torque measurements in [30].

In chapter 4, we focused on dynamic properties of isotropic quantum spin chains with spin S=1/2, respectively S=1. We have shown the fundamentally different dynamic structure factors of these two systems and their evolution under different temperatures and magnetic fields up to (and beyond) saturation field. While the effects of temperature predominantly comes down to softening sharp structures into a broad energy continuum which ultimately leads to very similar dynamic structure factors of S=1/2 and S=1 for $T \geq J$, the role of the magnetic field changes the system's dynamics completely. In the case of S=1/2 and longitudinal excitations, the impact of a magnetic field was manifold. Firstly we found a strong concentration of spectral weight at $q \to 0$ and $\omega \to 0$, due to $S^{zz}(q,\omega)$ being proportional to the square of the magnetization at zero frequency which lead to an increased concentration of weight into the static structure factor at q=0. Secondly, the spectrum developed a gap at $q = \pi$ with a field driven incommensurate mode moving from the zone boundary to the center with $q_s = \pi(1 - 2\langle S^z \rangle)$. In the case of the transverse dynamic structure factor, long wave-length excitations experience the Zeeman energy, which lead to a spin gap of size B/J at q=0. Additionally, and as in the longitudinal case, an incommensurate zero mode was observed. In the transverse case however, it developed out of the zone center and moved to the zone boundary with $q_s = 2\pi\langle S^z \rangle$. At critical magnetic fields the system is fully polarized at T=0. Consequently we found the expected magnon cosine dispersion, however with a a nontrivial finite temperature q-dependence which was explained by a model-calculation of two-magnon excitations in a polarized background. Beyond the critical field the sharp magnon dispersion finally became gapped while the finite temperature signature on the q-dependence persisted. Coming from this gapped state, we showed a condensing of magnons upon decreasing the magnetic field through the saturation field by means of a diverging NMR-rate - interestingly however, the maximum of the rate was observed slightly *below* the critical field, most likely due to thermal broadening of spectral features. The extracted $1/T_1$-rates as function of temperature and magnetic field were successfully compared to NMR experiments on CuPzN by H. Kühne in [31, 259] for three different magnetic fields with each having about 50 temperature points. This considerable numerical effort was rewarded with excellent qualitative agreement of the three most significant choices of the field: at essentially zero field we found $1/T_1$ to be largely proportional

to the temperature as suggested by zero-field Luttinger liquid results (Korringa law). At the critical field, we find a diverging rate at low temperatures as an indication for the magnon excitations crossing the ground state. Finally, beyond the critical field, the system becomes gapped, resulting in a vanishing $1/T_1$ rate once thermal excitations freeze out. The shift of the rate's maximum with increasing temperatures proved to be consistent with the experimental data even on a quantitative level. To achieve best agreement of experiment and theory, the longitudinal spin fluctuations were suppressed by careful sample orientation and we adjusted the form factor to reflect the asymmetric carbon nucleus position with respect to the Cu(II) ions. The results, published in [31], were later elected as scientific highlight by the Los Alamos National High Magnetic Field Laboratory [260] and received further attention as Editor's Choice of Physica B in march 2010 [259].

While the spin S=1/2 system starts with a gapless continuum of states at zero magnetic field, the Haldane system displays a gapped excitation spectrum. The particular form is divided into a sharp magnon-mode at large q-vectors with the smallest gap Δ at exactly $q = \pi$ while we found signs of a continuum for $q \leq \pi/3$ with very low overall weight. We detailed the low-q behavior by looking at the eight lowest q-vectors to confirm field theory and tDMRG predictions of a two-magnon excitation with energy 2Δ and wave vectors $\pi, -\pi$. Additionally we found a secondary peak at higher frequencies which is probably caused by higher magnon excitations. The overall weight distribution of the spectrum reflects that of the static structure factor with very low weight at the zone center, following its quadratic dependency with respect to q. For the zone boundary, we identified the Haldane-gap and confirmed its exponential opening with temperature, as suggested by other theories and experimental data. Additionally, we extracted $1/T_1$-relaxation rates for each of the four evaluated temperatures $T/J \in \{0.1, 0.25, 0.5, 1.0\}$, which clearly show an exponentially activated form. It is interesting to note the origin of the weight contribution to the $1/T_1$ rate. At high temperatures, intra-band excitations resulted in high spectral weight at the zone center and likewise, by thermally populating the gap, high weight contribution stem from the zone boundary as well. There is *no* contribution from intermediate wave vectors. For lower temperatures, the gap opens and intra-band excitations freeze out, suppressing the relaxation rate already at $T/J = 0.1$.
Upon applying a magnetic field, the transverse dynamic structure factor displayed a linear closing of the Haldane-gap. After resolving the spectrum into S^+S^- and S^-S^+ contributions, we found the linear closing attributed to S^+S^- contributions while S^-S^+ was linearly opening with the field. This behavior lead to a splitting of the sharp magnon-dispersion at $q = \pi$ with thermal smearing of the two sharp contributions. At the zone center we found the expected linear opening of a gap, owing to the Zeeman

energy as in the case of spin S=1/2. Both, the opening of a gap at $q = 0$ and the closing of the gap at $q = \pi$, lead to an exponentially increased NMR-rate, driven solely by spectral weight at the zone boundary. Therefor the weight distribution is fundamentally different compared to that of the zero field temperature dependence where zone center and zone boundary contributed nearly equally.
Beyond this first critical field B_{c_1}, we found Luttinger liquid behavior in the dynamic structure factor, conceptually equal to the region $0 \leq B \leq B_c$ of the spin S=1/2 system, with however very faint incommensurate Fermi vectors. Finally at saturation field, the Haldane system is described by a sharp magnon cosine dispersion and we find the very same q-dependence of the weight as for the S=1/2 systems which we explained with higher-magnon excitations over a polarized background. To close both sections, we assessed the quality of our analytic continuation by utilizing sum rules for the static structure factor and the static susceptibility, as two quantities which can be obtained by the QMC free of the analytic continuation. For both systems, we proved *excellent* agreement for all evaluated temperatures and magnetic fields as all comparisons were within QMC error bars.

On basis of the high-precision imaginary time QMC data evaluated for the isotropic spin S=1/2 chain, we finally presented an excursion to spin transport properties by supporting the claim of a diffusive channel in the regular part of the spin conductivity [261] in section 4.3. Our analysis was based on an approximate expression for the fourier transform of the retarded spin susceptibility $\chi_{ret}(q,\omega)$, given by bosonization [32]. Instead of working in real space where the QMC is subject to errors introduced by the analytic continuation, we transformed the susceptibility onto imaginary time $\chi(q,\tau)$ in order to compare with QMC free of the MaxEnt. On that basis, we performed fits of the analytic results for the six lowest q-vectors with respect to three parameters: the Luttinger parameter K_q, the spinon velocity v_q and the scattering rate γ_q. For the latter, we allowed three different choices, namely (i) $\gamma_{q,QMC}$ as optimized by fitting, (ii) γ_B taken from bosonization, and finally (iii) $\gamma_q = 0$. Our fit results demonstrated clearly, that QMC is inconsistent with $\gamma_q = 0$ for both evaluated temperatures $T/J = 0.1, 0.25$ and that increasing γ_q significantly increases the quality of the fit up to a point where the analytic form is identical to QMC within standard deviation 2σ for almost all $\tau \in [0,\beta]$. As consequence, our analysis opens up for the intriguing possibility of a finite temperature dynamical spin conductivity which comprises both, a finite Drude weight and a regular part with a very large mean free path at low temperatures. Besides the clear inconsistency with $\gamma_q = 0$, we found that $\gamma_{q,QMC} > \gamma_B$, which could indicate relevant corrections to diffusion. As consistency check, we related our fit parameters to the isothermal susceptibility at $q = 0$ and compared with Bethe ansatz results from [7]. Even though K_q is renormalized considerably, the fit parameters show excellent

agreement with the BA results. As for the q-dependence of the fit parameters, we found that Luttinger parameter and spin velocity are largely independent of q. The scattering rate $\gamma_{q,QMC}$ however showed a strong momentum dependence only for $T/J = 0.1$ which may be related to on-setting finite size effects. Finally, we speculated on the line-shape of the regular part of the conductivity on the imaginary frequency axis at the Matsubara frequencies, which, despite the lack of a thorough error analysis of the fourier transform, *clearly* discriminates between a conductivity with $\gamma = 0$ and one with $\gamma = \gamma_{q,QMC} \neq 0$.

Bibliography

[1] Science **288** (2000).

[2] J. G. Bednorz and K. A. Müller, Z. Phys. B **64**, 189 (1986).

[3] P. Fulde, J. Keller, and G. Zwicknagl, Solid State Physics - Advances in Research and Applications **41**, 1 (1988).

[4] U. Schollwöck, J. Richter, D. J. J. Farnell, and R. F. Bishop, *Lecture Notes in Physics: Quantum Magnetism* (Springer Verlag, 2004).

[5] P. Jordan and E. Wigner, Z. Phys. **47**, 631 (1928).

[6] H. Bethe, Z. Physik **71**, 205 (1931).

[7] D. C. Johnston *et al.*, Phys. Rev. B **61**, 9558 (2000).

[8] F. D. M. Haldane, Phys. Rev. Lett. **47**, 1840 (1981).

[9] T. Giamarchi, *Quantum Physics in One Dimension* (Clarendon Press, Oxford, 2003).

[10] A. O. Gogolin, A. A. Nersesyan, and A. M. Tsvelik, *Bosonization Approach to Strongly Correlated Systems* (Cambridge University Press, 2004).

[11] S. Zhang, H. J. Schulz, and T. Ziman, Phys. Rev. Lett. **63**, 1110 (1989).

[12] I. Affleck, D. Gepner, H. J. Schulz, and T. Ziman, J. Phys. A: Math. Gen. **22**, 511 (1989).

[13] C. Lanczos, J. Res. Natl. Bur. Stand. **45**, 255 (1950).

[14] D. G. Pettifor*The Recursion Method and Its Applications* Vol. 58 (Springer Ser. Solid-State Sci., 1985).

[15] U. Schollwöck, Rev. Mod. Phys. **77**, 259 (2005).

[16] H. G. Evertz, Adv. in Phys. **52**, 1 (2003).

[17] A. O. Gogolin, A. A. Nersesyan, and A. M. Tsvelik, *Bosonization and Strongly Correlated Systems* (Cambridge University Press, 1998).

[18] F. D. M. Haldane, J. Phys. C: Solid State Phys. **14**, 2585 (1981).

[19] F. D. M. Haldane, Phys. Lett. **93A**, 464 (1983).

[20] M. den Nijs and K. Rommelse, Pys. Rev. B **40**, 4709 (1989).

[21] S. M. Girvin and D. P. Arovas, Phys. Scr. **T27**, 156 (1989).

[22] H. Tasaki, Phys. Rev. Lett. **47**, 798 (1991).

[23] E. Dagottot and T. M. Rice, Science **271**, 618 (1996).

[24] T. Nikuni, M. Oshikawa, A. Oosawa, and H. Tanaka, Phys. Rev. Lett. **84**, 5868 (2000).

[25] T. Giamarchi and A. M. Tsvelik, Phys. Rev. B **59**, 11398 (1999).

[26] R. M. Konig and P. Fendley, Phys. Rev. B **66**, 144416 (2002).

[27] M. E. Fischer, Amer. J. Phys. **32**, 342 (1964).

[28] C. Mennerich *et al.*, Phys. Rev. B **73**, 174415 (2006).

[29] O. Waldmann, L. Zhao, and L. K. Thompson, Phys. Rev. Lett. **88**, 066401 (2002).

[30] O. Waldmann *et al.*, Phys. Rev. Lett. **92**, 096403 (2004).

[31] H. Kühne *et al.*, Phys. Rev. B **80**, 045110 (2009).

[32] J. Sirker, R. G. Pereira, and I. Affleck, arXiv:0906.1978v1 [cond-mat.str-el] (2009).

[33] M. Karbach, K. Hu, and G. Müller, cond-mat/9809163 (1998).

[34] M. Karbach, K. Hu, and G. Müller, cond-mat/008018 (2000).

[35] M. P. Gelfand, R. R. Singh, and D. A. Huse, J. Stat. Phys. **59**, 1093 (1990).

[36] N. Elstner, R. L. Glenister, R. R. P. Singh, and A. Sokol, Phys. Rev. B **51**, 8984 (1995).

[37] C. Domb and M. S. Green, *Phase Transitions and Critical Phenomena* (Academic Press, 1974).

[38] M. Karbach and G. Müller, cond-mat/9809162 (1997).

[39] J. Sirker and A. Klümper, Phys. Rev. B **71**, 241101(R) (2005).

[40] T. Barthel, U. Schollwöck, and S. R. White, Phys. Rev. B **79**, 245101 (2009).

[41] J. Kokalj and P. Prelovšek, Phys. Rev. B **80**, 205117 (2009).

[42] A. W. Sandvik and J. Kurkijärvi, Phys. Rev. B **43**, 5950 (1991).

[43] J. K. Kim, D. P. Landau, and M. Troyer, Phys. Rev. Lett. **79**, 1583 (1997).

[44] P. Helenius and A. W. Sandvik, Phys. Rev. B **62**, 1102 (2000).

[45] J. Wojtkiewicz, Phys. Rev. B **75**, 174421 (2007).

[46] N. Metropolis, A. W. Rosenbluth, M. N. Rosenbluth, A. H. Teller, and E. Teller, J. of Chem. Phys. **21**, 6 (1953).

[47] D. C. Handscomb, Proc. Cambridge Philos. Soc. **58**, 594 (1962).

[48] A. W. Sandvik, Phys. Rev. B **56**, 11678 (1997).

[49] A. W. Sandvik, Phys. Rev. B **59**, R14157 (1999).

[50] O. F. Syljuåsen and A. W. Sandvik, Phys. Rev. E **66**, 046701 (2002).

[51] A. W. Sandvik and O. F. Syluåsen, cond-mat/0306542 (2003).

[52] S. Chandrasekharan and U.-J. Wiese, Phys. Rev. Lett. **83**, 3116 (1999).

[53] Linear-Programming-Solver, http://groups.yahoo.com/group/lp_solve/ .

[54] O. F. Syljuåsen, Phys. Rev. E **67**, 046701 (2003).

[55] S. Meshkov and D. Berkov, Int. J. Mod. Phys. C **5**, 987 (1994).

[56] J. Skilling and R. K. Bryan, Mon. Notices R. Astron. Soc. **211**, 111 (1984).

[57] http://www.netlib.org/lapack/ .

[58] A. N. Tikhonov and V. Y. Vasiliy, *Solutions of ill-posed problems* (Wiley, New York, 1977).

[59] J. Skilling, *The axioms of maximum entropy* (Kluwer Academic Publishers, 1988).

[60] S. Gull and G. Daniell, Nature **272**, 686 (1978).

[61] J. Skilling, *Maximum Entropy and Bayesian Methods* (Kluwer Academic Publishers, 1994).

[62] J. E. Gubernatis, M. Jarrell, R. N. Silver, and D. S. Sivia, Phys. Rev. B **44**, 6011 (1991).

[63] H. Touchette and D. Poulin, Aspects numériques des simulations du modele de hubbard: Monte carlo quantique et méthode d'entropie maximum, 1999.

[64] R. R. Bartkowski and B. Morosin, Phys. Rev. B **6**, 4209 (1972).

[65] A. U. B. Wolter *et al.*, Phys. Rev. B **68**, 220406(R) (2003).

[66] J. P. Renard *et al.*, J. Appl. Phys. **63**, 3538 (1988).

[67] J. P. Renard *et al.*, Europhys. Lett. **3**, 945 (1987).

[68] Z. Honda, H. Asakawa, and K. Katsumata, Phys. Rev. Lett. **81**, 2566 (1998).

[69] T. Ishida, S.-I. Mitsubori, T. Nogami, and H. Iwamura, Molecular Crystals and Liquid Crystals **233**, 345 (1993).

[70] D. B. Losee, H. W. Richardson, and W. E. Hatfield, J. Chem. Phys. **59**, 3600 (1973).

[71] G. Mennenga, L. J. de Jongh, W. J. Huiskamp, and J. Reedijk, J. Magn. Magn. Mater. **44**, 89 (1984).

[72] J. Villain and J. M. Loveluck, J. Phys. (France) Lett. **38**, L77 (1977).

[73] K. Ishida *et al.*, J. Phys. Soc. Jpn. **63**, 3222 (1994).

[74] N. Motoyama, H. Eisaki, and S. Uchida, Phys. Rev. Lett. **76**, 3212 (1996).

[75] D. C. Dender, P. R. Hammar, D. H. Reich, C. Broholm, and G. G. Aeppli, Phys. Rev. Lett. **79**, 1750 (1997).

[76] K. Katsumata *et al.*, Phys. Rev. Lett. **63**, 86 (1989).

[77] Y. Ajiro, T. Goto, H. Kikuchi, T. Sakakibara, and T. Inami, Phys. Rev. Lett. **63**, 1424 (1989).

[78] S. Ma, C. Broholm, D. H. Reich, B. J. Sternlieb, and R. W. Erwin, Phys. Rev. Lett. **69**, 3571 (1992).

[79] R. M. Morra, W. J. L. Buyers, R. L. Armstrong, and K. Hirakawa, Phys. Rev. B **38**, 543 (1988).

[80] Z. Tun, W. J. L. Buyers, R. L. Armstrong, K. Hirakawa, and B. Briat, Phys. Rev. B **42**, 4677 (1990).

[81] M. Steiner, K. Kakurai, J. K. Kjems, D. Petitgrand, and R. Pynn, J. Appl. Phys. **61**, 3953 (1987).

[82] K. Kakurai, M. Steiner, R. Pynn, and J. K. Kjems, J. Phys. Condens. Matter **3**, 715 (1991).

[83] J. Darriet and L. P. Regnault, Solid State Commun. **86**, 409 (1993).

[84] Y. Chen *et al.*, Phys. Rev. Lett. **86**, 1618 (2001).

[85] M. Hagiwara, Z. Honda, K. Katsumata, A. K. Kolezhuk, and H.-J. Mikeska, Phys. Rev. Lett. **91**, 177601 (2003).

[86] A. Zheludev, Z. Honda, C. Broholm, and K. Katsumata, Phys. Rev. Lett. **88**, 077206 (2002).

[87] A. Zheludev *et al.*, Phys. Rev. B **68**, 134438 (2003).

[88] A. Zheludev *et al.*, Phys. Rev. B **69**, 054414 (2004).

[89] H. Kadowaki, K. Hirakawa, and K. Ubukoshi, J. Phys. Soc. Jpn. **52**, 1799 (1983).

[90] S. Itoh, Y. Endoh, K. Kakurai, and H. Tanaka, Phys. Rev. Lett. **74**, 2375 (1995).

[91] G. E. Granroth *et al.*, Phys. Rev. Lett. **77**, 1616 (1996).

[92] R. J. Birgenau, R. Dingle, M. T. Hutchings, G. Shirane, and S. L. Holt, Phys. Rev. Lett. **26**, 718 (1971).

[93] M. T. Hutchings, G. Shirane, R. J. Birgenau, and S. L. Holt, Phys. Rev. B **5**, 1999 (1972).

[94] P. W. Anderson, Phys Rev. **86**, 694 (1952).

[95] R. Kzbo, Phys. Rev. **87**, 568 (1952).

[96] T. Oguchi, Phys. Rev. **117**, 117 (1960).

[97] G. S. Rushbrooke and P. J. Wood, Mol. Phys. **1**, 257 (1958).

[98] G. A. Baker, H. E. Gilbert, J. Eve, and G. S. Rushbrooke, Phys. Rev. **164**, 800 (1967).

[99] E. Ising, Z. Physik **31**, 253 (1925).

[100] H. L. Davis, Phys. Rev. **120**, 789 (1960).

[101] D. Huse, Phys. Rev. B **37**, 2380 (1988).

[102] A. Klümper and D. C. Johnston, Phys. Rev. Lett. **84**, 4701 (2000).

[103] W. Hiller *et al.*, J. Am. Chem. Soc. **106**, 329 (1984).

[104] R. B. Griffiths, Phys. Rev. **133**, A768 (1964).

[105] S. R. White and D. A. Huse, Phys. Rev. B **48**, 3844 (1993).

[106] X. Wang, S. Qin, and L. Yu, Phys. Rev. B **60**, 14529 (1999).

[107] C. H. Weng, PhD thesis, Carnegie-Mellon University, Pittsburg, 1968.

[108] A. Meyer, A. Gleizes, J.-J. Girerd, M. Verdaguer, and O. Kahn, Inorg. Chem. **21**, 1729 (1982).

[109] S. Eggert, I. Affleck, and M. Takahashi, Phys. Rev. Lett. **73**, 332 (1994).

[110] E. Dagotto and T. M. Rice, Science **271**, 618 (1996).

[111] E. Dagotto, Rep. Prog. Phys. **62**, 1525 (1999).

[112] E. Dagotto, J. Riera, and D. Scalapino, Phys. Rev. B **45**, 5744 (1992).

[113] I. Afflek, T. Kennedy, E. H. Lieb, and H. Tasaki, Phys. Ref. Lett. **59**, 799 (1987).

[114] T. Takeuchi *et al.*, J. Phys. Soc. Jp. **61**, 3255 (1998).

[115] D. Sénéchal, Phys. Rev. B **52**, 15319 (1995).

[116] D. Allen and D. Sénéchal, Phys. Rev. B **61**, 12134 (2000).

[117] S. Todo, M. Matsumoto, C. Yasuda, and H. Takayama, Phys. Rev. B **64**, 224412 (2001).

[118] W. Chen, K. Hida, and B. Sanctuary, Phys. Rev. B **67**, 104401 (2003).

[119] F. Cooper, B. Freedman, and D. Preston, Nucl. Phys. B **210**, 210 (1982).

[120] B. Barbara and L. Gunther, Physics World **35** (1999).

[121] A. Caneschi *et al.*, J. magn. Mater, **200**, 182 (1999).

[122] J. M. Clemente-Juan and E. Coronado, Coordin. CHem. Rev. **193-195**, 361 (1999).

[123] R. E. P. Winpenny, Adv. Inorg. Chem. **52**, 1 (2001).

[124] D. Gatteschi and R. Sessoli, Angew. Chem. Int. Ed. **42**, 268 (2003).

[125] R. Basler *et al.*, Chem. Phys. Chem. **4**, 910 (2003).

[126] S. J. Blundell and F. L. Pratt, J. Phys. Condens. Matter **16**, R771 (2004).

[127] D. Gatteschi, A. Caneschi, L. Pardi, and R. Sessoli, Science **265**, 1054 (1994).

[128] T. Guidi *et al.*, Phys. Rev. B **69**, 104432 (2004).

[129] D. J. Earl and M. W. Deem, Phys. Chem. Chem. Phys. **7**, 3910 (2005).

[130] T. Ami *et al.*, Phys. Rev. B **51**, 5994 (1995).

[131] M. Takigawa, N. Motoyama, H. Eisaki, and S. Uchida, Phys. Rev. Lett. **76**, 4612 (1996).

[132] D. B. Losee, H. W. Richardson, and W. E. Hatfield, J. Chem. Phys. **59**, 3600 (1973).

[133] M. B. Stone *et al.*, Phys. Rev. Lett. **91**, 037205 (2003).

[134] M. Takigawa, O. A. Starykh, A. W. Sandvik, and R. R. P. Singh, Phys. Rev. B **56**, 13681 (1997).

[135] K. R. Thurber, A. W. Hunt, T. Imai, and F. C. Chou, Phys. Rev. Lett. **87**, 247202 (2001).

[136] A. U. B. Wolter *et al.*, Phys. Rev. Lett. **94**, 057204 (2005).

[137] F. L. Pratt, S. J. Blundell, T. Lancaster, C. Baines, and S. Takagi, Phys. Rev. Lett. **96**, 247203 (2006).

[138] F. Heidrich-Meisner, A. Honecker, and W. Brenig, Eur. Phys. J. Special Topics **151**, 135 (2007).

[139] A. V. Sologubenko, T. Lorenz, H. R. Ott, and A. Freimuth, J. Low. Temp. Phys. **147**, 387 (2007).

[140] J. des Cloizaux and J. J. Pearson, Phys. Rev. **128**, 2131 (1962).

[141] T. Yamada, Prog. Theor. Phys. Jpn. **41**, 880 (1969).

[142] G. Müller, H. Thomas, H. Beck, and J. C. Bonner, Phys. Rev. B **24**, 1429 (1981).

[143] J. C. Bonner and H. J. W. Blöte, Phys. Rev. B **25**, 6959 (1982).

[144] K. Lefmann and C. Rischel, Phys. Rev. B **54**, 6340 (1996).

[145] T. D. Kuhner and S. R. White, Phys. Rev. B **60**, 335 (1999).

[146] D. Gobert, C. Kollath, U. Schollwöck, and G. Schutz, Phys. Rev. E **71**, 036102 (2005).

[147] A. H. Bougourzi, M. Couture, and M. Kacir, Phys. Rev. B **54**, 12669 (1996).

[148] M. Karbach, G. Müller, A. H. Bougourzi, A. Fledderjohann, and K. H. Mütter, Phys. Rev. B **55**, 12510 (1997).

[149] A. H. Bougourzi, M. Karbach, and G. Müller, Phys. Rev. B **57**, 11429 (1998).

[150] A. H. Bougourzi, Mod. Phys. Lett. B **10**, 1237 (1996).

[151] A. Abadaa, A. H. Bougourzib, and B. Si-Lakhala, Nucl. Phys. B **497**, 733 (1997).

[152] B. S. Lakhal and A. Abada, Physica B **369**, 196 (2005).

[153] J. S. Caux and R. Hagemans, J. Stat. Mech. **P12013** (2006).

[154] N. Kitanine, J. M. Maillet, and V. Terras, Nucl. Phys. B **567**, 554 (2000).

[155] J. S. Caux, R. Hagemans, and J. M. Maillet, J. Stat. Mech.: Theor. and Expm. **123**, 9003 (2005).

[156] D. Biegel, M. Karbach, and G. Müller, Europhys. Lett. **59**, 882 (2002).

[157] D. Biegel, M. Karbach, and G. Müller, J. Phys. A: Math. Gen. **36**, 5361 (2003).

[158] J. Sato, M. Shiroishi, and M. Takahashi, J. Phys. Soc. Jp. **73**, 3008 (2004).

[159] M. Karbach and G. Müller, Phys. Rev. B **62**, 14871 (2000).

[160] J.-S. Caux and J. M. Maillet, Phys. Rev. Lett. **95**, 077201 (2005).

[161] H. J. Schulz, Phys. Rev. B **34**, 6372 (1986).

[162] M. Pustilnik, M. Khodas, A. Kamenev, and L. I. Glazman, Phys. Rev. Lett. **96**, 196405 (2006).

[163] R. G. Pereira *et al.*, Phys. Rev. Lett. **96**, 257202 (2006).

[164] R. G. Pereira *et al.*, J. Stat. Mech. **P08022** (2007).

[165] K. Fabricius, U. Löw, and J. Stolze, Phys. Rev. B **55**, 5833 (1997).

[166] K. Fabricius and B. M. McCoy, Phys. Rev. B **57**, 8340 (1998).

[167] F. Heidrich-Meisner, A. Honecker, D. C. Cabra, and W. Brenig, Phys. Rev. B **68**, 134436 (2003).

[168] J. Sirker, Phys. Rev. B **73**, 224424 (2006).

[169] M. Jarrell and J. E. Gubernatis, Phys. Rep. **269**, 133 (1996).

[170] J. Deisz, M. Jarrell, and D. L. Cox, Phys. Rev. B **42**, 4869 (1990).

[171] J. Deisz, M. Jarrell, and D. L. Cox, Phys. Rev. B **48**, 10227 (1993).

[172] O. A. Starykh, A. W. Sandvik, and R. R. P. Singh, Phys. Rev. B **55**, 14953 (1997).

[173] I. Affleck, Phys. Rev. B **41**, 6697 (1990).

[174] I. Affleck, Phys. Rev. B **43**, 3215 (1991).

[175] E. S. Sorensen and I. Affleck, Phys. Rev. Lett. **71**, 1633 (1993).

[176] A. Oosawa, H. A. Katori, and H. Tanaka, Phys. Rev. B **63**, 134416 (2001).

[177] C. Rüegg *et al.*, Nature **423**, 62 (2003).

[178] G. Misguich and M. Oshikawa, J. Phys. Soc. Jpn. **73**, 3429 (2004).

[179] S. E. Sebastian *et al.*, Nature **441**, 617 (2006).

[180] G. Chaboussant *et al.*, Phys. Rev. B **55**, 3046 (1997).

[181] B. C. Watson *et al.*, Phys. Rev. Lett. **86**, 5168 (2001).

[182] T. Lorenz *et al.*, Phys. Rev. Lett. **100**, 067208 (2008).

[183] V. S. Zapf *et al.*, Phys. Rev. Lett. **96**, 077204 (2006).

[184] S. A. Zvyagin *et al.*, Phys. Rev. Lett. **98**, 047205 (2007).

[185] H. Manaka, I. Yamada, Z. Honda, H. A. Katori, and K. Katsumata, J. Phys. Soc. Jpn. **67**, 3913 (1998).

[186] V. O. Garlea *et al.*, Phys. Rev. Lett. **98**, 167202 (2007).

[187] M. P. Nightingale and H. W. J. Blöte, Phys. Rev. B **33**, 659 (1986).

[188] M. Takahashi, Phys. Rev. Lett. **62**, 2313 (1989).

[189] S. R. White, Phys. Rev. Lett. **69**, 2863 (1992).

[190] Y. Wang, ond-mat/0306365 .

[191] W. J. L. Buyers *et al.*, Phys. Rev. Lett. **56**, 371 (1986).

[192] A. Zheludev, Z. Honda, K. Katsumara, R. Feyerherm, and K. Prokes, Europhys. Lett. **55**, 868 (2001).

[193] H. Mutka *et al.*, Phys. Rev. Lett. **67**, 497 (1991).

[194] I. A. Zaliznyak, S.-H. Lee, and S. V. Petrov, Phys. Rev. Lett. **87**, 017202 (2001).

[195] I. A. Zaliznyak, J. Appl. Phys. **91**, 8390 (2002).

[196] C. Rüegg *et al.*, Appl. Phys. A: Mater. Sci. Process. **74**, S840 (2002).

[197] C. Rüegg *et al.*, Nature **423**, 62 (2003).

[198] M. B. Stone, I. A. Zaliznyak, T. Hong, C. L. Broholm, and D. H. Reich, Nature **440**, 187 (2006).

[199] C. Rüegg *et al.*, Phys. Rev. Lett. **101**, 247202 (2008).

[200] B. Thielemann *et al.*, Phys. Rev. Lett. **102**, 107204 (2009).

[201] I. Affleck and R. A. Weston, Phys. Rev. B **45**, 4667 (1992).

[202] T. Jolicoeur and O. Golinelli, Phys. Rev. B **50**, 9265 (1994).

[203] F. H. L. Essler and I. Affleck, J. Stat. Mech. , P12006 (2004).

[204] A. M. Tsvelik, Phys. Rev. B **42**, 10499 (1990).

[205] O. F. Syljuåsen, Phys. Rev. B **78**, 174429 (2008).

[206] S. V. Meshkov, Phys. Rev. B **48**, 6167 (1993).

[207] S. R. White and I. Affleck, Phys. Rev. B **77**, 134437 (2008).

[208] X. Zotos, F. Naef, and P. Prelovšek, Phys. Rev. B **55**, 11029 (1997).

[209] J. P. Groen *et al.*, Phys. Rev. B **22**, 5369 (1980).

[210] N. Bloembergen, Physica (Amsterdam) **15**, 386 (1949).

[211] P. G. de Gennes, J. Phys. Chem. Solids **4**, 223 (1958).

[212] Y. J. Kim, M. Greven, U.-J. Wiese, and R. J. Birgeneau, Eur. Phys. J. B **4**, 291 (1998).

[213] L. N. Bulaevskii, Sov. Phys. JETP **16**, 685 (1963).

[214] S. Inawashiro and S. Katsura, Phys. Rev. **140**, A 892 (1965).

[215] A. J. Silverstein and Z. G. Soos, J. Chem. Phys. **53**, 326 (1970).

[216] M. D. Johnson and M. Fowler, Phys. Rev. B **34**, 1728 (1986).

[217] J. B. Parkison and J. C. Bonner, Phys. Rev. B **32**, 4703 (1985).

[218] E. Pytte, Phys. Rev. B **10**, 4637 (1974).

[219] N. Ishimura and H. Shiba, Prog. Theor. Phys. Jpn. **57**, 1862 (1977).

[220] M. Karbach, K.-H. Mütter, and M. Schmidt, J. Phys.: Condens. Matter **7**, 2829 (1995).

[221] T. Moriya, Prog. Theor. Phys. **16**, 23 (1956).

[222] P. R. Hammar *et al.*, Phys. Rev. B **59**, 1008 (1999).

[223] T. Lancaster *et al.*, Phys. Rev. B **73**, 020410(R) (2006).

[224] A. V. Sologubenko *et al.*, Phys. Rev. Lett. **98**, 107201 (2007).

[225] L. J. Azevedo, A. Narath, P. M. Richards, and Z. G. Soos, Phys. Rev. B **21**, 2871 (1980).

[226] B. S. Lakhal and A. Abada, J. Phys. A: Math. Gen. **37**, 497 (2005).

[227] P. C. Hohenberg and W. F. Brinkman, Phys. Rev. B **10**, 128 (1974).

[228] S. Grossjohann and W. Brenig, Phys. Rev. B **79**, 094409 (2009).

[229] A. Kolezhuk and S. Sachdev, Phys. Rev. Lett. **96**, 087203 (2006).

[230] M. Sato, J. Stat. Mech. , P09001 (2006).

[231] A. Furusaki and S. C. Zhang, Phys. Rev. B **60**, 1175 (1999).

[232] Z. Honda, K. Katsumata, M. Hagiwara, and M. Tukunaga, Phys. Rev. B **60**, 9272 (1999).

[233] K. Damle and S. Sachdev, Phys. Rev. B **57**, 8307 (1998).

[234] S. Yamamoto and H. Hori, J. Phys. Soc. Jpn. **73**, 822 (2004).

[235] M. Takigawa, T. Asano, Y. Ajiro, and Y. J. Uemura, Phys. Rev. Lett. **76**, 2173 (1996).

[236] S. Maslov and A. Zheludev, Phys. Rev. B **57**, 68 (1998).

[237] P. Gaveau, J. P. Boucher, L. P. Regnault, and J. P. Renard, Europhys. Lett. **12**, 647 (1990).

[238] N. Fujiwara, T. Goto, S. Maegawa, and T. Kohmoto, Phys. Rev. B **45**, 7837 (1992).

[239] N. Fujiwara, T. Goto, S. Maegawa, and T. Kohmoto, Phys. Rev. B **47**, 11860 (1993).

[240] J. Sagi and I. Affleck, Phys. Rev. B **53**, 9188 (1996).

[241] B. S. Shastry and B. Sutherland, Phys. Rev. Lett. **65**, 243 (1990).

[242] X. Zotos, Phys. Rev. Lett. **82**, 1764 (1999).

[243] J. Benz, T. Fukui, A. Klümper, and C. Scheeren, J. Phys. Soc. Jpn. Suppl. **74**, 181 (2005).

[244] Z. Qiu-Lan and G. Shi-Jian, Chinese Physics Letters **24**, 1354 (2007).

[245] J. V. Alvarez and C. Gros, Phys. Rev. B **66**, 094403 (2002).

[246] D. Heidarian and S. Sorella, Phys. Rev. B **75**, 241104(R) (2007).

[247] B. N. Narozhny, A. J. Millis, and N. Andrei, Phys. Rev. B **58**, R2921 (1998).

[248] P. Jung and A. Rosch, Phys. Rev. B **76**, 245108 (2007).

[249] S. Mukerjee and B. S. Shastry, Phys. Rev. B **77**, 245131 (2008).

[250] F. Heidrich-Meisner, A. Honecker, and W. Brenig, Phys. Rev. B **71**, 184415 (2005).

[251] M. Michel, O. Hess, H. Wichterich, and J. Gemmer, Phys. Rev. B **77**, 104303 (2008).

[252] T. Prosen and M. Znidaric, J. Stat. Mech.: Theor. Exp. **(2009)**, P02035.

[253] S. Langer, F. Heidrich-Meisner, J. Gemmer, I. P. McCulloch, and U. Schollwöck, Phys. Rev. B **79**, 214409 (2009).

[254] X. Zotos and P. Prelovšek, Phys. Rev. B **53**, 983 (1996).

[255] F. Naef and X. Zotos, J. Phys. C **10**, L183 (1998).

[256] S. Lukyanov, Nucl. Phys. B **522**, 533 (1998).

[257] Fits performed using *mathematica*®.

[258] A. Klümper, private communication.

[259] H. Kühne *et al.*, Physica B **247**, 671 (2010).

[260] http://www.magnet.fsu.edu/usershub/publications/sciencehighlights/2009/reyes-27july2009.pdf.

[261] S. Grossjohann and W. Brenig, Phys. Rev. B **81**, 012404 (2010).

The very last lines ...

... will be dedicated to the people who gave advice, support and joy during the time of my thesis.

First of all, I would like to thank my supervisor Prof. Dr. W. Brenig for his incredible patience, his well chosen words and his continued support during all those years. In the very beginning you claimed, that I would lose my respect someday, but it turns out that this claim is the only thing you were ever wrong about.

Also, I want to honor my closest co-workers during the time in Braunschweig, namely Christopher Mennerich and Hannes Kühne, both inspiring by their enthusiasm, thoroughness and positive attitude. We have spent quite some time together, be it on DPG conferences, working on publications or by trying to figure out the little details of experiment versus theory. Their supervisor, Hans-Henning Klauß, has also earned my special gratitude for being the reason I actually dared to study physics. In just one hour he managed to distract weeks of worries by his lovely tour through the physic institutes. Also he kindly accepted to attend my defense as representative of the experimental physics department to close the chapter he started. Two other people who have their certain spot in this list of inspiration and motivation are Fabian Heidrich-Meißner and Andreas Honecker. I will always admire your all-embracing interest and your competence on so many levels and lastly, who did not simply love the sight of Andreas Honecker 'flying' back home on his bike?

After the co-workers of my thesis, it is time to give a shout out to my *actual* co-workers, namely my current workgroup members. In fact, the term workgroup has evolved quite a bit during my thesis – what started as AG Motschmann, AG Zwicknagl and AG Brenig with merely shared subnets has come together in a refreshing way during the last two years. I will always remember our fierce go-cart races, our heroic wake-board and water-ski experiments on the Salzgitter lake and the daily dose of lunch and after-lunch table-tennis, which is probably the sole reason I can still walk upright. Special thanks for the great time go out to Björn Willenberg, Rachid Darradi, Robin Steinigeweg, Marcelo Arlego from AG Brenig, Alexander Bößwetter, Jean-Matthias Griessmeier, Sven Simon, Joachim Müller, Hendrik Kriegel, Erik Johansson, Christoph Koenders, Stefan Wiehle from AG Motschmann and Matthias Neef and Brendan E. Coughlan from AG Zwicknagl. At this point I also have to mention our lovely secretaries, Renate Strassek and Conny Schmidt, for generously sharing precious sweets, for filling the corridors of the third floor with laughter, and for being tough contenders in our table-tennis rounds. As member of our friday seminar, without attending our water- and motorsport sessions however, I am deeply indepted to Prof. Dr. G. Zwicknagl for her kind offer to review my diploma and also my phd thesis.

Finally I want to thank everyone outside the world of physics – my parents, my little-but-not-so-little-afterall brother, my grandmums and my two granddads who both sadly missed out on the final chapter of my time at the physics department. Lastly, all my love to the two girls at my side, Malaika and Amy. Where would I be without your patience, support and cheering up. Also, how would I ever get up in the morning without that furry nose in my face?